UNIVERSITÉ PARIS-SUD XI
INSTITUT DE PHYSIQUE NUCLÉAIRE D'ORSAY

École doctorale : Modélisation et Instrumentation en Physique, Energies, Géosciences et Environnement

THÈSE DE DOCTORAT

Discipline : Physique Nucléaire

présentée par

Tingting LIU

pour obtenir le grade de Docteur de l'Université Paris-Sud

Exclusive measurements with the spectrometer HADES in proton-proton reactions at 1.25 GeV

Soutenue publiquement le 13 décembre 2010 devant le jury composé de :

M. Jörg AICHELIN	Rapporteur
Mme. Hélène FONVIEILLE	Examinateur
M. Romain HOLZMANN	Rapporteur
M. Frank MAAS	Examinateur
Mme. Béatrice RAMSTEIN	Directrice de thèse
M. Hagop SAZDJIAN	Président de jury

Table des matières

Outline

Systematic investigations of di-electron production are performed with HADES (High Acceptance Di-Electron Spectrometer) at GSI, Darmstadt. The main goal of this experiment is to study hadronic matter at moderate temperatures and densities using the di-electron probe. This requires a detailed understanding of the di-electron emission from hadronic systems. The strategy of HADES is to start with light $A + A$ systems and $N + N$ reactions which allow for a validation of the detector performance and a good control of different individual di-electron sources. In this PhD work, new results obtained in proton-proton collisions at 1.25 kinetic energy are presented. They pave the way to a detailed understanding of the processes involving the $\Delta(1232)$ resonance and, especially the Dalitz decay of the Δ^+ resonance ($\Delta^+ \rightarrow pe^+e^-$).

In chapter one, I will start with the presentation of the general physics motivations of HADES experiments. The first data measured by HADES in heavy-ion reactions will be briefly discussed. From the results of the heavy-ion reactions, the importance of elementary reactions is deduced. Finally, I will outline the knowledge about the Δ (1232) resonance production which is the most important process in the $p + p$ reactions at 1.25 GeV and will be studied in this PhD.

In chapter two, the description of the HADES spectrometer will be given with emphasis on the MDC (Mini-Drift Chamber) sub-detector. The experimental conditions specific to the $p + p$ run at 1.25 GeV will be presented as well.

In chapter three, the simulation framework together with the models/ingredients used for this PhD work will be shown. A detailed study of the reaction kinematics and the influence from the detector acceptance and efficiency will be presented, for $pp \rightarrow np\pi^+$ reaction which is the main reaction channel studied in this PhD.

In chapter four, I aim at demonstrating the experimental data analysis methods which have been developed in the framework of this thesis : event selection, trigger condition correction and error estimation, etc.

In chapter five, the results of exclusive one-pion production channels in $p + p$ reactions will be discussed, with main emphasis on the $pp \rightarrow np\pi^+$ channel. The measured spectra, such as invariant mass and angular distributions, are compared to the simulation and an integrated cross section is extracted. At the end, the hadronic channels measured at 1.25 GeV combined with the same measurements also performed at 2.2 GeV will be shown to give a global view of the pion production and role of resonances in the 1-2 GeV range in $p + p$ reactions.

In chapter six, I will talk about the data analysis and simulations of another exclusive channel $pp \rightarrow ppe^+e^-$ which is suited to reconstruct exclusively the Δ Dalitz decay process. The data analysis which is currently in progress by the HADES collaboration will be briefly shown, while I will stress in more detail my contribution to the simulation study of the helicity distribution

in this channel.

In chapter seven, the PhD work presented in this document will be summarised. The conclusions and outlook will be derived.

Chapitre 1

Introduction

The main goal of the HADES[1] experiment at SIS[2] is to explore strongly interacting matter in heavy-ion collisions in the 1-2 A GeV range. In these conditions, moderate temperatures ($T < 80$ MeV) but rather high densities ($\rho \sim (2-3) \cdot \rho_0$) can be achieved.

In ultra-relativistic heavy-ion reactions as studied at RHIC[3] or at CERN[4], an unconfined state, the so-called Quark-Gluon Plasma (QGP) can be reached. At SIS energies, a hadronic matter made of interacting mesons and baryonic resonances is formed. Although quarks and gluons remain confined, sizeable modifications of the properties of hadrons are predicted [Leupold et al., 2010].

In quark models, medium modifications are due to the change of the structure of the QCD (Quantum ChromoDynamics) vacuum, induced by the partial restoration of chiral symmetry [Rapp et al., 2009]. These models predict a decrease of hadron masses of the order of 20% for the ρ meson at normal density [Brown and Rho, 1991, Hatsuda and Lee, 1992].

In hadronic models, in-medium spectral functions of vector mesons (will be introduced in section 1.1.1) are calculated from their propagation in the hadronic matter. The main effect comes from the excitation of resonance-hole states ($N(1520)N^{-1}$, $\Delta(1232)N^{-1}$, ...) (see fig. 1.1) and the result is mainly a broadening of the spectral function with respect to the free meson.

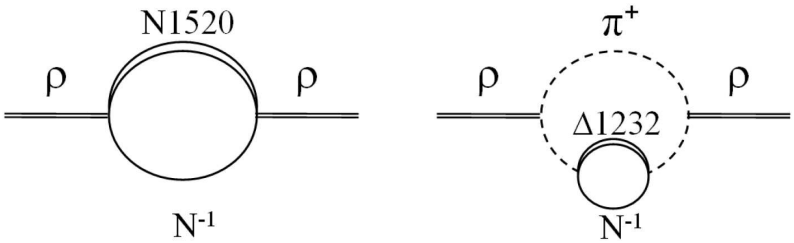

FIG. 1.1 – Dressing of the ρ in the nuclear medium by coupling to baryonic resonances. **Left :** The modification of the ρ self-energy through its coupling to resonance-hole states ; **Right :** $\Delta(1232)$-nucleon-hole polarization.

[1] High Acceptance Di-Electron Spectrometer
[2] SchwerIonen Synchrotron
[3] Relativistic Heavy-Ion Collider
[4] Conseil Européen pour la Recherche Nucléaire

1.1 Di-lepton probe as a tool to study medium effects

Di-lepton (e^+e^- pair, or called di-electron) probe is considered as a reliable tool to study the medium effects because of its insensitivity to strong interaction. In fact di-electrons come out from the dense matter without interacting much with the other particles, thus an undistorted signal can be observed. In this section, I will at first introduce an important di-electron source vector mesons. Then other sources, like baryonic resonances, which also contribute to di-electron production, will be discussed.

1.1.1 Vector mesons

The vector mesons are those mesons with total spin 1 and odd parity, usually noted as $J^P = 1^-$. They have a direct decay to di-electron channels, as summarized in table 1.1. Despite the small branching ratio, di-electron spectroscopy is the ideal tool to study the in-medium vector mesons. In particular, the ρ meson has the largest probability to decay inside the dense medium due to its very short life time, thus the di-electron decay from the ρ can bring the proper information from in-medium properties.

Meson	**Mass** [**MeV**/c^2]	Γ [**MeV**/c^2]	**c**τ [**fm**]	**Main decay**	e^+e^- **branching ratio**
ρ	775.5	149.1	1.3	$\pi^+\pi^-$	$4.72 \cdot 10^{-5}$
ω	782.7	8.49	23.4	$\pi^+\pi^-\pi^0$	$7.28 \cdot 10^{-5}$
ϕ	1019.5	4.26	44.4	K^+K^-	$2.95 \cdot 10^{-4}$

TAB. 1.1 – Vector meson main characteristics. [Nakamura et al., 2010]

The principle is to reconstruct the in-medium mass distribution, or spectral function of vector mesons using the di-electron invariant mass. In practice, a di-electron invariant mass spectrum is reconstructed, which is a superposition of different di-electron sources.

1.1.2 Di-electron sources

In the 1-2 A GeV energy range, the main di-electron sources can be separated into four categories listed as following :

- The vector meson decays (see table 1.1),
- The Dalitz decay of mesons :
  - $\pi^0 \rightarrow \gamma e^+e^-$ with branching ratio 1.2%.
  - $\eta \rightarrow \gamma e^+e^-$ with branching ratio $7 \cdot 10^{-3}$.
  - $\omega \rightarrow \pi^0 e^+e^-$ with branching ratio $8 \cdot 10^{-4}$.
- The Dalitz decay of baryonic resonances :
  - $\Delta \rightarrow Ne^+e^-$.
  - $N(1535) \rightarrow Ne^+e^-$, etc.
- The nucleon-nucleon bremsstrahlung : $NN \rightarrow NNe^+e^-$.

1.1.3 Importance of baryonic resonances in di-lepton emission

In the 1-2 A GeV range, baryonic resonances are very important for meson production.

The role of the $\Delta(1232)$ resonance is dominant, but the higher lying resonances start to play an increasing role when the incident energy increases. Besides its pionic decay, the $N^*(1535)$ is also important for the η production and the $N^*(1520)$, $\Delta(1620)$ for the ρ production. Through the direct decay or Dalitz decay of these mesons, for example $\pi^0 \rightarrow \gamma e^+e^-$, $\rho \rightarrow e^+e^-$, ..., the baryonic resonances therefore contribute on one hand indirectly to the di-electron production. On the other hand, di-electrons can be emitted directly by baryonic resonances via their own Dalitz decay modes. For example, the Dalitz decay of $\Delta(1232)$ ($\Delta \rightarrow pe^+e^-$) has never been measured up to now but the QED calculation predicts a very small branching ratio of $4.2 \cdot 10^{-5}$. Thus, it is an experimental challenge to study this Dalitz decay mode.

The Δ Dalitz decay implies an electromagnetic transition from the Δ resonance (fig. 1.2 (a)) to a nucleon. In this transition, the four-momentum transfer q^2 is equal to the e^+e^- invariant mass squared, it is therefore a positive quantity. This transition is then referred as Time-Like type. In electron scattering on proton (fig. 1.2 (b)), transitions from a nucleon to Δ are also studied. In this case, the four-momentum squared is negative and the transition is then of the Space Like type. In the latter case, the form factors have been measured over a quite large range of q^2. As the nucleon and Δ are composite particles, and the Δ has spin 3/2, the electromagnetic hadronic current consists in 3 independent terms, which can be taken as a magnetic, an electric and a Coulomb term, each weighted by a form factor ($G_M(q^2)$, $G_E(q^2)$ and $G_C(q^2)$ as magnetic, electric and Coulomb form factors respectively).

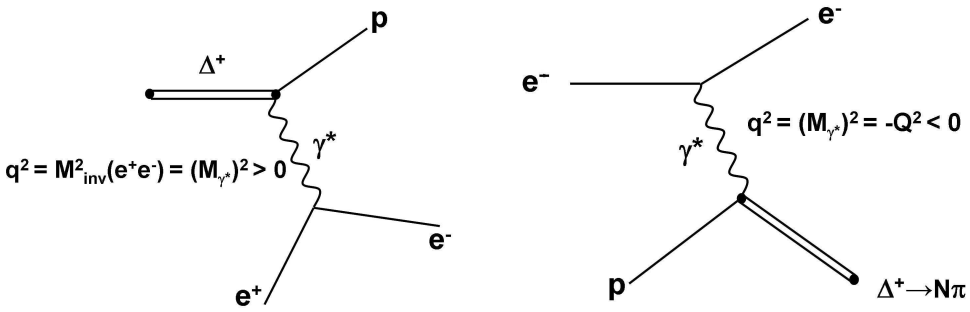

(a) Δ Dalitz decay (b) Pion electro-production

FIG. 1.2 – Illustration of the (a) Time-Like electromagnetic $N - \Delta$ transition in the Δ Dalitz decay and (b) the Space-Like $N - \Delta$ transition in pion electro-production experiments.

The di-electron yield mainly depends on the value of the form factors at q^2=0 ($G_M \sim 3, G_E \sim 0$ and $G_C \sim 0$) [Tiator et al., 2003]. On the other hand, for the largest q^2 (i.e. $q^2 \sim (M_\Delta - M_N)^2$), which are not too far from the vector meson poles, the Vector Dominance Model (VDM) can be checked. It stipulates that the coupling of a real or virtual photon to any electromagnetic hadronic current is mediated by a vector meson (see fig. 1.3) [Sakurai, 1969]. Despite the limitation of low q^2, the kinematics probed by the Δ Dalitz decay is suited to test the VDM.

1.1.4 Nucleon-nucleon bremsstrahlung and Δ Dalitz decay

The nucleon-nucleon bremsstrahlung is the emission of a virtual photon in the strong interaction field created by the interaction of two nucleons (see fig. 1.4). The description of this process has to take into account both the $NN\gamma^*$ electromagnetic vertex and the nucleon-nucleon interaction, as in the Soft Photon Approximation (SPA) [Gale and Kapusta, 1987] which is widely used

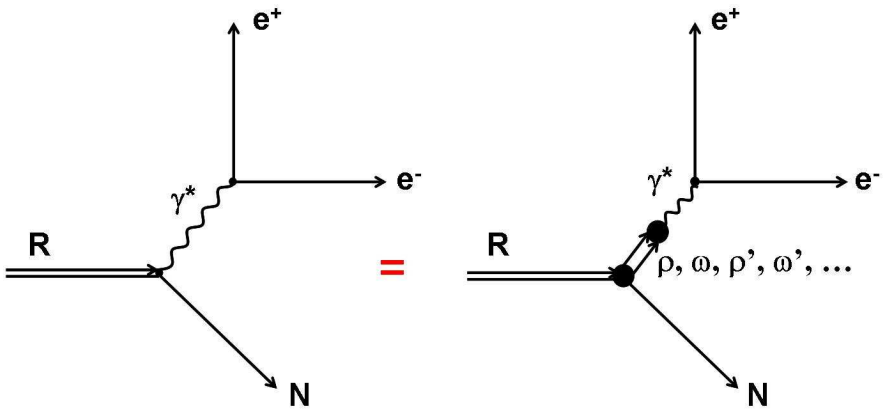

FIG. 1.3 – Vector Dominance Model in a baryonic electromagnetic transition.

in transport models. Although the calculation is in principle valid only for low mass di-electrons the SPA gave reasonable agreement with more complete calculations [Shyam and Mosel, 2003], at least for the $n + p$ case, where the bremsstrahlung process is the most important.

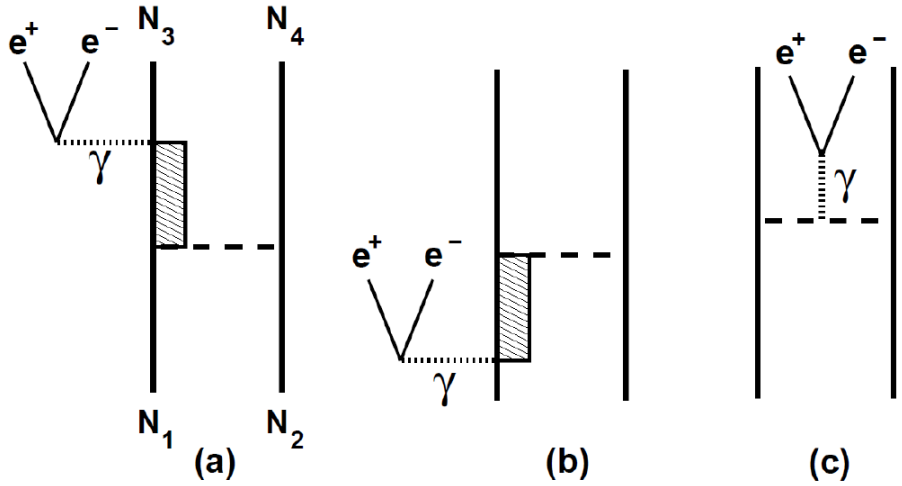

FIG. 1.4 – Diagrams for the reaction $NN \rightarrow NNe^+e^-$. (a) post-emission, (b) pre-emission and (c) in-flight emission (for $n + p$ reaction only). The box represents an off-shell nucleon or a Δ. [Shyam and Mosel, 2009]

In the transport model calculations, the Δ Dalitz decay and NN bremsstrahlung processes are usually treated in the way, that the SPA is used to describe bremsstrahlung ; and the di-electron yield from the Δ Dalitz decay is then calculated independently and added incoherently. But the description of their processes can be done reliably only through a full quantum mechanical and gauge invariant calculation. Two One Boson Exchange (OBE) models [Kaptari and Kämpfer, 2006, Shyam and Mosel, 2009], which fulfill these requirements were presented recently, but the yields obtained in these two calculations were found to differ by factors 2-3 for both $p + p$ and $p + n$ reactions. The [Shyam and Mosel, 2009] calculation was in agreement with the SPA, but the predictions by [Kaptari and Kämpfer, 2006] were a factor 2-3 higher. This higher NN bremsstrahlung was taken into account by a renormalisation of the bremsstrahlung contribution in the HSD transport model. The latter calculation overestimates

however the di-electron yield of $p+p$ as we will show in section 1.6. Inconsistenties in the description of $NN \rightarrow NN\gamma^*$ remain therefore.

1.2 Evidences of medium effects

Experiments looking for medium effects have been started since late 1980's using heavy-ion reactions by many worldwide collaborations. Experiments induced by protons and photons are also performed to study matter at normal density. We have summarized the main results in table 1.2.

A lot of observations have been reported, but a global understanding is still missing. The in-medium mass shift which was expected from quark models has been seen only in the KEK experiment for the ρ meson. The strongest evidence of medium effect is the broadening of the ρ meson in ultra-relativistic heavy-ion reactions which agrees with the calculations from Rapp and Wambach [Rapp and Wambach, 1999].

Experiment	**Reaction /Energy** [GeV]	**Momentum acceptance** [GeV/c]	**Vector mesons**		
			ρ	ω	ϕ
KEK-E325	pA 12 GeV	p>0.6	$\Delta\, m/m \sim -9\%$ $\Delta\, \Gamma \sim 0$	$\Delta\, m/m \sim -9\%$ $\Delta\, \Gamma \sim 0$	$\Delta\, m/m \sim -3.4\%$ $\Gamma \sim 15$ MeV/c^2
CLAS	γA 0.6-3.8 GeV	p>0.8	$\Delta\, m \sim 0$ $\Delta\, \Gamma \sim 70$ MeV $\rho \sim \rho_0/2$	$\Delta\, \Gamma \sim 200$ MeV* $\langle p \rangle > 1.$ GeV/c	$\Delta\, \Gamma \sim 70$ MeV
CBELSA /TAPS	γA 0.9-2.2 GeV	p>0	—	$\Delta\, m \sim 0$ $\Delta\, \Gamma \sim 200$ MeV $\langle p \rangle \sim 1.1$ GeV/c	—
SPring8	γA 1.5-2.4 GeV	p>1.0	—	—	$\Delta\, m \sim 70$ MeV* $\langle p \rangle \sim 1.8$ GeV/c
CERES	Pb+Au 158 AGeV	p_t >0	broadening favored over mass shift	—	—
NA60	In+In 158 AGeV	p_t >0	$\Delta\, m \sim 0$ strong broadening	—	—

TAB. 1.2 – Experimental results on in-medium modifications of the ρ, ω and ϕ mesons measured by different experiments (for details see [Metag, 2007]). The lower limit in p (momentum) or p_t (transverse momentum) is indicated in the third column. The results indicated with a star correspond to transparency ratio measurements.

On the other hand, in 1998, the DiLepton Spectrometer (DLS) experiment at the BEVALAC facility at Berkeley reported a strong excess of the di-electron production over the hadronic cocktail [Porter et al., 1997, Wilson, 1998] measured in a $Ca+Ca$ and $C+C$ experiments at 1 AGeV. Even when medium effects were included, no model was able to explain these enhancements at that time [Ernst et al., 1998, Bratkovskaya et al., 1998]. This was known as the "DLS puzzle" and remained unexplained, until 2008 when the HADES collaboration published the results of the di-electron production measured in C+C collisions at 1 A GeV [Agakichiev et al., 2008]. The former results from DLS were fully confirmed by the HADES data.

1.3 The HADES program

The HADES collaboration runs a di-electron experimental program since 2001. The whole activities and future plan are listed in table 1.3. The first goal was to revisit the di-electron production in the 1-2 A GeV energy range with the light systems using a much better experimental set-up than DLS. After confirming the DLS data, the main motivation of HADES is put on the question of in-medium modification of vector mesons, using the heavy-ion reactions, e.g. $Ar + KCl$ and also $p + Nb$, to check effects at normal density. Besides, a series of elementary reaction experiments induced by protons and projected with pions on nuclei were and will be performed to give an understanding of elementary processes. Experiments with heavier systems are scheduled in the near future.

Date	System	Physics goal
2001-2002	C+C 2 AGeV	• Di-electron spectrum in small size system
2004	C+C 1 AGeV	• Check of DLS data
2004	p+p 2.2 GeV	• Validation of detector performance by pp elastic scattering • π^0 and η Dalitz decays (helicity distribution)
2005	Ar+KCl 1.75 AGeV	Medium effects
2006	p+p 1.25 GeV	• Δ Dalitz decay • Exclusive $pp \rightarrow ppe^+e^-$ analysis
2007	d+p 1.25 AGeV	pn bremsstrahlung
2007	p+p 3.5 GeV	Inclusive ρ and ω production cross section
2008	p+Nb 3.5 GeV	Vector meson at normal density
2009-2010	HADES upgrade	
2011-2012	Ni+Ni 1.65 AGeV Au+Au 1.25 AGeV	Vector meson at high density
2013-2014	π^-+A, π^-+p 1.17 GeV, 1.8 GeV	Vector meson at normal densities and off-shell production

TAB. 1.3 – The HADES di-electron experimental program.

The main goals of di-electron measurement in different systems are mentioned in table 1.3, as well. In all these experiments, hadrons are also detected. The detection of kaons allows for very fruitful studies of strangeness production [Agakichiev et al., 2009a]. The measurement of pions brings a lot of interest as well. On one hand, the pion detection in heavy ion collisions has been used to extract information from thermal emission [Agakichiev et al., 2009b]. On the other hand, in elementary reactions, the pion emission channels can be studied in an exclusive way as will be shown in chapter 5. For example, $pp \rightarrow np\pi^+$, $pp \rightarrow pp\pi^0$ and $pp \rightarrow pp\pi^+\pi^-$ can be studied in $p+p$ collisions or $pn \rightarrow pp\pi^-$, $pn \rightarrow pn\pi^+\pi^-$ and $pn \rightarrow pp\pi^-\pi^0$ can be studied in quasi-free $p+n$ reactions.

1.4 $C + C$ collisions at 1-2 A GeV with HADES

The first results of the HADES experiment came from the $C + C$ system studied at 1 and 2 A GeV [Agakichiev et al., 2007, 2008]. At 1 A GeV, a nice agreement was found between HADES and DLS data. Recently many transport model calculations, such as Hadron String Dynamics (HSD) [Bratkovskaya and Cassing, 2008], Ultra-Relativistic Quantum Molecular Dynamics (UrQMD) [Schmidt et al., 2009], Isospin Quantum Molecular Dynamics (IQMD) [Thomère et al., 2007] and Relativistic Quantum Molecular Dynamics (RQMD) [Cozma et al., 2006], have been performed and the description of DLS and HADES $C+C$ data improved. This

put an end to the DLS puzzle. On fig. 1.5, four examples of such calculations are shown for the di-electron spectra measured by HADES in $C + C$ reactions at 2 A GeV.

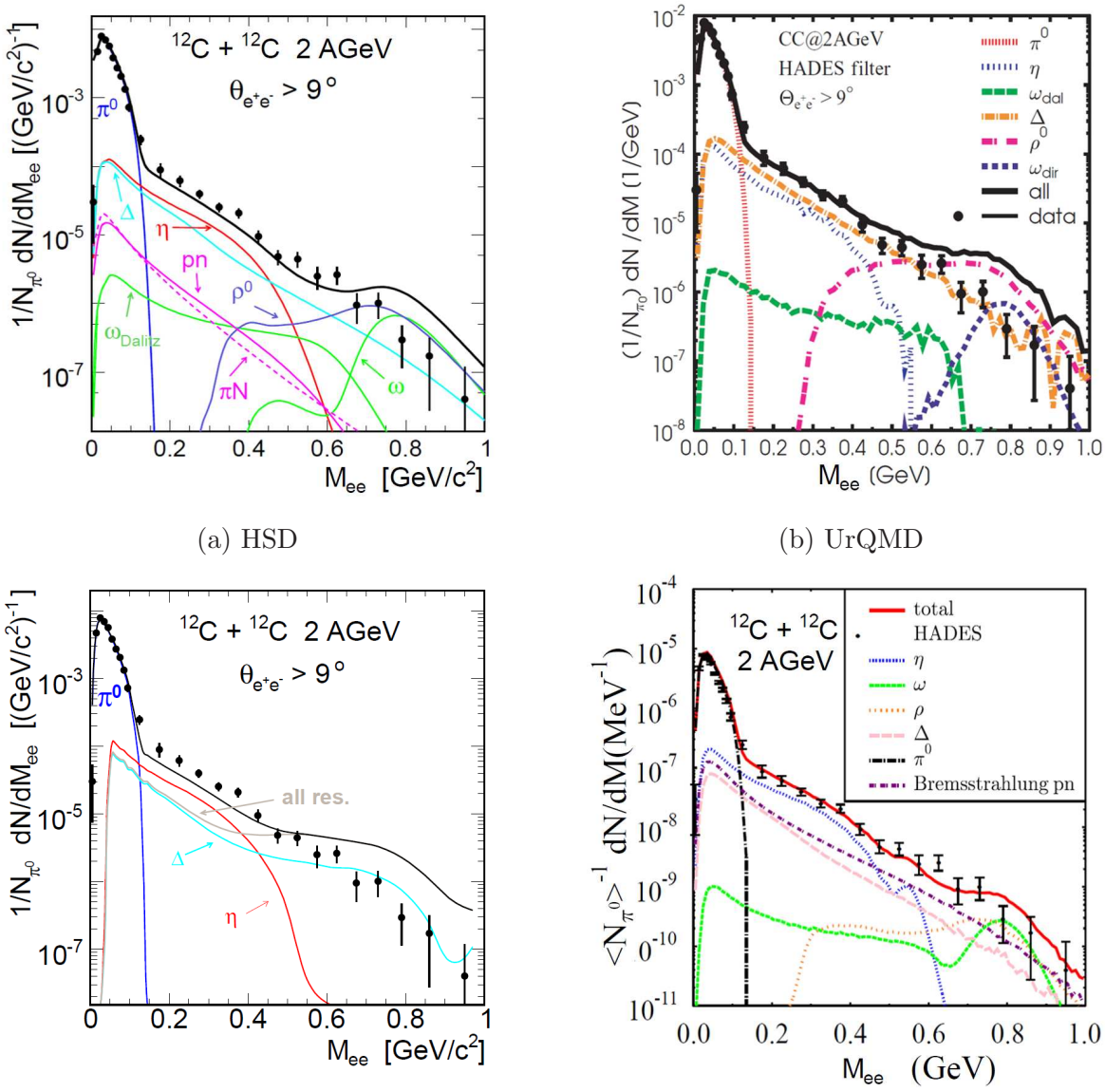

(a) HSD

(b) UrQMD

(c) RQMD

(d) IQMD

FIG. 1.5 – Di-electron mass distribution measured in $C+C$ reactions at 2 A GeV compared with the vacuum calculations from different transport codes : (a) HSD, (b) UrQMD , (c) RQMD and (d) IQMD transport models. Black dots show the efficiency corrected HADES data and different color lines present various di-electron sources implemented in the calculations.

Resonably agreement is found between parts of the data and these four transport model calculations. However, the ingredients in models as well as the treatment of the di-electron sources are very different from one model to another, especially in the intermediate di-electron invariant mass region where the excess was observed. In this region, Δ Dalitz decay and NN bremsstrahlung play important roles, beyond the η Dalitz.

For a better understanding of the contribution from such processes and their relationship

to the excess yield, the elementary reactions are needed. In the following, we will focus on the discussion related to the role of the baryonic resonances, mainly the $\Delta(1232)$ resonance.

1.5 $\Delta(1232)$ resonance production

1.5.1 Results from π production experiments

The $\Delta(1232)$ resonance is a spin 3/2 and isospin 3/2 state whose main decay channel is a two-body decay into a π (spin 0, isospin 1) and N (spin 1/2, isospin 1/2) ($> 99\%$). The excitation of the $\Delta(1232)$ resonance is known as the main process of pion production in the 1-3 A GeV range in $p+p$ and $n+p$ reactions. The cross sections as well as angular distributions of the pion production have been measured in many previous experiments.

The π^0 and π^+ exclusive production were measured in the 1960s using bubble chambers at Brookhaven National Laboratory (BNL) at 2 GeV ($\sqrt{s} = 2.70$ GeV) [Fickinger et al., 1962] and later on at 1.48 GeV ($\sqrt{s} = 2.51$ GeV) [Eisner et al., 1965]. Similar measurements done at the Birmingham proton synchrotron can also be found at 0.97 GeV ($\sqrt{s} = 2.31$ GeV) [Bugg et al., 1964]. The problem in these experiments was the limited statistics (between 1000 and 1400 events for $pp \rightarrow np\pi^+$ channel), but the advantage was a full coverage of acceptance. Another measurement which refers to the $pp \rightarrow np\pi^+$ reactions measured at 0.8 GeV at the Los Alamos Meson Physics Facility (LAMPF) can be found in [Hudomalj-Gabitzsch et al., 1978]. In the 1980s, Shimizu *et al.* [Shimizu et al., 1982] have reported measurements of $pp \rightarrow pp\pi^0$ and $pp \rightarrow np\pi^+$ reactions between $2.0 < \sqrt{s} < 2.43$ GeV done at KEK using bubble chamber.

A series of recent studies also related to the Δ production mechanisms have been carried out with newer experimental set-ups. The neutral pion production in $p+p$ collisions, i.e. $pp \rightarrow pp\pi^0$, has been measured at the PNPI synchrocyclotron with beam momenta at 1.581 and 1.683 GeV/c with a hydrogen bubble chamber [Sarantsev et al., 2004]. The COSY-TOF collaboration reported on π production also in $p+p$ reactions measured using the COSY-TOF spectrometer at a beam energy of 0.95 GeV/c, for both $pp \rightarrow pp\pi^0$ and $pp \rightarrow np\pi^+$ channels [Abd El-Samad et al., 2006, 2009]. The recent measurements of the CELSIUS-WASA collaboration in the $p+p$ reactions at 1.1-1.3 GeV were mainly focused on two-pion production. Preliminary results concerning exclusive one-pion production channels can be found in [Zhen et al., 2009, Skorodko, 2009, Clement et al., 2006]. The emphasis is put on the contribution of higher lying resonances, such as $N^*(1440)$ and $N(1520)$.

1.5.2 The One-Pion Exchange Model

These results mentioned above have been satisfactorily explained by the One-Pion Exchange Model (OPEM) [Ferrari and Selleri, 1961, König and Kroll, 1981] in the $pp \rightarrow n\Delta^{++}$ channel, considering that the $pp \rightarrow p\Delta^+$ channel and the non-resonant pion production are less important. We show here (fig. 1.6), the comparison of Dmitriev's OPEM predictions [Dmitriev and Sushkov, 1986] with the spectra measured at 0.97 GeV [Bugg et al., 1964].

The studies are realized in fact by using the $pp \rightarrow np\pi^+$ channel : the invariant mass distribution of (π^+, p) pairs (or it's excitation energy) shows the Δ^{++} resonance and the center-of-mass angular distribution of the neutron reflects the Δ^{++} resonance production angular distribution (see fig. 1.6). It was found that the Δ production shows a strongly forward/backward peaked

angular distribution and the mass distribution is slightly asymmetric. Within the relative big error bars, the OPEM gives a good description of the data.

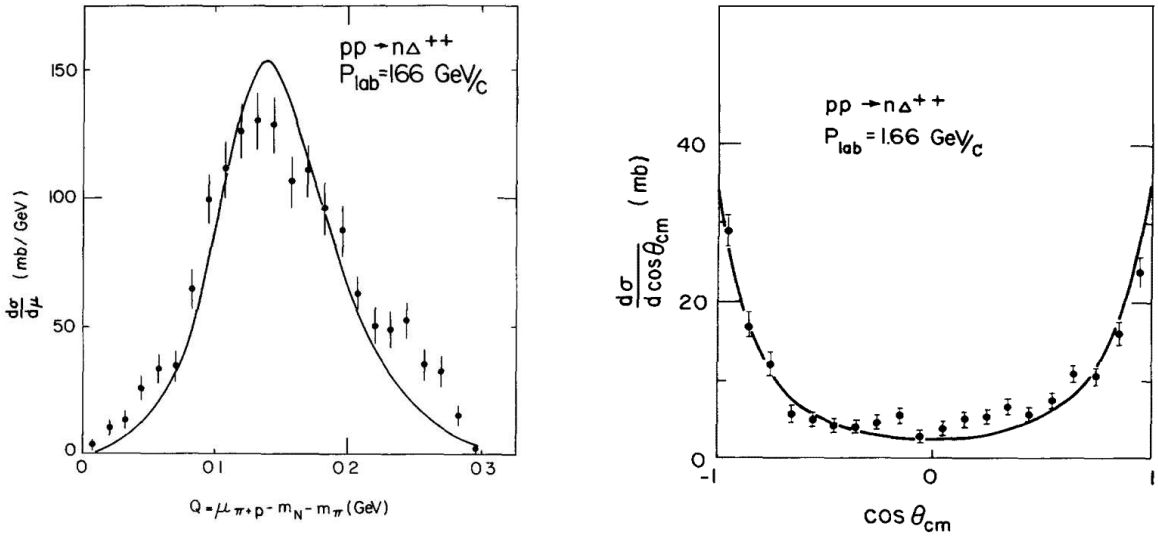

(a) (b)

FIG. 1.6 – (a) Excitation energy of the (π^+, p) pairs and (b) angular distribution of the neutron in the $p+p$ center-of-mass system in $pp \rightarrow np\pi^+$ reactions at a proton kinetic energy of 0.97 GeV. The solid curve is an OPEM calculation which is compared to experimental data (dots) [Bugg et al., 1964].

1.5.3 Pion angular distribution

The Δ decay angular distribution depends on the population of different spin states excited in the $NN \rightarrow N\Delta$ process. The latter can be described in terms of a 4×4 spin density matrix ρ_{ij} [Gottfried and Jackson, 1964]. By choosing the axes in an appropriate way (see section 3.2.4), the pion angular distribution can be expressed quite simply in function of spin density matrix elements :

$$\begin{aligned}\frac{d\sigma}{d\Omega} \sim \{ & (1/2-\rho_{33}) \ (3\ \cos^2\theta+1) \\ & + \rho_{33}\ \ 3\ \sin^2\theta \\ & - \rho_{31}\ \ 4\sqrt{3}\ \sin\theta\ \cos\theta\ \cos\phi \\ & - \rho_{3-1}\ \ 2\sqrt{3}\ \sin^2\theta\ \cos 2\phi\}\end{aligned} \tag{1.1}$$

In the HADES case, there is no ϕ dependence since we are always looking at observables integrated over the full azimuthal range and the integration gives zero. One can write therefore the pion angular distribution as :

$$\frac{d\sigma}{d\cos\theta} \sim B(1+A\cos^2\theta) \tag{1.2}$$

where B is the normalization factor and $A = (3-12\ \rho_{33})/(4\ \rho_{33}+1)$. It means that the differential cross section depends only on ρ_{33}.

In the case of pure one-pion exchange, one can show that $\rho_{33} = 0$ hence the π angular distribution is in $1+3\cos^2\theta$. In the case of ρ exchange contribution, ρ_{33} is expected to be different from 0.

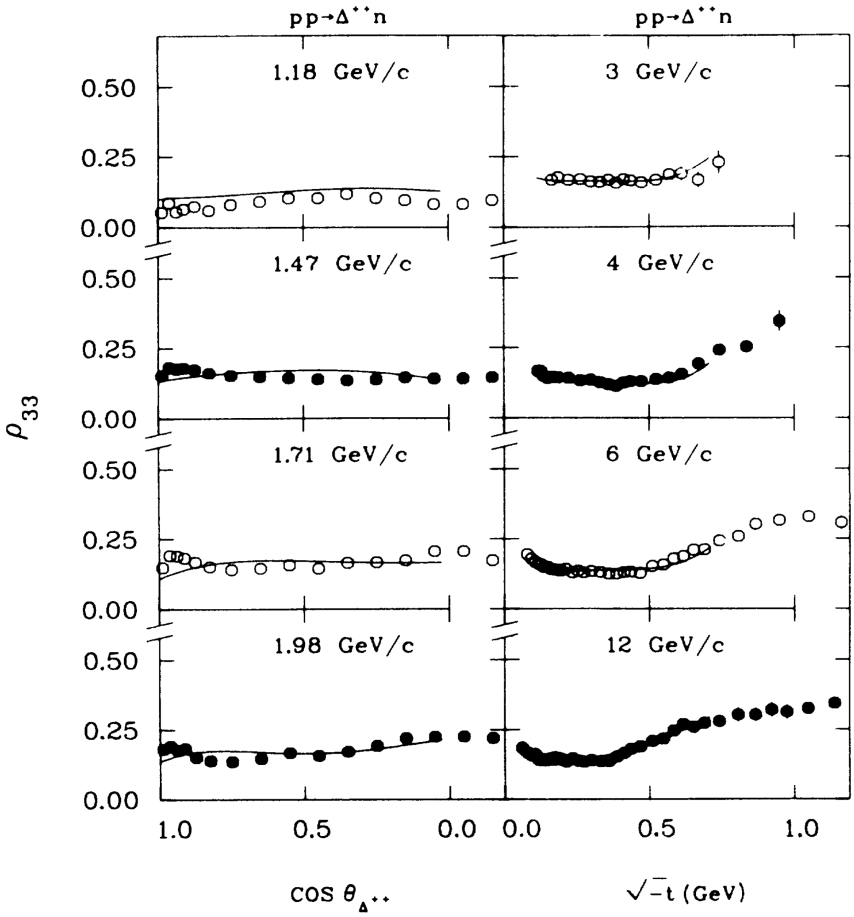

FIG. 1.7 – ρ_{33} parameter extracted from the pion angular distributions in the $pp \to np\pi^+$ reaction [Wicklund et al., 1987]. The Δ^{++} is reconstructed by the (p, π^+) pair.

The spin density matrix coefficients have been extracted from the π^+ angular distribution in $pp \to np\pi^+$ reaction using Effective Mass Spectrometer at Argonne from 1.18 to 1.98 GeV/c [Wicklund et al., 1986, 1987]. The ρ_{33} value has been found to have a smooth distribution as a function of the Δ production angle (see fig. 1.7). For forward emitted Δ^{++} the ρ_{33} is found to be equal to 0.16 ± 0.03, which results in an anisotropy coefficient $A = 0.66 + 0.29 - 0.25$, smaller than the value 3 derived from the OPEM.

The evidence is in agreement with the investigation by the same reaction but at higher energy 2.8 GeV/c performed at BNL using a bubble chamber [Bacon et al., 1967]. In this study they showed an anisotropic pion angular distribution and obtained $\rho_{33} = 0.14 \pm 0.03$, so $A = 0.85 + 0.32 - 0.28$ (see fig.1.8). The same study also performed at BNL at 2.5 GeV/c had been reported in [Eisner et al., 1965], that they found $A \simeq 0.55$ but announced the fit quality was not satisfactory. In addition, Shimizu *et al.* [Shimizu et al., 1982] also mentions $\rho_{33} \sim 0.2$.

It has to be noted that in these experiments only effective matrix elements could be derived, considering that only one graph contributes, with excitation either of the projectile or of the target. As we will see in section 3.2.3, this is valid only for the forward or backward angles, and assuming that the Δ^{++} excitation is the dominant contribution.

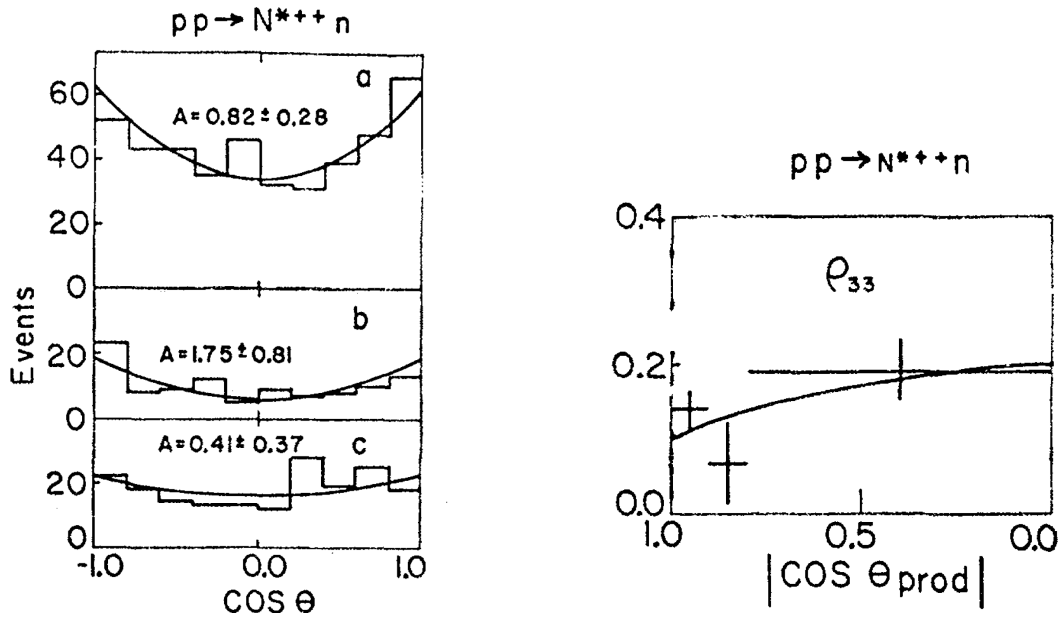

FIG. 1.8 – **Left :** π^+ angular distribution in (p, π^+) reference frame (noted as $\cos\theta$) for three regions of Δ^{++} production angles (noted as $\cos\theta_{\text{prod}}$) : a) $1.0 \geq \cos\theta_{\text{prod}} > 0.9$, b) $0.9 \geq \cos\theta_{\text{prod}} > 0.8$ and c) $0.8 \geq \cos\theta_{\text{prod}} > 0.0$. **Right :** ρ_{33} parameter extracted from the pion angular distributions. Both are measured in the $pp \to np\pi^+$ reaction at 2.8 GeV/c at Brookhaven National Laboratory [Bacon et al., 1967].

As a conclusion, the analysis of the π angular distribution that came out with the previous experiments was in agreement with an anisotropic Δ decay, but with an anisotropy smaller than expected from a pure OPEM. It has to be mentioned that also the spin observable was in disagreement with the OPEM [Prout et al., 1996], while the yield and neutron angular distribution were in good agreement with OPEM. Different types of interactions were tested to reconcile all these data, $\pi + \rho$ for example, with no real success [Dahl, 1995]. Note that in transport models, the pionic decay of the Δ resonance is taken isotropic. In our event generator, we implemented an anisotropic angular distribution according to the results above.

1.5.4 Teis fits

The Teis analysis [Teis et al., 1997] starts from the observation that, in the 1-3 GeV range, pion production is mainly driven by the excitation of intermediate resonances. The contribution of the $\Delta(1232)$, which is dominant for pion production at the lowest energies is taken from the OPEM, which describes quite well the measured cross-sections, invariant mass distributions, and angular distributions of the $pp \to np\pi^+$ reaction at incident momenta around 1.5 GeV/c. The available cross-section values for one or two pion production in $p+p$ and $p+n$ reactions were used to fit the contributions of the different resonances, which are linked by isospin factors in the different isospin channels (see fig. 1.9).

The systematics is based on [Baldini et al., 1988]. In the energy range of the $p+p$ reaction at 1.25 GeV, the data measured in the 1960's with bubble chambers are taken into account [Eisner et al., 1965, Bugg et al., 1964, Fickinger et al., 1962]. The point at $\sqrt{s}$=2.3 GeV, appearing higher than the latter ones in both $pp\pi^0$ and $np\pi^+$ channels, originates from nuclear emulsion measurements at Birmingham [Hughes et al., 1957]. The KEK data, were not included in the Teis systematics, although they were already available at that date. We will compare our cross section measurements to a more up to date systematics in section 5.11.3. In transport models, an extensive use of the resonance model is made to derive the baryonic resonance production cross sections in $p+p$ and $p+n$ reactions.

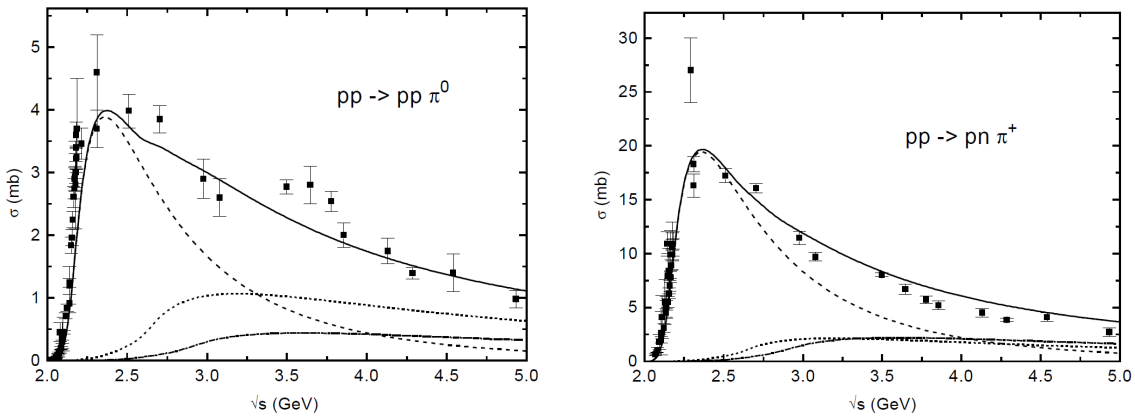

(a) (b)

FIG. 1.9 – Cross sections of $pp \to pp\pi^0$ (a) and $pp \to np\pi^+$ (b) reactions used by Teis *et al.*

1.5.5 Isospin correlations

In $p+p$ reactions, the amplitudes for $pp \to p\Delta^+$ and $pp \to n\Delta^{++}$ differ only by the product of the isospin coefficients at each vertex (see appendix A). It results in the following relations for two production channels :

$$\begin{aligned} \sigma_{pp\to p\Delta^+} &= \frac{1}{4}\,\sigma_{pp\to N\Delta} \\ \sigma_{pp\to n\Delta^{++}} &= \frac{3}{4}\,\sigma_{pp\to N\Delta} \end{aligned} \tag{1.3}$$

and the following branching ratios for the $\Delta \to N\pi$ channels are :

$$\begin{aligned} \Delta^+ &\rightarrow p\pi^0 \quad (2/3) \\ \Delta^+ &\rightarrow n\pi^+ \quad (1/3) \\ \Delta^{++} &\rightarrow p\pi^+ \quad (1) \end{aligned} \tag{1.4}$$

As a consequence, if the π production proceeds only through Δ excitation, the cross sections of the two isospin channels in $p+p$ reactions are correlated by :

$$\sigma_{pp\rightarrow np\pi^+} \sim 5\ \sigma_{pp\rightarrow pp\pi^0} \tag{1.5}$$

1.6 HADES results in $p+p$ and $p+n$ experiments

In this section, I would like to discuss the di-electron production investigated by HADES with the $p+p$ and $d+p$[5] experiments at 1.25 GeV. At this energy, the di-electron productions can come from π^0 Dalitz decay ($\pi^0 \rightarrow \gamma e^+e^-$), $\Delta(1232)$ Dalitz decay ($\Delta^+ \rightarrow pe^+e^-$) and nucleon-nucleon bremsstrahlung ($NN \rightarrow NNe^+e^-$). As seen in fig. 1.10 for an incident energy at 1.25 GeV, according to the OBE model, the Δ graphs are widely dominant in the case of the $p+p$ reaction, while the NN bremsstrahlung becomes more important for the $p+n$ reaction. This is due to the isospin effects for the charged mesons exchange and the different interference effects in $p+p$ and $n+p$ channels [Kaptari and Kämpfer, 2009].

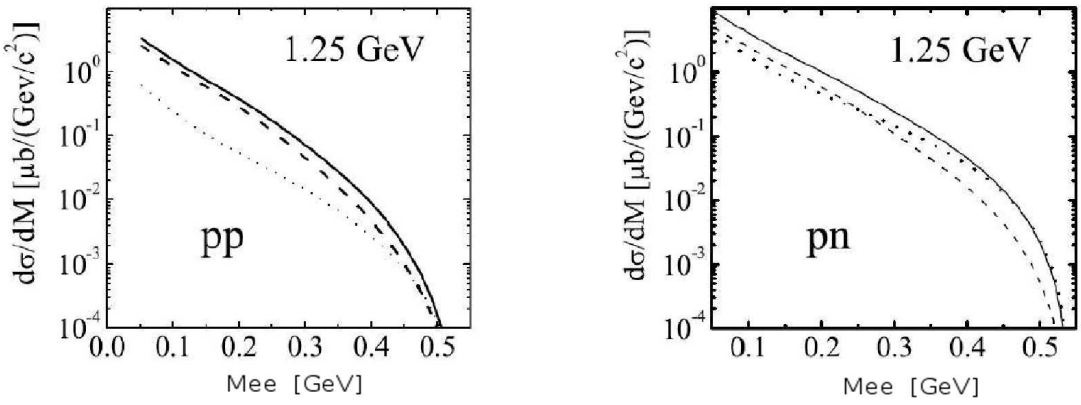

FIG. 1.10 – OBE prediction for di-electron invariant mass distribution in $p+p$ (left) and $p+n$ (right) collisions at 1.25 GeV : the dashed and dotted curves present the contribution from the Δ graphs and nucleon graphs respectively and the solid line presents the full calculation [Kaptari and Kämpfer, 2006].

Figure 1.11 shows the di-electron mass spectra measured in the $p+p$ and quasi-free $n+p$ reactions by HADES compared to Pluto simulation (detailed information and ingredients of simulations can be found in the PhD thesis of T. Galatyuk [Galatyuk, 2009]) with π^0 inclusive cross sections and the Δ contribution taken from the Teis fits (see table 1.4). In the simulation, the π^0 and Δ Dalitz decay are parameterized using the QED formalism and acceptance cuts are

[5]The $d+p$ run was performed in May 2007, using a deuteron beam of 1.25 A GeV kinetic energy shooting on a liquid hydrogen target. The main goal of this experiment was to measure the e^+e^- pair emission in quasi-free $n+p$ collisions which is expected to be sensitive to the np bremsstrahlung process. The Forward Hodoscope Wall covering a polar angle between 1-7^o was used in this experiment to measure the spectator proton, in which way we could suppress the $p+p$ interactions and measure quasi-free $n+p$ interactions [Lapidus].

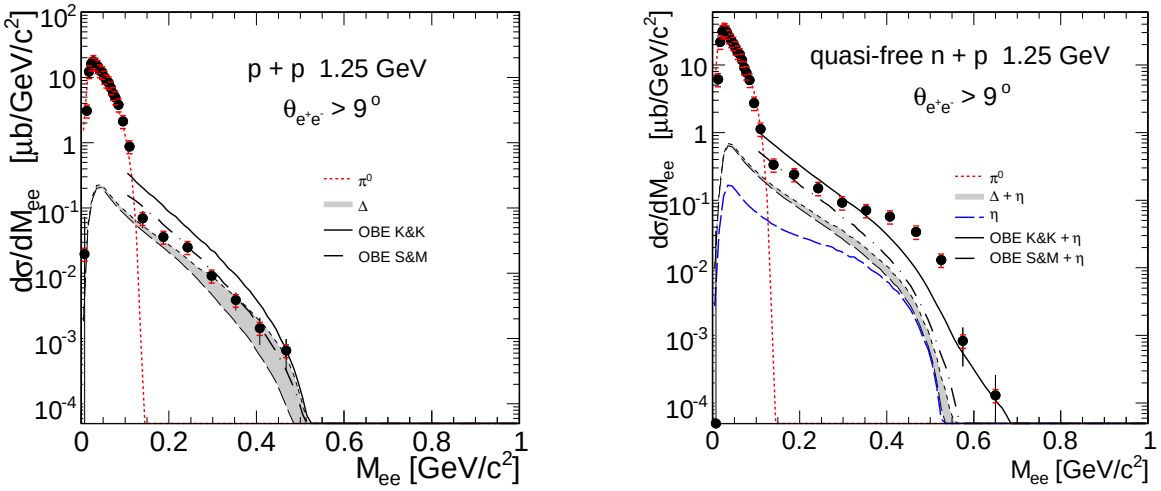

(a) (b)

FIG. 1.11 – Di-electron mass distribution measured in $p+p$ (a) and quasi-free $n+p$ (b) reactions at 1.25 GeV compared with Pluto simulations. The experimental data are shown by black dots and the systematical errors (constant in whole mass range) are indicated by red horizontal bars and statistical errors by black vertical bars. In simulation, different sources are presented by different lines : Red dotted line π^0 Dalitz decay, blue long-dashed line : η Dalitz decay, black dashed line and long-dashed line : Δ Dalitz decay, shaded area : the enhancement due to the $N-\Delta$ transition form factor. In the mass region above π^0 the transport calculations, e.g. total cocktail with K&K OBE [Kaptari and Kämpfer, 2006] (black solid line) and total cocktail with S&M OBE [Shyam and Mosel, 2003] (black dashed-dotted line) are also shown.

applied before comparing to the measured spectra.

Both reactions show a good agreement in the low mass region where the π^0 Dalitz decay is dominant. It confirms the normalization and analysis procedures. In the case of the $p+p$ reaction, the spectrum can be explained by a simple sum of the π^0 Dalitz decay and Δ Dalitz decay. An even better agreement can be found when the $N-\Delta$ transition form factor ([Wan and Iachello, 2005]) is included. The grey zone shows the effects of the form factor, a more important effect in the high mass region has been found. These data show the sensitivity to the $N-\Delta$ form factor.

$p+p$ **channel**	**Cross section [mb]**
$\sigma_{pp\to pp\pi^0} = \frac{2}{3}\,\sigma_{pp\to p\Delta^+}$	4
$\sigma_{pp\to pp\pi^0\pi^0}$	0.1
$\sigma_{pp\to pn\pi^+\pi^0}$	0.5
sum π^0 **in** $p+p$	**4.6**

TAB. 1.4 – Cross sections for exclusive channels of π^0 production in $p+p$ reactions in [Teis et al., 1997].

The shape of the spectrum changes dramatically when going from $p+p$ to $p+n$ reactions. In $p+p$ reactions, the di-electron yields from the Δ^+ Dalitz decay and the π^0 Dalitz decay are correlated by the isospin relation $\sigma_{pp\to pp\pi^0} = \frac{2}{3}\,\sigma_{pp\to p\Delta^+}$ (see table 1.4), neglecting the two-π

processes and assuming that all the π^0 are produced via the Δ^+ resonance. Thus in the $n+p$ case, the π^0 contribution is expected to be 2 times higher than in $p+p$ because π^0 come from Δ^+ and Δ^0 with equal weights (see equation 1.6).

$$\begin{aligned}\sigma_{pp\to p\Delta^+\to pp\pi^0} &= \sigma_{np\to n\Delta^+\to np\pi^0} \\ &= \sigma_{np\to p\Delta^0\to np\pi^0}\end{aligned} \tag{1.6}$$

This is in agreement with the experimental result. But in the mass range between 0.15 and 0.35 GeV/c^2, the data are even a factor 9 higher in the case of $n+p$ reaction. Even with the η contribution and the $N-\Delta$ transition form factor, the $n+p$ case can not be explained [Agakichiev et al., 2010].

For the mass range above the π^0 Dalitz decay, the OBE calculations (OBE K&K [Kaptari and Kämpfer, 2006] and OBE S&M [Shyam and Mosel, 2009]) are also compared to the data. They are expected to provide a more accurate description than the resonance model because they take into account all graphs involving the Δ resonance or nucleons as shown in section 1.1.4. The predictions in OBE K&K overestimate $p+p$, while the one in OBE S&M give pretty good description of the data. However, both calculations fail to explain the $n+p$ data even when the nucleon-nucleon bremsstrahlung is included. This is considered as new "HADES puzzle". Nevertheless, the quite recent results from [Shyam and Mosel, 2010] improve the situation. An implementation of the π form factor does not change much the $p+p$ spectrum, but brings the calculated cross sections closer to the data in the higher di-electron mass region in the $n+p$ case.

The di-electron production has been studied in the inclusive channel ($NN \to Xe^+e^-$). Meanwhile, the exclusive channel analysis is in progress using the pe^+e^- events measured in these $p+p$ and $p+n$ experiments at 1.25 GeV. The $pp \to ppe^+e^-$ reaction is selected using the missing mass. In this case, pe^+e^- spectra and other differential spectra can also be used to identify the Δ resonance excitation. For this analysis, the resonance model is used. Due to the selection of the proton, the measured yields and distributions are in this case also sensitive to the proton distributions. We will present the results from the on-going analysis in section 6.2. A similar analysis has also been started in $p+n$ reactions with pne^+e^- events, where a stronger contribution of pn bremsstrahlung is expected than in $p+p$.

1.7 Motivation of exclusive pion production experiments

With the HADES $p+p$ and $p+n$ experiments, it is possible to analyse the pionic channels : i.e. $pp \to np\pi^+$, $pp \to pp\pi^0$, $pp \to pp\pi^+\pi^-$, $np \to pp\pi^-$, $np \to pp\pi^-\pi^0$.

The interest is to have consistency checks of the different channels measured with HADES. It allows also to validate the resonance model [Teis et al., 1997], used for the di-electron analysis and more specifically its dominant feature : the excitation of the $\Delta(1232)$ resonance within the OPEM. Pionic and di-electron channels are indeed linked by the π^0 Dalitz decay ($\pi^0 \to e^+e^-\gamma$) and Δ Dalitz decay ($\Delta^+ \to e^+e^-p$). Thanks to the high statistics achieved in the pion channels, the measured spectra can also be useful to test more sophisticated models.

In this PhD thesis, the analysis of exclusive one-pion production channel $pp \to np\pi^+$ will be presented. The same studies as performed in previous experiments, such as Δ mass distribution and angular distributions measured with the HADES $p+p$ experiment at 1.25 GeV will be shown in detail in this document. The HADES data will be compared with a simulation based

on OPEM for Δ production and the sensitivity to other resonances will be tested as well.

Chapitre 2

The HADES spectrometer

The HADES detector, as shown in fig. 2.1, consists of 6 identical sectors covering the full azimuthal range and polar angles from 18^o to 84^o with respect to the beam direction. Each sector contains : A Ring Imaging CHerenkov (RICH) detector used for electron identification ; two sets of Mini-Drift Chambers (MDC) with 4 modules per sector placed in front and behind the magnetic field to determine momenta of charged particles ; Time-Of-Flight detectors (TOF/TOFINO) and Pre-Shower detector improving the electron identification. For reaction time measurement, a START detector is located in front of the target.

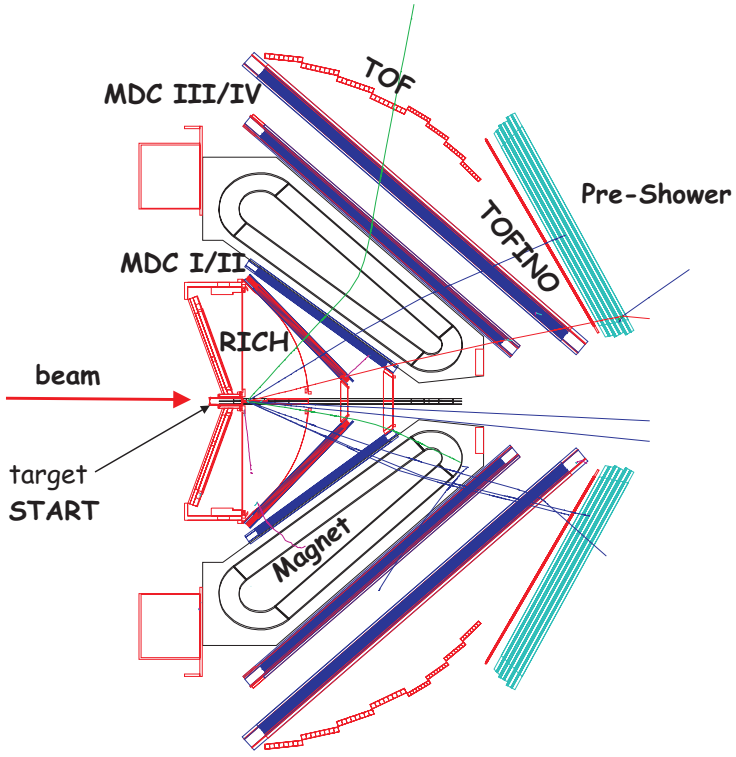

FIG. 2.1 – Schematic layout of the HADES detector.

A di-electron invariant mass resolution at the ω peak of $\sim 2.7\%$ and a momentum resolution for protons of 4% can be achieved. The first level trigger is obtained by a fast multiplicity signal coming from the TOF/TOFINO wall, combined with a reaction signal from the START detector, while the second level trigger is made by using the information from the RICH and Pre-Shower to enrich the recorded events with lepton candidates. The HADES detector is de-

signed for di-electron spectroscopy, but because of its large acceptance and good mass resolution it is also suited for the detection of hadrons.

In the following sections, the target used for the $p+p$ reactions as well as each sub-detector system will be explained in more details.

2.1 Target

In the $p+p$ experiment, the liquid-hydrogen (LH_2) target, which has been developed at IPN Orsay, was used (see fig. 2.2). The target consists of a 5 cm long cylinder with a diameter of 2.5 cm which is filled with LH_2 at atmospheric pressure and a temperature of 20 K. The liquid is contained in a vessel built out of Mylar foils of 100 μm thickness, glued together. The thermal insulation is achieved using a carbon fiber housing, 4 cm in diameter and 0.5 mm in thickness, placed around the vessel and covered by 10 layers of 6 μm thick aluminized Mylar which is super-insulation. The forward endcap is made of a 100 μm thick Mylar foil.

FIG. 2.2 – The liquid hydrogen target vessel with a diameter of 2.5 cm. The entrance window is glued on a stainless steel cylinder.

2.2 The Ring Imaging Cherenkov detector

The HADES Ring Imaging Cherenkov detector (RICH) (see fig. 2.3) constitutes the innermost part of the spectrometer and is built to identify e^+e^- pairs.

The detector is designed based on the Cherenkov effect, which is the electromagnetic radiation emitted when a charged particle passes through a transparent medium of refraction index n at a speed greater than the speed of light in that medium (so $v > c/n$). The opening angle

between the emitted cone of light and the particle direction is given by :

$$\cos\theta = \frac{1}{n\beta}, \qquad \beta = \sqrt{1 - \frac{1}{\gamma^2}}, \tag{2.1}$$

where θ is the opening angle, β and γ are the velocity and Lorentz factor of the particle respectively.

In the energy range of our experiment, i.e. 1-2 GeV, electrons have velocities close to the speed of light, while most of the hadrons have much lower velocities. By choosing a dielectric medium with an appropriate refraction index, the Cherenkov effect becomes a reliable tool to discriminate leptons from hadrons.

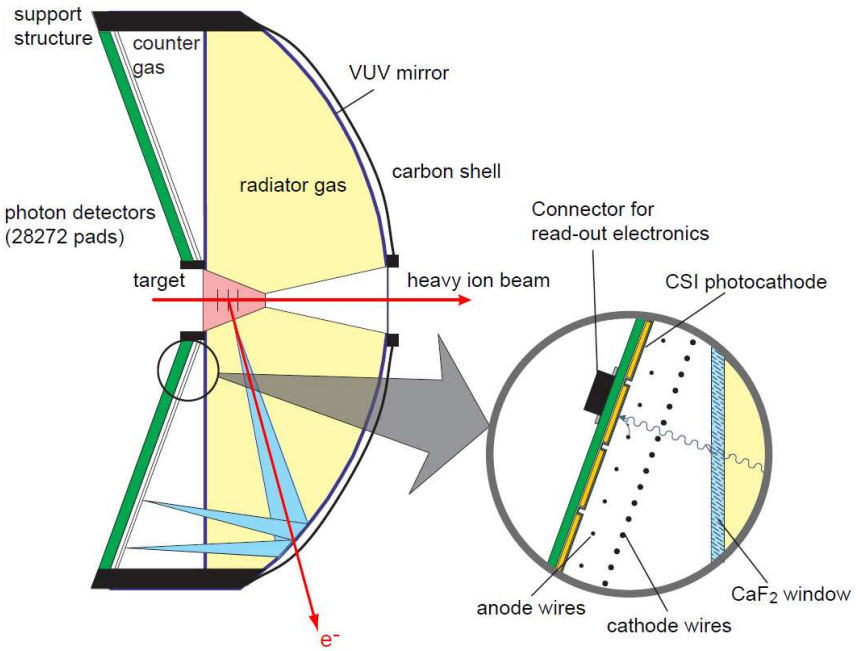

FIG. 2.3 – Schematic layout of the RICH, consisting of a Carbon shell mirror, a CaF_2 window and a photon detector.

As one of the most important components, the radiator gas in HADES RICH detector is chosen as C_4F_{10}. It has a refraction index of $n = 1.00151$ and the corresponding Cherenkov threshold is $\gamma > 18.2$. It means that, to produce the Cherenkov light, the velocity β of a particle should be greater than 0.9985, which corresponds to : 0.009 GeV/c for an electron, 2.5 GeV/c for a pion and 17 GeV/c for a proton. In the HADES experiment energy range, the momentum of electrons is much higher than the 0.009 GeV/c threshold and most of the protons and pions have momenta significantly below the threshold. Just to give an idea, in $p+p$ collisions at 1.25 GeV, the maximum momenta are about 2 GeV/c for protons and 1 GeV/c for π^+. The radiator gas offers also high transparency to the wavelengths down to $\lambda \geq 145$ nm, which is well suited since the produced photons are mostly at ultra-violet frequencies.

The spherical carbon mirror is placed downstream of the gas radiator and reflects the Cherenkov light (average reflectivity is $\sim 80\%$) to the photon detector which is able to detect a

signal photon providing an information about position. Typically an electron with a momentum of 0.1 GeV/c produces about 110 photons along its trajectory in the radiator.

2.3 The tracking system

The tracking system of HADES consists of a toroidal field provided by the superconducting coils and four planes of low-mass mini drift chambers (MDC) (see left panel of fig. 2.4). It allows to reconstruct the particle trajectories in a large solid angle (θ from 14^o to 86^o) and to determine the particle momentum with a resolution of $\triangle\, p/p \sim 4\%$ for protons.

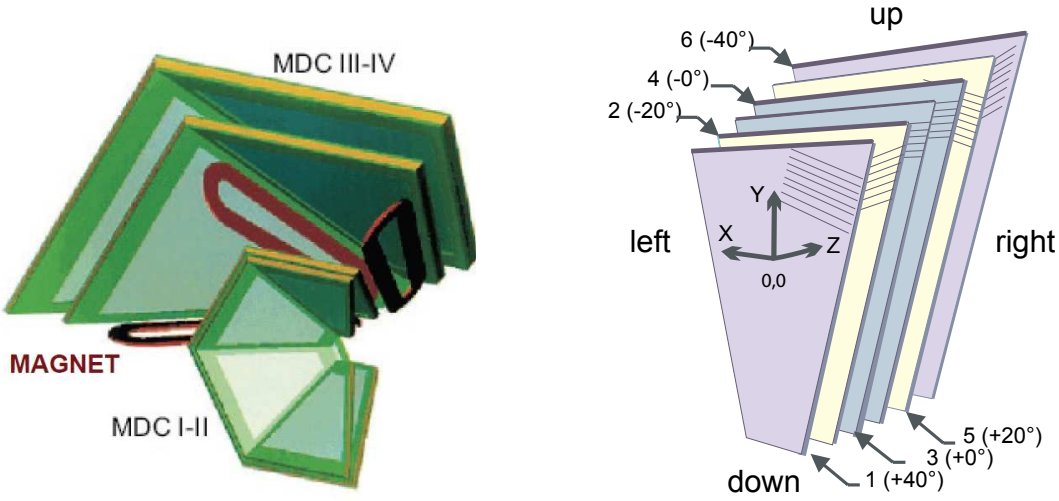

FIG. 2.4 – Schematic layout of the HADES tracking system. **Left :** Arrangement of the MDC chamber with respect to the magnetic coils. **Right :** View of the six anode wire frames inside a HADES MDC, with the respective wire angles.

2.3.1 The superconducting Magnet

The Iron-Less Superconductive Electromagnet (ILSE) [Bretz, 1999] consists of 6 superconducting coils, producing an inhomogeneous magnetic field up to a maximum value of 0.7 T within the acceptance region. This value corresponds to

$$\begin{aligned} \int B \cdot dl &\simeq 0.3 \text{ T} \cdot \text{m}, \text{ at } \theta = 20^o \\ \int B \cdot dl &\simeq 0.12 \text{ T} \cdot \text{m}, \text{ at } \theta = 70^o \end{aligned} \tag{2.2}$$

where $\int B \cdot dl$ is the integrated magnetic field. Moreover, a field free region is required (below $5 \cdot 10^{-3}$ T) at the position of the RICH and the TOF/TOFINO detectors.

At maximum field value, the transverse momentum kick p_k ranges between 0.03 and 0.1 GeV/c, where p_k is the momentum difference between the incoming and outgoing momentum vectors in the plane perpendicular to the field. For example, for a particle of charge ± 1 having momentum $p = 1$ GeV/c and emitted at $\theta = 20^o$, its momentum kick p_k amounts to 0.1 GeV/c (so the deflection angle is $\triangle\, \theta = 5.7^o$).

2.3.2 The MDC detector

The tracking is performed by 24 trapezoidal Mini-Drift Chambers(MDC) divided into 6 identical sectors of 4 planes. The sectors are symmetrically arranged around the beam direction. In each sector, 4 planes are placed, two in front of and two behind the magnetic field with increasing size. All the 24 chambers together provide a polar coverage between 14^o to 84^o and nearly full azimuthal coverage.

Each chamber is composed of six sense/field wire layers (called anode planes) oriented in different stereo angles from the inner layer to the outer : $+40^o$, -20^o, $+0^o$, -0^o, $+20^o$, -40^o in order to have a maximum spatial resolution (see right panel of fig. 2.4). There are also seven cathode wire layers (called cathode planes), so that each sense/field wire layer is in between two cathode planes. For MDC IV, the gap between anode plane and cathode plane is 5 mm. The space between anodic and field wires defines a drift cell. All four chambers contain about 1100 drift cells each with a size in average varying from 5×5 to 14×10 mm^2 from plane I to plane IV to achieve a constant detector occupancy.

In each chamber, the windows consist of aluminized Mylar foils. Inside the chamber, a Helium :Isobutane (= 60 :40) gas mixture is circulated during operation with an overpressure below 1 millibar. A new gas mixture based on argon (Argon :Isobutane = 84 :16) has been tested and is foreseen for the next coming experiments.

When a particle crosses these drift cells, it ionises the gas and produces electron/positive ion pairs along its trajectory. The electrons migrate towards the anode wires and produce further ionisation especially close to the anode wire. The collected charges induce a signal on the anode wires. For each hit wire the corresponding drift times depend on the minimal distance of the particle trajectory from the wire. Note that the relation between drift time and the drift distance is not linear in our case due to the fact that the electric field is not constant in the drift cells and it is calculated by a Garfield simulation [Markert, 2005].

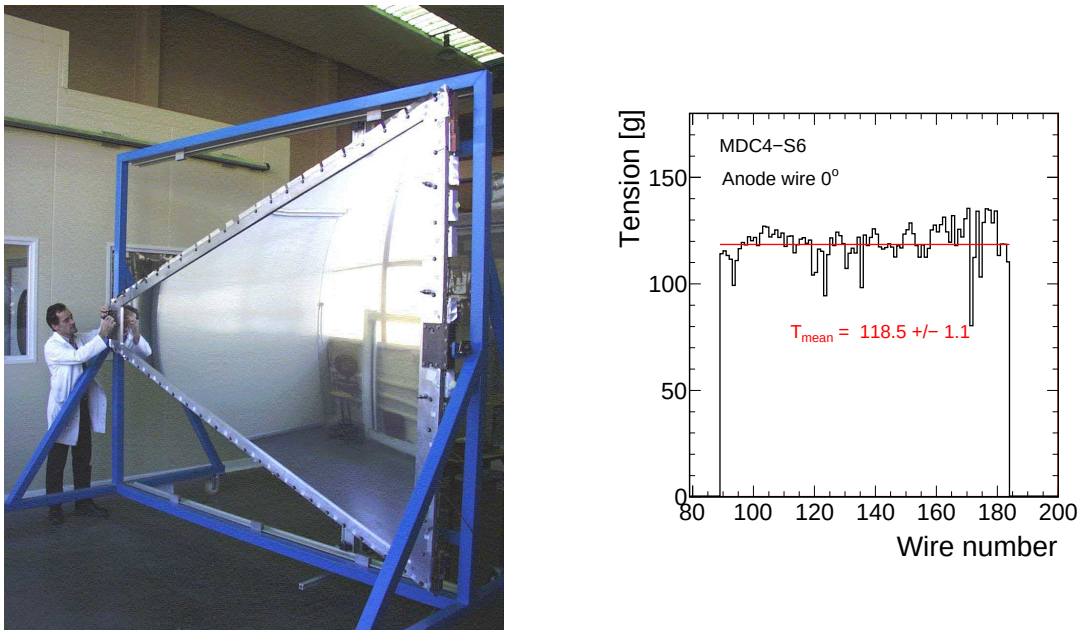

FIG. 2.5 – **Left :** View of the one HADES Mini-Drift-Chamber, MDC plane IV. **Right :** An example of measured tension of sense wire of anode plane.

The IPN Orsay was responsible for the construction of the MDC plane IV during 2001-2006. Those planes measure 280 cm high and 230 cm long from the bottom and are the biggest MDC chambers among the 4 HADES MDC planes (see left panel of fig. 2.5). Due to the unusual big size of the chamber, a lot of difficulties were addressed during construction and finally solved. For example, a careful winding is realized to obtain the designed tension and to make sure in the meantime that even for the longest wire we are well below the instability limit of the wire. The diameter of the gold-plated tungsten sense wire was chosen to be 30 μm in order to reduce the breaking probability of the wires. A carbon bar was added to maintain the wire tension at the value of 110 N after mounting to the frame.

In spring 2009, we repaired one of the Orsay chambers (MDCIV-Sector6) in which a short-circuit had been found. Taking advantage of this repair action, a systematic study of tension stability for all the layers in this chamber has been performed. Unfortunately this measurement is realized when the chamber was mounted to a frame for reparation which is different from the one used for the construction. It is thus impossible to identify a possible global tension loss. It is however interesting to check the homogeneity of the wire tension after 5 years of operation. Figure 2.5 shows an example of the measured tensions of anode plane 0^o as a function of wire number. Apart from some exceptions (for example wire No.172), the distribution of tension is quite homogeneous. A detailed investigation of the positions at both ends of each wire was also made for one layer and the distribution was found Gaussian-like with a σ of about 50 μm. After reparation, the chamber can operate stably with a high voltage of up to 2.6 kV in air and at 2.4 kV with the gas mixture (Helium :Isobutane = 60 :40). Currents of the order of 15 nA per layer (without beam) at the maximum high voltage were measured.

2.4 The Multiplicity Electron Trigger Array system

The Multiplicity Electron Trigger Array (META) system is positioned downstream behind the outer MDCs and used for particle identification and triggering. The system is formed by two sets of time-of-flight detector (TOF and TOFINO) and an electromagnetic shower detector.

2.4.1 The Time-Of-Flight detector

For the time-of-flight measurements in the polar angle region from 44^o to 88^o, the TOF detector is used. Following the hexagonal geometry of the whole spectrometer, the TOF detector is divided into six sectors (left panel of fig. 2.6). Each sector consists of 64 scintillator rods (384 rods in total) coupled on both ends to photo-multipliers (PMT). The rod length increases while ranging from the smaller to larger polar angles. This geometry allows to have a finer granularity in the forward polar angle region, where the multiplicity of produced charged particles is higher, to reduce the probability that two particles hit the same rod. The time resolution is about 150 ps.

From the measured signals the following information can be extracted : the time-of-flight ($t_{\rm tof}$) of particles, the hit position on the rod (x), and the energy deposited in the rod ($\triangle E$) with following formulas :

$$\begin{aligned} t_{\rm tof} &= \frac{1}{2}(t_{\rm left} + t_{\rm right} - \frac{L}{v_{\rm group}}), \\ x &= \frac{1}{2}(t_{\rm left} - t_{\rm right}) \cdot v_{\rm group}, \\ \triangle E &= k \cdot \sqrt{A_{\rm left} A_{\rm right}} \cdot e^{L/2\lambda_{\rm at}} \end{aligned} \tag{2.3}$$

where t_{left} and t_{right} is the time measured on the left and the right side of the rod corresponding to the time between the reaction and the readout of the signal, v_{group} is the group velocity in the rod (average velocity of light in the rod), L is the length of the rod, A_{left} and A_{right} are the signal amplitudes at the left and the right ends of the rod, λ_{at} is the light attenuation length of the rod and k is a constant.

For time-of-flight measurements, the region of polar angle below 45^o was covered by a low granularity system called TOFINO. It is divided into six sectors each consisting of four scintillator pads (see right panel of fig. 2.6), arranged radially with respect to the beam axis.

The basic principle is the same as for the TOF detector. In the case of the TOFINO detector, only one end is coupled to a PMT, so there is no information about the hit position. But directly behind the TOFINO detector, the Pre-Shower detector (will be described in the next section) is mounted, which provides the coordinate information of the particle hit on the paddle (x). The time-of-flight (t_{tof}) can be calculated using the following equation :

$$t_{\text{tof}} = t - \frac{x}{v_{\text{group}}} \tag{2.4}$$

where t is interval between the reaction and the arrival of the light pulse at the PMT, v_{group} the light group velocity in the pad and x the distance from the particle hit position to the PMT. The time resolution of TOFINO is about 420 ps, worse than TOF.

A Resistive Plate Chamber (RPC) wall has been installed in 2010 to overcome the shortcomings of the TOFINO. The new RPC detector replaces the TOFINO detector and will operate for the future experiments.

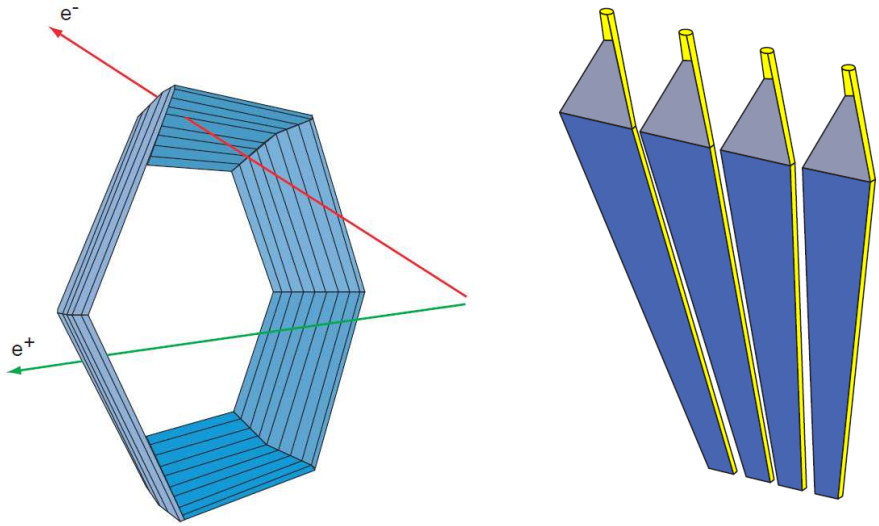

FIG. 2.6 – Schematic view of the **Left :**TOF and **Right :**TOFINO detector (one sector only).

2.4.2 The Pre-Shower detector

In the lower polar angle region, the separation of electrons from protons by time-of-flight measurements is more difficult, due to the higher momenta of hadrons. In order to improve the lepton/hadron discrimination, a detector of electromagnetic showers (Pre-Shower) is used.

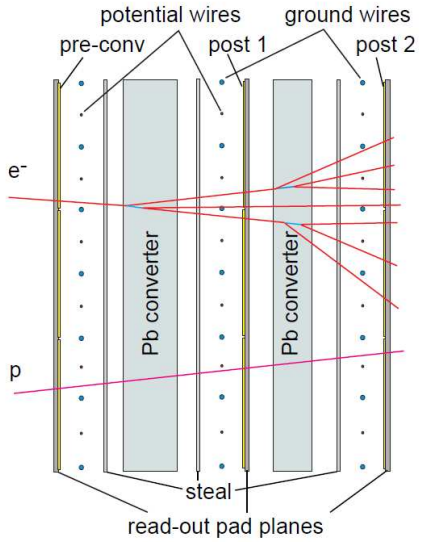

FIG. 2.7 – Side view of the Pre-Shower detector (one sector) with an example of electromagnetic shower.

The Pre-Shower detector consists of a stack of three trapezoidal wire chambers (pre-chamber, post1-chamber, post2-chamber), separated by two lead converter plates. Each cathode plane is further divided into individual pads. A charged particle passing through the gas chambers produces an ionisation avalanche, with electrons drifting towards the closest anode wire ; the cloud motion induces a positive charge on the nearby cathode pads, connected to charge-sensitive preamplifiers. The integrated charge is proportional to the avalanche charge, and an integration over several pads around the pad with the highest charge value (local maximum) has to be performed, in order to obtain the complete charge of the electromagnetic shower. By comparing the integrated charge of the same track in different layers it is possible to distinguish electromagnetic showers from hadronic tracks. The replacement of Pre-Shower detector by a lead glass calorimeter is foreseen in the near future.

2.5 The trigger system

A two level trigger system is used in the HADES experiments :

– 1^{st} level trigger : The first level trigger (noted as LVL1) consists of a fast hardware selection of central collisions, by measuring the hit multiplicity in META system. It is possible to apply multiplicity selections in TOF and TOFINO separately and sectorwise, in order to select only interesting decay channels, which is used for example in elementary reactions, such as $p + p$ collisions.

– 2^{nd} level trigger : The second level trigger (noted as LVL2) is based on an online search for lepton candidates in the event. (ring in RICH and META matching)

2.5.1 Principle of trigger system

The events accepted by the LVL1 trigger decision are sent to the matching unit board and processes with the following options :

- If the events contain a lepton candidate, they are accepted by the LVL2 trigger and then are all written to the file for inclusive di-electron analysis. They are called LVL2 events.

- Disregarding whether the events contain a lepton candidate or not, all the events are sent to a downscaling box which reduces the number of events by a corresponding factor (called LVL1 dsf). They are finally recorded in the files, for hadronic analysis and normalization factors. They are called downscaled LVL1 events.

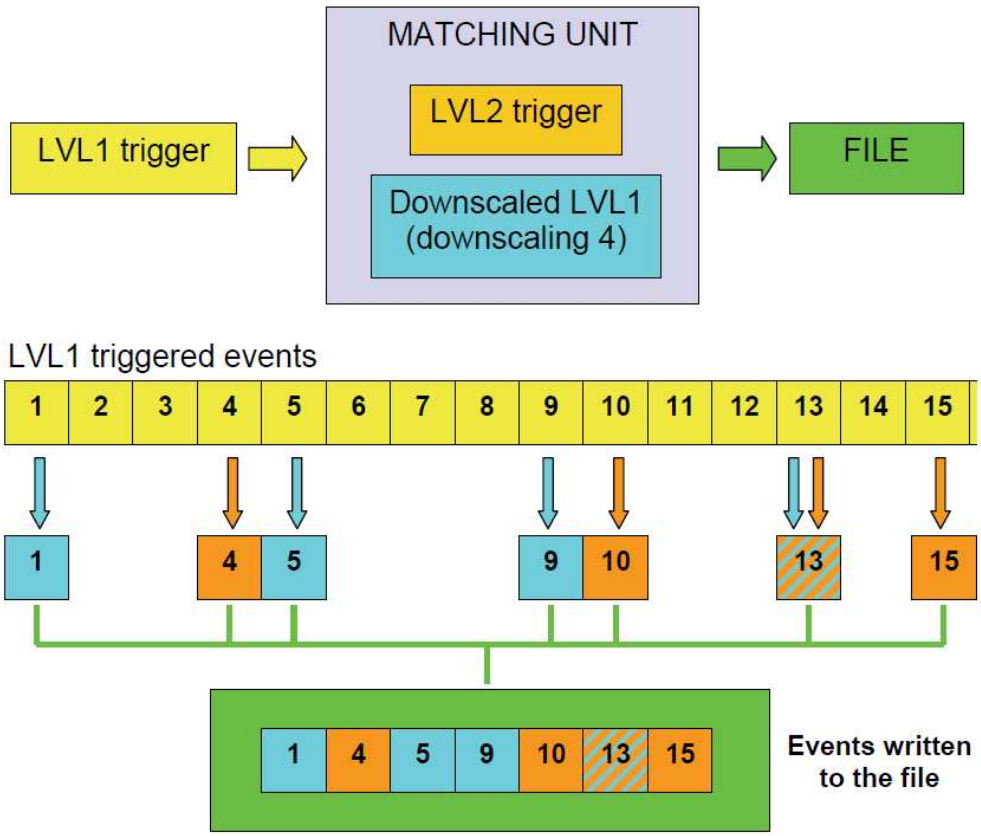

FIG. 2.8 – Sketch of the event selection used for data acquisition.

The downscaled LVL1 events are recorded because we are also interested in events which contain hadrons. However, the rate of hadronic events is so high that their numbers has to be reduced.

Fig. 2.8 gives a schematic explanation of the event selection used for data acquisition. A first selection of the events is done by the LVL1 trigger (yellow boxes), and they are sent to the matching unit afterwards where the downscaling factor is 4. This means that one event out of four is stored (event number 1, 5, 9, 13, ...) (labeled by blue boxes), no matter the LVL2 trigger decision. In the meantime, all the events with a recognized lepton pair are stored as well (labeled orange boxes). It can happen that an event can be at the same time downscaled by the LVL1 trigger and be accepted by LVL2 trigger, like for instance the event number 13 in the example. If we want to have the total number of the LVL1 trigger events, we must multiply the number of downscaled LVL1 events (4) by the downscaling factor (4). In this case, we obtain 16 triggered events against 7 which are effectively stored to file. This means that in the example we found 4 lepton pair candidates by storing only 7 events instead of 16. In this particular case, we have roughly saved half of the disk space, and half of the time needed for the data processing.

For the $p+p$ run in April 2006, the LVL1 downscaling factor is set to 5.

2.5.2 Experimental conditions set in the $p+p$ run at 1.25 GeV

In order to favour the different reaction channels, different trigger types are used for the LVL1 with an additional corresponding downscaling factor (called trigger box dsf) . As listed in table 2.1, three different trigger settings were used.

Trigger type	**LVL1 dsf**	**Trigger box dsf**
M3	5	1
M2 Opp. Sec. & TS (only TOFINO)	5	64

TAB. 2.1 – Different LVL1 trigger types in $p+p$ run at 1.25 GeV in April 2006.

The M2 Opp. Sec. & TS (only TOFINO) trigger required two charged particles detected in opposite sectors and asked in addition that one of the charged particles hits the TOFINO detector as a Time Signal (TS). This trigger is optimized for the detection of $p+p$ elastic scattering which will be used for normalization of the final results (see section 4.4), but it is also used for other hadronic channel analyses e.g. $pp \to pp\pi^0$ and $pp \to np\pi^+$ which will be discussed in detail in this thesis. Since the cross section of the elastic channel is high, a trigger box dsf equal 64 is set.

The M3 trigger requiring at least three charged particles detected in the META is used to favor an exclusive reconstruction of a four-prong final state (e.g. of the type ppe^+e^-), which allows an exclusive study of the Δ Dalitz decay (see chapter 6). As it is the main goal of this experiment and the corresponding events are rare, no downscaling is set.

2.6 Proton-proton reaction at 1.25 GeV running conditions

During the April 2006 experiment we used a proton beam of 1.25 GeV kinetic energy, with an intensity of up to 10^7 particles per second. The target consisted of a 5 cm long Mylar vessel, filled with liquid hydrogen with about $2 \cdot 10^{23}$ protons/cm^2. It resulted in an interaction probability of about 1%.

The detector setup consisted of the RICH, META detectors which have been fully installed. While the tracking system was partially operational : the inner MDCs were working in each sector, but MDC III, sector 0, sector 1 and MDC IV, sector 5 were not turned on. Data were taken with a current of $I = 2497\ A$, corresponding to 72% of the maximum strength of the magnetic field, which is optimized for the best detection of both electrons and protons at 1.25 GeV. The system of START-VETO detectors was not used in this experiment.

Chapitre 3

Simulations

3.1 Pluto - Monte-Carlo simulation tool

The simulation work in this thesis is performed with the Pluto event generator [Froehlich et al., 2007, 2010]. The Pluto event generator is a ROOT-based [Brun and Rademakers, 1997] package which allows to describe the production of particles in elementary reactions and their hadronic and leptonic decays. Moreover, it allows also to simulate heavy-ion induced reactions by using a fireball model (thermalized source) and tabulated production cross sections. The development of Pluto was mainly motivated by the physics program of the HADES experiment and its goal is to provide reference spectra based on the known experimental information for the model predictions.

3.2 Inputs for simulation

We will give in this section the ingredients for the simulation of pionic channels in $p + p$ reactions at 1.25 GeV.

3.2.1 Cross sections

Isospin channel	**Cross section**	**Outgoing channel**	**Cross section**
Elastic scattering	22 mb	$pp \rightarrow pp$	
1-pion production	23.4 mb	$pp \rightarrow np\pi^+$	19.4 mb
		$pp \rightarrow pp\pi^0$	4.0 mb
2-pion production	0.951 mb	$pp \rightarrow pn\pi^+\pi^0$	0.515 mb
		$pp \rightarrow pp\pi^0\pi^0$	0.105 mb
		$pp \rightarrow pp\pi^+\pi^-$	0.241 mb
		$pp \rightarrow nn\pi^+\pi^+$	0.09 mb
3-pion production	0.00195 mb	$pp \rightarrow pp\pi^0\pi^0\pi^0$	0.00032 mb
		$pp \rightarrow pp\pi^+\pi^-\pi^0$	0.00163 mb
		$pp \rightarrow pn\pi^+\pi^+\pi^-$	0 mb
Di-lepton production	0.0002227 mb	$pp \rightarrow ppe^+e^-$	

TAB. 3.1 – Main pion and di-electron production channels in the $p + p$ reaction at 1.25 GeV [Teis et al., 1997].

Table 3.1 gives the possible reactions and the corresponding cross sections in $p+p$ collisions at 1.25 GeV. The main contributions come from the elastic scattering which has a cross section equal to 22 mb and therefore represents 47% of the total cross section on the one hand and on the other hand the one-pion production channels with final states $np\pi^+$ and $pp\pi^0$. The multi-pion production is much less probable. The di-lepton production channel is even more rare.

The simulation is performed for the one-pion production channels $pp \to pp\pi^0$ and $pp \to np\pi^+$. The cross sections of involved resonant processes are taken from Teis [Teis et al., 1997], as listed in table 3.2.

Outgoing channel	**Cross section**	**Production processes**	**Cross section**
$pp \to np\pi^+$	19.4 mb	$pp \to n\Delta^{++}$	17.0 mb
		$pp \to p\Delta^+$	1.9 mb
		$pp \to pN^*$	0.34 mb
$pp \to pp\pi^0$	4.0 mb	$pp \to p\Delta^+$	3.8 mb
		$pp \to pN^*$	0.2 mb

TAB. 3.2 – Channels used for the simulation of exclusive one-pion production in $p+p$ reaction at 1.25 GeV.

3.2.2 Two-step generation

In the Pluto generator, the process of pion production via a resonant state consists of two-steps : the resonance production and the resonance pionic decay. In the following sections, we will describe the two-step generation procedure in the case of the Δ resonance ($pp \to N\Delta$ and $\Delta \to N\pi$), which is the main process at 1.25 GeV and will be studied in this PhD thesis.

3.2.3 Production of Δ resonance

In the Pluto generator, the cross section of Δ production at a fixed mass m is factorized as :

$$\frac{d^2\sigma}{dm\ dt} = \frac{d\sigma}{dt}\rho(m) \tag{3.1}$$

where :

- $\rho(m)$ is the relativistic Breit-Wigner distribution of the Δ mass ;
- $\frac{d\sigma}{dt}$ is the differential cross section of the $NN \to N\Delta$ process.

More precisely, $\rho(m)$ is in the form

$$\rho(m) = 2m[\frac{1}{\pi}\frac{m\Gamma(m)}{(m^2 - m_\Delta^2)^2 + m^2(\Gamma(m))^2}] \tag{3.2}$$

where

$$\Gamma(m) = \Gamma_\Delta \frac{m_\Delta}{m}\left(\frac{k}{k_\Delta}\right)^3\left(\frac{k_\Delta^2 + \delta^2}{k^2 + \delta^2}\right)^2 \tag{3.3}$$

with

- $m_\Delta = 1232$ MeV/c^2, the resonance mass ;

- $\Gamma_\Delta = 120$ MeV/c^2, the resonance width ;
- k and $k_\Delta = 229$ MeV/c are the three-momenta of the pion in the reference frame of a Δ resonance with mass m and m_Δ, respectively.

The factor $\left(\frac{k}{k_\Delta}\right)^3$ is related to the fact that the Δ resonance is a $N-\pi$ wave of angular momentum $l = 1$. The effect is a very large increase of the width as a function of the Δ resonance mass, while the cut-off factor $\left(\frac{k_\Delta^2+\delta^2}{k^2+\delta^2}\right)^2$ takes into account the Δ off-shell correction. This factor is taken from Moniz with $\delta = 300$ MeV/c, and was adjusted to reproduce the $N-\pi$ phase shifts [Moniz and Sevgen, 1981]. A slightly different parametrization is used in [Dmitriev and Sushkov, 1986]. The influence of this factor on the mass and angular distributions has been studied in the PhD thesis [Morinière, 2008] and it has been found to be small.

Assuming a fixed mass of the Δ, the differential cross section of the processes $NN \to N\Delta$ is based on the One-Pion Exchange Model (OPEM) [Dmitriev and Sushkov, 1986] and can be written in the form of :

$$d\sigma/dt = \frac{1}{64\pi I^2} \left|M_{NN\to N\Delta}\right|^2 , \tag{3.4}$$

where :

- $\frac{1}{64\pi I^2}$ is a constant related to the beam momemtum and the center of mass energy of the reaction ;
- $t = q^2 = (k_1 - k_3)^2$ is the four-momentum transfer squared of the direct graph (fig. 3.1(a)) ;
- $|M_{NN\to N\Delta}|^2$ is the $NN \to N\Delta$ transition amplitude squared summed over the spins of the final particles and averaged over the spins of the initial particles ;
- $I = \sqrt{(k_1 k_2)^2 - M^4}$ is the flux factor.

(a) (b)

FIG. 3.1 – Direct and exchange graphs for the Δ production in $p + p$ collisions with the OPE model.

The direct $\pi-$exchange amplitude squared result is :

$$\frac{1}{4}\sum_{\lambda_1\lambda_2\lambda_3\lambda_4} |M_{NN\to N\Delta}(direct)|^2 = \left(\frac{g_\pi f_\pi^*}{m_\pi}\right)^2 \frac{F^4(t)}{(t-m_\pi^2)^2} \times t\{t-(m_\Delta - m_N)^2\} \frac{[(m_\Delta + m_N)^2 - t]^2}{3m_\Delta^2} \tag{3.5}$$

where

- $g_\pi = 13.6$ is the πNN coupling constant ;
- f_π^* is the $\pi N\Delta$ coupling constant, the value is 2.202 and corresponds to a $\Gamma_\Delta = 120$ MeV/c^2 ;

- $F(t)$ is the form factor of the $\pi N\Delta$ vertex. It is in the form of $F(t) = \frac{\Lambda_\pi^2 - m_\pi^2}{\Lambda_\pi^2 - t}$, where m_π is the π mass and $\Lambda_\pi = 0.63$ GeV is called the cut-off parameter. $F(t) = 1$ when the exchanged π is on-shell ($t = m_\pi^2$) and $F(t) < 1$ when the exchanged π is off-shell. In addition, $F(t)$ strongly cuts the four-momentum transfer squared $-t \gg \Lambda_\pi^2$.

In the same way, the expression of the exchange graph (fig. 3.1(b)) can be obtained by changing momentum transfer squared t to $u = q^2 = (k_3 - k_2)^2$.

The interference between direct and exchange graph is of the form :

$$\begin{aligned}
&\frac{1}{4}\sum_{\lambda_1\lambda_2\lambda_3\lambda_4} \left|M^+(direct)M(exchange) + M^+(exchange)M(direct)\right| \\
&= (\frac{g_\pi f_\pi^*}{m_\pi})^2 \frac{F^2(t)F^2(u)}{(t-m_\pi^2)(u-m_\pi^2)} \\
&\times \frac{1}{2m_\Delta^2}\{\ [tu + (m_\Delta^2 - m_N^2)(t+u) - m_\Delta^4 + m_N^4][tu + m_N(m_\Delta + m_N)(m_\Delta^2 - m_N^2)] \\
&\times \frac{1}{3}[tu - (m_\Delta + m_N)^2(t+u) + (m_\Delta + m_N)^4][tu - m_N(m_\Delta - m_N)(m_\Delta^2 - m_N^2)]\ \}\,.
\end{aligned} \tag{3.6}$$

Taking the $pp \to n\Delta^{++}$ reaction at 1.25 GeV as an example, the final results generated from Pluto are shown in fig. 3.2. The mass distribution is slightly asymmetric. This is due to the effect of the mass dependent width, which is however compensated by the cut-off factor $\left(\frac{k_\Delta^2 + \delta^2}{k^2 + \delta^2}\right)^2$. The strongly forward and backward peaking angular distribution is characteristic of the peripheral character of the one-pion exchange. Both distributions give a nice description of existing data. An example was shown at an incident beam momentum ($p_{\text{lab}} = 1.66$ GeV/c) slightly lower than in our experiment on fig. 1.6.

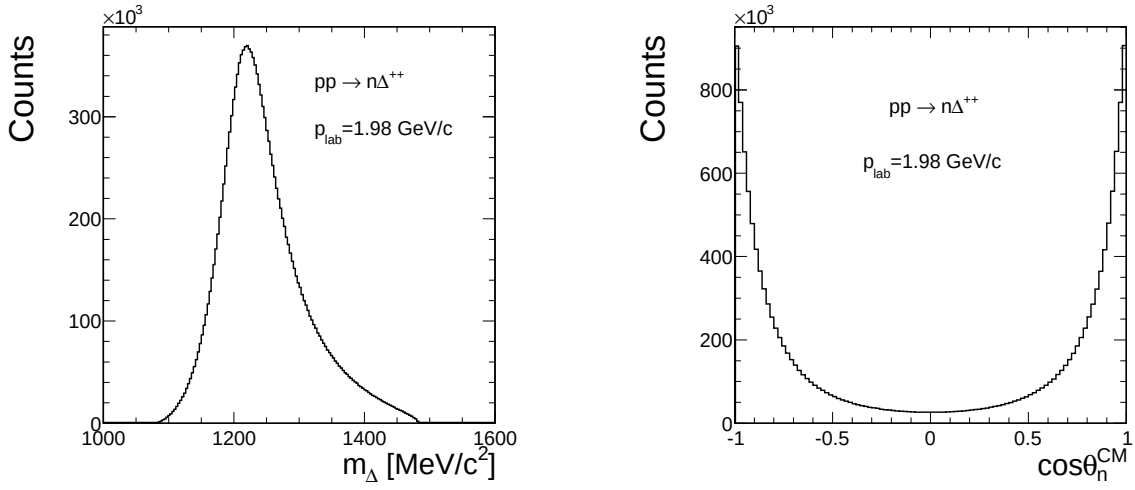

(a) (b)

FIG. 3.2 – **Left :** Δ mass distribution and **Right :** neutron angular distribution in the $p + p$ center-of-mass system in $pp \to n\Delta^{++}$ reaction in Pluto simulation.

Fig 3.3 shows the ratios of amplitudes of direct and exchange graphs as function of the neutron angular distribution in the $p + p$ center-of-mass system. We can see that the direct term

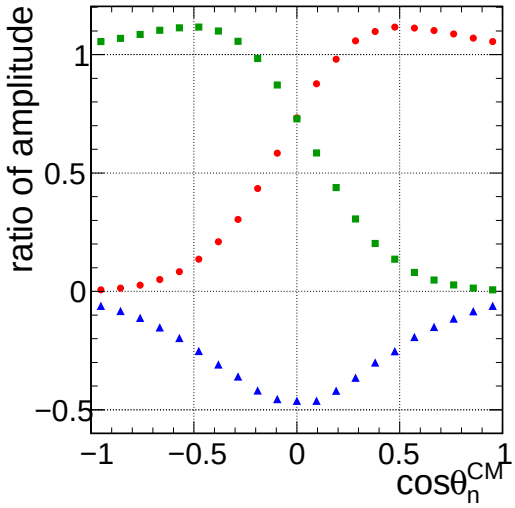

FIG. 3.3 – The ratio of direct graph (red circles), exchange graph (green rectangles) and interference (blue triangles) to total amplitude as a function of $\cos\theta_n^{CM}$.

(red circles) is dominant for the backward going Δ (so forward going neutron), while the exchange term (green rectangles) is symmetric with the direct one with respect to $\cos\theta_{\Delta^{++}}^{CM} = 0$ (so $\cos\theta_n^{CM} = 0$), i.e. dominant for forward going Δ's (so backward going neutron). The interference plays an important role especially in the intermediate angular region, where it contributes up to 25% of the total cross section.

3.2.4 Parametrization of the Δ decay angular distribution

In Pluto, the pion angle θ in the processes $\Delta \rightarrow N\pi$ is sampled with respect to the momentum transfer in the reference frame where the excited nucleon is at rest. As shown in (fig. 3.4), q is the momentum transfer between the nucleon and Δ resonance and θ is the quantity we are interested in.

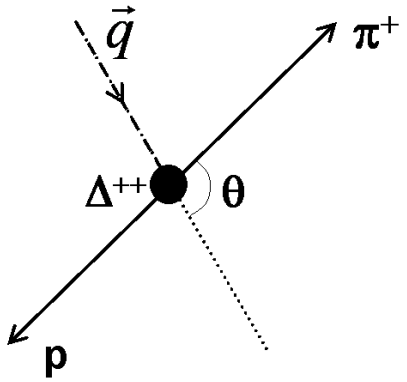

FIG. 3.4 – Sketch of the π angle in the Δ pionic decay process.

Neglecting the ϕ-dependence, the π angular distribution in the Δ rest frame is :

$$d\sigma/d\cos\theta \sim 1 + Acos^2\theta. \tag{3.7}$$

where A is the anisotropy coefficient (see section 1.5.3).

Reference frame for π^+ angle sampling

In the $\Delta \rightarrow N\pi$ process, in order to have the π angular distribution in the Δ reference frame as in equation 3.7, the z-axis has to be defined as the direction of the momentum transfer q in the reference frame where the excited nucleon is at rest [Gottfried and Jackson, 1964, Dahl, 1995].

So, for the direct graph (fig. 3.1(a))

$$\vec{q} = \vec{p}_{\Delta} - \vec{p}_{p_{target}}, \tag{3.8}$$

and for exchange graph (fig. 3.1(b))

$$\vec{q} = \vec{p}_{\Delta} - \vec{p}_{p_{beam}}. \tag{3.9}$$

In the literature, e.g. [Wicklund et al., 1987], another definition of this z-axis can be also found. It is defined as the direction of the excited proton in the outgoing (p, π^+) reference frame. In fact, these two definitions are equivalent. We will demonstrate it in the following, considering the process $pp \rightarrow n\Delta^{++} \rightarrow np\pi^+$. On can always write :

$$\begin{aligned} \vec{p}_{p_{exc}} + \vec{p}_{p_{scatt}} &= \vec{p}_n + \vec{p}_{p\pi^+} \\ \vec{p}_{p_{scatt}} - \vec{p}_n &= \vec{p}_{p\pi^+} - \vec{p}_{p_{exc}} \end{aligned} \tag{3.10}$$

where p_{scatt} is the scattered proton and p_{exc} is the excited proton. Since

$$\vec{p}_{p_{scatt}} - \vec{p}_n = \vec{p}_{p\pi^+} - \vec{p}_{p_{exc}} = \vec{q} \tag{3.11}$$

we have

$$\vec{q} = \vec{p}_{p\pi^+} - \vec{p}_{p_{exc}} \tag{3.12}$$

If we stand in the (p, π^+) reference frame, $\vec{p}_{p\pi^+}$ is 0 and we can deduce :

$$\vec{q} = -\vec{p}_{p_{exc}} \tag{3.13}$$

Thus

$$\vec{q} \;//\; \vec{p}_{p_{exc}} \tag{3.14}$$

which means that the two definitions are equivalent.

One can also note, that depending on the papers, the direct graph is considered as corresponding to excitation from the target (e.g. in [Dmitriev and Sushkov, 1986]) or from the projectile (e.g. in [Wicklund et al., 1987]).

Anisotropy coefficient A

The formalism of the density matrix implies that the direction of the momentum transfer q is known. But because of the mixture of direct and exchange graph in the production the proper reconstruction of q is inaccessible.

However we can learn from fig. 3.3 that in the region of $|\cos\theta_n| > 0.8$, the contribution from the direct graph or exchange graph is definitely dominant while the other two terms contribute to the cross section by less than 10%. With the dominance of direct or exchange graph in these regions, the direction of q is well defined. This is the reason why we considered only the results obtained for $|\cos\theta_n| > 0.8$ in our energy range (see section 1.5.3) and use the π anisotropy coefficient $A = 0.66$ found in this angular region as the anisotropy parameter.

This parameter is implemented in Pluto in the following way : for each mass and angle in the Δ production process, the direction of the Δ is sampled according to the direct and exchange graph weights, neglecting the interference. The π angle is then sampled according to the distribution : $1 + 0.66\ \cos^2\theta$.

In this way, we obtain the Δ decay angular distribution shown in fig. 3.5 generated from Pluto with anisotropy coefficient $A = 0.66$ and compare it to the isotropic decay ($A = 0$) and the decay in a pure OPEM ($A = 3$). As expected, in this angular region ($\cos\theta_n > 0.8$), the $\cos\theta_{\pi^+}^{(p,\pi^+)}$ directly reflects the Δ decay angular distribution.

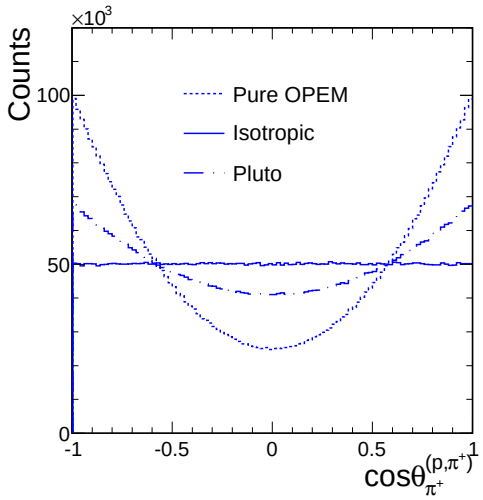

FIG. 3.5 – Δ decay angular distribution in $\Delta^{++} \to p\pi^+$ processes in the region of $\cos\theta_n > 0.8$ following different models : isotropic decay $A = 0$ (solid line), pure OPEM $A = 3$ (dotted line) and Wicklund decay $A = 0.66$ (dot-dashed line).

3.2.5 $N^*(1440)$ resonance production and decay in Pluto

The $N^*(1440)$ resonance with spin 1/2 also contributes to the $pp \to NN\pi$ processes.

In the Pluto simulation, the mass distribution of the N^* is parameterized in a similar way to the Δ production. The resonance mass is set to be 1440 MeV/c^2 and the width is 350 MeV/c^2. In the $p + p$ reaction at 1.25 GeV, the center-of-mass energy of the system is $\sqrt{s} = 2420$ MeV.

This is why the N^* mass can not be larger than 1480 MeV/c^2 (see left panel of fig. 3.6).

The production angular distribution of the N^* is treated to be isotropic in Pluto by default. In order to have a more realistic description, we have customized the distribution as in [Huber and Aichelin, 1994] according to the One Boson Exchange model. The result is shown in the right panel of fig. 3.6.

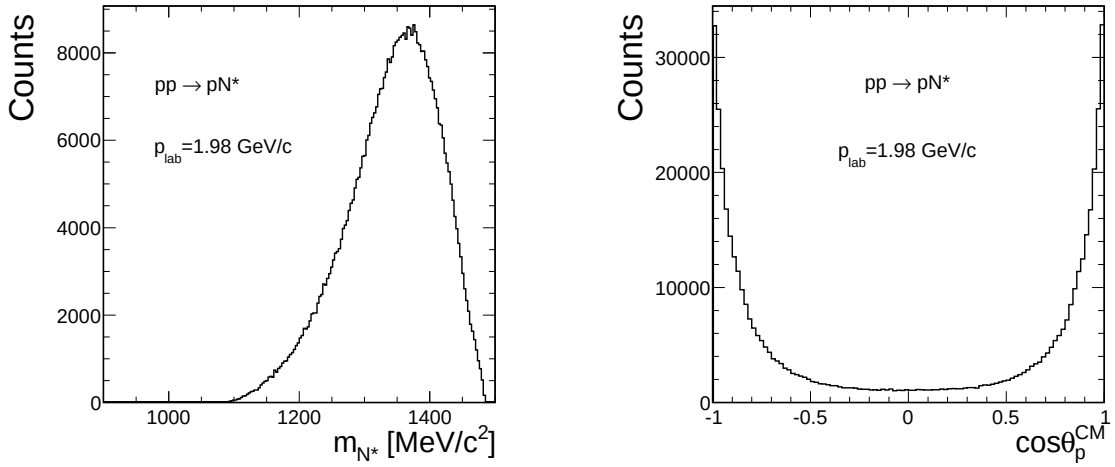

FIG. 3.6 – **Left :** Mass and **Right :** angular distribution for $N^*(1440)$ resonance in p+p reactions at 1.25 GeV, in Pluto simulation.

3.3 Advantages and limitations of the used simulation with Pluto event generator

The simulation work in this thesis is performed using the Pluto event generator. One should first mention that Pluto is a very versatile event generator which can be used in different ways [Froehlich et al.]. In particular, it can use differential cross-sections provided by theoretical models, as was done for the $pp \rightarrow ppe^+e^-$ channel. Here, we use a cocktail of processes which are treated in a incoherent way. So there are following limitations :

- The interference effect between different processes with the same exit channel is not taken into account.
- The cross sections are set for each process as a normalization factor independent of the model used to sample the distributions. For example, in the case of $pp \rightarrow n\Delta^{++}$ the OPEM is used for the four-momentum transfer distribution, while the cross-section can be set independently.
- Only dominant graphs are taken into account. For example, emission of pions from graphs involving only nucleons (non-resonant contribution) or emission of the pion before the Δ excitation (pre-emission) are not taken into account.
- The production and decay process of the resonances is done in two-steps, assuming a factorization of the cross sections. The polarization effects are however taken into account although in a rather crude way (see section 3.2.4).
- As a consequence of the last point, the indistinguishability of the particles in the exit channel is not taken into account properly. In the case of $p + p$ collision, the $pp \rightarrow pp\pi^0$ and $pp \rightarrow ppe^+e^-$ channel are concerned.

The mentioned limitations (point 1,2 and 3) are maybe not so important in our specific case, due to the dominance of the Δ resonance. It will however be stressed many times that full models should also be used.

The advantage of using the Pluto simulation tool is also obvious.
- Using simple models and parametrization, it allows a very fast and easy simulation.
- The design of Pluto provides also a convenient way to implement and customize the model by users. The sensitivity to the parameters of the models can be therefore easily estimated.
- The data samples generated by Pluto can be directly filtered by the efficiency and acceptance matrices (will be introduced in next sections) to take into account the detector geometry and working performance.

3.4 Kinematics of $pp \rightarrow N\Delta \rightarrow np\pi^+$ process in 4π

3.4.1 Dalitz plot in 4π

The Dalitz plot, introduced in 1953 by R.H. Dalitz, is a scatter plot often used in particle physics to present the kinematics of three-body decays. The variables on the axes of the plot are the squares of the invariant masses of two pairs of decay products. Considering a process as in fig. 3.7 (a), a system of center-of-mass energy $\sqrt{s}$ gives 3 outgoing particles labeled 1, 2 and 3, with the mass m_i and momentum p_i.

The Dalitz plot for this process could be a plot for example of $(m_{12})^2$ versus $(m_{23})^2$. If the process is a direct production from system $\sqrt{s}$ to particles 1, 2 and 3, the distribution on the Dalitz plot is uniform with kinematical limits :

$$\begin{aligned} (m_1+m_2)^2 \;&\leq\; (m_{12})^2 \;\leq\; (\sqrt{s}-m_3)^2 \\ (m_2+m_3)^2 \;&\leq\; (m_{23})^2 \;\leq\; (\sqrt{s}-m_1)^2. \end{aligned} \tag{3.15}$$

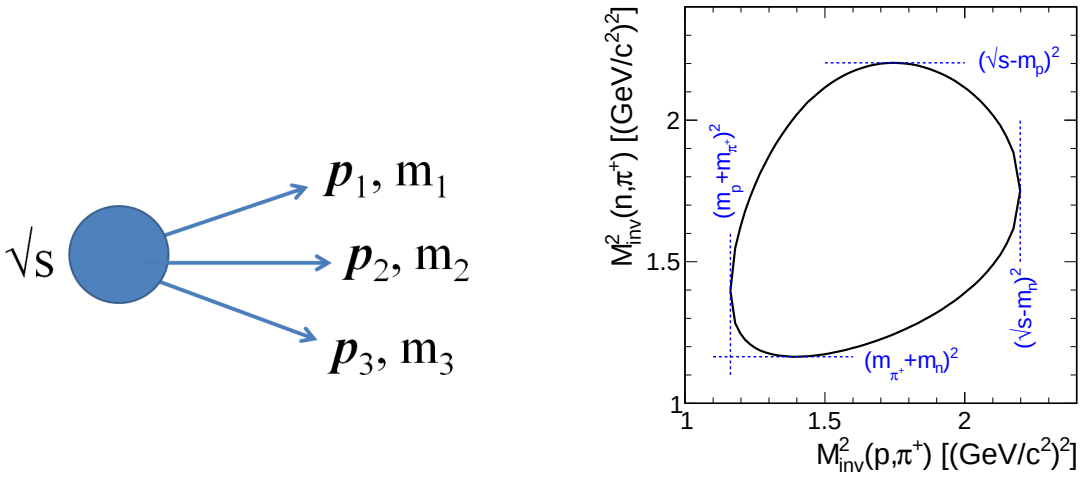

(a) (b)

FIG. 3.7 – (a) : Definitions of variables for three-body decays : the system of center-of-mass energy $\sqrt{s}$ gives 3 outgoing particles labeled 1, 2 and 3, with the mass m and momentum p. (b) : Dalitz plot for a three-body final state $np\pi^+$ at 1.25 GeV. The solid curve indicates the boundary of the 3-body kinematical limits and the maximum and minimum value of invariant masses are given.

However, three-body decays are often dominated by resonant processes, in which the particle decays into two decay products, with one of them decaying into two other particles. In this case, the Dalitz plot will show a non-uniform distribution, with a peak around the square mass of the decaying resonance.

Fig. 3.7 (b) gives an example of a Dalitz plot for a three-body final state at 1.25 GeV, where the particles 1, 2 and 3 correspond to neutron, proton and π^+ respectively. The invariant mass squared of the (p,π^+) pair is shown on the x-axis and the invariant mass squared of the (n,π^+) pair is on the y-axis. The solid line indicates the kinematical limits of this decay process, which means the allowed region of invariant masses squared. The boundary in fig. 3.7 (b) is nearly

symmetric with respect to the diagonal, since the masses of neutron and proton are quite close.

Fig. 3.8 shows a series of Dalitz plots corresponding to the reaction $pp \rightarrow np\pi^+$ generated from Pluto simulations. The panel (a) refers to the direct $np\pi^+$ production (noted as non-resonant) simulated using phase space distribution. It is uniform as expected. Panels (b), (c) and (d), show Dalitz plots obtained in the simulation when either the (n, π^+) pair or the (p, π^+) pair corresponds to the decay of a resonance. The boundaries of the plots stay the same, and the various distributions which reflect the intermediate resonance state can be seen. Taking (b) as an example, where the (p, π^+) is emitted from the $\Delta^{++}(1232)$ resonance, a prominent peak around 1.5 $(\mathrm{GeV}/c^2)^2$ can be found right at the squared mass of $\Delta^{++}(1232)$. The $\Delta^+(1232)$ and N*(1440) show up in (c) and (d).

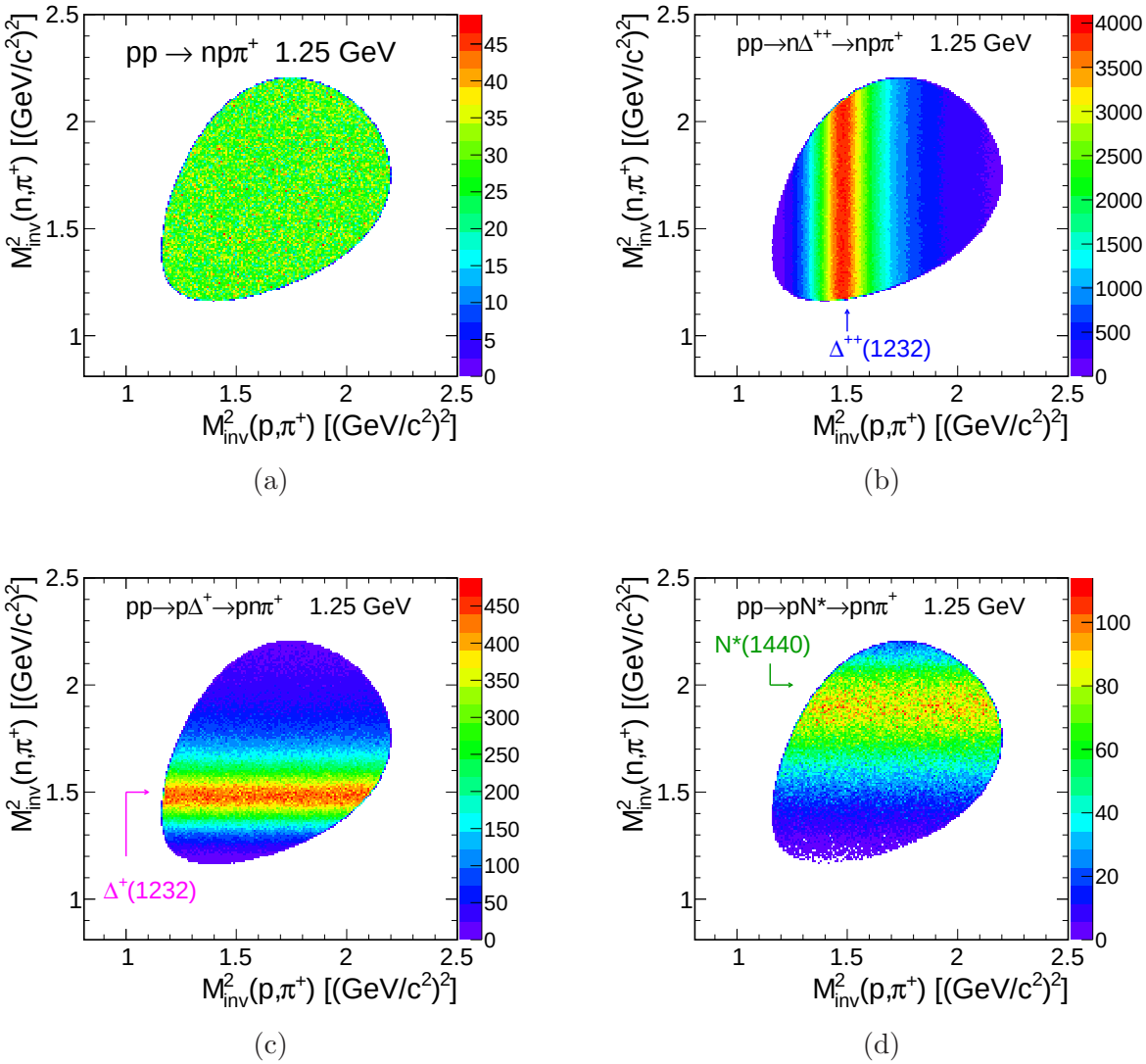

(a) (b) (c) (d)

FIG. 3.8 – 4π Dalitz plot for events coming from Pluto simulation of $pp \rightarrow np\pi^+$ reactions at 1.25 GeV. (a) through direct decay and via intermediate resonances, (b) $\Delta^{++}(1232)$, (c) $\Delta^+(1232)$ and (d) $N^*(1440)$.

3.4.2 Momentum and polar angle distributions in 4 π

The momentum and polar angle distributions of detected particles, i.e. proton and π^+, have been studied as well, in the case of production via different resonances ($\Delta^{++}(1232)$, $\Delta^{+}(1232)$ and $N^*(1440)$) respectively.

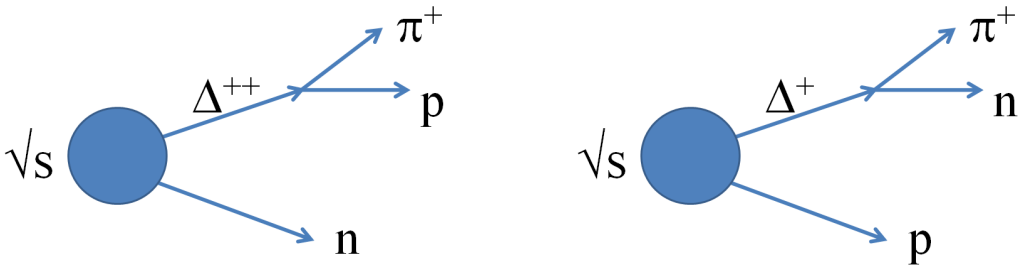

FIG. 3.9 – Diagrams for Δ production and decay process.

$pp \rightarrow n\Delta^{++} \rightarrow np\pi^+$

This reaction can be decomposed into two steps : first the two-body reaction $pp \rightarrow n\Delta^{++}$; then the Δ^{++} produced in the first step decays into a proton and a π^+. The proton carries most of the energy of the resonance because its mass is close to the resonance's and much higher than the one of the π^+. The two branches of proton in the left panel of fig. 3.10 reflect indeed the forward and backward peaked Δ production angular distribution.

In each branch, the events are distributed in a broader region, with respect to the very focused peaks in the case of fig. 3.11, because of the Δ^{++} decay distribution. The boundary of the plot represents the kinematical limit, i.e. limit angle ($\theta_p < 60^o$) and momentum ($p_p < 1.78$ GeV/c), of this proton. The right panel of fig. 3.10 shows the same plot for π^+. We can see that the π^+ can reach the maximum polar angle ($\theta_{\pi^+} = 180^o$) and is limited in a smaller momentum range ($p_{\pi^+} < 1$ GeV/c) because of its small mass. As a decay product of the Δ^{++}, the π^+ keeps however some memory of the production process. Two forward and backward branches still can be recognized, but they overlap in the region of intermediate θ and p.

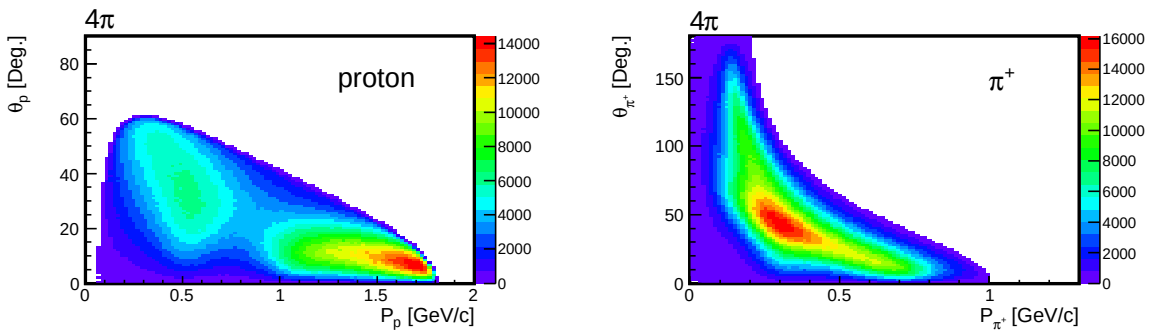

FIG. 3.10 – Polar angle versus momentum in laboratory frame for proton (left panel) and π^+ (right panel) in 4π, in reaction $pp \rightarrow n\Delta^{++} \rightarrow np\pi^+$ at 1.25 GeV from Pluto simulation.

$pp \rightarrow p\Delta^+ \rightarrow pn\pi^+$

In the case of $pp \rightarrow p\Delta^+ \rightarrow pn\pi^+$ channel (see fig. 3.11), the distribution of π^+ is exactly the same as the channel above because it comes from the decay of a resonance with the same mass. But the kinematics of the proton is different, because this proton is scattered from beam or target and has a momentum opposite to the Δ^+ in the $p+p$ center-of-mass system. Thus this proton presents directly the behavior of the Δ^+ resonance production reaction, where the forward branch of the proton corresponds to the backward going Δ^+, while the backward branch of proton corresponds to the forward going Δ^+.

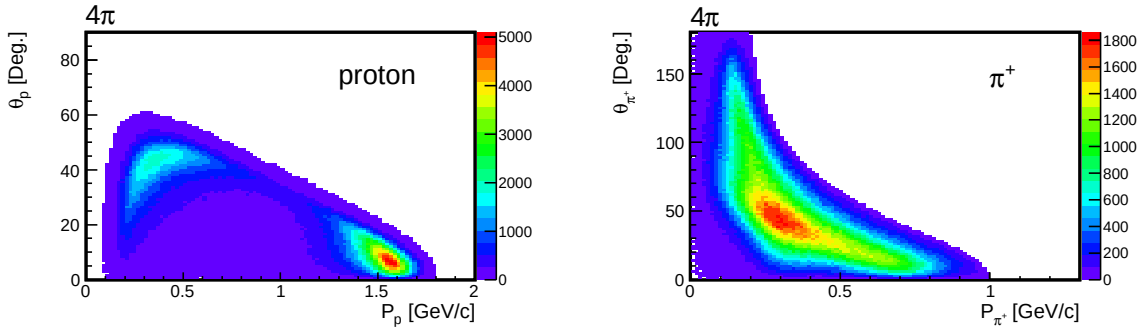

FIG. 3.11 – Polar angle versus momentum in laboratory frame for proton (left panel) and π^+ (right panel) in 4π, in reaction $pp \rightarrow p\Delta^+ \rightarrow pn\pi^+$ at 1.25 GeV from Pluto simulation.

$pp \rightarrow pN^*(1440) \rightarrow pn\pi^+$

Figure 3.12 shows the kinematical behavior of proton and π^+ in the $pp \rightarrow pN^* \rightarrow pn\pi^+$ reaction. This reaction process is very similar to $pp \rightarrow p\Delta^+ \rightarrow pn\pi^+$ just by changing Δ^+ to N*. But as we discussed in 3.2.5, in the OBE model [Huber and Aichelin, 1994] the production angular distribution of N^* is predicted to be even more peaked in the $p+p$ center-of-mass system than the Δ. For that we see clearly in the left panel of fig. 3.12 two branches which present the forward and backward peaked N^*. Since the N^* resonance has a higher mass, on average the scattered proton has lower momentum and smaller polar angle than in the case of the Δ^+, and the emitted π^+ has in average larger momentum.

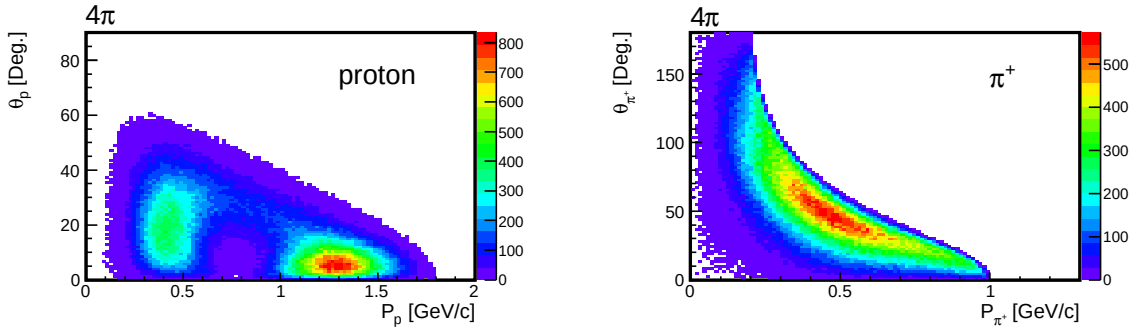

FIG. 3.12 – Polar angle versus momentum in laboratory frame for proton (left panel) and π^+ (right panel) in 4π, in reaction $pp \rightarrow pN^* \rightarrow pn\pi^+$ at 1.25 GeV from Pluto simulation.

3.5 Detection acceptance and efficiency

3.5.1 Definitions

As mentioned in chapter 2, the HADES spectrometer has a high acceptance but still does not cover the full solid angle. In order to describe the geometrical coverage, acceptance matrices are produced for different particles individually. These matrices are defined in three dimensions corresponding to p (momentum), θ (polar angle) and ϕ (azimuthal angle) in the laboratory frame.

In practice, we generate white tracks, i.e. the tracks generated from Monte-Carlo simulation which are uniformly distributed in a given range of (p, θ, ϕ). For acceptance matrices : p is typically set from 0 to 3000 MeV/c with 20 MeV/c per bin , θ from 0^o to 90^o with 2 ^{o} per bin and ϕ is usually chosen from 0^o to 60^o with 4^o per bin which corresponds to the coverage of one sector, assuming the acceptances are the same from one sector to another. Then the generated events are sent to the GEANT simulation tool where the geometry of HADES detector is embedded. The events which hit the active volume of the detector are retrieved afterwards and considered as detected. Finally the acceptance matrix is calculated using equation 3.16, as a ratio of the number of detected particles in the HADES detector and the number of particles sent in the beginning, assuming a perfect (100%) detection efficiency.

$$F_{\text{Acc}}\ (p, \theta, \phi) = \frac{N_{\text{Acc}}\ (p, \theta, \phi)}{N_{\text{Total}}\ (p, \theta, \phi)}, \tag{3.16}$$

The other aspect about the detection is the track reconstruction efficiency. After accepting an event in HADES detector, its (p, θ, ϕ) and need to be reconstructed for further analysis. All the accepted events are treated in the same way as the experimental data, going through the full event reconstruction chain using Runge-Kutta [Agakichiev et al., 2009c] tracking method. The efficiency is determined as the ratio of reconstructed particles for a given (p, θ, ϕ) to the test particles accepted in HADES following equation 3.17. For efficiency matrices : p is typically taken from 0 to the maximum momentum to be achieved with 20 MeV/c per bin , θ from 0^o to 90^o with 3 ^{o} per bin and ϕ is chosen from -180^o to 180^o with 4 ^{o} per bin.

$$F_{\text{Eff}}\ (p, \theta, \phi) = \frac{N_{\text{Rec}}\ (p, \theta, \phi)}{N_{\text{Acc}}\ (p, \theta, \phi)}, \tag{3.17}$$

The efficiency matrices are calculated for each experiment and taking into account the corresponding run conditions.

3.5.2 Acceptance and efficiency matrices

In this section we will discuss the acceptance and efficiency of HADES detector for the proton and π^+ detection which are both required for the $pp \rightarrow np\pi^+$ reaction measurement.

Figure 3.13 gives the projections on two pairs of variables of the three-dimensional acceptance matrices for one sector. All sectors are assumed equal in the case of acceptance matrices. We can see the nearly homogeneous acceptance of about 90% for both proton and π^+ for θ ranging from 15^o to 85^o due to the geometry of the sectors. A drop of acceptance can be observed at both edges of ϕ distribution due to the gap between the neighboring sectors. This effect is even

larger at the low θ values. Both proton and π^+ are bent by the magnetic field towards the beam axis when they fly through the detector. For a given momentum, the particle is detected only if its polar angle is between two limits which are shifted to lower values when the momentum increases. The limits around 300 MeV/c for protons and 100 MeV/c for π^+ are due to the energy loss in the target and RICH.

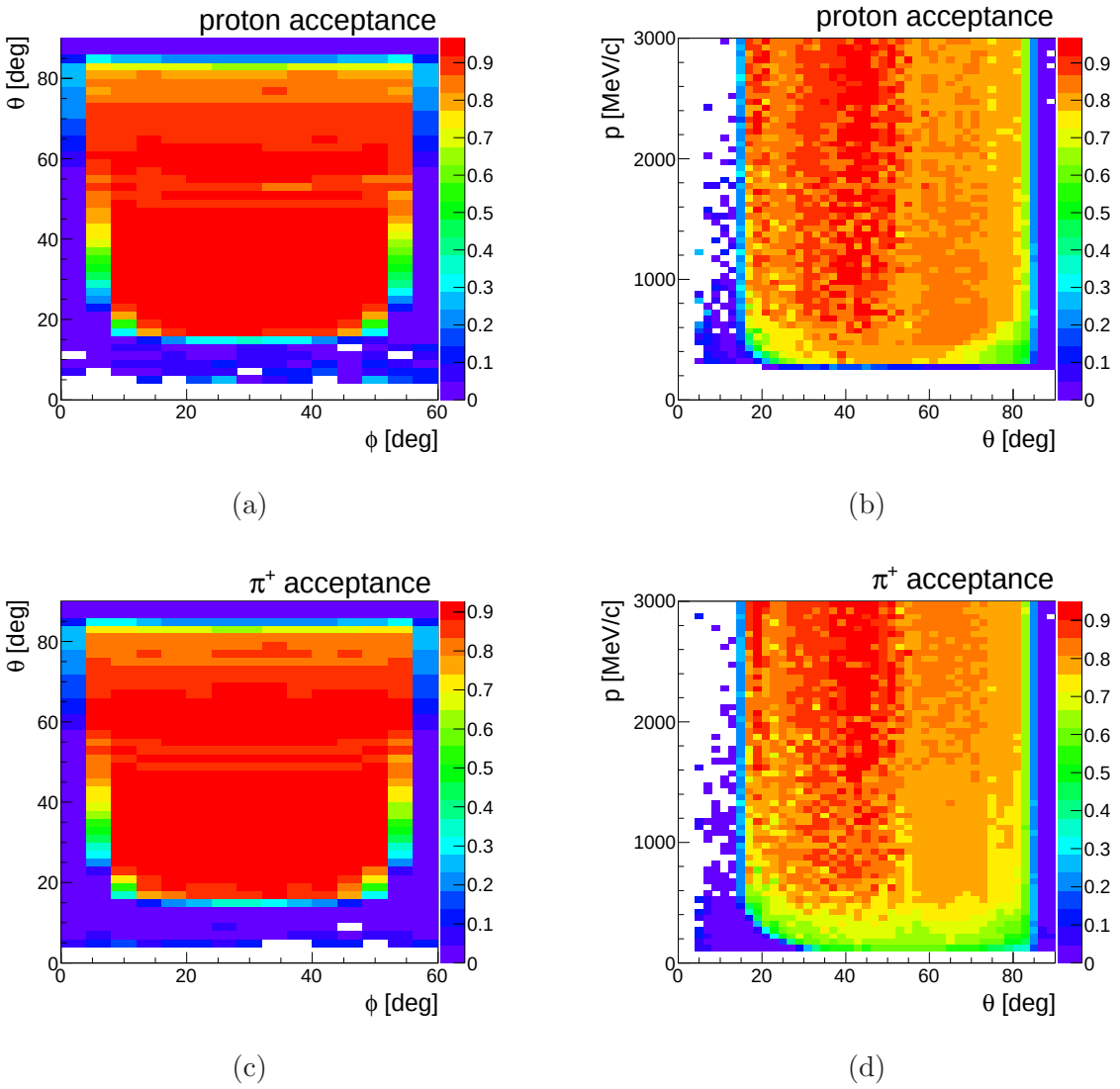

FIG. 3.13 – Projections of the three-dimensional acceptance matrices for one sector centered at $\phi = 30^o$. (a) proton acceptance as a function of azimuthal angle ϕ and polar angle θ; (b) proton acceptance as a function of polar angle θ and momentum p; (c) π^+ acceptance as a function of azimuthal angle ϕ and polar angle θ; (d) π^+ acceptance as a function of polar angle θ and momentum p.

In the same way, the detector efficiencies are shown in fig. 3.14. The six bumps along the ϕ axis represent the six sectors covering 60^o each. The lowest efficiencies are located in the region of low momentum and small polar angle for proton and π^+. A sharp drop of efficiency can also be seen for both particles for polar angles lower than 45^o, since the efficiency of the TOFINO ($F_{\text{Eff}} \sim 0.85$) is lower than the one of the TOF ($F_{\text{Eff}} \sim 0.95$). Right at this transition area where

the TOF and TOFINO overlap, the efficiency decreases even lower, i.e. close to 0.8. This bias is in fact caused by a more strict analysis requirement, i.e. instead of requiring one signal in either TOF or TOFINO, here both sub-detectors should be fired. High efficiency values can be seen at the edges and even outside the HADES polar angular coverage, due to the resolution smearing.

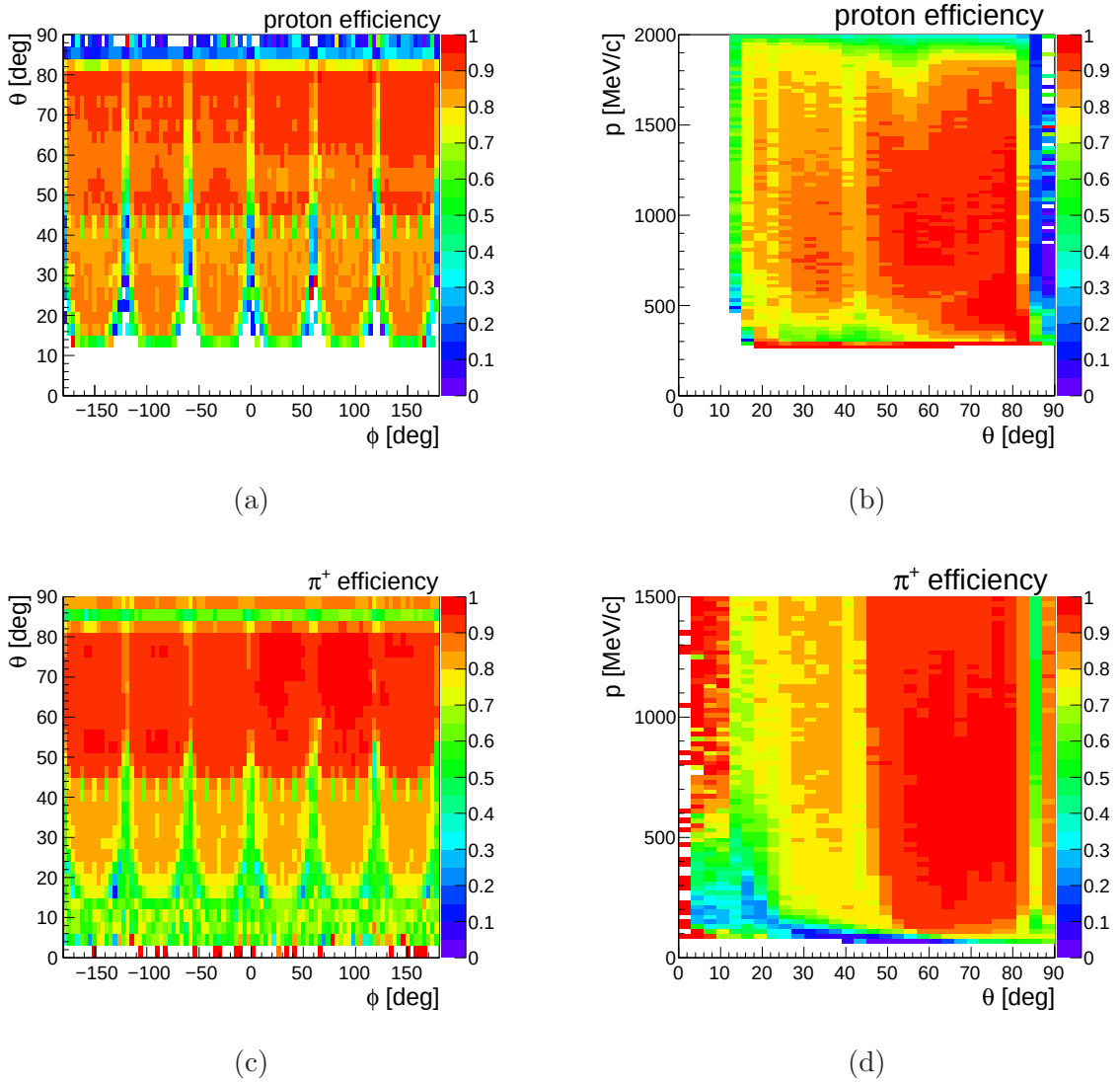

FIG. 3.14 – Projections of the three dimensional efficiency matrices. (a) proton efficiency as a function of ϕ and θ; (b) proton efficiency as a function of θ and p; (c) π^+ efficiency as a function of ϕ and θ; (d) π^+ efficiency as a function of θ and p.

In the data analysis which will be shown in chapter 5, the acceptance matrices are used to filter the simulated events to take into account the HADES geometry coverage. While, the efficiency matrices are used for both measured data and simulation, i.e. the data are corrected by efficiency with a threshold and the simulated events are weighted by 0 if the corresponding efficiencies are below the threshold.

In section 3.8, the acceptance and efficiency will be treated together to illustrate the effects.

3.6 Opposite sector condition

Besides of detector acceptance and efficiency effects, the hadronic channels measurement is distorted for a third reason : the trigger condition "M2 opposite sectors" (see section 2.5.2). Its influence on the event distributions will be shown in 3.8.

3.7 Momentum resolution

For $p + p$ experiment at 1.25 GeV, Runge-Kutta algorithms [Agakichiev et al., 2009c] have been employed to reconstruct the particle momentum.

The resolution is dominated at low momentum by multiple scattering, consequently is particle dependent, and goes like $\frac{1}{\beta}$. The position resolution on the MDC chambers gives a contribution $\frac{\triangle p}{p}$ which is linear in momentum and particle independent. This position resolution is directly relates to the knowledge of the detector geometry of wires in space, but also depends on the calibration of the electronics (details can be found in [Morinière, 2008]).

The resolution has been investigated using the proton-proton elastic collisions at 2.2 GeV. As the angle resolution is much better than the momentum resolution, the nearly exact momentum (p_{cal}) of scattered protons can be calculated from their reconstructed polar angle. Using the Runge-Kutta method, we can also reconstruct the momentum (p_{RK}). By comparing these two values, the resolution $\frac{\triangle p}{p} = \frac{p_{\mathrm{cal}} - p_{\mathrm{RK}}}{p_{\mathrm{cal}}}$ can be measured event by event. For each (p, θ, ϕ) cell, the obtained values are fitted by Gaussians as was shown in more details in [Morinière, 2008]. The $\sigma(p, \theta, \phi)$ are then used to smear the simulation. For each event $(p_{\mathrm{sim}}, \theta_{\mathrm{sim}}, \phi_{\mathrm{sim}})$ in the simulation, the simulated momentum p_{sim} is replaced by a random value p_{smear} drawn from the Gaussian distribution with mean value equals to p_{sim} and variance equals to $\sigma(p_{\mathrm{sim}}, \theta_{\mathrm{sim}}, \phi_{\mathrm{sim}})$.

3.8 Acceptance and efficiency effects on the $pp \rightarrow np\pi^+$ reaction

3.8.1 Momentum and polar angle distributions

In this section, I will demonstrate the influence of the acceptance, efficiency and Opp. Sec. condition on the momentum, polar angle and Dalitz distributions of the $N\Delta \rightarrow NN\pi$ process. The main emphasis will be put on distortions due to acceptance and efficiency and the bias due to the Opp. Sec. trigger condition. Figure 3.15, 3.16 and 3.17 show these effects for the different reaction processes.

Taking $pp \rightarrow n\Delta^{++} \rightarrow np\pi^+$ as an example, the lower angle limit ($\theta > 15^o$) has a strong effect for forward going protons (forward emitted Δ^{++}). On the other hand, the π^+ are strongly affected by the large polar angle cut ($\theta < 84^o$), which eliminates mostly the forward going Δ^{++}. The Opp. Sec. condition reduces dramatically the number of events (see table 3.3), as can be read from the bottom row of figure 3.15. The reduction is higher for Δ produced around 90^o in the center-of-mass.

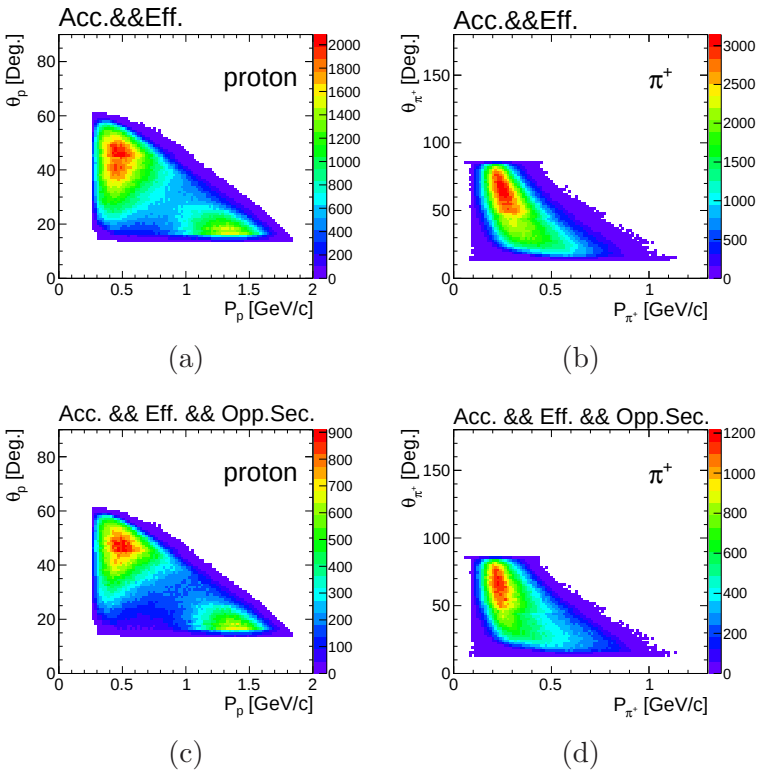

FIG. 3.15 – Polar angle versus momentum in the laboratory frame in reaction $pp \rightarrow n\Delta^{++} \rightarrow np\pi^+$ for proton (left) and π^+ (right). Upper row : acceptance and efficiency matrices applied ; bottom row : acceptance, efficiency matrices and Opp. Sec. condition applied. Pluto simulation.

	Acceptance && Efficiency	**Opposite Sectors (in addition)**
$pp \rightarrow n\Delta^{++} \rightarrow np\pi^+$	10.1%	3.8%
$pp \rightarrow p\Delta^{+} \rightarrow np\pi^+$	10.4%	3.2%
$pp \rightarrow pN^{*} \rightarrow np\pi^+$	26.1%	6.27%

TAB. 3.3 – Detection probabilities for $pp \rightarrow np\pi^+$ channel with different conditions : acceptance, efficiency and M2 trigger conditions. The values are estimated using Pluto simulations for different processes : Δ^{++}, Δ^{+} and N^{+} respectively.

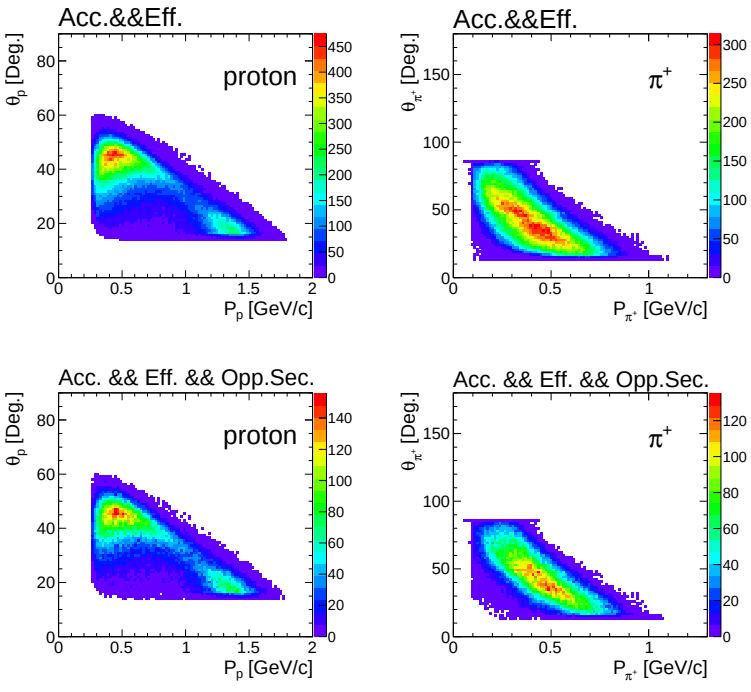

FIG. 3.16 – Polar angle versus momentum in the laboratory frame in reaction $pp \rightarrow p\Delta^+ \rightarrow np\pi^+$ for proton (left) and π^+ (right). Upper row : acceptance and efficiency matrices applied ; bottom row : acceptance, efficiency matrices and Opp. Sec. condition applied. Pluto simulation.

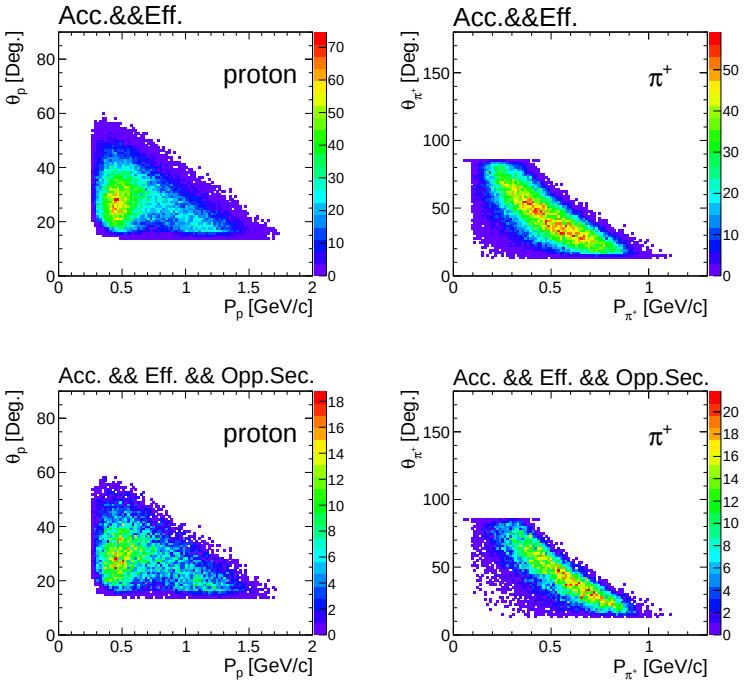

FIG. 3.17 – Polar angle versus momentum in the laboratory frame in reaction $pp \rightarrow pN^* \rightarrow np\pi^+$ for proton (left) and π^+ (right). Upper row : acceptance and efficiency matrices applied ; bottom row : acceptance, efficiency matrices and Opp. Sec. condition applied. Pluto simulation.

3.8.2 Dalitz plot after all cuts

Finally, we show the Dalitz plots (fig. 3.18) of $pp \rightarrow np\pi^+$ reactions at 1.25 GeV via different resonances, including detector acceptance and efficiency cut, with the specific M2 Opp. Sec. trigger requirement and smearing on angles and momentum. Compared with fig. 3.8, the numbers of counts are much reduced for all three processes. The event distributions have been changed as well. The Dalitz boundaries are also smeared by the resolution.

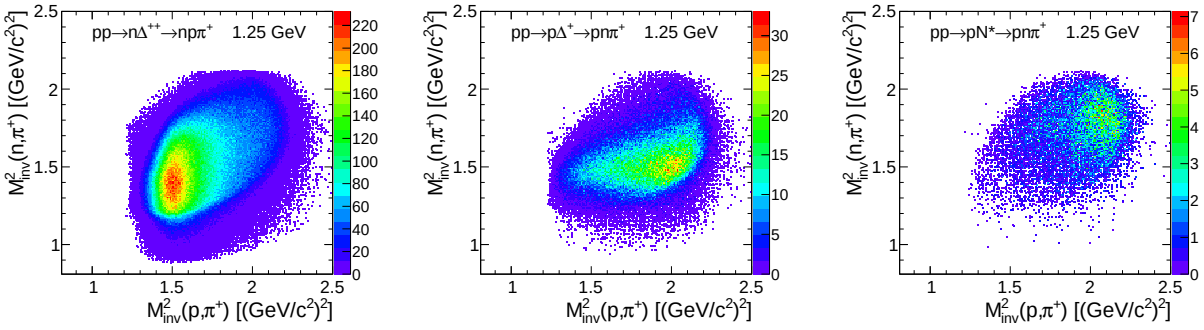

(a) (b) (c)

FIG. 3.18 – Simulated Dalitz plot in $p + p$ collisions with final states $np\pi^+$ via intermediate resonances, including (a) $\Delta^{++}(1232)$, (b) $\Delta^{+}(1232)$ and (c) $N^*(1440)$ at 1.25 GeV. Acceptance, efficiency matrices, Opp. Sec. condition and resolution effects have been applied.

Chapitre 4

Experimental data analysis

The experimental data analysis method developed for the hadronic channels analysis in $p+p$ reaction will be presented in this chapter. We will start with a brief discussion about the special Particle Identification algorithms used in the analysis. Then event selection methods will be presented for different channels. A detail event correction strategy which is related to the M2 Opp. Sec. trigger condition will be discussed in detail, since it causes a lot of difficulties for the $pp \to np\pi^+$ channel data analysis. Other steps, such as efficiency and acceptance correction will also be demonstrated. At the end, a summary of the systematic errors related to all the analysis steps will be given.

4.1 Particle identification

The Particle Identification (PID) is realized by using the velocity ($\beta = v/c$) and momentum correlation. On one hand, the momentum can be reconstructed by measuring the particle's deflection by the magnetic field using different tracking algorithms. On the other hand, to obtain the velocity, one needs the time-of-flight from the target and the track length which can be known from tracking algorithms.

In HADES experiments, one usually measures the time interval :

$$t^{\text{meas}} = t^{\text{stop}} - t^{\text{start}} \tag{4.1}$$

The "stop" signal is generated at the time t^{stop} by the TOF or TOFINO detector and is related to the time-of-flight (t^{tof}) of the particle between the target and the TOF or TOFINO by

$$t^{\text{tof}} = t^{\text{stop}} - t_0, \tag{4.2}$$

where t_0 takes into account the propagation of the signal before reaching the Time to Digital Converter (TDC).

The "start" signal t^{start} is usually produced by the START detector placed in the beam, which provides a time information that is directly related to the interaction time.

However, in the April 2006 experiment, no START detector could be used. With proton beams, the deposited signal in diamond detectors is too small. A start system based on a scintillator hodoscope has been tested, but a high number of secondaries were produced, resulting in instabilities in the RICH detector.

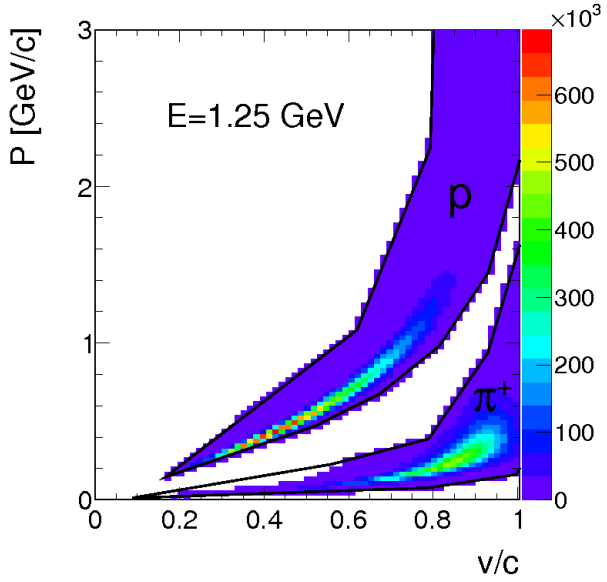

FIG. 4.1 – The momentum versus velocity distribution. The black solid curves define the banana cut used for p and π^+ separation in the $pp \to np\pi^+$ channel analysis.

So, in the absence of a fast signal from a START detector, the data acquisition was started at the time t^{start} when the fastest particle gave a signal in the TOF or TOFINO scintillator. In this case, the START time t^{start} depends both on the time of interaction and on the time of flight of this fastest particle. The reconstruction of t^{start} is therefore needed for each event to determine the time-of-flight and hence the PID of the particles.

To identify the detected particles corresponding to the $pp \to np\pi^+$ channel, the following procedure was used :

- First, by requiring the presence in the event of only two positively charged tracks with no matching with the RICH, only "two-prong" events with π^+ and protons are selected.
- Then to select events with one π^+ and one proton exclusively and to affect the correct identification to each particle, the "event hypothesis" method is used.

We will now illustrate the way how the "event hypothesis" works. A given hypothesis is made, for example particle 1 is a proton and particle 2 is a π^+. Using the corresponding masses m_p and m_{π^+}, the measured momenta (p_1 and p_2) and the reconstructed track lengths of the particles, we can calculate the times of flight $t_1^{\text{calc}}(p_1, m_p)$ and $t_2^{\text{calc}}(p_2, m_{\pi^+})$ for both particles. If the hypothesis is true, we have :

$$t_1^{\text{calc}}(p_1, m_p) = t_1^{\text{tof}} = t_1^{\text{meas}} + t^{\text{start}} - t_0 \tag{4.3}$$

$$t_2^{\text{calc}}(p_2, m_{\pi^+}) = t_2^{\text{tof}} = t_2^{\text{meas}} + t^{\text{start}} - t_0, \tag{4.4}$$

These equations are used to deduce

$$t^{\text{start}} - t_0 = \frac{1}{2}(t_1^{\text{calc}}(p_1, m_p) + t_2^{\text{calc}}(p_2, m_{\pi^+}) - (t_1^{\text{meas}} + t_2^{\text{meas}})) \tag{4.5}$$

and then, we obtain

$$\begin{aligned} t_1^{tof} &= t_1^{\text{meas}} + \frac{1}{2}(t_1^{\text{calc}}(p_1, m_p) + t_2^{\text{calc}}(p_2, m_{\pi^+}) - (t_1^{\text{meas}} + t_2^{\text{meas}})) \\ t_2^{tof} &= t_2^{\text{meas}} + \frac{1}{2}(t_1^{\text{calc}}(p_2, m_p) + t_2^{\text{calc}}(p_2, m_{\pi^+}) - (t_1^{\text{meas}} + t_2^{\text{meas}})) \end{aligned} \tag{4.6}$$

Using the track lengths and the time-of-flights deduced from equation 4.6, the velocities are calculated. Depending on the correlation with the momentum (see fig. 4.1), the initial hypothesis is validated or rejected. All the possible hypotheses for two-prong events with protons and π^+ are tested in the same way.

The event hypotheses algorithm was developed as a common work by Marcin Wiśniowski, Ingo Fröhlich and Björn Spruck and the efficiency for the particle identification has been estimated to be above 90% [Wiśniowski, 2009].

4.2 Event selection

Following the event hypothesis method described above, the $pp\pi^0$ and the pp elastic scattering channels are selected by asking two protons in the exit channel, while the $np\pi^+$ channel is selected by requesting one proton and one positive pion.

4.2.1 Event selection for pp events

$pp \rightarrow pp$

For the elastic scattering events, the angular correlations are checked, using the fact that the two outgoing protons are expected to be colinear in the total center-of-mass system because of the momentum conservation. These can be checked by the relations :

$$\begin{aligned} |\phi_{p1} - \phi_{p2}| &= 180^o, \\ tan\theta_{p1} * tan\theta_{p2} &= \frac{1}{\gamma_{CM}^2}, \end{aligned} \tag{4.7}$$

where ϕ_{p1} and ϕ_{p2} are the azimuthal angles and θ_{p1} and θ_{p2} the polar angles of two protons in lab. γ_{CM} is the Lorentz factor of the center-of-mass system. For the 1.25 GeV collision, $1/\gamma_{CM}^2 = 0.6$.

In fig. 4.2 (left), these two angular correlations are shown and the prominent peaks centered at $|\phi_{p1} - \phi_{p2}| = 180^o$ and $\tan\theta_{p1} * \tan\theta_{p2} = 0.6$ are due to the elastic events. An elliptical cut (the semi-major axis $a = 3.2^o$ and the semi-minor axis $b = 0.04$) is imposed to select the elastic events for further analysis.

$pp \rightarrow pp\pi^0$

The inelastic events, which only consist in pion(s) production channels since the energy is below the η threshold, can also be seen in fig. 4.2 (left). They appear as a cloud located below $\tan\theta_{p1} * \tan\theta_{p2} = 0.6$. The elastic and inelastic events however overlap because of the finite resolution. As the first step, a loose graphical cut is applied in order to eliminate most of the elastic events and keep as many as possible inelastic ones.

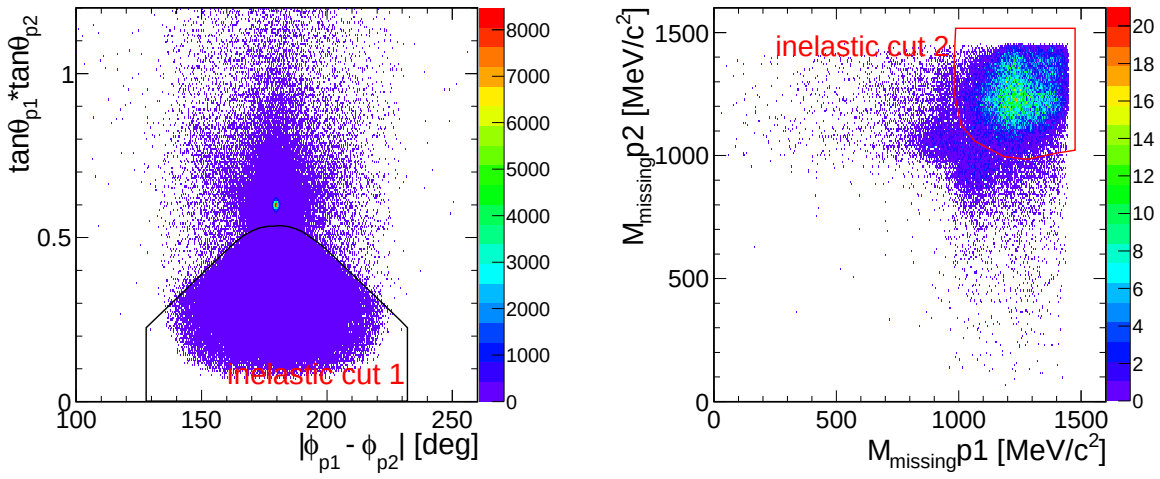

FIG. 4.2 – **Left :** 1^{st} step of $pp\pi^0$ event selection : angular correlation. **Right :** 2^{nd} step of $pp\pi^0$ event selection : missing mass of proton2 versus missing mass of proton1.

In the second step, a proton missing mass cut is then imposed to remove the residual elastic events. It exploits the fact that for the inelastic events, the missing particle(s) should be one or several pion(s) while for elastic events there should be no missing particle. After a second graphical cut shown in fig. 4.2 (right), the proper inelastic events are selected from elastic ones.

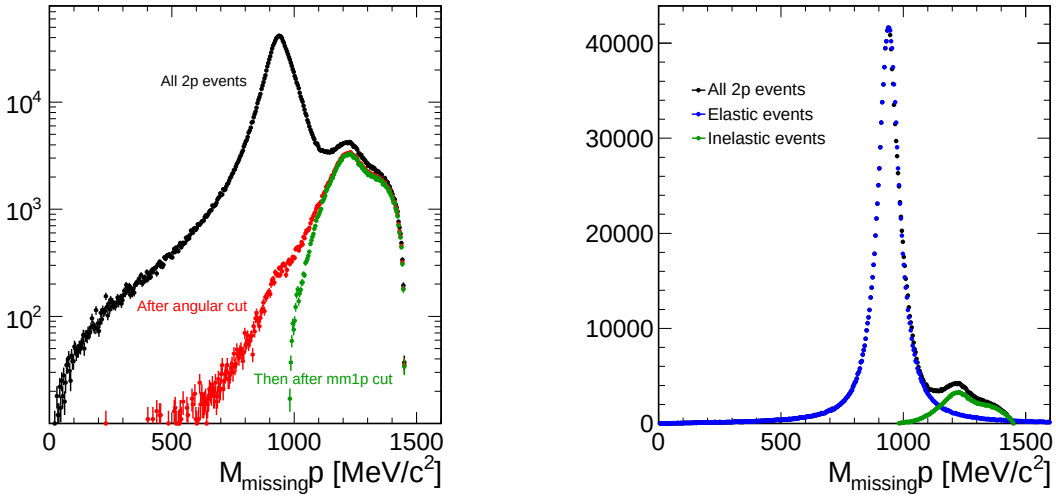

FIG. 4.3 – **Left :** One proton missing mass distribution. Black : of all the two protons detected events ; red : after the angular cuts ; green : after in addition the one proton missing mass cut. **Right :** One proton missing mass spectra. Black : for all the two protons detected events ; blue : elastic events ; green : inelastic events.

Fig. 4.3 (left) shows the evaluation of the one proton missing mass spectrum with the event selection procedure as described above. We can see that the elastic events are efficiently removed. pp events are then well separated into elastic and inelastic parts (right panel of fig. 4.3), and can be used for further analysis. In this thesis, for the pp elastic channel and the $pp \rightarrow pp\pi^0$ channel analysis, I only discuss the event selection strategy since it was developed by the Orsay

team. More detailed data analysis results on these channels will be presented in the PhD thesis of Anna Kozuch.

4.2.2 Event selection for $np\pi^+$ events

The $pp \rightarrow np\pi^+$ channel is selected by using the missing mass technique as well. From the (p, π^+) missing mass spectrum (fig. 4.4), we can see a prominent peak centered at 941 MeV/c^2 with FWHM=30 MeV/c^2 which indicates the missing neutron as expected. In addition, the two-π production process can be observed as a small bump starting at 1080 MeV/c^2, where is located the threshold of the second π production. On the left hand side of the neutron peak, some mis-identified pp elastic events are found because of the loose cut used in particle identification (see 4.1). However the neutron peak is well separated, so we simply applied a hard-cut on the (p, π^+) missing mass spectrum from 800 to 1080 MeV/c^2.

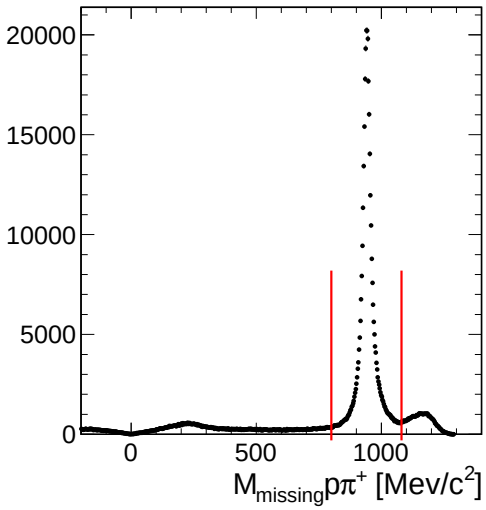

FIG. 4.4 – The (p, π^+) missing mass distribution. The red bars correspond to the window used for the $np\pi^+$ event selection.

4.2.3 Uncertainty of event selection methods for the $pp \rightarrow np\pi^+$ reaction

Comparison of two event selection methods

Two methods are considered for the selection of $pp \rightarrow np\pi^+$ reactions. Both of them are based on the missing mass of (p, π^+) :

- hard-cut method
  The first one is the hard-cut method as described in the last section which has finally been used in the analysis.
- fit method
  The second method consists in fitting the missing mass spectra as a sum of two gaussian functions centered at the same position and a polynomial function to take into account the background. The fit is done in the region where the missing mass spectrum is well symmetric. For each bin, the signal yield is defined as the sum of the two gaussians.

We will show here an example of reconstructing the angular distribution of neutron (missing particle in the $pp \rightarrow p\pi^+X$ reaction) in the $p + p$ center-of-mass system. In the case of the fit method, the yield is obtained by fitting the (p, π^+) missing mass distribution and summing the

two Gaussian in each neutron angle bin. In the case of the hard-cut method, the same condition is put for all the neutron angles. One can of course conclude that the advantage of the fit method is that the selection depends on the neutron angle bin, which takes into account the fact that both the signal width and the background might be different from one bin to another. We will compare in the following these two methods.

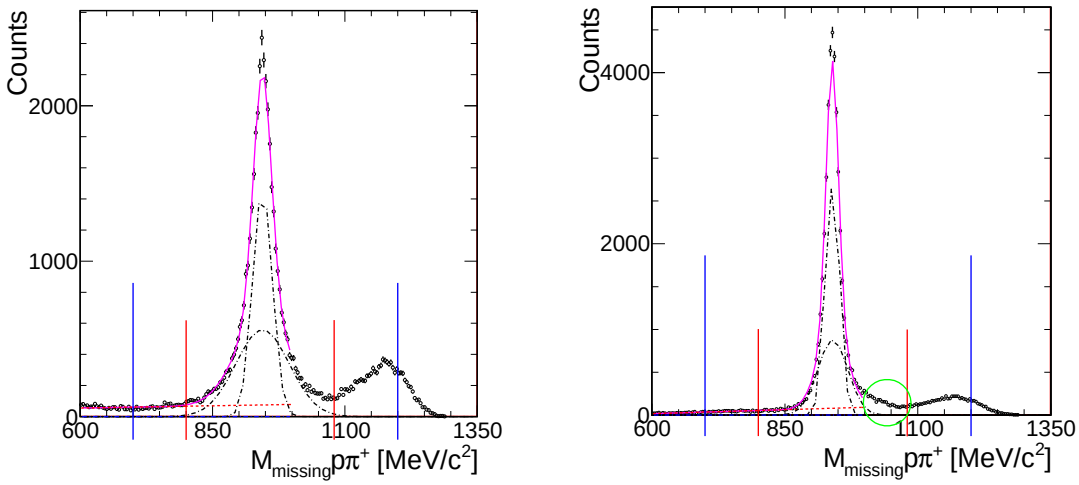

FIG. 4.5 – Event selection for the $pp \to np\pi^+$ reaction using the missing mass of the (p, π^+) distribution, in different neutron angular regions. **Left :** $-0.2 < \cos\theta_n^{CM} < 0$, **Right :** $0.75 < \cos\theta_n^{CM} < 0.8$. Data are shown by open circles. For the hard-cut method, the lower and upper limits are shown as red bars. For the fit method, the spectra are fitted as a sum (pink solid curve) of two gaussian functions (black dot-dashed line), and a polynomial function (red dashed line), then the signal yield is defined as the sum of the two Gaussians integrated between the blue bars.

Two examples are shown in fig. 4.5. Both event selection methods are compared with each other in two different neutron angle regions. When $-0.2 < \cos\theta_n^{CM} < 0$ (left panel of fig. 4.5), the two-pion contribution (one neutron and one pion missing) which is centered close to 1200 MeV/c^2 plays a significant role and its tail goes down below the production threshold 1080 MeV/c^2. In this case, the fit method gives a better result in the sense of subtracting efficiently the two-pion background. When $0.75 < \cos\theta_n^{CM} < 0.8$ (right panel of fig. 4.5), the contribution of two-pion is less pronounced and the separation between the neutron and the two-pion contribution is clearer. In addition, the neutron peak is asymmetric. In the region shown by the green ellipse, most of the events correspond to the $pp \to np\pi^+$ reaction, but are shifted by the resolution. Thus in this case, the hard-cut method gives a better estimate of the signal yield. It indeed allows to take into account signal events which are wrongly considered as background in the fit method.

In the $pp \to np\pi^+$ reaction analysis at 1.25 GeV we have in most of the cases the latter situation. For the neutron angular distribution, the difference of the total selected yield from the two methods is about 5%. The hard-cut method is considered to be more precise in determining the yields for the $pp \to np\pi^+$ analysis.

Systematic error on the hard-cut method

The systematical errors introduced by the hard-cut method will be investigated in the following. The hard-cut is imposed symmetrically around the neutron peak from 800 MeV/c^2 to

1080 MeV/c^2. The basic idea is to check the sensitivity to the cut limits.

The limit on the right side aims at removing the two pion contribution. By varying this limit on $M_{\text{missing}}(p,\pi^+)$ from 1050 MeV/c^2 to 1110 MeV/c^2, the change of yield is found to be less than 1.5%.

The situation for the limit on the left hand side is more complicated. Figure 4.6 shows the $\tan\theta_p \cdot \tan\theta_{\pi^+}$ versus the missing mass of (p,π^+) distributions in two slices of $\cos\theta_n^{CM}$. On the left panel ($-1.0 < \cos\theta_n^{CM} < -0.8$), apart from the prominent neutron peak at 940 MeV/c^2 and two-pion contribution starting from 1080 MeV/c^2, we can also see a line at low $M_{\text{missing}}(p,\pi^+)$ and a spot located around 500 MeV/c^2. In both cases, one proton is misidentified as a pion. The line is identified as being due to the pp elastic scattering because of the correlation $\tan\theta_p \cdot \tan\theta_{\pi^+} = 0.6$. The spot is identified as residual $pp\pi^0$ events since the $\tan\theta_p \cdot \tan\theta_{\pi^+}$ is lower than for the elastic events (see fig. 4.2).

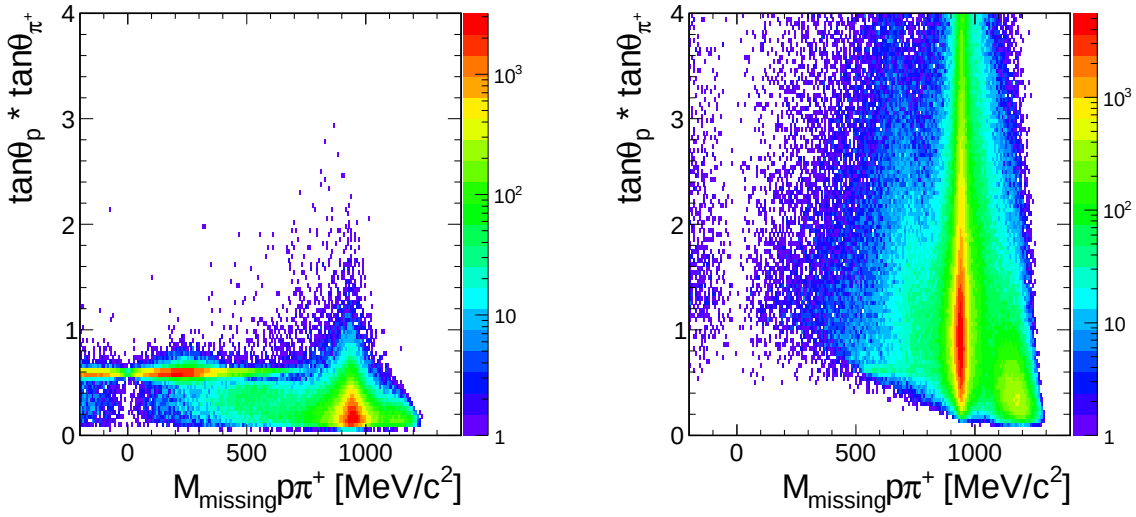

FIG. 4.6 – $\tan\theta_p \cdot \tan\theta_{\pi^+}$ versus (p,π^+) missing mass, in different neutron angle regions. **Left :** $-1.0 < \cos\theta_n^{CM} < -0.8$, **Right :** $0.8 < \cos\theta_n^{CM} < 1.0$.

On the right panel ($0.8 < \cos\theta_n^{CM} < 1.0$), we can see an unexpected accumulation of events around $M_{\text{missing}}(p,\pi^+)$ =700 MeV/c^2. By selecting these events and looking at their θ versus p distributions (see upper row of fig. 4.7), we can draw some conclusions about the origin of these events. Using a graphical cut on the θ versus p of π^+, we separate the events in two groups. We then show with different colors θ versus p correlations for the proton and the π^+ for each group of events.

For the first group (black color), the proton follows the kinematics of elastic scattering, while the π^+ follows the kinematics of the $pp \to np\pi^+$ process (see fig. 3.15). We conclude that this group of events corresponds to a random coincidence between a π^+ from the $pp \to np\pi^+$ process and a proton from elastic scattering. It is interesting to note that the acceptance for these protons is different from the case of correlated two protons, where protons with $\theta_p > 65^o$ are suppressed (see fig. 3.15).

For the second group (red color), the "π^+" has a kinematical correlation close to the elastic protons, while the proton is in agreement with the $pp \to np\pi^+$ kinematics (see fig. 3.15). So, they are likely to be due to a coincidence between an elastic proton misidentified as a π^+ and a

well identified proton coming from the $pp \rightarrow np\pi^+$ reaction.

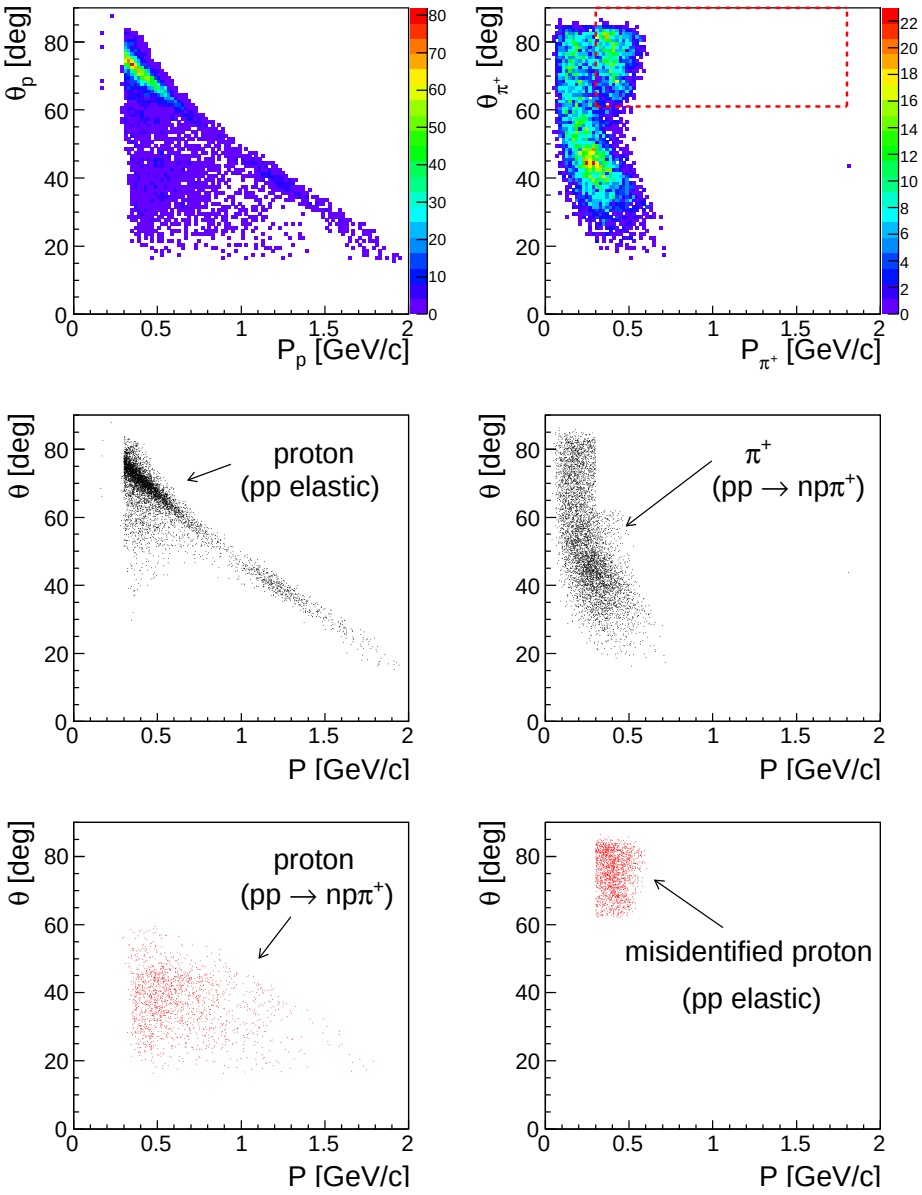

FIG. 4.7 – Polar angle versus momentum distribution in $pp \rightarrow np\pi^+$ reaction for proton (left) and π^+ (right), with condition $0.8 < \cos\theta_n^{CM} < 1.0$ and $M_{\text{missing}} < 700$ MeV/c^2. The red box on the π^+ distribution in the first row indicates the graphical cut. First row : all selected events ; second row : events outside graphical cut ; third row : events inside graphical cut.

As a conclusion, most of the events removed by the lower limit on the (p, π^+) missing mass are due either to bad identified elastic protons or to random events. The aim of this study was to understand in detail the origin of these events. They correspond however to a very small fraction of the total yield ($< 3\%$). In the meantime, the number of good events removed by the lower limit cut is estimated for each bin and is used to calculate the error bars on the yields.

The systematic error due to the event selection using the hard cut method is adjusted in detail as a function of neutron angle. For each bin, the final error is calculated as a quadradic

sum of the uncertainties due to the lower limit and to the higher limit. It varies from 4.6% at $\cos\theta_n$ close to -1 to 1.7% for $\cos\theta_n$ close to 0. The average global uncertainty on the event selection is estimated to be 1.8%.

4.3 Trigger efficiency correction

4.3.1 Event loss due to Time Signal condition

In the hadronic channel data analysis, the event sample has been taken using the M2 trigger (see section 2.5.2) which is optimized for the elastic scattering detection. This trigger is fired when two conditions are fulfilled :

- M2 Opposite Sectors (Opp. Sec.) : at least two scintillators (either from TOF or TOFINO) from Opp. Sec. are hit ;
- Time Signal (TS) : at least one particle goes into the TOFINO detector, covering approximately the polar angles $16^o < \theta < 45^o$. Note that the θ here is defined with respect to the target.

The latter condition then causes an event loss because it eliminates the case of both particles hitting the TOF detector, i.e. both particles being emitted with $\theta < 45^o$. The pp elastic channel and $pp \rightarrow pp\pi^0$ are not affected by this condition because of their kinematic limits but the influence can be clearly seen in the $pp \rightarrow np\pi^+$ channel.

Fig. 4.8 shows the correlation between the polar angle of the proton and the π^+ in the data. A discontinuity is observed around 45^o corresponding to the transition from TOFINO to TOF. However, the boundary is not strictly at 45^o and shows a dependence on momentum. It is on one hand because of the deviation of the particles trajectories due to the magnetic field ; and on the other hand due to the smearing from the triggers different from M2. In the data analysis, we ask "inclusive M2" as trigger condition, which means that the events fitting in addition M3 (see section 2.5.2) are also selected (table 4.1). This kind of events can originate either from a coincidence between the $np\pi^+$ event and a randomly distributed charged particle or from a $np\pi^+$ event in which the proton or π^+ drops into the TOF/TOFINO overlap and causes a double hit.

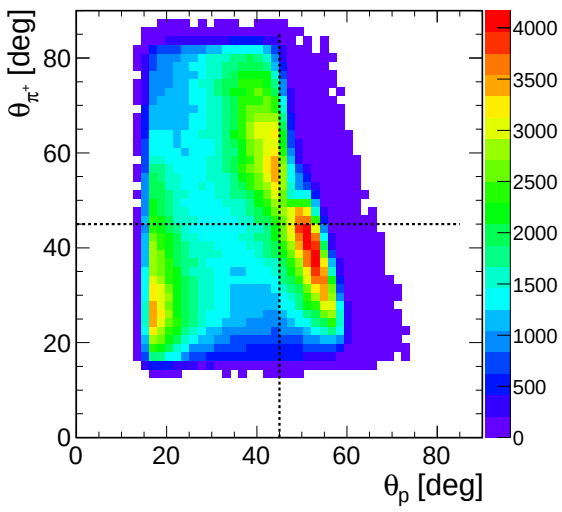

FIG. 4.8 – Polar angle of π^+ versus polar angle of proton in lab.

Trigger requirement	Proportion
Inclusive : M2 Opp. Sec. & TS	100%
Exclusive : M2 Opp. Sec. & TS	$\sim$ 71%
Exclusive : M2 Opp. Sec. & TS & M3	$\sim$ 21%

TAB. 4.1 – Proportion of the two charged particle events with different trigger conditions.

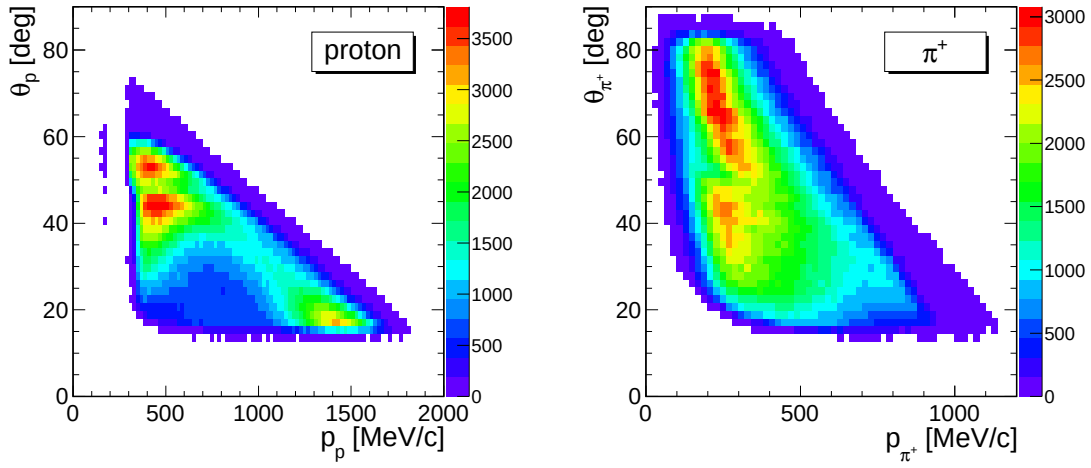

FIG. 4.9 – Polar angle as a function of momentum. Left : proton. Right : π^+.

Due to the correlation between polar angle and momentum, the loss is mostly concentrated around $\theta_p \sim 46^o$ and $\theta_{\pi^+} \sim 50^o$ where the maximum of the distribution is found (see fig. 4.9). Taking protons as an example (left panel of fig. 4.9) : In the region of $\theta_p < 45^o$ the trigger condition is fulfilled since the proton hits the TOFINO. Then for angles larger than 45^o, the proton goes into the TOF and we start to lose events until the corresponding π^+ starts to fire the TS. That's the origin of the depression around 47^o.

The borders of depressed region in fig. 4.9 (left) correspond to decreasing polar angles when the momentum increases. This can be understood because before reaching the TOF or TOFINO detectors, the proton was bent by the magnetic field towards the beam axis depending on its momentum. The higher momentum the proton has, the smaller the deviation is. The same phenomena can be found even more clearly in the case of π^+, because the relevant momenta are smaller.

The total event loss due to TS is estimated to be 3.5%, which represents a quite small fraction of the total cross section. However, this loss is concentrated close to the maximum of the proton angular distribution and therefore induces a quite distinct hole in the distribution (left panel of fig. 4.9), as well as a reduction of counts in a broader region in the π^+ angular distribution (right panel of fig. 4.9).

4.3.2 Strategy of correction for TS

In order to correct for this event loss, an accurate correction depending on the polar-angle and momentum is needed. The basic idea is to extrapolate the π^+ polar angle distribution using the shape of the simulation (based on the resonance model as mentioned in 3.2).

First of all, the detailed comparison of the polar angle distributions with the simulation in momentum slices is realized and presented in fig. 4.10 and fig. 4.11. Only event loss concerned momentum ranges are shown : for protons 100 MeV/c per slice from 200 MeV/c to 1000 MeV/c and for π^+ 50 MeV/c per slice from 100 MeV/c to 500 MeV/c. The π^+'s spectra are normalized to the surface in the region where no correction is needed (32^o to 50^o depending on momentum slice), while the proton's spectra are normalized to have the same maximum yield.

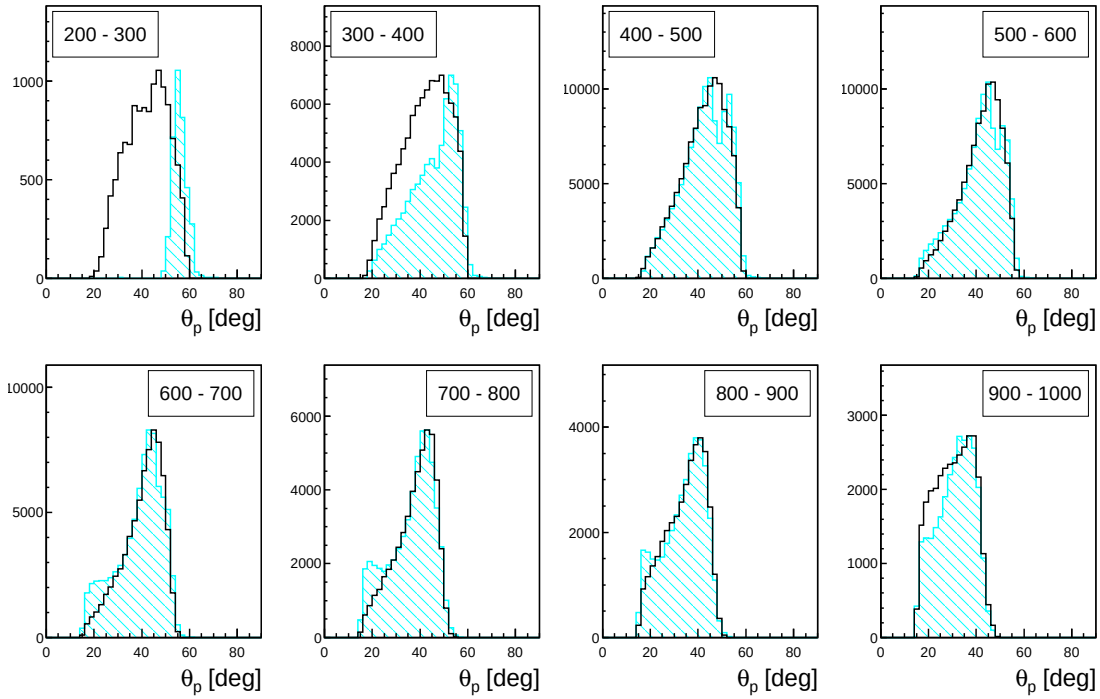

FIG. 4.10 – Distribution of proton polar angle in different momentum slices. The filled spectrum drawn with solid line presents the measured data and the dashed line presents the simulation. Both spectra are selected for the same proton momentum region as indicated (in MeV/c) and are normalized to have the same maximum yield.

For those extreme momentum regions, for example the first slices for proton, the simulation and the data diverge a lot due to the imperfect description of the resolution effects on the edge of the detector acceptance. From fig. 4.9, it can be seen that the correction is needed in the region with $\theta_p > 42^o$ and $p_p < 800$ MeV/c. In this region, the shape of data is in global agreement with simulation in the TOFINO region (fig. 4.10 and 4.11). Considering on one hand that the proton angular distribution is very narrow and the maximum of the distribution is sometimes missed due to the inefficiency (e.g. for p_p in $400-500, 500-600$ and $600-700$ MeV/c), on the other hand that the polar angle of π^+ distributes more widely than proton, we decided to use the shape of simulated spectra to correct the polar-angle of π^+ with a dependence on its momentum in the region $\theta_p > 47^o$. Meanwhile, doing the correction in small phase space regions allows us to minimize the model dependence.

The correction factors are calculated as

$$F_{\text{trigger corr.}} = \frac{N(\theta,p)^{\text{sim}}_{\pi^+}}{N(\theta,p)^{\text{data}}_{\pi^+}}, \tag{4.8}$$

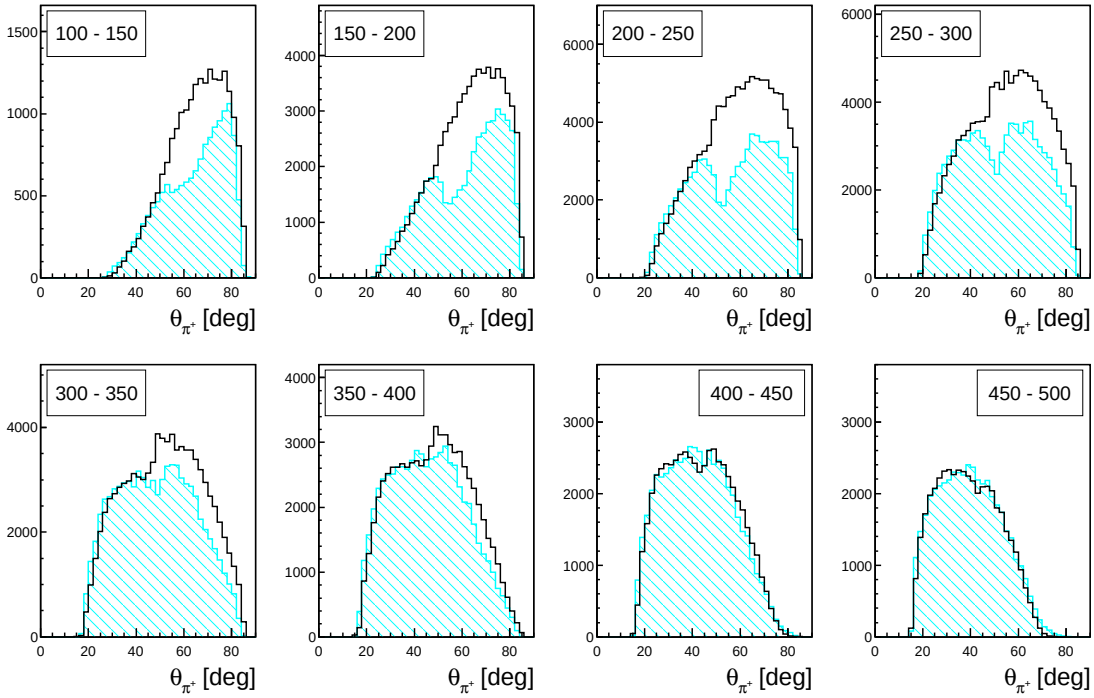

FIG. 4.11 – Polar angle of π^+ in different momentum slices. The filled spectrum drawn with solid line presents the measured data and the dashed line presents the simulation. Both spectra are selected for the same π^+ momentum region as indicated (in MeV/c) and are normalized to the same surface in the θ range where the correction is not needed.

where $F_{\text{trigger corr.}}$ is the correction factor, $N(\theta,p)^{\text{sim}}_{\pi^+}$ and $N(\theta,p)^{\text{data}}_{\pi^+}$ are the counts in each $\Delta\theta_{\pi^+}$ bin of 1^o and Δp_{π^+} bin of 20 MeV/c with the condition of $\theta_p > 46.6^o$ for simulation and data respectively. The value of $\theta_p > 46.6^o$ is adjusted to obtain the best correction.

Fig. 4.12 shows these correction factors bin per bin. In "correction not-needed" region ($\theta_{\pi^+} < 45^o$), we can see that the correction factor is close to 1. It means that the model used in simulation works well for the description of (θ, p), which confirms our strategy to use the simulated shape to realize the correction. The description of the data by the simulation will be discussed in more details in the next chapter.

Then, these correction factors are applied to scale the θ_{π^+}, event by event, when $\theta_{\pi^+} > 45^o$ and $\theta_p > 46.6^o$. For the very low momentum π^+, the correction is not applied because the statistics in this region is poor and the correction could easily introduce big errors. As the last step, a smearing of the correction factor as a fuction of θ_p is realized in the range of $45^o < \theta_p < 48^o$ to have smooth and continuous distributions.

All the correction procedure is controlled using different spectra to avoid creating artificial structures.

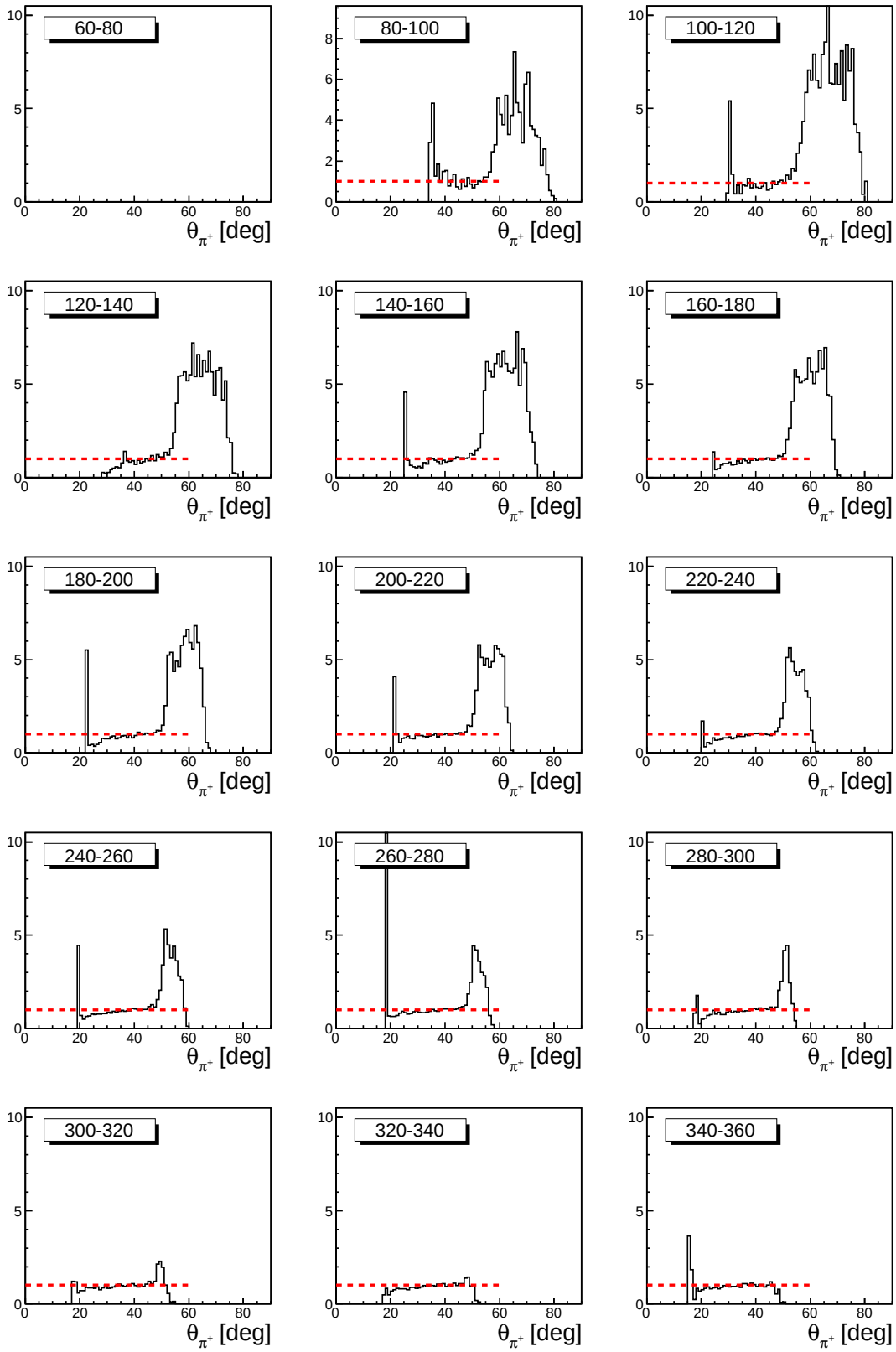

FIG. 4.12 – Correction factors as a function of π^+ polar angle in different π^+ momentum ranges as labeled (in MeV/c) to be applied in the region of polar angle of proton greater than 46.6^o. The ratios are normalized to have that the mean value equals to 1 in $30^o < \theta_{\pi^+} < 42^o$.

4.3.3 Angular distribution after correction

Fig. 4.13 shows the spectrum of π^+ polar-angle distribution after correction in $\theta_p > 46.6^o$. The corrected fraction is very important because we are in the specific region where no proton hits the TOFINO. So, here the measured yields come either from the π^+ hitting the TOFINO ($\theta_{\pi^+} < 45^o$) or from the M3 trigger.

Once we look at the corrections in the whole momentum and polar angle region, the corrected fraction is much smaller however (fig. 4.14 and fig. 4.15). The correction is reasonable because it gives back a continuous and smooth polar angle distribution for both proton and π^+ (fig. 4.16 and fig. 4.17).

The related systematical errors will be estimated in the following.

4.3.4 Uncertainty of trigger condition correction

This uncertainty only concerns the specific regions where the corrections are realized. By varying the $F_{\text{trigger corr.}}$ (see equation 4.3.2), we determined the errors on these factors as 22%. This is mainly due to the model dependence of the correction, based on the simulation. The uncertainty at the level of total cross section due to this correction is estimated to be about 0.7%. We want to stress again that the events affected by this correction represent however a small fraction which is 3.5% of the total cross section.

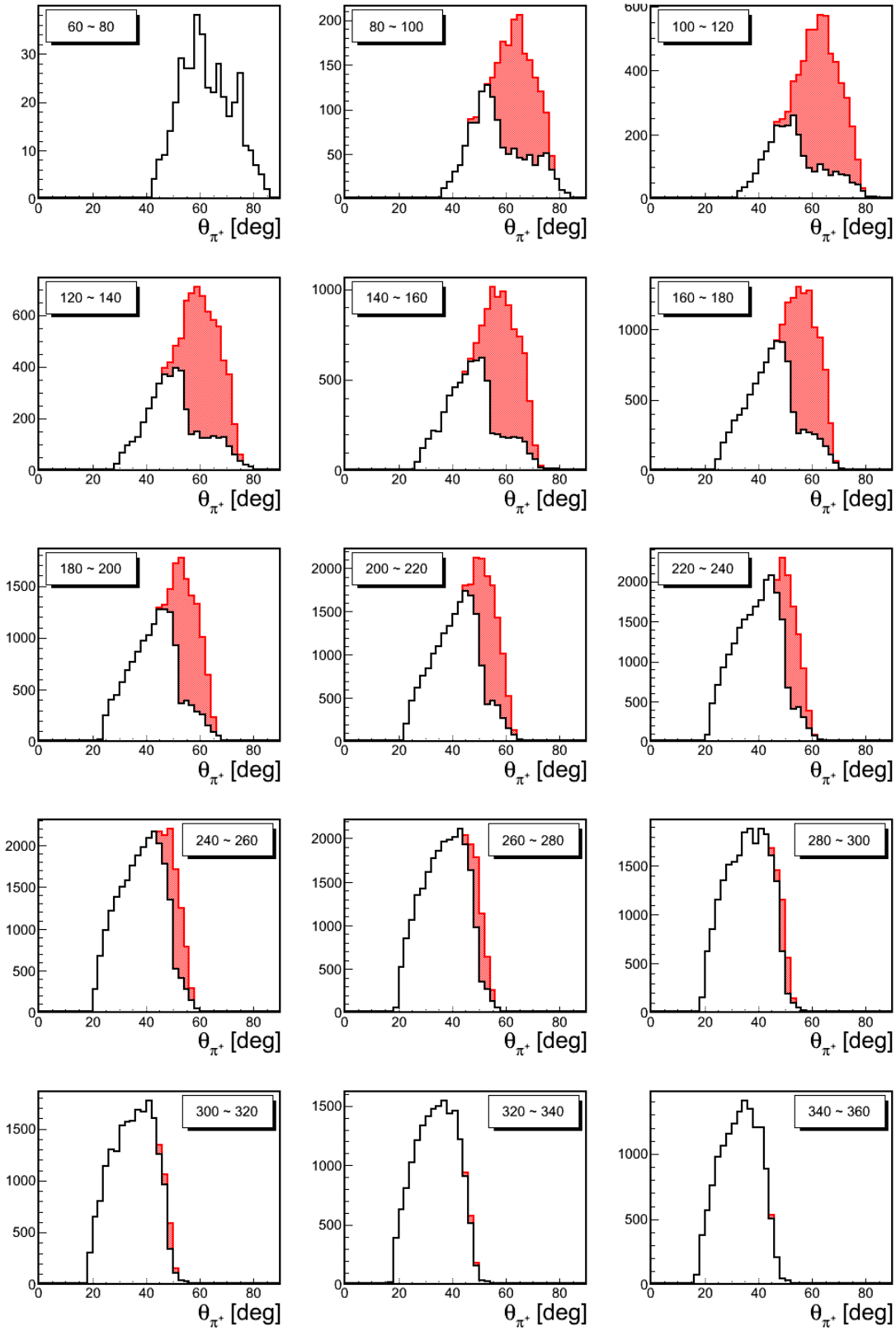

FIG. 4.13 – Polar angle of π^+ in different momentum slice after correction for the M2 Opp. Sec. trigger condition in the region $\theta_p > 46.6^o$. The spectra drawn with solid line present the data before correction, compared with the spectra after correction drawn with dashed-dotted line. The areas filled in red indicate the correction contribution.

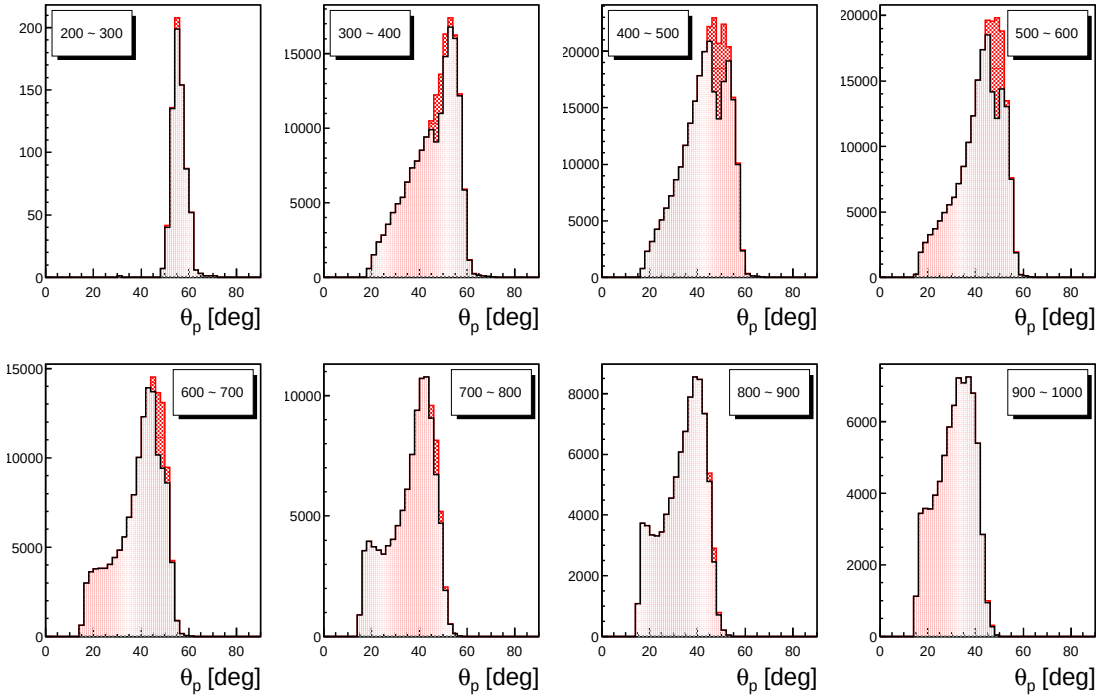

FIG. 4.14 – Polar angle of proton in different momentum slice after correction for the M2 Opp. Sec. trigger condition. The spectra drawn in solid line present the data before correction, compared with the spectra after correction drawn with dashed-dotted. The areas filled in red indicate the correction contribution.

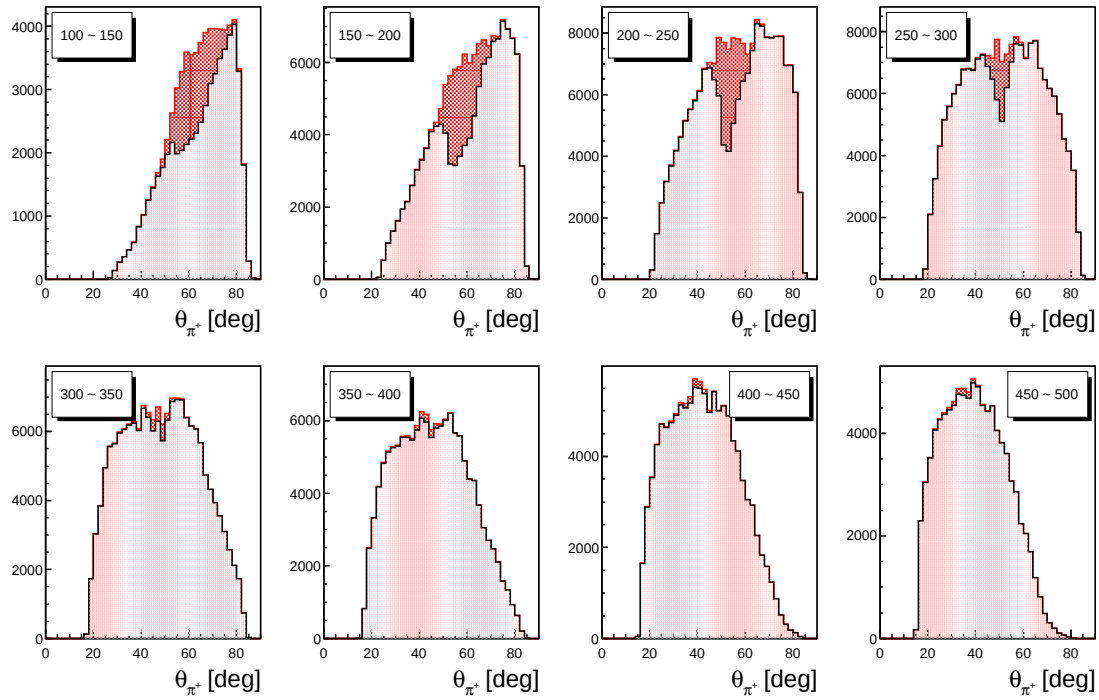

FIG. 4.15 – Polar angle of π^+ in different momentum slice after correction for the M2 Opp. Sec. trigger condition. The spectra drawn in solid line present the data before correction, compared with the spectra after correction drawn with dashed-dotted. The areas filled in red indicate the correction contribution.

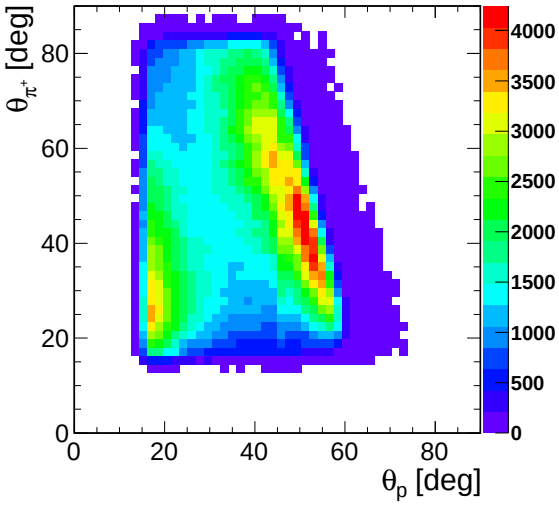

FIG. 4.16 – Polar angle of π^+ versus polar angle of proton after correction for the M2 Opp. Sec. trigger condition.

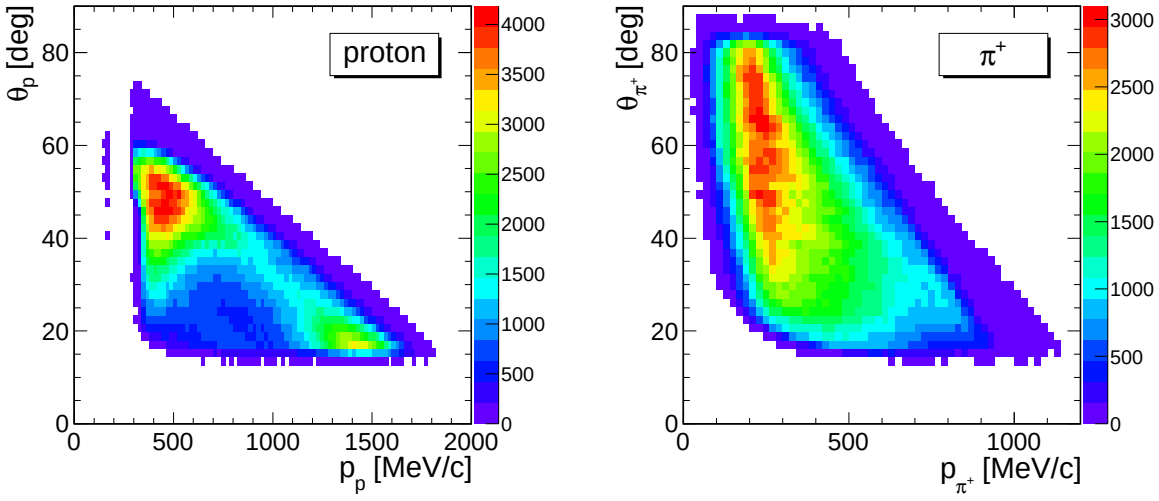

FIG. 4.17 – Polar angle as a function of momentum after correction for the M2 Opp. Sec. trigger condition. **Left :** proton. **Right :** π^+.

4.4 Normalization procedure

The normalization procedure used in the hadronic channel analysis will be explained in this section, for both simulation and data.

4.4.1 Normalization for simulation

In the simulation, a certain number of events $N_{sim}^{4\pi}$ is generated in 4π solid angle, corresponding to a process with cross section $\sigma_{\mathrm{sim}}^{4\pi}$. The simulated yields have therefore to be multiplied by the factor

$$K_{\mathrm{sim}} = \frac{\sigma_{\mathrm{sim}}^{4\pi}}{N_{\mathrm{sim}}^{4\pi}} \tag{4.9}$$

4.4.2 Normalization for experimental data

σ/N measured by pp elastic scattering

For experimental data, the normalization of the yields measured in any channel is realized by using the yield determined by the simultaneously measured elastic events. This work was done by Radek Trebacz (Krakow) and the principle will explained in the following.

The *pp* elastic scattering cross section is known from the EDDA experiment [Albers et al., 2004] which covered the polar angles from 35^o to 145^o in the center-of-mass system. HADES measures the elastic events in 42^o to 145^o (in CM) polar angle region because of the need to detect the two protons. The basic idea is to compare the measured *pp* elastic event to a simulation using the EDDA angular distribution, then scale the data to have the same yield in the common polar angle region between EDDA and HADES, so in 42^o to 145^o (corresponding to 16^o to 69^o in the lab frame).

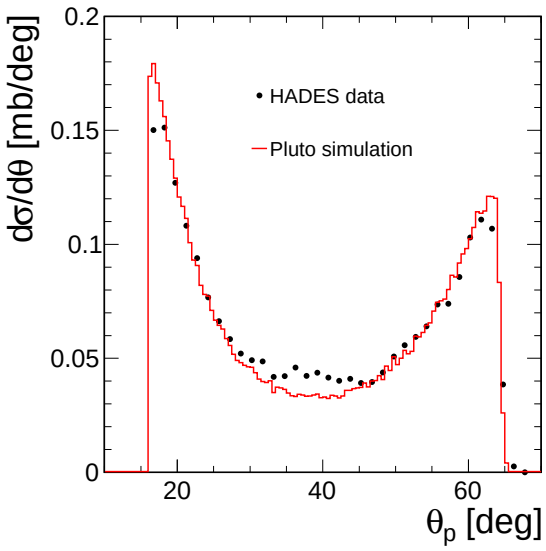

FIG. 4.18 – Angular distribution of *pp* elastic events (black dots) measured by HADES compared to a Pluto simulation using a parametrization of the EDDA data as input [Albers et al., 2004].

The normalization factor is therefore

$$K_{\text{exp}} = \frac{\sigma^{\text{elast}}}{N^{\text{elast}}} = \left(\frac{\sigma^{\text{elast}}_{\text{sim}}}{N^{\text{elast}}_{\text{exp}}}\right)^{16^{\text{o}}-69^{\text{o}}} \tag{4.10}$$

where $\sigma^{\text{elast}\ 16^{\text{o}}-69^{\text{o}}}_{\text{sim}}$=0.6 mb is the elastic cross section in the polar angle 16^o-69^o and $N^{\text{elast}\ 16^{\text{o}}-69^{\text{o}}}_{\text{data}}$ is the corresponding number of events measured by HADES.

The latter one is calculated in three steps :

$$N^{\text{elast}\ 16^{\text{o}}-69^{\text{o}}}_{\text{exp}} = N^{\text{elast}\ 16^{\text{o}}-69^{\text{o}}}_{\text{record}} \cdot F^{LVL1}_{dsf} \cdot F^{\text{M2 Opp.Sec.}}_{dsf} \cdot F^{\text{elast}\ 16^{\text{o}}-69^{\text{o}}}_{\text{Acc}}. \tag{4.11}$$

- Firstly, the number of recorded events corrected for efficiency $N^{\text{elast}\ 16^{\text{o}}-69^{\text{o}}}_{\text{record}} = 7.1 \cdot 10^6$ should be scaled by the global down scaling factor of the LVL1 $F^{LVL1}_{dsf} = 5$;
- Secondly, this number should be multiplied by a second specific down scaling factor of the M2 Opp. Sec. trigger $F^{\text{M2 Opp.Sec.}}_{dsf} = 64$;
- Thirdly $F^{\text{elast}\ 16^{\text{o}}-69^{\text{o}}}_{\text{Acc}} = 1.766$ is used to correct the acceptance for pp elastic events in the polar angle region $(16^o - 69^o)$;

Finally, the normalization factor results in $K_{\text{exp}} = (1.50 \pm 0.10) \cdot 10^{-12}$ mb.

Normalization procedure for $np\pi^+$ events

With the information of pp elastic events mentioned above, we normalize the $pp \rightarrow np\pi^+$ channel using equation 4.12.

$$\sigma^{np\pi^+}_{\text{exp}} = N^{np\pi^+}_{\text{exp}} \cdot K_{\text{exp}} \tag{4.12}$$

Note that, the measured counts for $np\pi^+$ events should also be corrected by F^{LVL1}_{dsf} and $F^{\text{M2 Opp.Sec.}}_{dsf}$.

4.4.3 Uncertainty of the normalization procedure

As mentioned before, the spectra are scaled to have their unit directly in cross section in mili-barn using the elastic scattering. A 6% uncertainty on the normalization factor should be considered. It includes on one hand the error of the pp elastic cross section measured by EDDA (main source close to 6%), on the other hand the uncertainty on the pp elastic event detection efficiency of HADES.

4.5 Efficiency correction

The measured spectra have been corrected for efficiency. The principle of the correction is based on the efficiency matrices introduced in section 3.5.2. For the $pp \rightarrow np\pi^+$ analysis, each event is corrected for p efficiency and π^+ efficiency. The correction is realized only when both the proton and π^+ efficiencies are above 0.4 ; otherwise the events will be weighted by 0.

Concerning the efficiency correction for $np\pi^+$ events, three kinds of systematic errors can be addressed :

– Error due to the efficiency threshold
  This has been checked by comparing the corrected spectra using different threshold values. It has been found that the difference between corrected spectra stay very small. Thus the related error is negligible.

– Global efficiency
The normalization procedure to pp elastic scattering cross section takes into account a possible global error on the proton efficiency. However, the detection efficiency for $np\pi^+$ events is different from pp elastic events because we require a (p, π^+) pair to be detected instead of two protons. To take that into account, we estimated a 2% global error corresponding to a possible global scaling of the $p\pi^+$ yield with respect to pp.

– π^+ angle dependent efficiency
Then, the polar angle spectra per sector pair for both proton and π^+ have been studied to check the detection efficiency correction (see fig. 4.19). Identical distributions should be found for each sector if the efficiency is perfectly described.

Figure 4.20 shows the ratio of counts between one sector pair and the average. The fluctuation indeed indicates quantitatively the difference between sector pairs. The difference remains however within 12% at maximum. As the spectra are always averaged over 6 sectors, the effect of this difference between the sectors has a very low effect on our data analysis.

The main problem is the variation of the efficiency as a function of the relevant variables (here the polar angle), which has to be taken into account correctly by the efficiency matrices. As can be seen from fig. 4.19, there are some fluctuations of the yields, which can be due to some local unexpected inefficiencies, either of the MDC's or of the TOF/TOFINO.

Especially, a jump appears for all the sectors, located right at the TOF/TOFINO transition. It is difficult to distinguish wether the jump is due to an overestimated efficiency in the TOF region or an underestimated efficiency in the TOFINO region. To take both effects into account, a 6% error has been estimated for each π^+ angle bin. To estimate the error on the yields integrated over θ_{π^+}, these errors are treated as uncorrelated for all bins inside the TOFINO ($\theta_{\pi^+} < 45^o$) or inside the TOF ($\theta_{\pi^+} > 45^o$) and correlated for the two groups of bins. More explicitly, this error is :

$$\sigma = (\sum_{i=1}^{i_0} N_i)^{-1}(\sum_{i=1}^{i_0} \delta^2 N_i^2)^{1/2} + (\sum_{i=i_0+1}^{N} N_i)^{-1}(\sum_{i=i_0+1}^{N} \delta^2 N_i^2)^{1/2} \tag{4.13}$$

where, $\delta = 6\%$ is the relative error in each bin, N_i is the number of events in each bin and i_0 is the bin corresponding to $\theta_{\pi^+} = 45^o$. Equation 4.13 yields $\sigma = 4.3\%$, which will be included in the point to point systematic errors for the spectra integrated over the π^+ polar angle.

As the correlation between the different variables which will be discussed in the next chapter (neutron angle, invariant mass and π^+ angle in (p, π^+)) reference frame, ...) is difficult to treat in detail, this error is taken into account both on each bin of the different spectra and as a global error for the cross section estimate. In this way, this error related to the π^+ angle dependence of the efficiency might be overestimated. However, it remains lower than the normalization error.

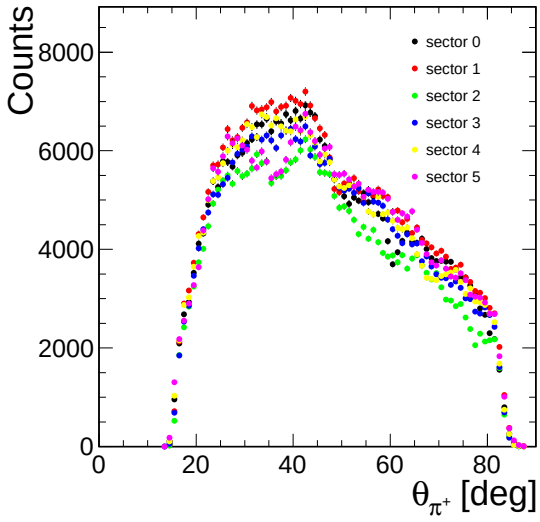

FIG. 4.19 – π^+ polar angle distribution in lab measured in $pp \rightarrow np\pi^+$ reaction at 1.25 GeV. The spectra are measured in HADES acceptance and corrected for efficiency. Different colors present 6 sectors.

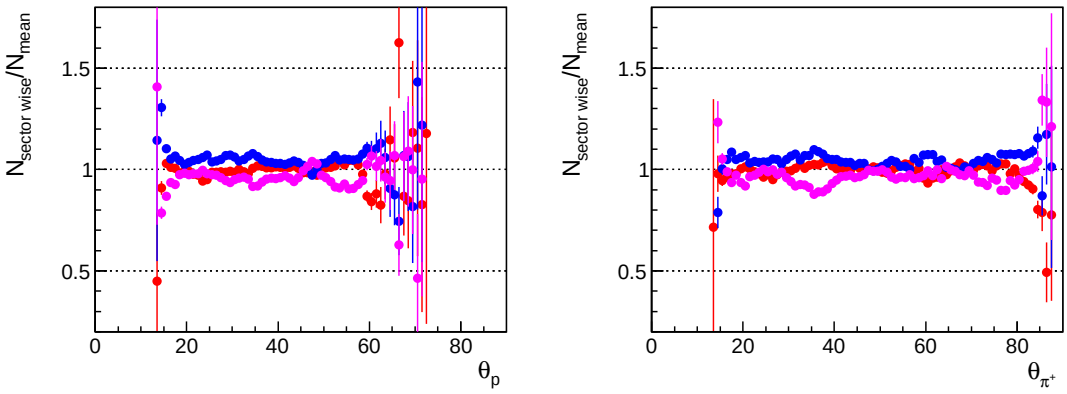

FIG. 4.20 – Ratio of counts between one sector pair and the average along θ. Left : proton, Right :π^+. Different colors correspond to different sector pairs : sector 0-3 (red), sector 1-4 (blue) and sector 2-5 (pink).

4.6 Acceptance correction

Acceptance correction has been performed in our analysis. The spectra in full phase space allow for a direct comparison to different models. The extrapolation is based on using the simulation.

We will give here the principle for this extrapolation. For example, for a spectrum of the variable x, we calculate for each bin i a $F(x)_i$ (see equation 4.14)

$$F(x)_i = \frac{N(x)_i^{\text{sim } 4\pi}}{N(x)_i^{\text{sim Acc}}}, \tag{4.14}$$

where $N_i^{\text{sim } 4\pi}$ is the 4π yield of x in bin i in simulation and $N_i^{\text{sim Acc}}$ is the extracted yield of x in bin i in simulation. Then the factors are applied to the experimental data.

However, this correction can not avoid the dependence on the models which are used in the simulation. The number of events in HADES indeed depends on the acceptance cuts on the other variables. Through this effect, the acceptance factor therefore depends on the distribution of other variables.

To reduce this effect, accurate two-dimensional corrections are realized afterwards. Instead of correcting directly the distribution of the variable x, we introduce a second variable y and calculate correction factor as $F(x,y)_j$ (see equation 4.15).

$$F(x,y)_j = \frac{N(x,y)_j^{\text{sim } 4\pi}}{N(x,y)_j^{\text{sim acc}}}, \tag{4.15}$$

In the same way as above, a more accurate correction can be done and less model dependent 4π spectra can be obtained. In the correction procedure, the variable bin size is adjusted according to the variation of statistics of the spectra. In high yield regions, the smaller bin size is taken to have distinct corrected spectra. While in the low statistic regions, the larger bin size is considered to avoid introducing huge errors. The related error determination will be discussed. The details about the adjustment of the bin size and choice of the second variable together with the acceptance corrected spectra will be shown in section 5.9.

4.6.1 Uncertainty of acceptance correction

From the acceptance correction procedure mentioned above, we can conclude that the uncertainty from this procedure can originate from two aspects, which are

- Error related to the precision of correction factor, which is related to the knowledge of the active volumes of the detector.
- Error due to the model dependence for the acceptance correction.

To take these two uncertainties into account, we estimate on one hand the point to point errors to be included in the spectra, and on the other hand a global value which determines the uncertainty for the total cross section. Note that these errors concern only acceptance corrected spectra.

A detailed discussion will be given in section 5.9, 5.10, directly related to the acceptance corrected spectra and the total cross section value.

4.7 Error evaluation

The total error on experimental spectra includs a statistical error and systematic uncertainties. Both are taken into account by a quadratic sum.

All sources of systematical uncertainties are summarised in the table 4.2 below, taking the angular distribution of neutron in center-of-mass system as an example. The errors related to the acceptance correction are not present here and will be discussed in section 5.9.

The point to point errors are included in the error bars on experimental spectra as a quadratic sum of errors listed in the table. The global uncertainties are also added quadratically and will

Source of systematic error	**Point to point error** [%]	**Global uncertainty** [%]
Event selection	1.7 to 4.6	1.8
Trigger efficiency correction (TS)	22 (over 3.5% of total events)	0.77
Global efficiency correction	—	2
π^+ angle dependent efficiency	4.3	4.3
Normalization	—	6
Total	—	**7.7**

TAB. 4.2 – Summary of systematic errors for the center-of-mass neutron angular distribution in the $pp \rightarrow np\pi^+$ reaction analysis.

be taken into account at the level of the total cross section.

Chapitre 5

Results of $pp \rightarrow np\pi^+$ reaction at 1.25 GeV

In this chapter the results for exclusive one-pion production measurements in the $p+p$ reactions will be discussed, with main emphasis on the $pp \rightarrow np\pi^+$ channel. The preliminary results of these measurements has been already presented in [Liu et al., 2010a,b]. The measured spectra, such as invariant mass and angular distributions, are compared in the HADES acceptance to the Pluto simulation based on the resonance model as introduced in section 3.2. We first compare the data to the standard Pluto model and then propose some improvements to describe better the data. Accurate acceptance corrections have also been performed. At the end, the hadronic channels measured at 1.25 GeV are combined with the same measurements performed at 2.2 GeV to give a global view of the pion production and the role of resonances in the 1-2 GeV range in $p+p$ reactions.

5.1 Dalitz distribution

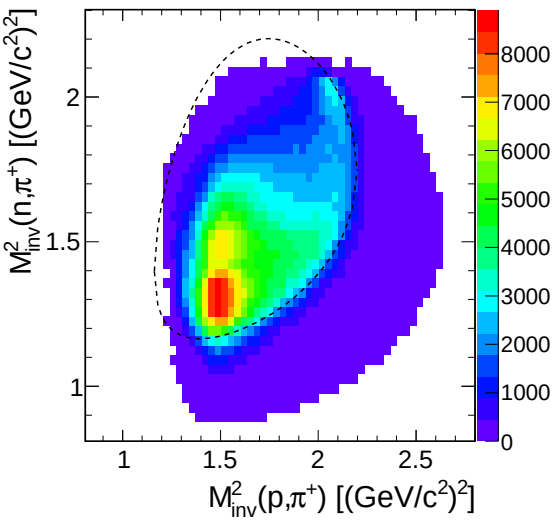

FIG. 5.1 – Dalitz plot of the $pp \rightarrow np\pi^+$ reaction at 1.25 GeV : (n, π^+) versus (p, π^+) invariant mass squared distribution (HADES data). The black dashed curve indicates the Dalitz boundary.

Figure 5.1 shows the Dalitz plot of $pp \rightarrow np\pi^+$ reactions at 1.25 GeV measured in HADES acceptance. The kinematically allowed region (inside the so called Dalitz boundary) for this reaction has been introduced in section 3.4.1 and is shown here by the black dashed line. Some events can be found out of the Dalitz boundary ; this is due to the finite detector resolution effect. We know from the simulation (see section 3.18) that the measured Dalitz distribution is distorted by the detector acceptance with respect to the 4π one. Even though, one can clearly see the Δ^{++} signal located around $M^2_{\text{inv}}(p,\pi^+) = 1.5$ (GeV/c^2)^2 corresponding to the squared mass of $\Delta^{++}(1232)$, which confirms the dominance of the $\Delta(1232)$ resonance production in $pp \rightarrow np\pi^+$ at this energy (see section 3.2.1). The Δ^+ is expected to have a cross section 9 times lower than the one of Δ^{++}, and the Δ^+ signal located around $M^2_{\text{inv}}(n,\pi^+) = 1.5$ (GeV/c^2)^2 is indeed hardly visible.

The spot appearing in the Dalitz plot for equal (n,π^+) and (p,π^+) invariant masses squared around 2 (GeV/c^2)^2 is due to the proton-neutron Final State Interaction (noted as FSI) as we will see in section 5.3.

5.2 π^+N invariant mass distribution

The invariant mass distributions for (p,π^+) and (n,π^+) pairs in the $pp \rightarrow np\pi^+$ reactions at 1.25 GeV as well as the first comparison to the resonance model will be shown in this section. In the following, and in the rest of this thesis, the experimental data are shown in the HADES acceptance.

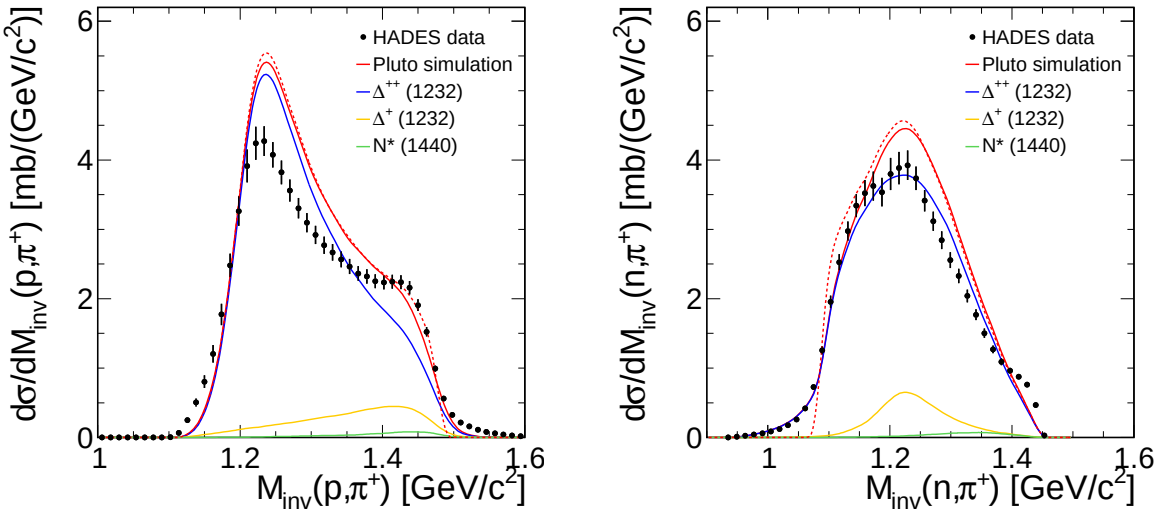

FIG. 5.2 – **Left :** (p,π^+) and **Right :** (n,π^+) invariant mass distributions compared to a Pluto simulation according to the resonance model : total (red), Δ^{++} (blue), Δ^+ (orange) and N* (green). The dashed red curves show the simulation with an ideal resolution. Both experimental data and simulations are normalized to the total pp elastic cross section (see section 4.4) and corrected for efficiency.

Figure 5.2 exhibits the projection on the (p,π^+) and (n,π^+) invariant masses together with a comparison to the Pluto simulation. Error bars include statistical and systematic errors, where the former ones are negligible while the latter one is mainly due to event selection and efficiency corrections (see section 4.7). The incertitude caused by the trigger condition correction procedure also contributes to the systematical error and it has been included in the way explained in

section 4.7. This is the reason for the larger error bars appearing on both (n, π^+) and (p, π^+) invariant masses around 1.2 GeV/c^2.

The prominent peak of $M_{\text{inv}}(p, \pi^+)$ around 1.23 GeV/c^2 found in the left panel of fig. 5.2 confirms quantitatively the dominance of π^+ production via the Δ^{++} resonance decay, although the shape of the resonance is distorted by the instrumental effects. Especially in the low mass region, where the spectra show a very steep rise caused by the kinematical coverage of the detector ($p_{\pi^+} > 0.1$ GeV/c^2 and $\theta_{\pi^+} < 84^o$), the data are very sensitive to the description of the detector acceptance and to the parametrization of momentum resolution in the simulation. The shoulder at 1.44 GeV/c^2 is mainly due to the acceptance effects for the Δ^{++} contribution and slightly to the Δ^+ contribution. In the simulation, this shoulder is present but not enough enhanced.

The $M_{\text{inv}}(n, \pi^+)$ is more suited to see the Δ^+ signal, but the distribution (right panel of fig. 5.2) here is quite broad and the resonance structure of the Δ^+ can not be seen due to the higher weight of the Δ^{++}. The N^* contribution is small.

Generally speaking, the shapes of the spectra, both $M_{\text{inv}}(p, \pi^+)$ and $M_{\text{inv}}(n, \pi^+)$, are in rather good agreement with the $pp \to n\Delta^{++}$ and $pp \to p\Delta^+$ simulations, especially after including the resolution effect. This is shown in fig. 5.2 where the dashed red curves show the simulation without resolution effects. In particular, the rise of the $M_{\text{inv}}(n, \pi^+)$ at the low mass side and to a lesser extent the tail of the $M_{\text{inv}}(p, \pi^+)$ at the high mass side (see red curves in fig. 5.2) are better reproduced when resolution effects are included. In these regions, the protons have indeed average higher momenta, therefore the resolution effect is expected to be more important.

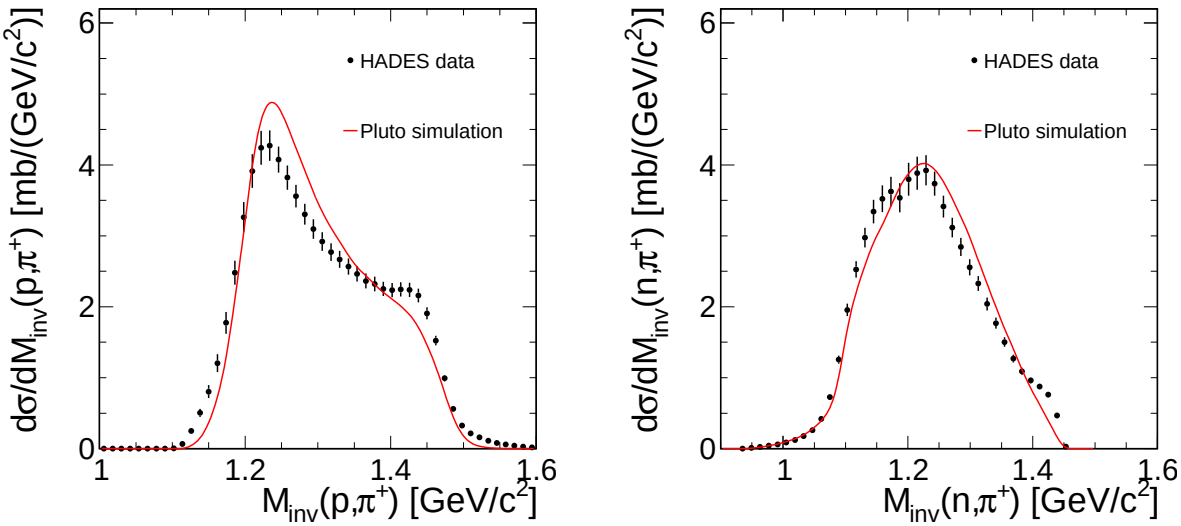

FIG. 5.3 – **Left :** (p, π^+) and **Right :** (n, π^+) invariant mass distributions compared to Pluto simulation according to resonance model. The simulated spectra are normalized to the same total yield as the measured one.

The cross section of the $pp \to np\pi^+$ reactions measured in the HADES acceptance has been extracted to be 0.91 mb by an integration through all the data points. It is found to be 10% less than in the simulation. However one has to keep in mind that we have in total an error of about 6% on the normalization (see section 4.7). In addition, this simulation is based on a fit of cross-sections which have a precision of about $10 - 15\%$ in our energy range [Teis et al.,

1997] (see fig. 1.9). So, the agreement with this "standard" simulation (called standard Pluto simulation in the rest of this thesis) is already quite satisfactory.

Figure 5.3 shows a direct comparison of the shape for both invariant mass distributions by normalizing the simulation to the same total yield as the measured one. Due to the dominance of the Δ^{++} in this channel, only the (p, π^+) invariant mass shows a resonance structure. Pluto simulation provide a reasonable description of the shape of these spectra. Some discrepancy can, however, still be found in both mass distributions, which we will investigate in more detail in the following.

Unless otherwise specified, in the following part of this thesis the measured and simulated spectra will always be normalized to the same total yield inside the HADES acceptance.

5.3 Proton-neutron final state interaction

In section 5.1, we have mentioned that a spot (like a comma) has been observed in the upper right corner of the Dalitz plot (see fig. 5.1), which is not taken into account by the Pluto simulation. Seeing the special location of this spot on the Dalitz distribution, i.e. it corresponds to the same (p,π^+) and (n,π^+) invariant mass, one can deduce that for each event in this region the neutron and proton momenta are very close. It thus leads us to think about the Final State Interaction (called FSI) between the neutron and the proton.

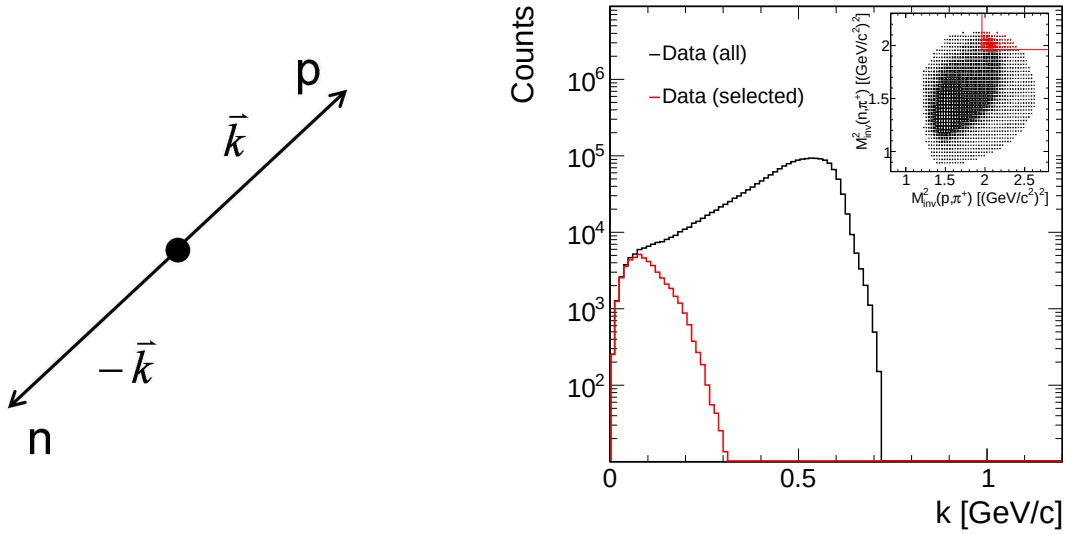

FIG. 5.4 – **Left :** Sketch for the definition of k : the momentum of the proton or neutron in the (p, n) center-of-mass system (corresponds to the half of the (p, n) relative momentum). **Right :** The reconstructed k distribution in $pp \rightarrow np\pi^+$ reactions, for all measured events (black) and the events in the "comma" region (red).

In order to prove that, we firstly check the reconstructed proton momentun k (definition see left panel of fig. 5.4) in the "comma" area by requiring both (p, π^+) and (n, π^+) invariant mass above 1.4 GeV/c^2. Then we compare the k distribution in this specific region to the one for all the events. As we can see in fig. 5.4, the total k distribution is peaked above 0.5 GeV/c while the fraction in the "comma" region occupies the very low k region (with a maximum yield below

0.1 GeV/c).

A more detailed investigation has been performed by implementing the pn FSI using the Jost function formalism in Pluto. Instead of taking into account the FSI effect in the production amplitude [Titov et al., 2000], we calculate a weight applied directly on the cross section [Froehlich et al., 2010] in the form of equation 5.1 :

$$\begin{aligned} W_{FSI} &= \frac{1}{|J(k)|^2} = |\frac{k+i\alpha}{k+i\beta}|^2 \\ \text{with } \alpha &= \frac{1}{r_0}(\sqrt{1-2r_0a_0^{-1}}+1) \\ \beta &= \frac{1}{r_0}(\sqrt{1-2r_0a_0^{-1}}-1) \end{aligned} \tag{5.1}$$

where the k is proton or neutron momentun in the (p,n) reference frame as defined in fig. 5.4 (left), $r_0 = 2.75\ fm$ and $a_0 = -23.768\ fm$ for pn singlet taken from Titov et al. [2000]. With this formula, one can calculate the probability to have the FSI (noted as W_{FSI}) as a function of k as shown in the left panel of fig. 5.5. It shows that the high W_{FSI} values concentrate in the low k region and it converges towards 1 when k is increasing. Seeing the k distribution for events measured in the HADES acceptance (fig. 5.4) and the correlation given by equation 5.1, one can conclude that the majority of events detected by HADES are not in a kinematical region where FSI play a significant role.

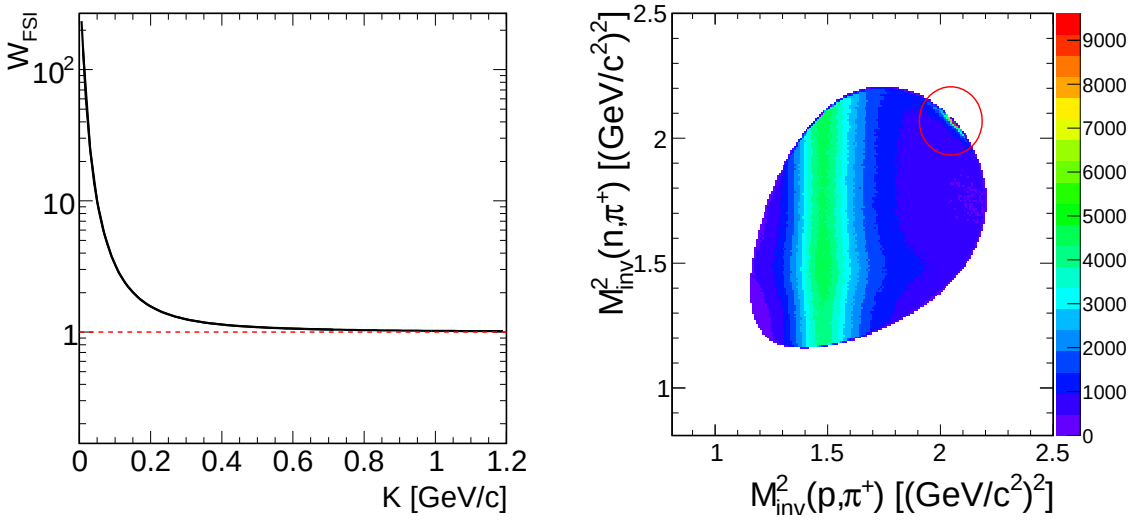

FIG. 5.5 – **Left :** Weight of proton-neutron final state interaction W_{FSI} as a function of momentum k. **Right :** Simulated Dalitz plot in 4π of the $pp \to n\Delta^{++} \to np\pi^+$ reaction, weighted by W_{FSI}.

To see the sensitivity of the Dalitz distribution to FSI, we plot the simulated 4π Dalitz plot based on the resonance model with the implementation of FSI (right panel of fig. 5.5). In practice, we simply weight the events by W_{FSI}. In the right panel of fig. 5.5, we obtain the 4π Dalitz plot including FSI effect and an enhancement appears in the very extreme end of the diagonal where (p,π^+) invariant mass squared equals (n,π^+) one.

This effect is much clearer after the acceptance cut. The spot appearing at high invariant masses in fig. 5.6 confirms at least qualitatively the FSI observation.

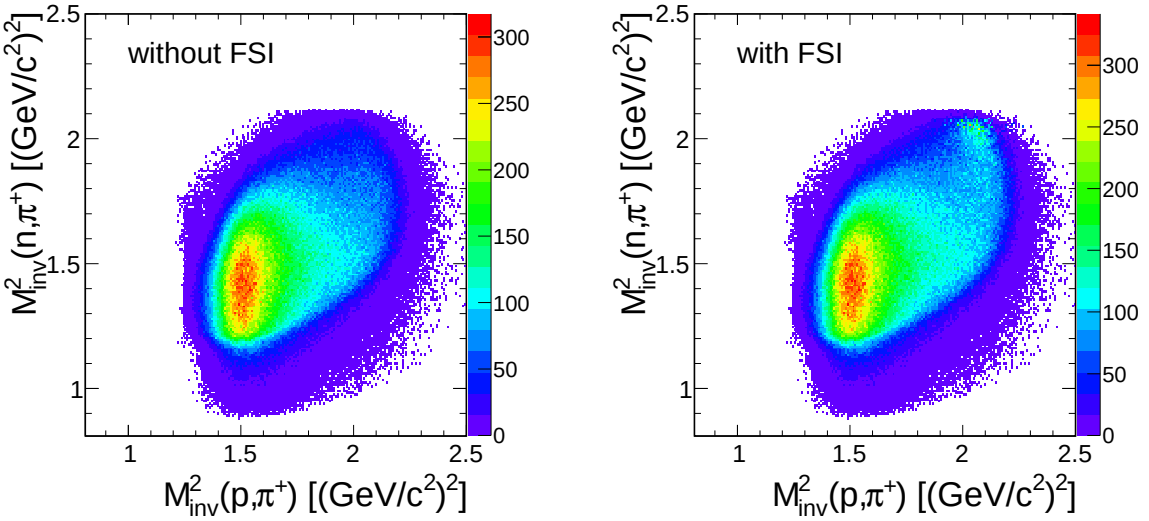

FIG. 5.6 – Simulated Dalitz plot of the $pp \rightarrow np\pi^+$ reaction : (n,π^+) against (p,π^+) invariant mass squared distribution in HADES acceptance. **Left :** Pluto simulation based on the resonance model and **Right :** Pluto simulation based on the resonance model weighted by W_{FSI}. The resolution effect is included.

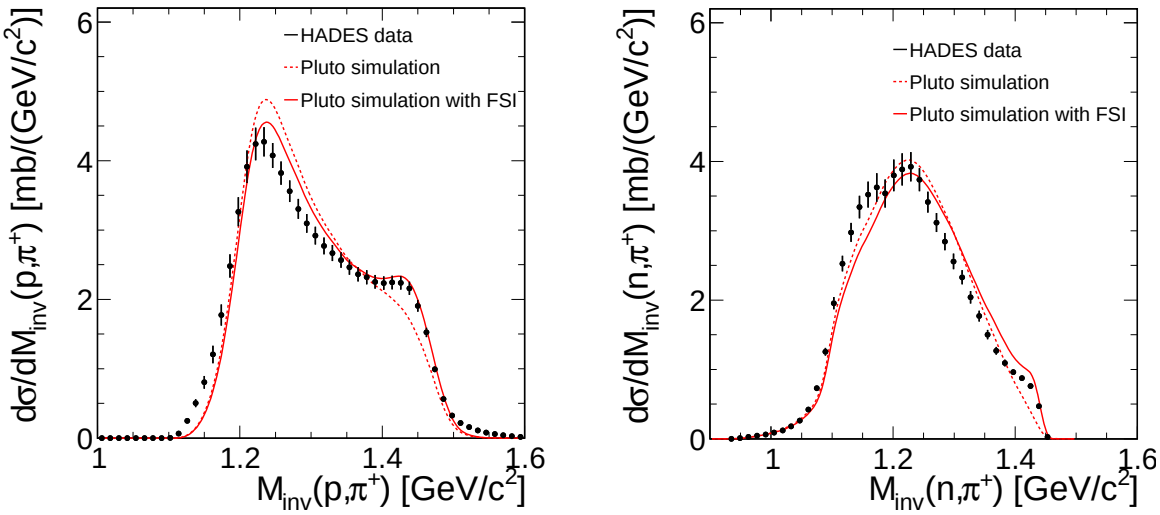

FIG. 5.7 – **Left :** (p,π^+) and **Right :** (n,π^+) invariant mass distributions compared to Pluto simulation in $pp \rightarrow np\pi^+$ reactions in HADES acceptance. The dashed line presents the standard Pluto simulation and the solid line shows the Pluto simulation with the FSI effect.

Then the measured invariant mass spectra are compared to the simulation with the FSI effect as shown in fig. 5.7. We would like to stress that the FSI effect is treated in a crude way in our analysis. However, the difference of the shape in the simulations is obvious. The FSI implementation gives more weight to the large invariant masses for both spectra. The shoulder at 1.45 GeV/c^2 can be clearly seen now. Despite the still existing discrepancy, the FSI is clearly needed and will be included in the simulation of the $pp \rightarrow np\pi^+$ channel in the rest of this work.

5.4 Sensitivity to the $N^*(1440)$ contribution

In the previous sections, we observed the dominance of $\Delta(1232)$ resonance production in $p+p$ reaction at 1.25 GeV. In this energy range, however, other contributions, such as the $N^*(1440)$, are also present.

In the resonance model, the π production via the $N^*(1440)$ resonance was obtained by Teis *et al.* by fitting the one-π and two-π production cross sections. The result is 0.34 mb for the $pp \rightarrow np\pi^+$ (1.8% of the total cross section) [Teis et al., 1997]. This value is used in the Pluto simulation and we use the production angular distribution taken from [Huber and Aichelin, 1994].

Based on preliminary data of the CELSIUS-WASA collaboration, an effective Lagrangian approach predicted a N^* contribution of 6 mb around 1.25 GeV, i.e. about 18 times as much as in the Teis fit, and a Δ resonance contribution of about 14 mb [Zhen et al., 2009]. Seeing the (p, π^+) invariant mass spectrum (fig. 5.2), values differing that much from Teis fits can be clearly excluded by our analysis. They seem also not to be confirmed by more recent WASA result ([Skorodko, 2009]), where the N^* contribution is found to be 2.3% of the total cross section. Though it is still higher than the value 1.8% found in the Teis fit, as can be deduced from fig. 5.2 our data are not sensitive to different $N^*(1440)$ contributions within a factor 2 or 3.

Further constraints on the N^* contribution can be obtained from the two-π measurements. Some of the results were not included in the Teis systematics, as [Shimizu et al., 1982], or were performed afterwards [Skorodko, 2009]. For the dominant $pp \rightarrow pp\pi^+\pi^-$ and $pp \rightarrow pn\pi^+\pi^0$ cross section about a factor 2 higher than the Teis systematics have been measured [Shimizu et al., 1982]. If these data were included in the Teis fits, higher values for N^* would be obtained.

Since our $np\pi^+$ data are not very sensitive to this contribution, we did not investigate it further. It would however be more important for the study of the $pp \rightarrow pp\pi^+\pi^-$ channel, which is also in progress in the HADES collaboration.

5.5 Sensitivity to non-resonant contribution

The sensitivity to the direct production of pions without any intermediate resonant state (so called non-resonant contribution) has been checked using a pure phase space simulation in $pp \rightarrow np\pi^+$ channel. The same test should be also done in the $pp \rightarrow pp\pi^0$ channel, with a correlation $\sigma^{non-res}_{pp\pi^0} = \frac{1}{2}\,\sigma^{non-res}_{np\pi^+}$ which can be indeed deduced from the isopin coefficients of the $NN\pi$ vertex given in Appendix A. In the Teis fit, the same correlation between the $np\pi^+$ and $pp\pi^0$ channel has been assumed and both cross sections are found to be 0 for $\sqrt{s} > 2.3$ GeV.

0.4 mb of non-resonant contribution in 4π is added in our simulation for the $np\pi^+$ channel. This corresponds to about 2% of the total cross section and can be taken as a maximum contribution, considering the precision of the previous data. The result is shown in fig. 5.8, where data are compared to simulations with and without additional non-resonant contribution. Due to the HADES acceptance, the non-resonant contribution gives a flat distribution on the (n, π^+) invariant mass whereas it causes a small bump around 1.4 GeV/c^2 in the (p, π^+) invariant mass spectrum. The shape of the (p, π^+) invariant mass is therefore more sensitive to the non-resonant contribution. More tests about the influence from this contribution will be shown in section 5.6

and 5.7.3.

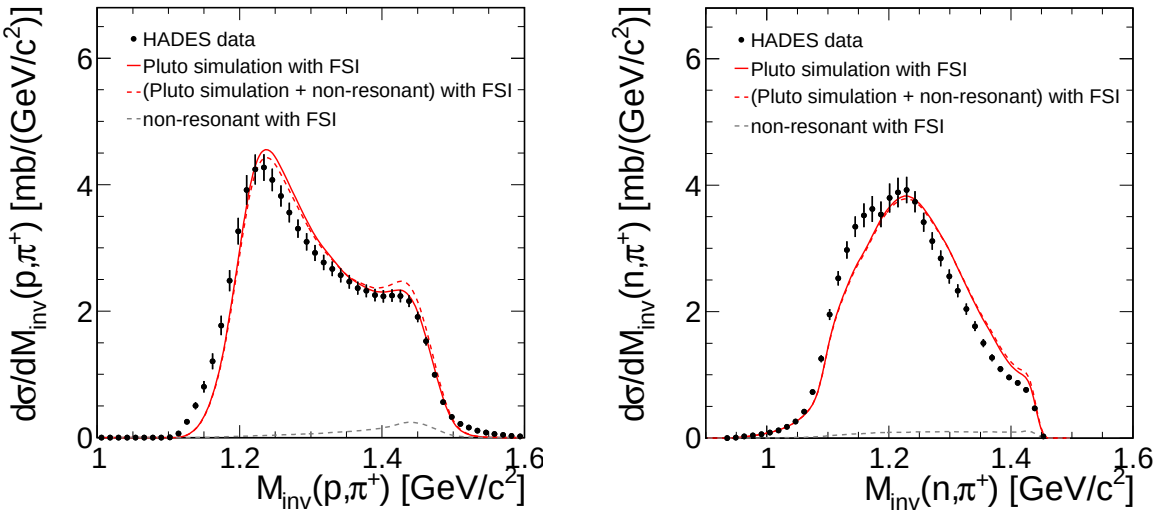

FIG. 5.8 – **Left :** (p, π^+) and **Right :** (n, π^+) invariant mass distributions compared to standard Pluto simulation (red solid line) and the simulation with additional non-resonant contribution (red dashed line). The non-resonant contribution is presented by grey dashed line.

5.6 Neutron angular distribution

The neutron angular distribution in the center-of-mass system is directly related to the angular distribution of the Δ resonance production because $pp \rightarrow n\Delta^{++}$ is the dominant process (left panel of fig. 5.9).

The distribution in the HADES acceptance has been compared with the simulation, as shown in fig. 5.9. Like for the mass spectra, the vertical error bars present the quadratic sum of statistical and systematic errors. But in the case of the neutron angular distribution the systematic error caused by event selection is included with a dependence along $\cos\theta_n^{CM}$ as mentioned in section 4.2.3. The errors caused by the trigger condition correction procedure play a more important role rather in the forward emitted neutron region, but they can hardly be seen due to the log scale. Note that the fluctuations in the simulation are due to their limited statistics only.

The neutron angular distribution is found to be asymmetric with respect to $\cos\theta_n = 0$. This is expected due to the lack of detector acceptance for positively charged particles emitted below 14^o. This effect is on overall well reproduced by simulation, which confirms the good control of the acceptance. The comparison shows globally a rather good agreement between data (black points) and simulation (red solid line). Still, the discrepancy can be seen for the extreme backward neutron angles ($\cos\theta_n = -1$) and in the central region ($|\cos\theta_n| < 0.5$). The neutron angular distribution is too much peaked in the simulation with respect to the data. Due to the dominance of Δ^{++} production, the natural explanation could be a too much peaked Δ^{++} (so for Δ^+) production angular distribution.

In the following, we will discuss possible explanations which can help to improve the agreement between simulation and data.

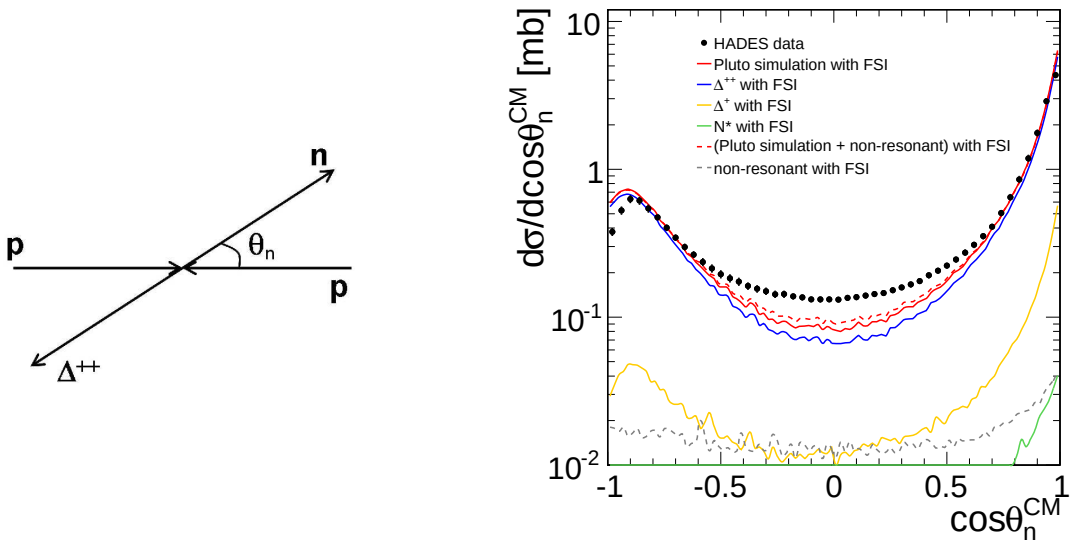

FIG. 5.9 – **Left :** Sketch of the definition of neutron angle θ_n in the $p+p$ center-of-mass system. **Right :** Angular distribution of neutron in the $p+p$ center-of-mass system measured in $pp \to np\pi^+$ reactions at 1.25 GeV. Data (black points) compared to simulations. Standard Pluto with FSI simulation (red solid line) including Δ^{++} (blue), Δ^+ (orange) and N^* (green) ; version of Pluto simulation (red dashed line) with additional non-resonant contribution (grey dashed line).

– Influence from the N^* and non-resonant contribution ;

First of all, similarly to the tests performed to the invariant mass distributions (see section 5.2), the sensitivity to other contributions has been studied using simulation. In particular, the influence from a non-resonant contribution has been tested because its $\cos\theta_n^{CM}$ distribution is found to be much flatter than that from the resonance contributions. By adding a non-resonant π production contribution with $\sigma = 0.4$ mb the simulation gets closer to the data points as seen on fig. 5.9. Even though, it can not fully explain the discrepancy. On the other hand, the cross section assumed here for the non-resonant contribution can not be larger since it is also constrained by the invariant mass distribution (see section 5.7.3).

– Limits of the OPEM ;

Then, the simulation performed in our analysis is based on the resonance model where the one-π exchange for Δ production is assumed. We have to point out that, in the region of the excess, the t and u four-momentum transfer squared are the highest (see section 3.2.3). Thus other mechanisms, as ρ exchange, might become more important in this region.

– Cut-off parameter Λ_π ;

Following the previous point, since we are sensitive to the four-momentum transfer in this region, we can test this sensitivity using the cut-off parameter Λ_π involved in the OPEM. As introduced in the description of Δ production in section 3.2.3, the form factor of the $\pi N\Delta$ vertex is parameterized simply as

$$F(t) = \frac{{\Lambda_\pi}^2 - m_\pi^2}{{\Lambda_\pi}^2 - t} \tag{5.2}$$

where m_π is the mass of the exchanged pion, t is the squared four-momentum transfer. Following equation 5.2, one can conclude that the higher Λ_π is, the larger transfers are allowed.

In [Dmitriev and Sushkov, 1986], $\Lambda_\pi = 0.63$ GeV is adjusted to give the best description of $pp \rightarrow p\Delta^{++}$ reaction at proton kinetic energies from 0.97 to 2.02 GeV. Because our data are exactly in this energy range, it is worthwhile to perform the test with different Λ_π value considering the big error bars in the previous measurements (see fig. 1.6).

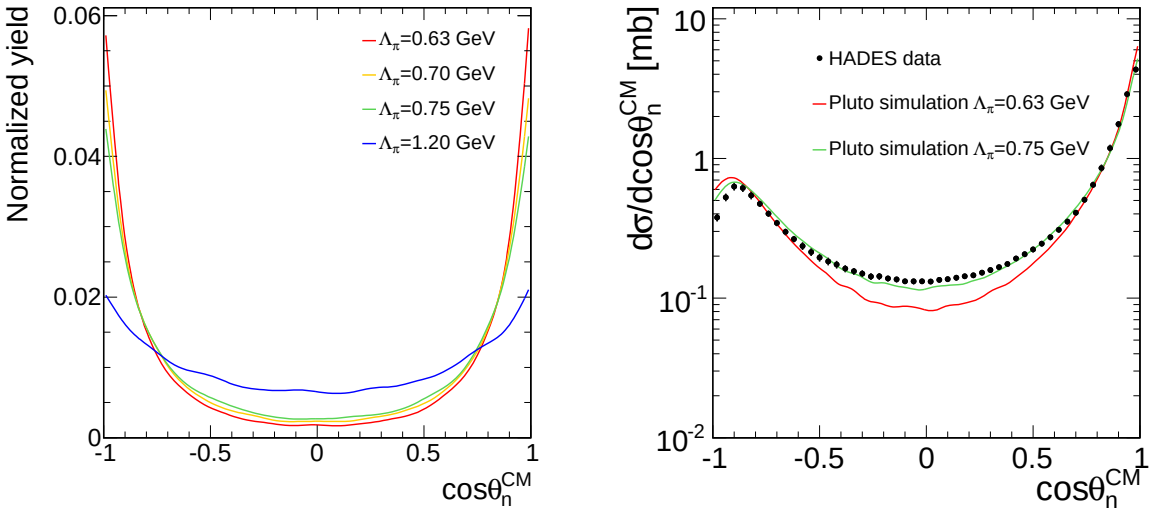

FIG. 5.10 – **Left :** Simulated 4π angular distribution of neutron in the p+p center of mass system measured in $pp \rightarrow n\Delta^{++}$ reactions at 1.25 GeV with different Λ_π values (Red : $\Lambda_\pi = 0.63$ GeV, Orange : $\Lambda_\pi = 0.70$ GeV, Green : $\Lambda_\pi = 0.75$ GeV and Blue : $\Lambda_\pi = 1.20$ GeV). **Right :** Angular distribution of neutron in the $p + p$ center of mass system measured in $pp \rightarrow np\pi^+$ reactions at 1.25 GeV. Data (black points) compared to simulations with different Λ_π values (Red : $\Lambda_\pi = 0.63$ GeV and Green : $\Lambda_\pi = 0.75$ GeV).

A series of Λ_π values are then applied in the simulation. The maximum value we test here, $\Lambda_\pi = 1.2$ GeV, is used in the $pp \rightarrow np\pi^+$ channel analysis of WASA. The (p, π^+) invariant mass distribution stays the same for different values of Λ_π. But the $\cos\theta_n^{\mathrm{CM}}$ distribution shows a great sensitivity (see left panel of fig. 5.10). Indeed, the larger Λ_π value gives a less peaked $\cos\theta_n^{CM}$ distribution. It has to be noted that increasing the Λ_π cut-off parameter results in principle in an increase of the cross section for the $pp \rightarrow N\Delta$ calculation in the OBE model which would deteriorate the agreement of OPEM calculations for the total cross section [Dmitriev and Sushkov, 1986]. Here in our simulation, we keep the cross section constant since our aim is just to get a better parametrization of the angular distribution.

After going through the full analysis chain, the models are compared to the data. We found that by assuming $\Lambda_\pi = 0.75$ GeV, the simulation gives a better description of the data (see right panel of fig. 5.10) in $pp \rightarrow np\pi^+$. As mentioned above, this should just be taken as a way to have a better description of the angular distribution. In addition, this new parametrization should also be tested in the $pp \rightarrow pp\pi^0$ channel.

– Lack of Δ^{++}/Δ^+ interference in simulation.

Last but not least, the interference between Δ^{++} and Δ^+, which is not included in our simulation can also stand out in the central region where the relative contribution of Δ^+ is the highest. A more detailed discussion related to this aspect can be found in the next section.

5.7 Differential $N\pi$ invariant mass distribution

More detailed investigations have been performed by looking at the differential $N\pi$ invariant mass distribution as a function of the neutron center-of-mass angle. The FSI effect, the role of the N^* and non-resonant contribution, the influence from the cut-off parameter Λ_π and the Δ^{++}/Δ^+ contribution will be shown in the following.

In practice, we divide $\cos\theta_n^{\mathrm{CM}}$ into 10 slices from -1 to 1. In each interval, the measured $M_{\mathrm{inv}}(p,\pi^+)$ and $M_{\mathrm{inv}}(n,\pi^+)$ are compared to the simulation with different assumptions.

The data are shown in the following pictures by open circles (see fig. 5.11 and 5.12). Vertical error bars denote the statistical and systematic errors which are defined in the same way as on the integrated spectra in fig. 5.2. The error bars are smaller than the size of the symbols for most of the bins. The large error bars appearing at the maximum of the spectrum in the last slices of the $M_{\mathrm{inv}}(n,\pi^+)$ spectra are due to the correction of trigger cut. The jumps visible in this region are also due to this correction but stay within the error bars. As in previous sections, the simulation is normalized to fit the total yield measured in the HADES acceptance for each bin. In other words, there is only one global normalization factor (of the order of 0.9).

5.7.1 Comparison to a simulation with FSI effect

First of all, the behavior of the FSI effect is checked. The measured differential mass spectra are compared to both a standard Pluto simulation (light blue curves) and a Pluto simulation with FSI effect (red curves) (see fig. 5.11 and 5.12).

As already seen in the global neutron angular distribution (fig.5.9), the Pluto simulation overestimates the data for the forward and backward neutron angles with respect to $\cos\theta_n^{CM} = 0$. However, it reproduces in general reasonably well the shapes of spectra for all the slices. The evolution of these shapes is mainly due to the acceptance and kinematics, and is rather well reproduced by the standard simulation.

The FSI (red line) implementation significantly improves the agreement between simulation and data. As explained in section 5.3, the FSI effect plays an important role mainly in the very high mass region. One can indeed see that the low mass region ($M_{\mathrm{inv}} < 1.3$ GeV/c^2) is not much affected by the FSI. But the peaks in the high mass region ($M_{\mathrm{inv}} > 1.3$ GeV/c^2) are nicely reproduced. Those peak structures in both invariant mass spectra are essentially due to the acceptance effects and FSI.

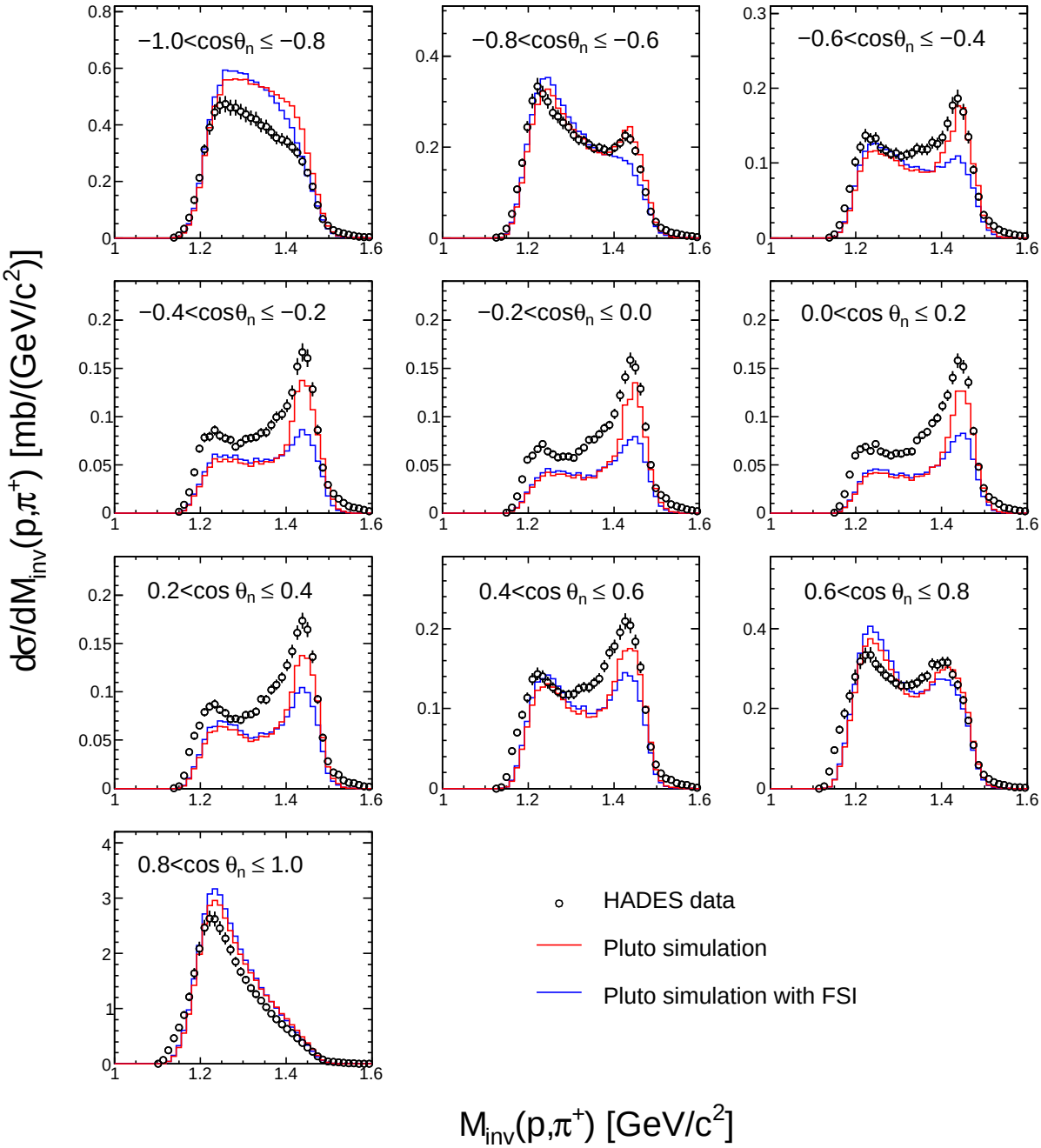

FIG. 5.11 – (p, π^+) invariant mass distributions in slices of $\cos\theta_n^{\mathrm{CM}}$ compared to Pluto simulation. The simulation based on the standard resonance model is drawn in blue and the simulation with FSI implementation is drawn in red.

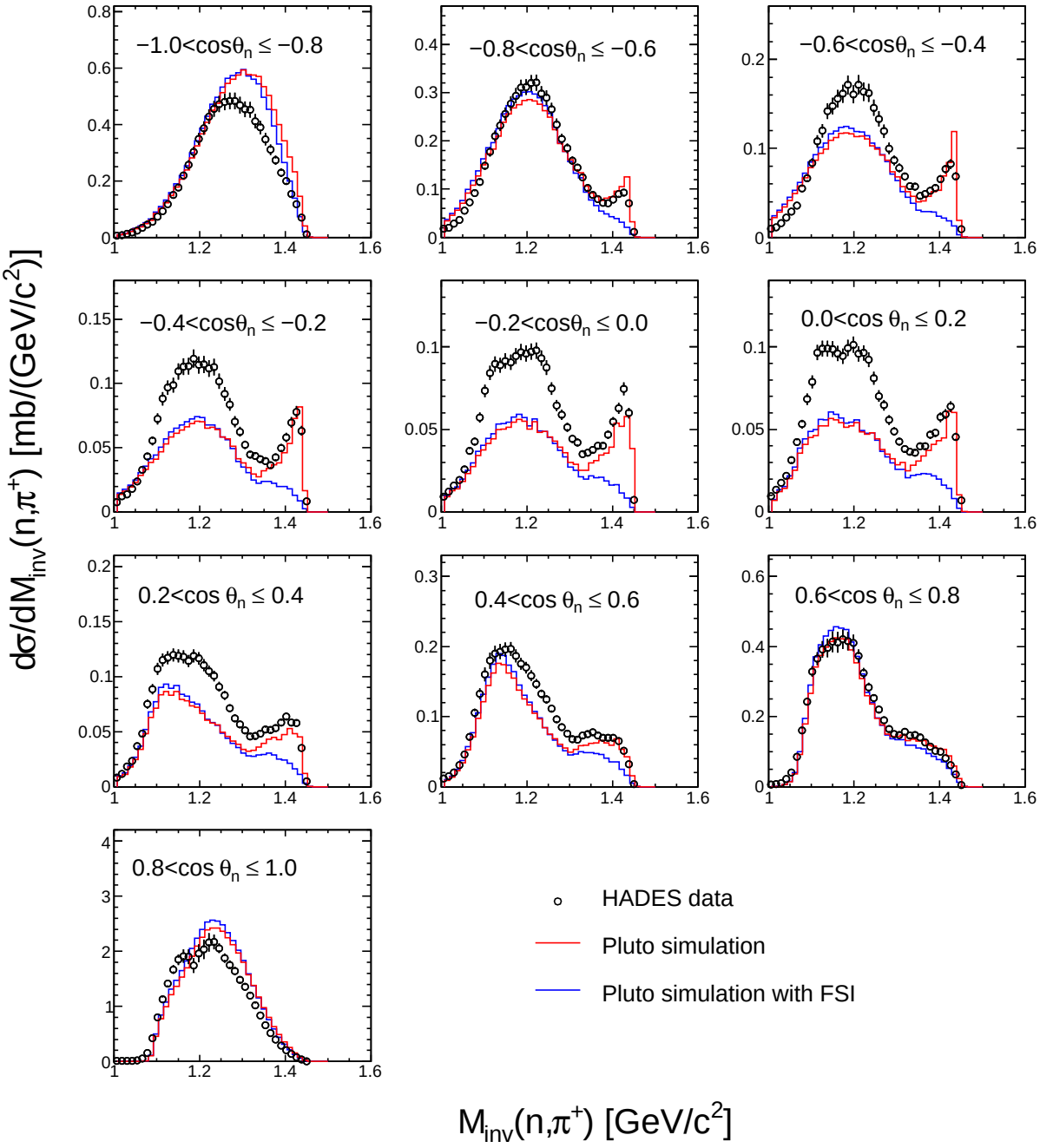

FIG. 5.12 – (n, π^+) invariant mass distributions in slices of $\cos\theta_n^{\mathrm{CM}}$ compared to Pluto simulation. The simulation based on the standard resonance model is drawn in blue and the simulation with FSI implementation is drawn in red.

5.7.2 Δ^{++} and Δ^{+} contributions

As mentioned in section 5.2, in the $pp \rightarrow np\pi^+$ reaction at 1.25 GeV the main contributions come from the Δ^{++}, Δ^{+} and $N^*(1440)$ resonances. According to Teis fits, the Δ^{++} contributes 90% of the total cross section.

Now we will discuss the role of different resonance contributions using the differential invariant mass spectra (see fig. 5.13 and fig. 5.14). In general, the Δ^{++} gives a dominant contribution for any neutron angle. The Δ^{+} contribution is higher for $M_{\text{inv}}(p, \pi^+)$ above 1.3 GeV/c^2, however the Δ^{++} remains dominant, so that the Δ^{+} contribution can not really be selected using an invariant mass cut.

Since in Pluto simulations the Δ^{++} and Δ^{+} are added incoherently, one can ask the question whether the interference between Δ^{++} and Δ^{+} production amplitude can be at the origin of the disagreement between the data and the simulation. The proportion of Δ^{++} and Δ^{+} indeed depends on the neutron angular distribution. In the large neutron angle region the Δ^{+} contribution is much higher than elsewhere, therefore the interference between Δ^{++} and Δ^{+} could be also more important.

In the analysis of the CELSIUS-WASA data [Skorodko, 2009], an arbitrary phase between the Δ^{++} and Δ^{+} amplitudes, $\phi = \frac{3\pi}{4}$ was introduced to better describe the data.

However, in principle, these interference effects derive from the calculation of the complex amplitudes. It would be interesting to compare these differential spectra to a full calculation including Δ^{++}, Δ^{+}, $N^*(1440)$ and non-resonant contributions in a coherent way.

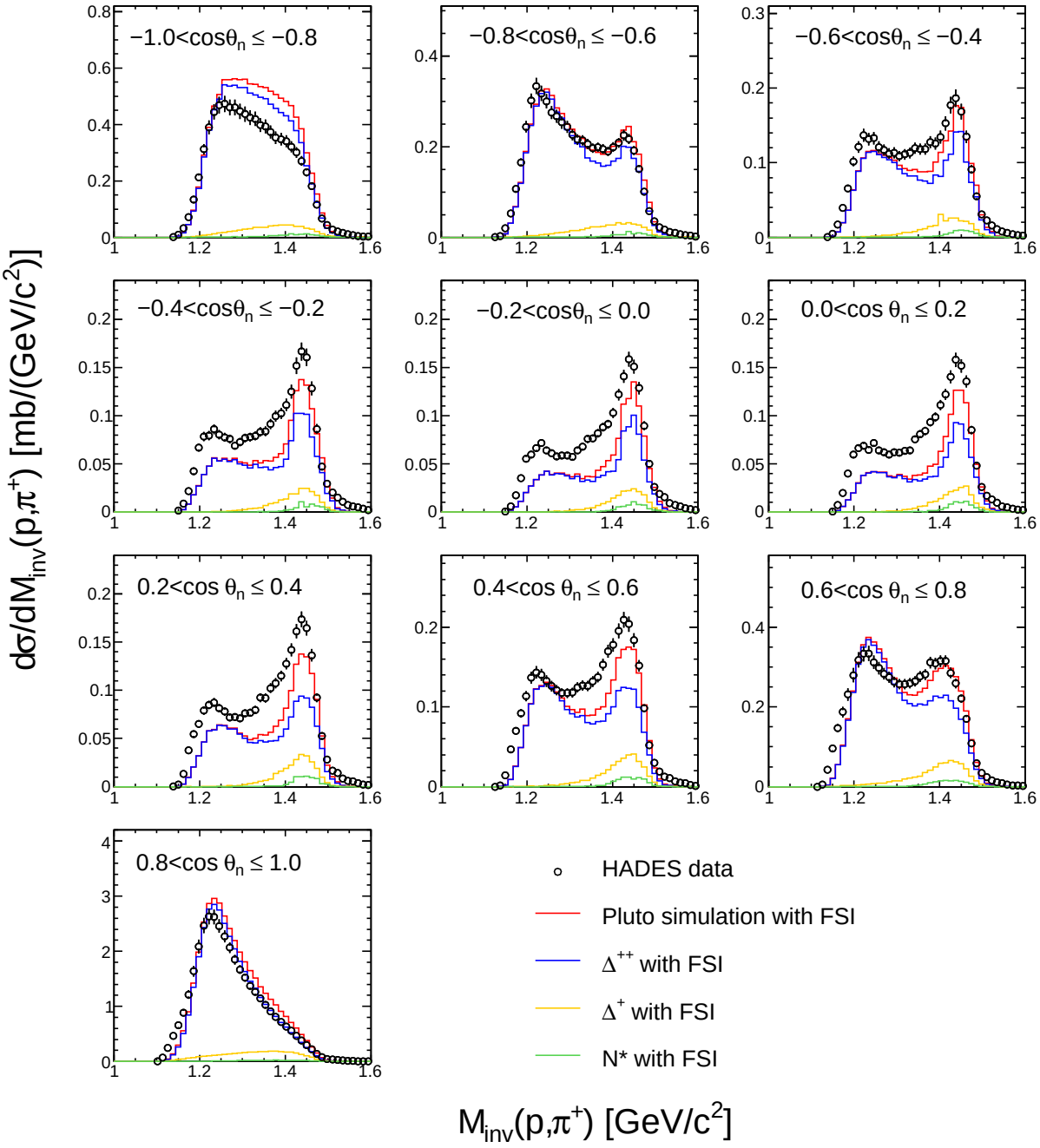

FIG. 5.13 – (p, π^+) invariant mass distributions in slices of $\cos\theta_n^{\mathrm{CM}}$ compared to Pluto simulation with FSI implementations. Total contribution is drawn in red, Δ^{++} in blue, Δ^{+} in orange and N^* in green.

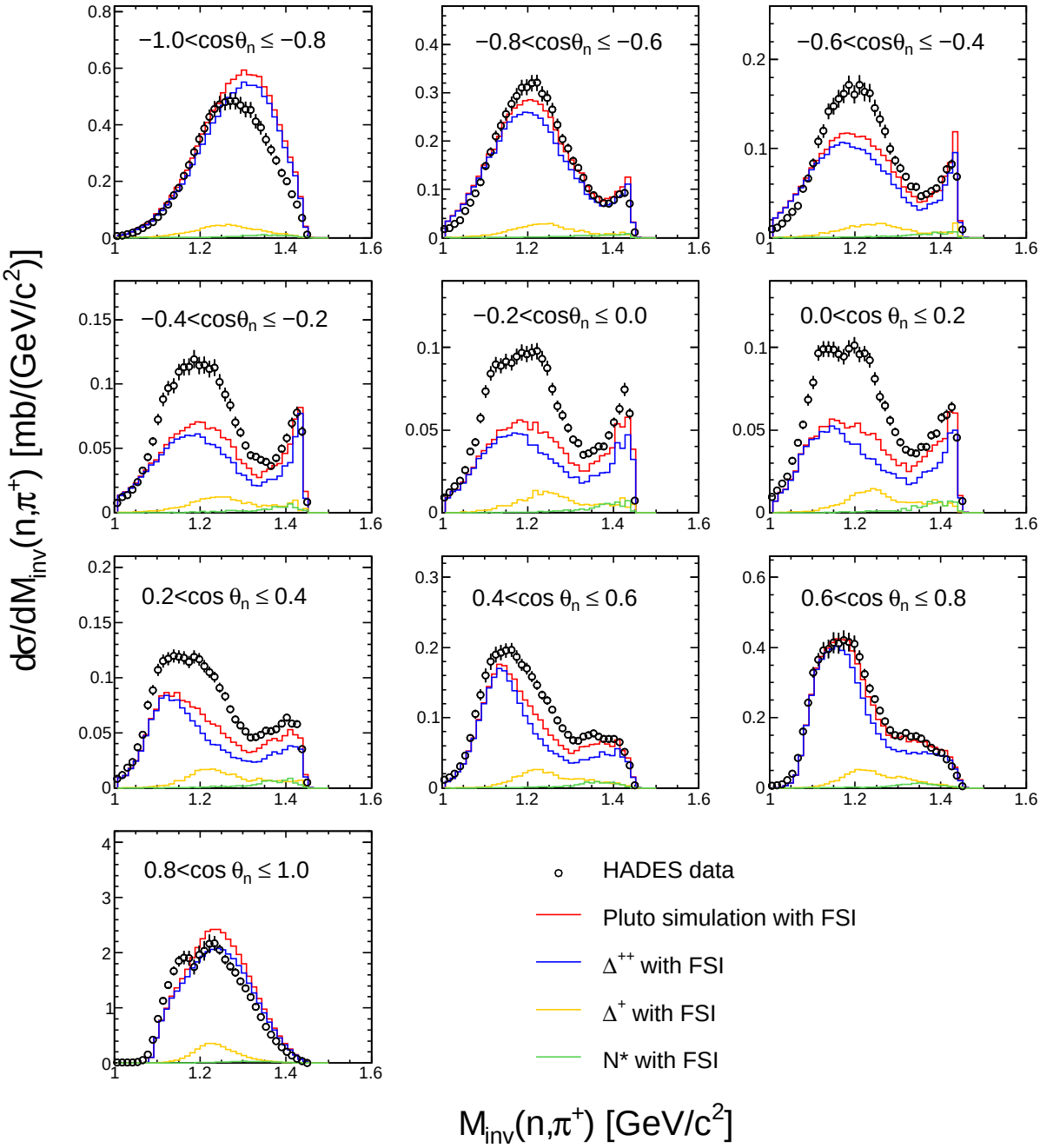

FIG. 5.14 – (n, π^+) invariant mass distributions in slices of $\cos\theta_n^{\mathrm{CM}}$ compared to Pluto simulation with FSI implementations. Total contribution is drawn in red, Δ^{++} in blue, Δ^+ in orange and N^* in green.

5.7.3 Influences from the phase-space contribution

We have introduced the non-resonant π^+ contribution in the previous sections. In section 5.5, we compared the integrated invariant mass spectrum to a simulation with an additional non-resonant π^+ production using a phase-space contribution. Due to the strong dominance of the Δ^{++}, the data do not show any sensitivity to this contribution. Then in section 5.6, the same test has been applied to the neutron angular distribution and an improvement of the description around $\cos\theta_n^{CM} = 0$ has been found.

In this section, we will correlate the invariant mass and neutron angular distributions and compare the simulation with an additional non-resonant contribution to the mass spectra by slices in neutron angles. In this context, we can check if a bigger sensitivity to a non-resonant contribution can be found.

The shape of the (n, π^+) invariant mass distribution is in fact not very much affected, even around $\cos\theta_n^{CM} = 0$. As already stressed, the (p, π^+) invariant mass distribution of this non-resonant contribution is very broad with a peak around 1.45 GeV/c^2, due to acceptance. This remains true at any neutron angle. The phase-space contribution therefore enhances the yield for high invariant mass.

One has to mention, that non-resonant contributions can deviate from phase-space. For example, the emission of pions from the graphs involving only nucleons can be described in OBE model. In addition the interference effects with the resonant contribution can also come into play.

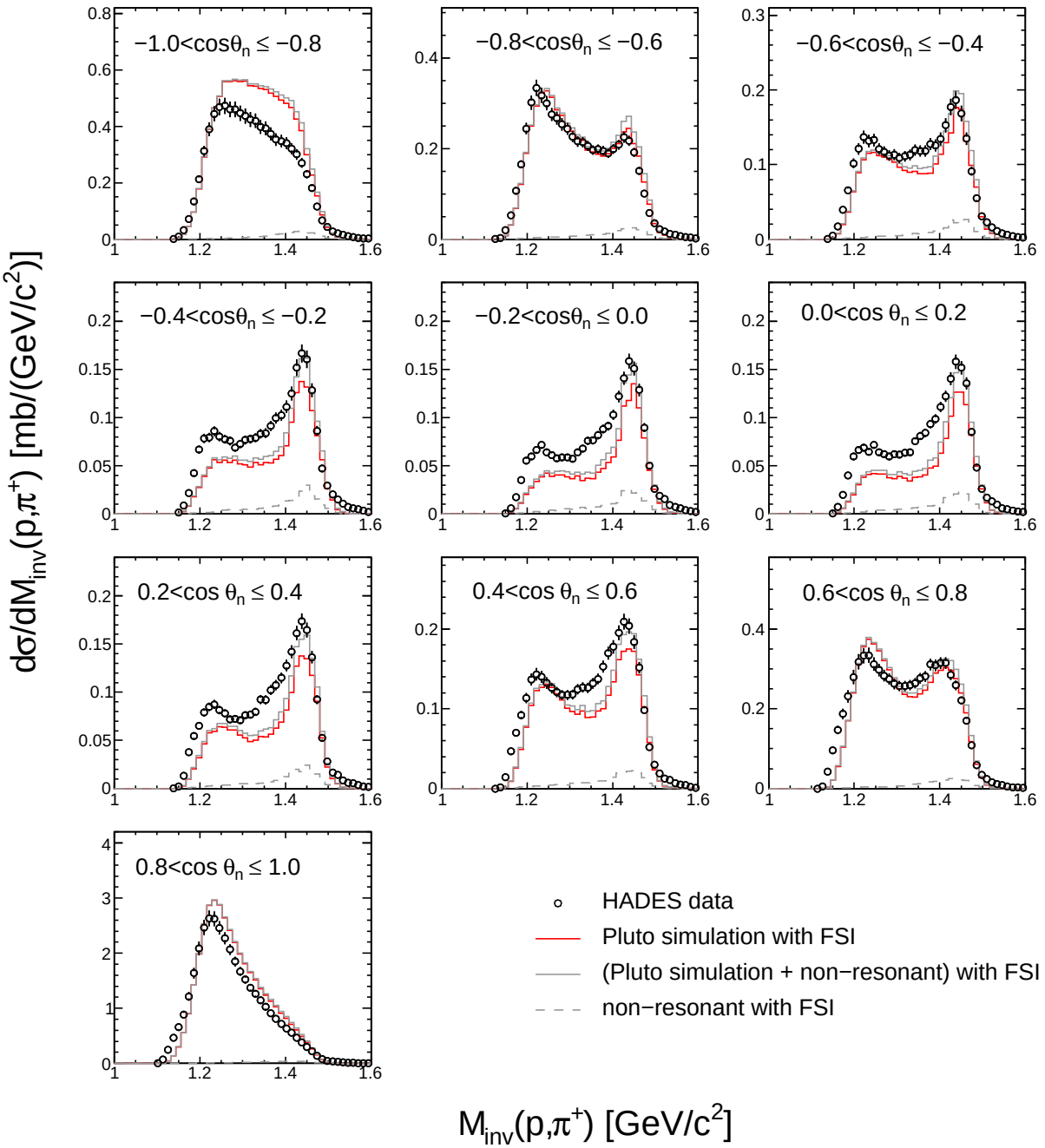

FIG. 5.15 – (p, π^+) invariant mass distributions in slices of $\cos\theta_n^{\mathrm{CM}}$ compared to standard Pluto simulation (red solid line) and the simulation with additional non-resonant contribution (grey solid line). The added non-resonant contributions is presented by grey dashed line.

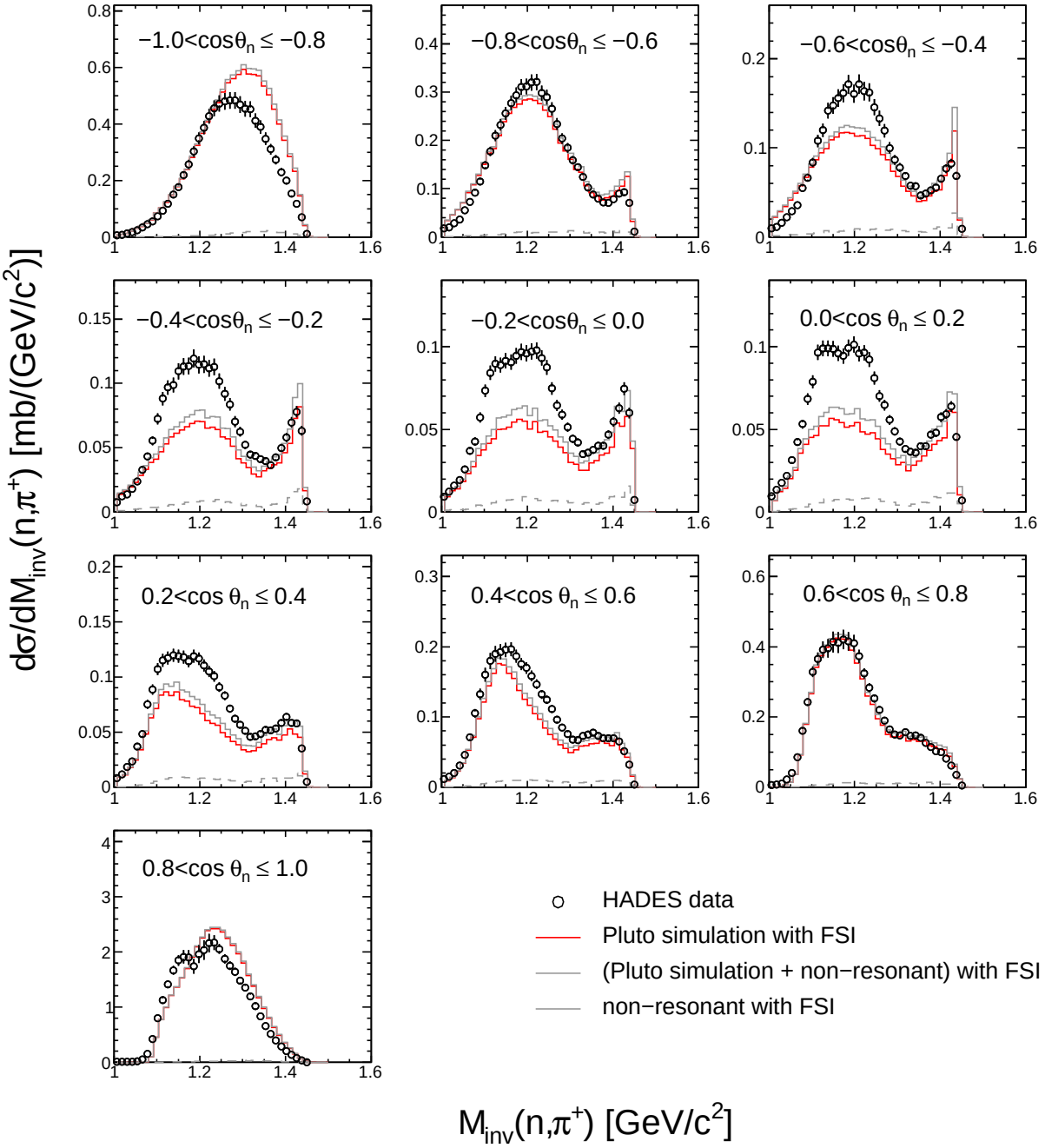

FIG. 5.16 – (n, π^+) invariant mass distributions in slices of $\cos\theta_n^{\mathrm{CM}}$ compared to standard Pluto simulation (red solid line) and the simulation with additional non-resonant contribution (grey solid line). The added non-resonant contributions is presented by grey dashed line.

5.7.4 Sensitivity to the cut-off parameter Λ_π

In section 5.6, we have adjusted the cut-off parameter Λ_π to the value 0.75 GeV to describe better the neutron angular distribution, while keeping the total cross section constant. Now the simulation with this new parametrization (green line) is checked for the differential mass spectra for both (p, π^+) (fig. 5.17) and (n, π^+) (fig. 5.18) where a more strict constraint is expected.

The better description of the yields as a function of $\cos\theta_n^{CM}$ is due to the smoother neutron angular distribution with $\Lambda_\pi = 0.75$ GeV, which is expected from fig. 5.10. Because of the acceptance effect, there is also a change of the shapes, more precisely a relative enhancement of low invariant masses. A good agreement is now reached around $\cos\theta_n^{CM} = 0$, both at the level of the yields and of the shapes.

As a conclusion, in general, the $\Lambda_\pi = 0.75$ GeV gives a pretty good improvement to the model not only for the global neutron angular distribution, but also for the differential $N\pi$ mass spectra. Nevertheless, some discrepancies e.g. in slices of $0.4 < |\cos\theta_n^{CM}| < 0.6$ can still be found. For these bins, the modified model yields a too much pronounced peak at lower invariant masses.

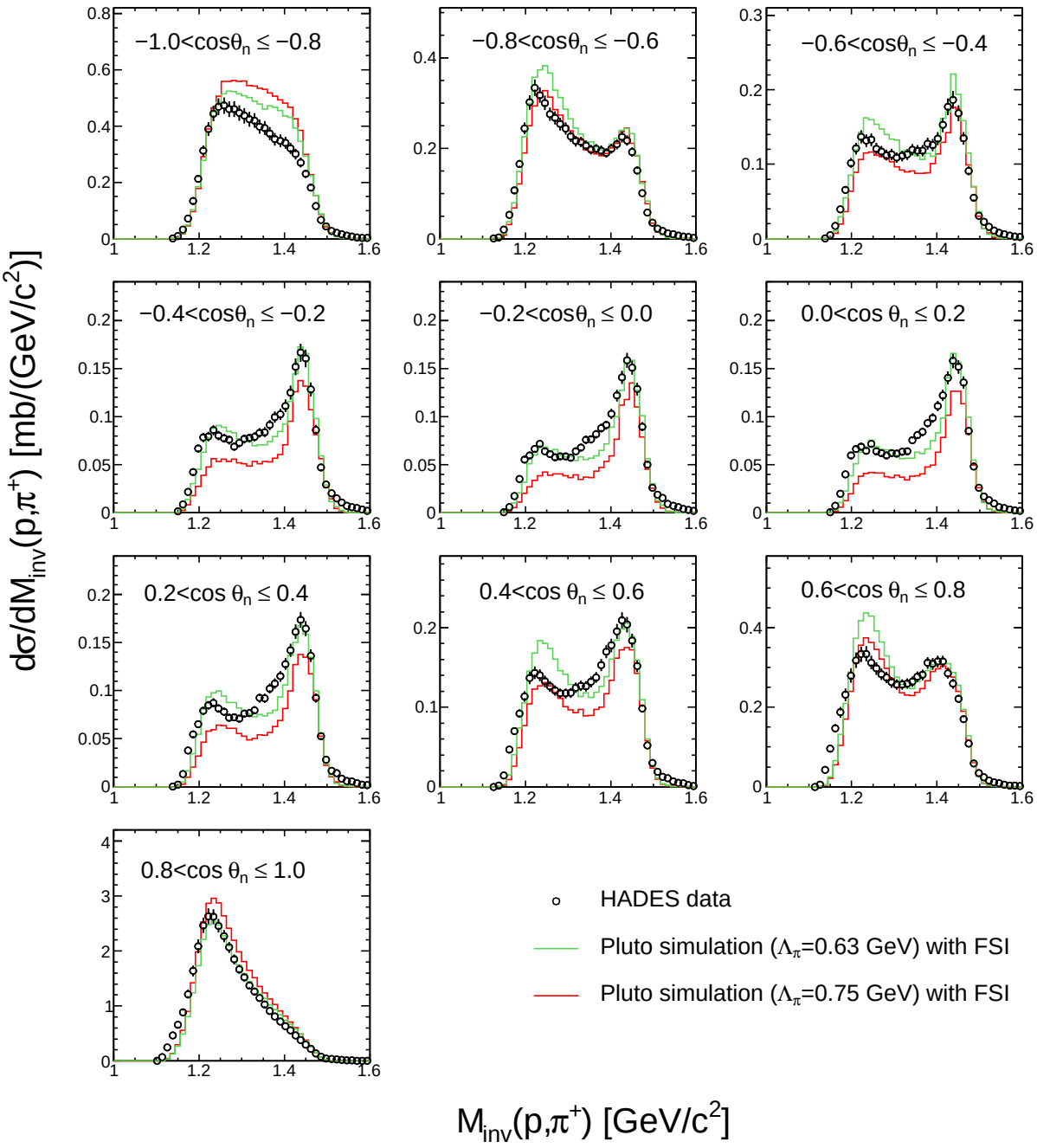

FIG. 5.17 – (p, π^+) invariant mass distributions in slices of $\cos\theta_n^{\mathrm{CM}}$ compared to Pluto simulations with FSI effect and different cut-off parameters. The simulation based on the standard resonance model with FSI and $\Lambda_\pi = 0.63$ GeV (red) and simulation with FSI and $\Lambda_\pi = 0.75$ GeV (green).

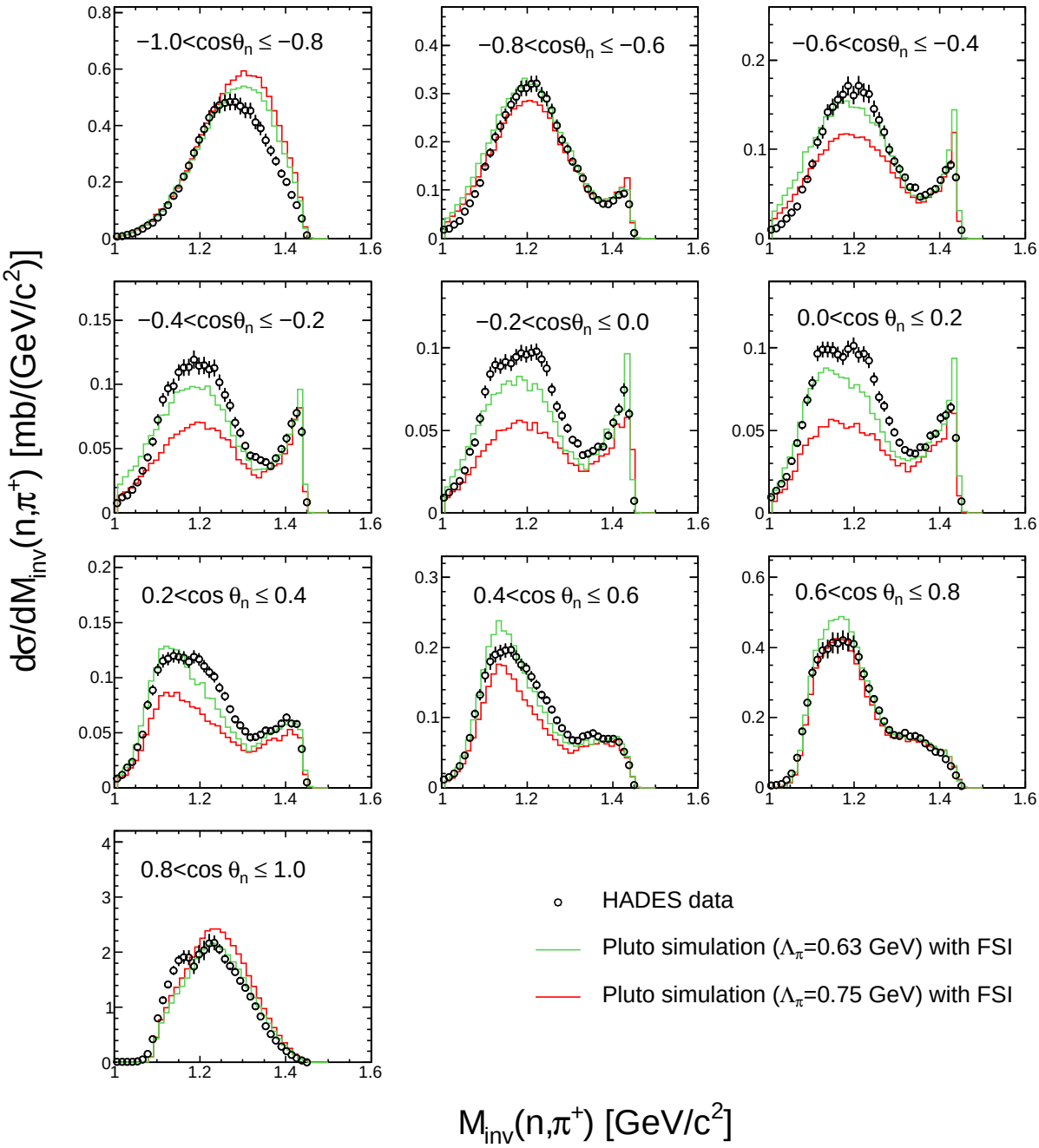

FIG. 5.18 – (n, π^+) invariant mass distributions in slices of $\cos\theta_n^{\mathrm{CM}}$ compared to Pluto simulations with FSI effect and different cut-off parameters. The simulation based on the standard resonance model with FSI and $\Lambda_\pi = 0.63$ GeV (red) and simulation with FSI and $\Lambda_\pi = 0.75$ GeV (green).

5.7.5 Conclusion for the tests with the differential $N\pi$ invariant mass distribution

From the investigations performed with the differential $N\pi$ invariant mass distributions, the conclusions drawn from the integral spectra are confirmed.

The FSI is clearly observed and our simple calculation is able to improve the description of the data. However, it should be taken into account at the level of the amplitudes.

The sensitivity to Δ^+, N^* and a non-resonant contribution is indeed small. The change of shape of the invariant mass spectrum (visible both for the spectra in the $\cos\theta_n^{CM}$ slices and for the integrated spectrum) shows the sensitivity of the measured invariant mass distribution to the details of the production model, which makes even more delicate the control of the $N^*(1440)$ or non-resonant amplitudes. However it seems that these contributions can not be larger than 0.4 mb. Last but not least, it is important to point out that any conclusion drawn from the $pp \to np\pi^+$ spectra should be always simultaneously validated by the $pp \to pp\pi^0$ channel.

This study also confirms that the lack of events around $\cos\theta_n^{CM} = 0$ seems to be related to a too small Δ production angular distribution in the simulation rather than non-resonant contributions or stronger interference effects. It has however to be stressed that these conclusions are drawn from a very crude model and would have to be checked in a full calculation with all amplitudes taken into account in a consistent way.

5.8 Δ decay angular distribution

In $pp \rightarrow np\pi^+$ reactions, the π^+ angular distribution in the (p, π^+) reference frame can be used to study the Δ decay angular distribution, with the z-axis taken as the direction of (p, π^+) pair in lab. system (see section 3.2.4).

Following this, the π^+ angular distribution has been reconstructed and is shown as black dots on fig. 5.19 (left panel). The forward and backward π^+ are strongly cut by the HADES acceptance.

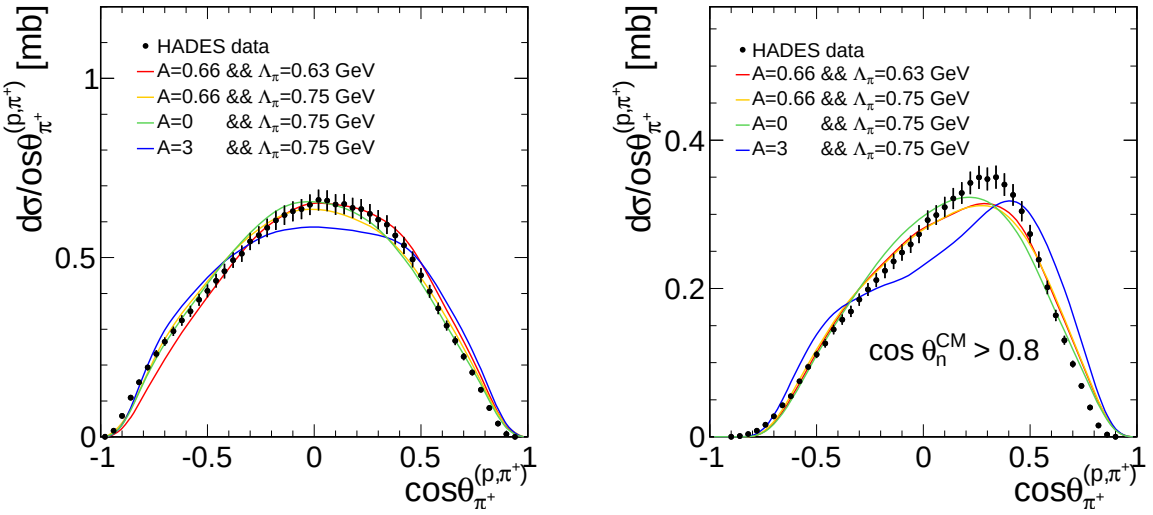

FIG. 5.19 – π^+ angular distribution in the (p, π^+) reference frame in $pp \rightarrow np\pi^+$ reactions in HADES acceptance. Different Δ decay angular distributions are implemented in the form of $1 + A\cos^2\theta$. Blue : pure OPEM $A = 3$, red : Wicklund's parametrization $A = 0.66$ and green : isotropic decay : $A = 0$. The orange one is based on the Wicklund's parametrization and uses $\Lambda_\pi = 0.75$. **Left :** integrated over $\cos\theta_n^{CM}$ range and **Right :** in the region where $\cos\theta_n^{CM} > 0.8$.

The data are first compared to the standard Pluto simulation with Wicklund's Δ decay angular distribution (red curve). As we are here discussing the shapes of the angular distribution, the simulation is normalized to the same total yield as the data. The agreement is reasonable.

The sensitivity of this distribution to the Δ production angular distribution is also investigated by comparing the results of the Pluto simulations using either the standard one-pion exchange cut-off parameter from Dmitriev $\Lambda_\pi = 0.63$ GeV (red) or a larger one $\Lambda_\pi = 0.75$ GeV (yellow) which better fits our neutron angular distribution (see section 5.6). The change of the distribution is small but still visible.

Then we have tested the sensitivity to different decay models using the Λ_π value 0.75 GeV which gives better agreement for the neutron angular distribution. The simulation with $A = 3$ (blue) clearly does not reproduce the data, a so strong anisotropy of the Δ decay can therefore be excluded from our data. Both the $A = 0.66$ (yellow) and the $A = 0$ (green) Δ decay give a fairly good agreement with this π angular distribution.

To increase the sensitivity to the Δ decay angular distribution, a supplementary condition $\cos\theta_n^{CM} > 0.8$ is imposed. As mentioned in section 3.2, in this condition, the direction of the

(p, π^+) system in the lab is close to the momentum transfer in the $N-\Delta$ transition, which favors the Δ^{++} excitation from the target. Therefore the sensitivity to the decay models is expected to be the strongest (see fig. 3.3).

From fig. 5.19 (right panel), we see that the sensitivity is indeed stronger in the simulation, and again the simulation with anisotropy (A=3) is clearly in disagreement with the data. Note that no dependence on Λ_π is observed, because in a small slice of neutron angle the dependence on Δ production angular distribution is negligible. But the agreement with the data becomes also worse than when integrated over $\cos\theta_n$ for the two other models. This is not fully satisfactory and shows the limit of our simple model.

One could conclude from this study that our data are compatible on average with a small anisotropy of the Δ decay $0 < A < 0.85$. Due to the limited HADES acceptance, the anisotropy parameter cannot be extracted more precisely than in the previous experiments, like for example in [Bacon et al., 1967], [Wicklund et al., 1987]. We can mention meanwhile that the isotropic decay angular distribution used in transport models is still a reasonable hypothesis.

Simulation type	**Acceptance** [%]	**σ in acceptance [mb]**
Pluto + ($\Lambda_\pi = 0.63$ GeV) + (A=0.66) (standard)	5.26	1.01 ± 0.10
Pluto + FSI + ($\Lambda_\pi = 0.63$ GeV) + (A=0.66)	5.33	1.03 ± 0.10
Pluto + FSI + ($\Lambda_\pi = 0.63$ GeV) + (A=0)	5.84	1.12 ± 0.11
Pluto + FSI + ($\Lambda_\pi = 0.63$ GeV) + (A=3)	4.45	0.86 ± 0.09
Pluto + FSI + ($\Lambda_\pi = 0.75$ GeV) + (A=0.66)	5.15	0.99 ± 0.10
Pluto + FSI + ($\Lambda_\pi = 0.75$ GeV) + (A=0)	5.60	1.08 ± 0.11
Pluto + FSI + ($\Lambda_\pi = 0.75$ GeV) + (A=3)	4.38	0.84 ± 0.08
HADES Data		**0.91 ± 0.07**

TAB. 5.1 – Global HADES acceptance for the $pp \to np\pi^+$ channel data at 1.25 GeV with different simulation parametrization and corresponding cross sections in the HADES acceptance using the total cross section $\sigma_{pp\to np\pi^+} = 19.24 \pm 1.92$ mb in 4π from Teis.

We now assume that the $pp \to np\pi^+$ cross section given by Teis is a good fit of the previous experimental data and has a precision of 10%. The yield in the HADES acceptance will vary depending on the models, as shown in table 5.1. One can see that the simulations with $A = 0$ (3^{rd} line and 6^{th} line) give a yield which is higher by 20% than the HADES data. So, one can consider that this extreme case is less favored.

Table 5.1 also shows the sensitivity of the acceptance to different models we have discussed before. This will be used to estimate the systematical errors on the acceptance correction (see section 5.9).

As a conclusion, using the cross sections measured in other experiments and taking into account both the shapes of the π^+ angular distributions and the yields measured in the HADES acceptance, we confirm the anisotropy of the Δ decay angular distribution of the order of 0.6. This anisotropy has already been implemented in the Pluto event generator and could also be implemented in transport models.

One should however stress that this anisotropy is just a parameter in the two-step model,

where production and decay of the Δ resonance are treated independently. This is a very crude approximation that is needed in transport models aiming at describing heavy-ion collisions. This anisotropy is related to the spin structure of the $N - \Delta$ excitation. In a full calculation of the nucleon-nucleon collision, the π angular distribution would come out naturally. Here we would like to stress again the need to compare the data to a full model calculation with all interference effects.

5.9 Acceptance correction for invariant masses and neutron angular distributions

In order to have physical spectra which are independent from the experimental set-up, it is useful to provide acceptance corrected distributions. This implies an extrapolation into the regions of phase space which are not covered by the detector. The problem is that this extrapolation requires the use of a model.

In our analysis, a pretty accurate acceptance correction procedure has been developed. The principle of this correction is explained in section. 4.6. The improved Pluto simulation (noted as new Pluto simulation) based on the resonance model with one-π exchange assumption is used here for acceptance correction :

- the production of Δ^{++}, Δ^{+} and N^* is included with cross sections 17.0 mb, 1.9 mb and 0.34 mb, respectively ;
- the cut-off parameter is set to $\Lambda_\pi = 0.75$ GeV for Δ production ;
- the decay anisotropy of the Δ is taken in the form of $1 + 0.66 \cdot \cos^2\theta$;
- proton-neutron FSI is implemented.

We will show in the following the neutron angular distribution and (p, π^+) invariant mass distribution corrected for acceptance and evaluate the related systematical errors.

5.9.1 Neutron angular distribution in 4π

For the neutron angular distribution in the center-of-mass system, a one-dimensional correction is considered as a first step. Following equation 4.14, the correction factor is calculated as the ratio of the simulated yields in 4π and in HADES for a given $\cos\theta_n^{CM}$ (left panel of fig. 5.20).

The bin size is optimized mainly according to the variation of the detector acceptance. In the forward neutron angle region, the bin size can be kept small in order to have precise spectra. In the backward neutron angle region, the bin size is set to be larger to keep a sufficiently precise correction.

The correction factor is about 25 on average. The smaller values down to below 10 are found for forward neutron angles, while a quite big value of 55 is obtained at very backward angles (due to the low acceptance in this region). The distribution of correction factors is rather smooth in the region $-0.8 < \cos\theta_n^{CM} < 1$. But they vary rapidly in the first two bins ($\cos\theta_n^{CM} < -0.8$).

The one-dimensional corrected $\cos\theta_n^{CM}$ spectrum is shown in fig 5.21 by blue triangles. By doing the acceptance correction, a very forward and backward peaked distribution is recovered. It is found to be almost symmetric with respect to $\cos\theta_n^{CM} = 0$. This is an important result which proves that the acceptance correction is well under control.

However, the validity of this acceptance correction depends on the validity of the distributions for variables other than the neutron angle. The main dependence is considered for two variables : the invariant mass distribution and Δ decay angular distribution.

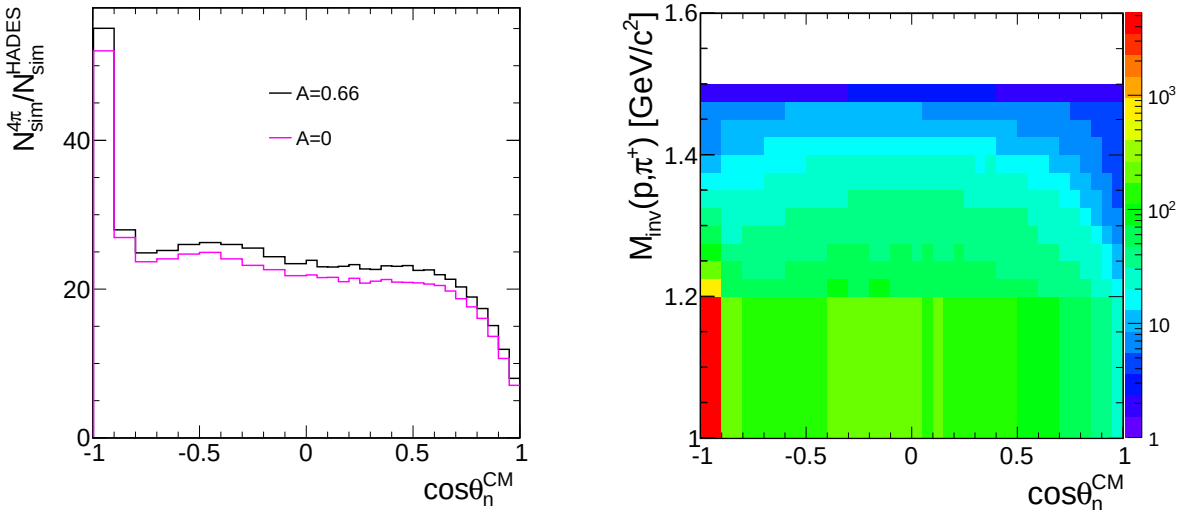

FIG. 5.20 – Acceptance correction factor deduced from the simulation and used for the center-of-mass neutron angular distribution correction. **Left :** One-dimensional correction factor calculated in $\cos\theta_n^{CM}$ bins and **Right :** Two-dimensional correction factor calculated in ($\cos\theta_n^{CM}$, $M_{\rm inv}(p,\pi^+)$ bins.

To reduce the model dependence on the (p,π^+) mass distribution, a two-dimensional acceptance correction has been performed as a second step. The correction factor is calculated in the same way as for the one-dimensional case, as a ratio of simulated yield in 4π and in HADES for a given $\cos\theta_n^{CM}$ bin and $M_{\rm inv}(p,\pi^+)$ bin (see right panel of fig. 5.20). Then the new factors are applied to correct the data. The bin width in $\cos\theta_n^{CM}$ is kept the same as in the one-dimensional case and for $M_{\rm inv}(p,\pi^+)$ the bin width is again adjusted to optimize the precision of the correction.

The black dots in fig. 5.21 represent the final neutron angular distribution in the center-of-mass frame in 4π after applying two-dimensional corrections. These results are consistent with the ones obtained with the one-dimensional correction (blue triangles). The two-dimensional correction reduces the model dependence of the correction due to the averaging over the (p,π^+) invariant mass distribution, but as the model reproduces rather well the mass distribution, the effect is small.

With the two-dimensional correction, the symmetry of the angular distribution is also better recovered. We take the two-dimensional corrected spectrum as the final spectrum. The corresponding errors are estimated as following and are summarized in table 5.2.

- First, the errors on the data measured in the HADES acceptance (see section 4.7) have to be scaled by the acceptance factor.
- Then, we consider the error due to the precision of the acceptance factors, due for example to possible dead zones at the edges of the detector. Following the variation of the acceptance factors as a function of $\cos\theta_n^{CM}$ (see fig. 5.20 left), we estimate the relative error on the acceptance correction factor to be 10% for the first bin ($\cos\theta_n^{CM} < -0.8$), 5% for the

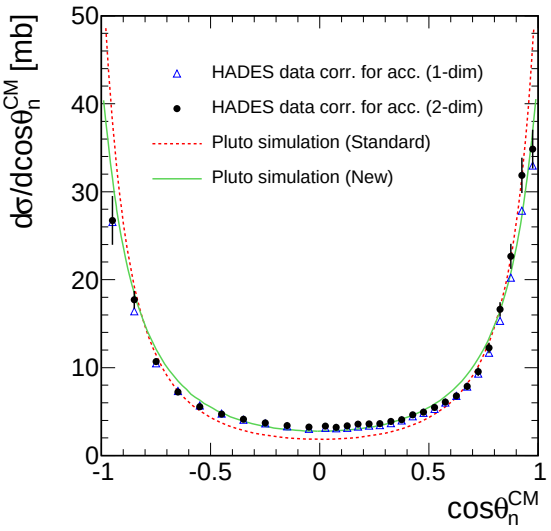

FIG. 5.21 – Angular distribution of the neutron in the center of mass system after acceptance correction. Data corrected with one-dimensional (blue triangles) and two-dimensional (black dots) factors compare to the standard Pluto simulation (red dashed line) and the new adjusted Pluto simulation (green solid line).

second bin ($-0.8 < \cos\theta_n^{CM} < 0.6$) and 2% for the other bins. These errors are included in the error bars in the spectrum of fig. 5.21 and are considered as independent from one bin to another. In addition, a 3% global error is estimated, which takes into account a global uncertainty on the correction, due to possible systematics effects independent on neutron angle.

– Last but not least, the error due to the Δ decay angular distribution is estimated using two different Δ decay anisotropies $A = 0.66$ and $A = 0$. Although $A = 0.66$ is favored by previous data and by our measured yield (see section 5.8), the different correction factors obtained for $A = 0$ can be used to estimate the maximum error due to the uncertainty in the Δ decay angular distribution. In practice, we calculate firstly the acceptance correction factor using both decay anisotropies $A = 0.66$ (black histogram fig. 5.20) and $A = 0$ (pink histogram). Secondly, we calculate for each bin the relative difference of the correction factors and smear the obtained values to obtain a smooth distribution. Thirdly, the smeared values are scaled by $1/\sqrt{3}$ assuming equal probabilities between $A = 0.66$ and the extreme case. Finally, we apply the smeared value as the systematic error related to the decay angular distribution for each corresponding bin in fig. 5.21. The dependence on decay anisotropy has also a global effect of 4.3%, which is taken into account for the errors on the total cross section.

The three types of systematic errors are added quadratically for each bin and the result is shown in fig. 5.21. The statistical errors are negligible.

From the acceptance corrected spectra, a less steep Δ production angular distribution is clearly observed in the data in comparison with the standard Pluto simulation. The distribution with larger cut-off parameter $\Lambda_\pi = 0.75$ GeV (green curve) gives a better description to the data which is fully consistent with our analysis done within the acceptance.

Source of systematic error	**Point to point error** [%]	**Global uncertainty** [%]
Measured data (in acceptance)	4.5 to 6	7.7
Acceptance correction factor	2 to 10	3
Model dependence (Δ decay)	2.7 to 6	4.3
Total	5 **to** 10.5	**9.3**

TAB. 5.2 – Systematic errors for the acceptance correction of $\cos\theta_n^{CM}$ in $pp \rightarrow np\pi^+$ reactions analysis.

5.9.2 (p, π^+) invariant mass in 4π

In the same way, the acceptance correction has been performed for the (p, π^+) invariant mass spectrum as well.

Instead of doing an average correction for a large bin, the choice is made to start the correction for invariant masses larger than 1.15 GeV/c^2 because no precise correction can be performed below 1.15 GeV/c^2 due to the very small acceptance. Again, the bin widths are adjusted according to the detector acceptance but in a slightly different way to obtain a precise shape of the invariant mass spectrum. The correction factor decreases as a function of the (p, π^+) invariant mass (see fig. 5.22). In the region of $1.5 < M_{\text{inv}}(p, \pi^+) < 1.6$ GeV/c^2, the acceptance is zero, but a few counts exist in the data due to the resolution effect. So the correction in this region is done using the correction factor of the closest bin [1.475, 1.5 GeV/c^2] and an average yield is calculated for the mass range [1.475, 1.5 GeV/c^2]. In addition,

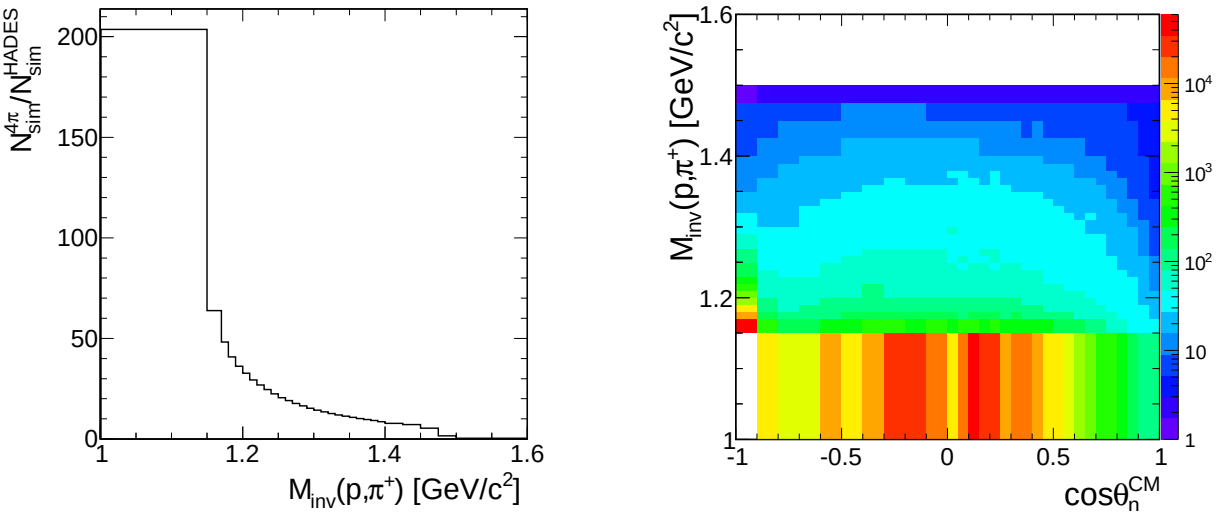

FIG. 5.22 – Correction factor for the (p, π^+) invariant mass distribution. **Left :** One-dimensional correction factor calculated in $M_{\text{inv}}(p, \pi^+)$ bin by simulation and **Right :** Two-dimensional correction factor calculated by simulation in $(\cos\theta_n^{CM}, M_{\text{inv}}(p, \pi^+))$ bin.

Fig. 5.23 shows the acceptance corrected $M_{\text{inv}}(p, \pi^+)$ spectrum compared to the simulation. The spectrum corrected with the two-dimensional factor results in a slightly higher yield with respect to the one-dimensional corrected one, but the results are still consistent. As for the neutron angular distribution, we consider the spectrum obtained with two-dimension factors as the final spectrum and estimate error bars. The procedure is very similar to the one for $\cos\theta_n^{CM}$

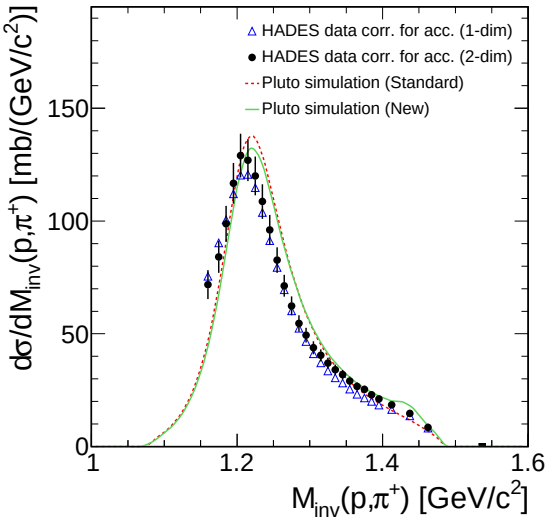

FIG. 5.23 – The (p, π^+) invariant mass distribution in 4π. Data corrected with one-dimensional (blue triangles) and two-dimensional (black dots) factors compared to Pluto simulations : standard (red dashed line) and new (green solid line).

distribution and the errors are summarized in table 5.3.

The systematical error due to the variation of correction factor as a function of invariant mass is estimated to be 4% for the first bin ($1.15 < M_{\text{inv}}(p, \pi^+) < 1.17$ GeV/c^2) and 2% for the other bins. The related global error (independent of invariant mass) is estimated to be 2%. The uncertainty on correction factors depending on the Δ decay models is set constantly to be 4.3% along $M_{\text{inv}}(p, \pi^+)$, since we found that the influence from changing the decay anisotropy is only a scaling of the Δ mass distribution.

Source of systematic error	**Point to point error** [%]	**Global uncertainty** [%]
Measured data (in acceptance)	4.5 to 12	7.7
Acceptance correction factor	2 to 4	2
Model dependence (Δ decay)	4.3	4.3
Extrapolation	—	3
Total	6 to 15	**9.5**

TAB. 5.3 – Systematical errors for the acceptance correction of $M_{\text{inv}}(p, \pi^+)$ in $pp \rightarrow np\pi^+$ reactions analysis.

The measured $M_{\text{inv}}(p, \pi^+)$ peak is shifted by 10 MeV/c^2 towards low masses in comparison with the simulation. The origin of this shift is unknown. The energy calibration can be checked within 2-3 MeV using the missing mass spectrum at the neutron mass. The simulated distribution is also slightly broader than the measured one. The tail of mass distribution on the right hand side goes further in the case of data. This is consistent with the result in the HADES acceptance (fig 5.2) and shows that the resolution effect is not fully reproduced in the simulation. One can also notice that the main effect of the change in the Pluto simulation is a small bump at high (p, π^+) invariant masses due to the FSI.

5.10 Cross section of the $pp \rightarrow np\pi^+$ reaction at 1.25 GeV

The total cross section of the $pp \rightarrow np\pi^+$ reaction at 1.25 GeV has been extracted from our data. The principle to obtain this value is to correct the measured cross section for acceptance using the simulation.

As mentioned in section 4.6, two kinds of methods have been used in our analysis :
- Using the global acceptance factor ;
- Integrating the acceptance corrected spectrum.

The first method, i.e. using the global acceptance factor, is applied by assuming that the average acceptance for the measured data can be deduced from the simulation. So the measured total cross section can be calculated by dividing the measured cross section in the acceptance by the global factor. From table 5.1, one can see that these global factors depend significantly on the model. We use here the new Pluto simulation which gives the best description of the data and we obtain a total cross section of the $pp \rightarrow np\pi^+$ reaction at 1.25 GeV of $\sigma = 17.67$ mb.

The second method is based on the acceptance corrected spectra mentioned in section 5.9. The total cross section value extracted using this method is considered to be more realistic because the dependence on models is reduced with respect to the first method. The acceptance correction is done for the neutron angular distribution and for the (p, π^+) invariant mass distribution. One can extract the total cross section from these two spectra.

In the case of the neutron angular distribution in the center-of-mass system, the correction is achieved for all the bins, thus the total cross section can be extracted by a simple integration. The systematic errors can be found in table 5.2.

In the case of the (p, π^+) invariant mass distribution, a precise correction can not be made in some bins where the acceptance is very low ($M_{\text{inv}}(p, \pi^+) < 1.15\text{GeV}/c^2$). As a consequence, an extrapolation has to be done using the simulation in this region. We estimate the related error by varying a little bit the limits of the region in which we apply the extrapolation. It results in 3% uncertainty for the total cross section, as indicated in table 5.3.

In table 5.4 we summarize the different values of the total cross section that can be deduced from the HADES measurements for $pp \rightarrow np\pi^+$ reactions at 1.25 GeV. Consistent values can be found for all correction procedures within error. The final value $\sigma = 18.17 \pm 1.85$ mb is obtained using the average value deduced from the integration of $\cos\theta_n^{CM}$ and $M_{\text{inv}}(p, \pi^+)$ spectra and taking the maximum error.

Acceptance correction method	σ_{Total} **[mb]**
Global Correction	17.30
$\cos\theta_n^{CM}$ (1-dim)	17.53
$\cos\theta_n^{CM}$ (2-dim)	18.32 $\pm$ 1.70
$M_{\text{inv}}(p, \pi^+)$ (1-dim)	17.27
$M_{\text{inv}}(p, \pi^+)$ (2-dim)	18.02 $\pm$ 1.71

TAB. 5.4 – Total cross section of the $pp \rightarrow np\pi^+$ reaction measured by HADES at 1.25 GeV. The values are obtained with different correction procedures and the errors are only put for the significant cross section values.

5.11 Systematic comparisons of one-π channels in $p+p$ runs at 1.25 and 2.2 GeV

A systematic study of exclusive one-pion production at 1.25 and 2.2 GeV for both isopin channels $pp \to pp\pi^0$ and $pp \to np\pi^+$ has been realized by the HADES collaboration [Ramstein et al., 2010]. These data analyses were mainly performed by the Krakow and Orsay teams in HADES collaboration. In the following, a global comparison of the Dalitz distribution and $N\pi$ invariant mass will be shown. The data analysis for 2.2 GeV was performed by Marcin Wiśniowski [Wiśniowski, 2009] and the analysis at 1.25 GeV is done by Anna Kozuch for the $pp \to pp\pi^0$ channel and myself for the $pp \to np\pi^+$ channel.

5.11.1 Dalitz plots

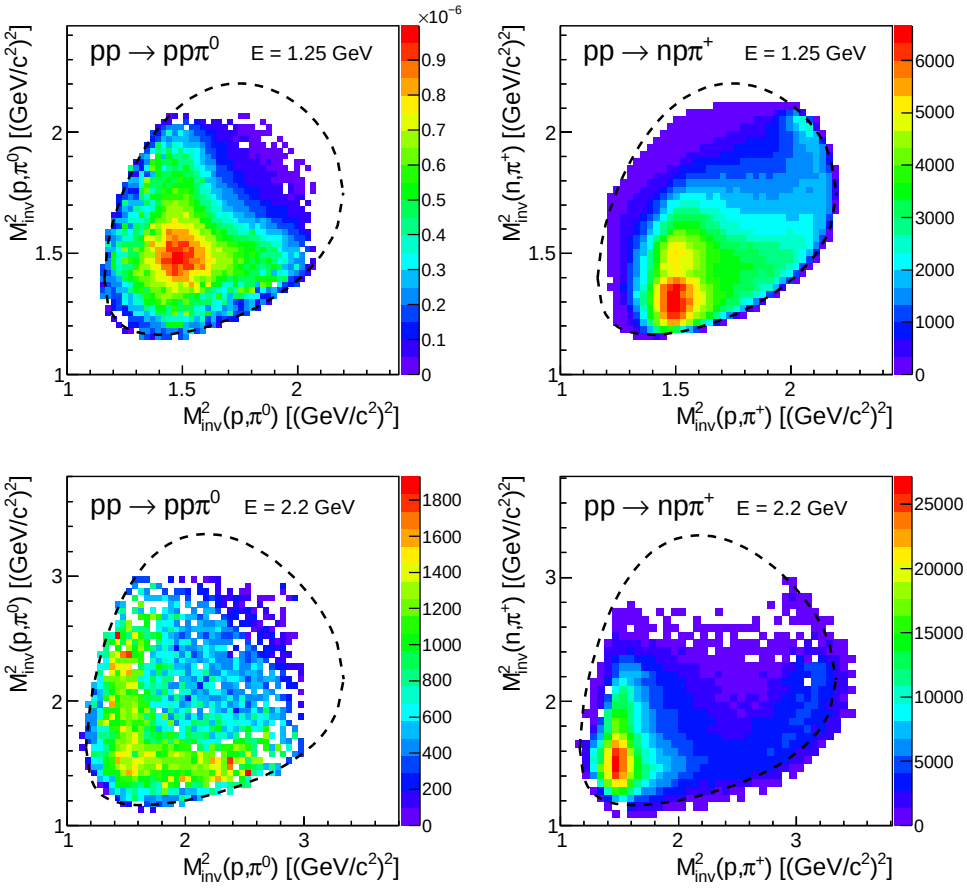

FIG. 5.24 – Dalitz plots of the $pp \to pp\pi^0$ and $pp \to np\pi^+$ reactions. The kinematical limit for the $pp \to NN\pi$ reaction is shown as a dashed line.

The Dalitz plots which allow to investigate the resonant behavior of the pion production are shown in fig. 5.24. For the $pp\pi^0$ channel, an accumulation of yield for $M^2_{\text{inv}}(p,\pi^0) = 1.5(\text{GeV}/c^2)^2$, corresponding to the excitation of the Δ^+ resonance can be clearly seen at both energies. For the $np\pi^+$ channel, the Δ^{++} signal stands out markedly at $M^2_{\text{inv}}(p,\pi^+) = 1.5(\text{GeV}/c^2)^2$, while the Δ^+ signal located at $M^2_{\text{inv}}(n,\pi^+) = 1.5(\text{GeV}/c^2)^2$ is less pronounced. The FSI is observed as a spot appearing for $M^2_{\text{inv}}(p,\pi^+)$ and $M^2_{\text{inv}}(n,\pi^+)$ at $2(\text{GeV}/c^2)^2$ in the $np\pi^+$ channel (for details see section 5.3). This effect is absent in the same channel at 2.2 GeV due to the forward

peaking of these events at angles below the acceptance limit and in the $pp\pi^0$ channel due to the trigger configuration, requiring two charged particles detected in opposite sectors of the HADES detector. Note that, in contrast to fig. 5.1, on these Dalitz plots the yields outside of the Dalitz boundary are not shown.

5.11.2 $N\pi$ invariant mass distributions

The projection on the (p, π^0) and (n, π^+) invariant masses and a comparison to a standard Pluto simulation are exhibited in fig. 5.25. The error bars include statistical and systematical errors which are mainly due to event selection. The trigger efficiency correction is also contributing to the systematical errors in the case of the $pp \rightarrow np\pi^+$ channel at 1.25 GeV as discussed in detail in section 4.3. This correction is however not needed for the other channels, since in this case, always at least one of the two charged particles is hitting the TOF detector. The uncertainty on the normalization to the pp elastic scattering is considered as a source of systematical error (6% for 1.25 GeV and 11% for 2.2 GeV) but not included in the error bars here. In general, both the yield and the shapes of the invariant mass distribution are consistent with the cocktail from the resonance model. At 1.25 GeV, the relation $\sigma_{pp\rightarrow np\pi^+} = 5 \cdot \sigma_{pp\rightarrow pp\pi^0}$ is found, as expected from the dominance of the Δ resonance and the isospin factors in different Δ decay channels. At 2.2 GeV, this ratio is lower, about 3.5 due to the contribution of N^* resonances. The higher lying resonances, like $N^*(1440)$ and $N^*(1520)$, also play a significant role at 2.2 GeV.

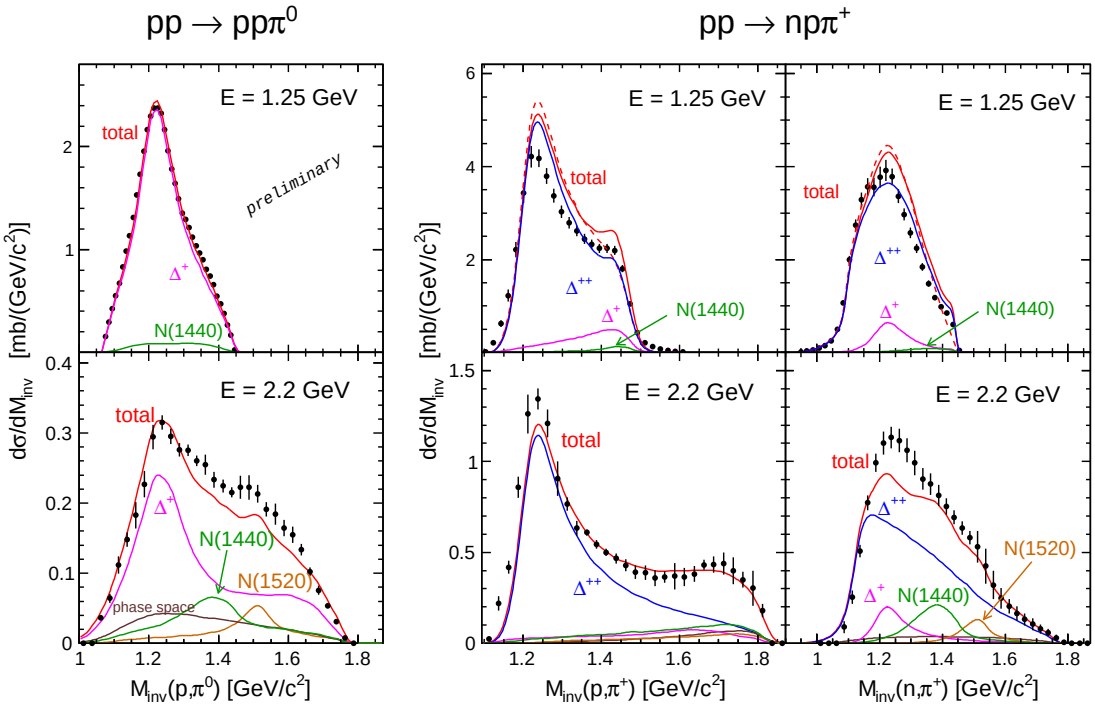

FIG. 5.25 – $N\pi$ invariant masses measured in $pp \rightarrow pp\pi^0$ and $pp \rightarrow np\pi^+$ reactions at 1.25 and 2.2 GeV. HADES data (black dots) are compared on an absolute scale to the predictions from the resonance model, with following contributions : $\Delta^+(1232)$ (pink), $\Delta^{++}(1232)$ (blue), $N^*(1440)$ (green), $N^*(1520)$ (light brown), $\Delta(1600)$ (light green) and an additional small phase space contribution (dark brown). The FSI effects are not included in the simulation, except for the $pp \rightarrow np\pi^+$ reactions at 1.25 GeV/c, the dashed lines showing the simulation without FSI effects.

5.11.3 HADES "homemade" cross section systematics for exclusive π^+ and π^0 production in $p+p$ reactions

The cross sections of the two one-pion production channels $pp \rightarrow np\pi^+$ and $pp \rightarrow pp\pi^0$ are obtained by extrapolating the yield to the 4π acceptance using the simulation, or, when possible, by integrating the acceptance corrected distributions (the case of the $np\pi^+$ channel at 1.25 GeV in section 5.9 and 5.10).

The results are shown in fig. 5.26 together with existing data and with the resonance model fits from Teis [Teis et al., 1997]. These plots are in fact a "homemade" systematics. We made the following changes with respect to the Teis systematics :

- We added the Shimizu points, [Shimizu et al., 1982] which were not included in the Teis systematics. Some details of the experiments corresponding to these data were introduced in section 1.5.1.
- We added a LAMPF point for $pp \rightarrow np\pi^+$ at 0.8 GeV [Hudomalj-Gabitzsch et al., 1978], although it has a quite large error bar.
- We added the newest HADES measurements.

It is worth mentioning that no cross section value is available for the WASA measurement at the moment.

A global agreement of the HADES data with the resonance model and with the previous data is observed. Especially, our $pp \rightarrow np\pi^+$ cross section at 1.25 GeV is in full agreement with the Shimizu results.

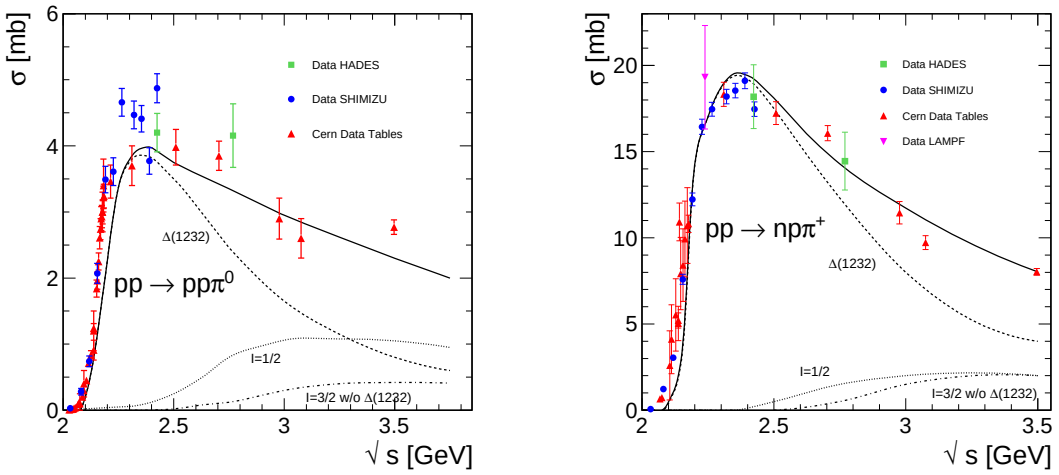

FIG. 5.26 – Total cross section as a function of the center-of-mass energy $\sqrt{s}$ for the **left :** $pp \rightarrow pp\pi^0$ and **right :** $pp \rightarrow np\pi^+$ reactions measured with HADES (green squares) compared to existing measurements (blue dots and red triangles). The lines show the resonance model fit with different contributions ($\Delta(1232)$), I=1/2 and other I=3/2.

Other distributions, such as neutron and π angular distribution have also been extracted in all of these channels. All results obtained at 2.2 GeV can be found in the PhD thesis [Wiśniowski, 2009] and a paper which will describe the one pion and one eta production measurements in $p+p$ 1.25 and 2.2 GeV with HADES will be published in the near future.

5.12 The π^+ angular distribution in CM

In heavy-ion reactions, π angular distributions in the center-of-mass frame are studied to investigate the thermalization of the system. Isotropic angular distributions are expected in the case of a fully thermalized system, where the anisotropy of each individual collision is smeared. However we must also consider that in heavy-ions collisions, the angular distribution of pions (and other paticles) is influenced by collective effects (flow of nuclear matter) and by effects of shadowing by spectator matter of target and projectile. These effects depend in addition to the impact parameter.

As a reference to such studies, it is interesting to investigate the π angular distribution anisotropies in NN collisions and to check how well they are reproduced by the resonance model. These studies have been realized with the simulation in $pp \rightarrow np\pi^+$ reaction at 1.25 GeV, and the results will be shown in the following.

5.12.1 π^+ angular distribution in the center-of-mass system in $C+C$ reactions

The distribution of π^+ angle in the center-of-mass system (noted as $\theta^{CM}_{\pi^+}$) has been studied by the HADES collaboration in $C+C$ collisions at 1 and 2 A GeV [Agakichiev et al., 2009b]. In this symmetric collision system, the distribution can be fitted with the following expression :

$$\frac{dN}{d\cos\theta^{CM}_{\pi^+}} = A_1(1 + A_2\cos^2\theta^{CM}_{\pi^+}), \tag{5.3}$$

where the fit parameter A_2 characterizes the anisotropy of the angular distribution, and A_1 is the normalization factor.

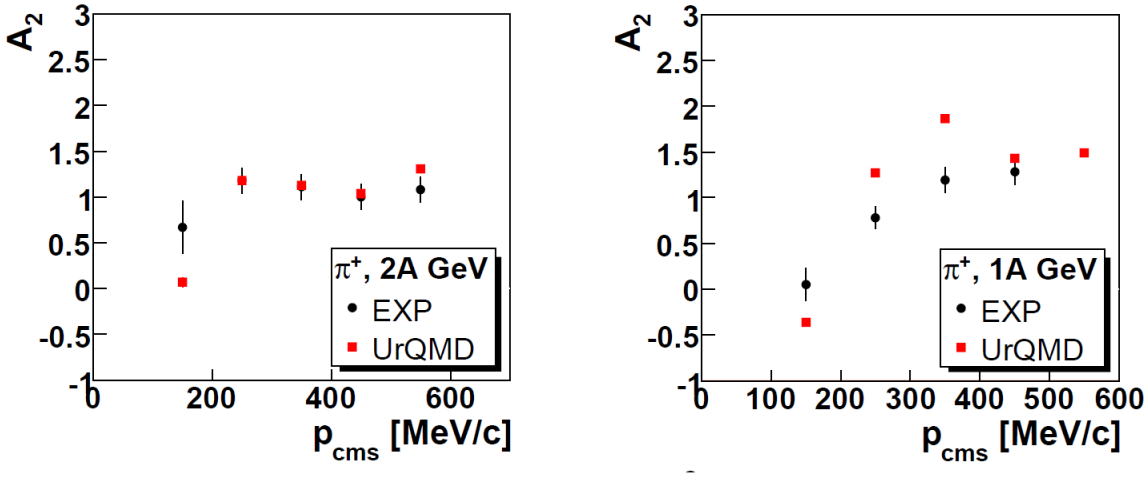

FIG. 5.27 – Dependence of the anisotropy parameter (A_2 in the figure) on the momentum in the center-of-mass system for π^+ produced in $C+C$ collisions at 1A GeV (**Right**) and 2A GeV (**Left**). Black dots with error bars are the results of the fits to the data, while squares exhibit the result from the fits to UrQMD simulations. Statistical errors on the UrQMD points are smaller than the symbol size. [Agakichiev et al., 2009b]

Fig. 5.27 shows the anisotropy parameter A_2 as a function of the pion momentum in the center-of-mass system extracted from the analysis of π^+ production in $C+C$ collisions at 1 and 2 A GeV with HADES. In these inclusive measurements, π angular distribution could be measured in center-of-mass for $|\cos\theta_\pi^{CM}| < 0.8$ at 1 A GeV and $|\cos\theta_\pi^{CM}| < 0.7$ at 2 A GeV. It was found that the anisotropy of π^+ production depends significantly on the π^+ center-of-mass momentum. It is close to 0 at low momenta, but increases with momentum. This effect is qualitatively well reproduced by the UrQMD transport model (red squares) [Schmidt et al., 2009]. As we know, the main process for π production in the 1-2 A GeV range is the decay of the Δ resonance. The anisotropy at low momenta is therefore interpreted as a remnant of the characteristic forward and backward peaking of the Δ production in inelastic NN scattering which is indeed observed in our data in $p+p$ reaction (see fig. 5.21).

It would be interesting to perform the same study, i.e. analyse the π^+ angular distribution in the center-of-mass system in the $pp \rightarrow np\pi^+$ data, since they can in principle provide a reference for the heavy-ion reactions. To take into account the unexpected π^+ angle dependent inefficiency observed in the $np\pi^+$ data (see section 4.5) and the quite complicated angular versus momentum correlation, very accurate and careful error estimates are indispensable, which was unfortunately not possible within the time limit of this PhD work. Nevertheless, we have used the $pp \rightarrow np\pi^+$ simulation to check the interpretation from heavy-ion experiments, taking into account the anisotropy of the Δ resonance decay.

5.12.2 Investigations in simulations of $pp \rightarrow np\pi^+$ reactions at 1.25 GeV

The study is performed with the Pluto simulation in the $pp \rightarrow np\pi^+$ channel for different bins in center-of-mass momentum of π^+. In each bin, the distribution of the cosine of the π^+ angle in the $p+p$ center-of-mass system ($\cos\theta_{\pi^+}^{CM}$) is plotted in full solid angle (see fig. 5.28).

To study the sensitivity to the Δ resonance production angular distribution, we first use an isotropic Δ decay angular distribution (green curve). The π^+ angular distribution in the center-of-mass is clearly forward/backward peaked for the highest pion momenta (panel (d)). So, in this case, it is clear that the very strong anisotropy of the Δ production results in an anisotropic π^+ angular distribution in the center-of-mass system. However, at low momenta, this is not the case and the π^+ angular distribution presents a more complex but in overall flatter shape. This can be explained quantitatively by the fact that the higher π^+ momenta in center-of-mass are obtained when the π^+ is emitted in a direction close to the Δ, while the direction is more smeared for lower π^+ momenta.

In the meantime, we have tested the sensitivity of $\theta_{\pi^+}^{CM}$ to the cut-off parameter Λ_π, since the missing neutron angular distribution is found to be better fitted using the Λ_π= 0.75 GeV as seen in section 5.6. However, the π^+ angular distribution is not sensitive to such a small change of the Δ production angular distribution.

The sensitivity to the Δ decay angular distribution has been investigated as well by using three different anisotropies (as discussed in section 5.8) as shown in fig. 5.28. One can see that increasing the π^+ anisotropy shifts the yields towards forward and backward angles, so that the angular distribution has a flatter bottom for the extreme $1+3\cos^2\theta$ like angular distribution than for the isotropic one.

This shows clearly the dependence of the center-of-mass pion angular distribution on the Δ

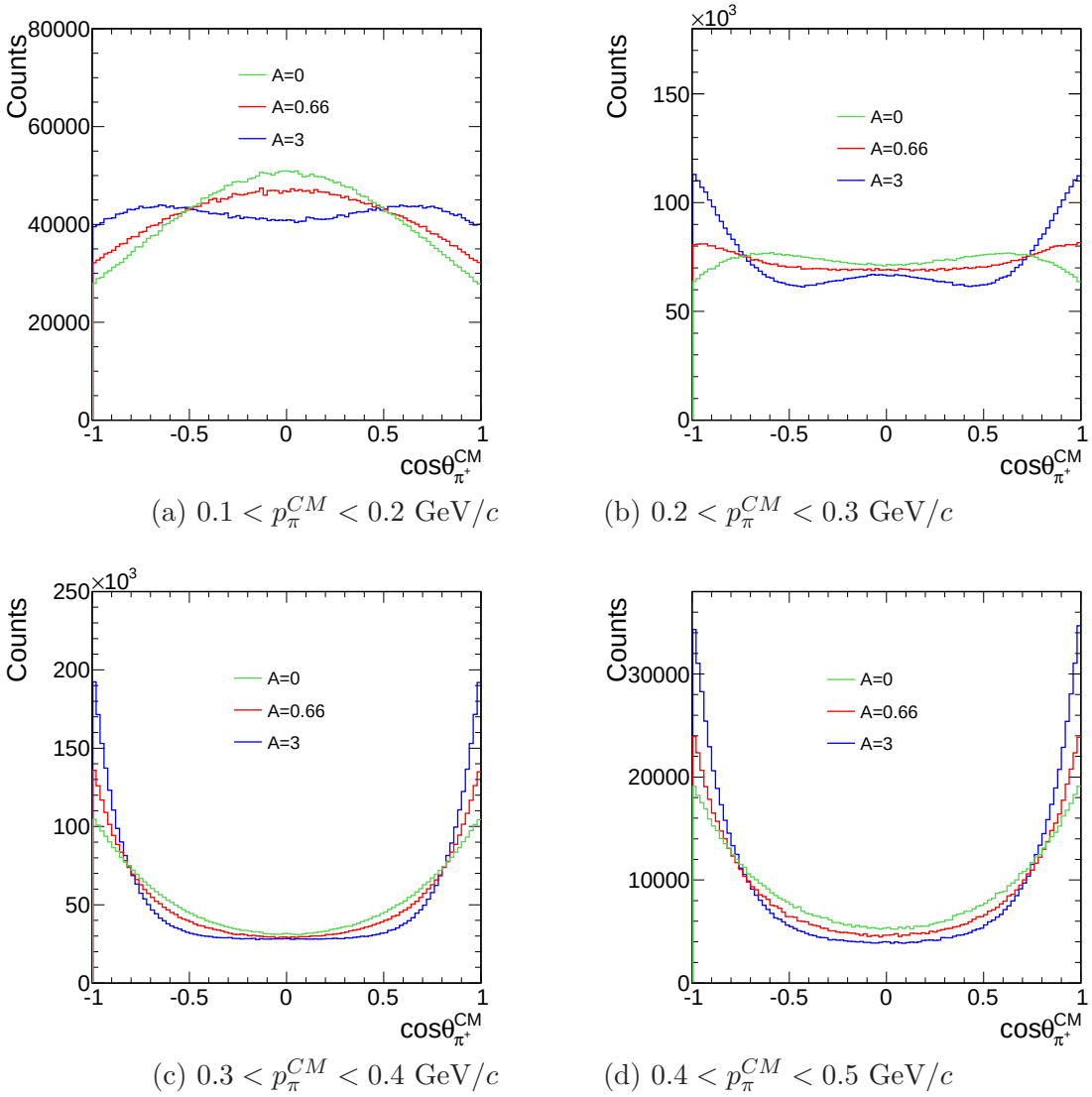

(a) $0.1 < p_\pi^{CM} < 0.2$ GeV/c (b) $0.2 < p_\pi^{CM} < 0.3$ GeV/c

(c) $0.3 < p_\pi^{CM} < 0.4$ GeV/c (d) $0.4 < p_\pi^{CM} < 0.5$ GeV/c

FIG. 5.28 – Simulated π^+ angular distribution in the $p+p$ center-of-mass frame in $pp \to np\pi^+$ reactions in 4π for different bins in π^+ center-of-mass momentum. Blue : pure OPEM ($A = 3$), green : isotropic decay ($A = 0$) and red : Wicklund's parametrization ($A = 0.66$).

decay angular distribution. In practice, as shown in section 5.8, the extreme case $1 + 3\cos^2\theta$ is excluded by the data. But with anisotropies like found in [Wicklund et al., 1987] and also in agreement with our data, the shape of the π angular distribution in the center-of-mass is still significantly different in 4π with respect to the isotropic one.

Since these angular distributions clearly do not follow a $1 + A_2\cos^2\theta_{\pi^+}^{CM}$ trend, we did not try to extract the A_2 parameter. But it seems clear that the anisotropy is increasing very much as a function of $p_{\pi^+}^{CM}$. It leads to the conclusion that the smaller anisotropies observed at low $p_{\pi^+}^{CM}$ in the case of heavy-ion collisions can not be taken as a proof of the thermalization of the system, since qualitatively the same trend is observed in $p+p$ collisions.

5.13 Conclusion for the exclusive $pp \rightarrow np\pi^+$ analysis at 1.25 GeV/c

In this section, we have discussed in detail the exclusive analysis of $pp \rightarrow np\pi^+$ reactions measured by HADES at 1.25 GeV/c. The mass distributions as well as angular distributions are compared to a Pluto simulation which is a "HADES homemade" model based on the Teis resonance model where the different processes are added incoherently. The aim of studying this channel is to check the validity of the resonance model used to interpret di-electron production in $p + p$ reactions and in heavy-ion reactions.

An overall good agreement with the standard Pluto simulation is observed in our analysis.

The dominance of π production via Δ resonance production is clearly seen in this channel. $N\pi^+$ invariant mass and neutron angular distribution are in fairly good agreement with the one-π exchange model for Δ production. The neutron-proton final state interaction has been observed in this channel and has been nicely described by the simulation with the Jost function. However, a discrepancy at $\cos\theta_n^{CM}$ close to 0 has been seen from the comparison of data to Pluto simulations even with the FSI effect included. A cut-off parameter $\Lambda_\pi = 0.75$ GeV has been adjusted to better describe the data. The influence from the $N^*(1440)$ resonance as well as a non-resonant contribution has been tested, but the sensitivity to these contributions is small due to the strong dominance of Δ^{++} production. The π angular distribution has been studied as well since it is expected to be sensitive to the Δ decay processes. From the comparison to different decay anisotropy coefficients, our data confirm the $1 + 0.66\cos^2\theta$ which was measured by previous experiments, but the isotropic decay shows also a fairly good agreement to our data. We therefore propose some improvements to better describe the data, including FSI implementation, cut-off parameter $\Lambda_\pi = 0.75$ GeV and Δ decay anisotropy $A = 0.66$.

The acceptance correction has been achieved for the neutron angular distribution and (p, π^+) invariant mass distribution. The acceptance corrected spectra are fully consistent with the ones measured in the HADES acceptance. The total cross section of $pp \rightarrow np\pi^+$ has been extracted from the acceptance corrected spectra. It results in 18.17 ± 1.85 mb. This value was compared to existing data and good agreement was found.

These exclusive data should be compared to more sophisticated models. Despite the unexpected inefficiency problems and a not well suited trigger, they have indeed a high statistics and could allow precise tests of models. Such a model could be for example including one of the OBE models which was already compared to the di-electron measurements. It would be a good test of the consistency of these models.

These checks of resonance model are useful for di-electron analysis, since this model is used for analysis and acceptance corrections. Following the resonance model, the $pp \rightarrow np\pi^+$ and $pp \rightarrow pp\pi^0$ channels are coupled by isospin relations. However, it is necessary to make the same kind of detailed tests for the $pp \rightarrow pp\pi^0$ channel which is more directly linked to the π^0 and Δ^+ Dalitz decay channels which dominate in the inclusive e^+e^- production at 1.25 GeV.

Inclusive di-electron production via π^0 and Δ Dalitz decay is not very sensitive to the details of π^0 and Δ production. Here, the main ingredient is the π^0 and Δ production cross section, although the Δ mass distribution has also an influence on the yield at high e^+e^- invariant masses. From our analysis, it is shown that the Δ mass distribution is well reproduced in the high mass region (acceptance corrected spectrum). The cross section measured in $pp \rightarrow np\pi^+$

channel is 10% lower than the resonance model cross section used for the di-electron analysis. This difference has however a small influence considering the uncertainties related to normalization and efficiency correction used in the di-electron analysis (of the order of 22%).

For the exclusive pe^+e^- analysis, the sensitivity to the Δ resonance production is higher due to the detection of the proton. If the analysis of the $pp \to pp\pi^0$ channel confirms that the proposed improvements in the simulation better describe the data, it should be used for the analysis of the exclusive $pp \to ppe^+e^-$ channel. We will discuss this point a little bit further in the next chapter.

Chapitre 6

Contribution to the study of Δ Dalitz decay process

The exclusive measurement of the Δ Dalitz decay using $pp \to ppe^+e^-$ events has been realized in parallel with the inclusive measurements using $pp \to Xe^+e^-$ events. As mentioned in section 1.6, in the $p+p$ reaction at 1.25 GeV the main di-electron production processes are the π^0 and Δ Dalitz decays, pp bremsstrahlung is expected to be small. E. Morinière had studied the feasibility of these exclusive measurements in her PhD [Morinière, 2008]. The data analysis is now performed by W. Przygoda [Przygoda, 2009] in Krakow. The exclusive measurement has a great interest since it allows to reconstruct the Δ signal and to identify unambiguously its Dalitz decay process which has never been measured experimentally so far.

In this chapter, I will introduce at first briefly the strategy of this measurement and the model used in the simulation for the data interpretation. Then I will focus on the simulation of helicity distributions in the Δ Dalitz decay in which I took an active part in collaboration with W. Przygoda.

6.1 Simulation for the Δ Dalitz decay in $p+p$ reactions

The simulation for the Δ Dalitz decay process illustrated by fig. 6.1 is performed with the Pluto event generator. A short summary of the inputs is given below.

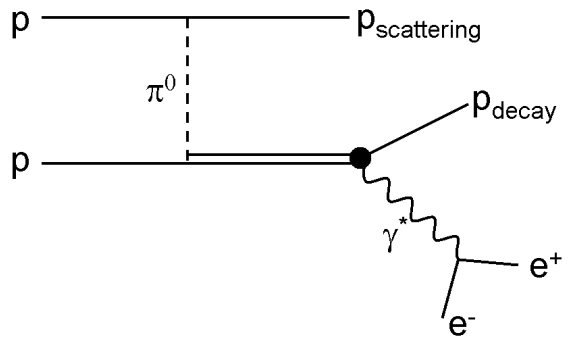

FIG. 6.1 – Diagram of Δ Dalitz decay process in $p+p$ reaction.

– **Δ production :**

The production of the Δ resonance is described in the same way as in the hadronic channel simulation. As explained in detail in section 3.2.3, the mass and angular distribution of the $pp \to N\Delta$ process is calculated within the OPEM [Dmitriev and Sushkov, 1986].

– **Δ Dalitz decay branching ratio :**
The di-electron mass-dependent differential decay width of the Δ Dalitz decay derives from QED calculations. By choosing the electric, coulomb and magnetic covariant, one can obtain the Dalitz decay width as a function of the corresponding form factors. We used the expression from [Krivoruchenko and Faessler, 2002], which was checked by J. Van de Wiele. It has to be mentioned that inconsistent expressions can be found in the litterature for this differential Dalitz decay width, as was already pointed out in [Krivoruchenko et al., 2002].

– **Iachello $N - \Delta$ transition from factor :**
The two-component quark model form factor from Iachello which is in fact a VDM model has been implemented in the Pluto simulation [Wan and Iachello, 2005]. With respect to the constant form factor, the VDM form factor has an influence in the higher mass region, i.e. for $M_{\text{inv}}e^+e^- > 0.3$ GeV/c^2.

– **γ^* angular distribution :**
Similarly to the pionic decay angular distribution (see section 3.2.4), the γ^* angular distribution in the $\Delta \to N\gamma^*$ decay is sensitive to the polarization of the Δ resonance and hence to the Δ production mechanism. In Pluto, we implement this distribution as $5 - 3\cos^2\theta$, in the Δ reference frame with the z-axis taken as the momentum transfer direction in the reference frame of the excited nucleon, assuming the pure one-π exchange case. Technically, the same recipe based on the direct and exchange graph amplitudes, as for the pionic decay (see section 3.2.4), was used to define the momentum transfer direction.

– **helicity distribution :**
The di-electron angular distribution is described through the helicity angle distribution as will be shown in section 6.3.

The simulated events are filtered by the acceptance matrices, and proceeded through the whole analysis chain to compare with the data.

6.2 Δ Dalitz decay reconstruction

One of the important problems in the exclusive $pp \to ppe^+e^-$ channel is the background subtraction. First, a series of cuts are applied to remove as much as possible the conversion pair which are produced in the interaction of real photons with detector material. Second, as in any e^+e^- channel, the combinatorial background has to be subtracted carefully. This is achieved in our analysis using the like-sign method considering that the combinatorial pairs have the same yield as the like-sign e^+e^+ and e^-e^- pairs. Then comes the problem of $pp \to ppe^+e^-$ signal selection. The π^0 Dalitz decay ($\pi^0 \to \gamma e^+e^-$) has a cross section about a factor 200 higher than the Δ Dalitz decay in the low mass region. A method was proposed, consisting of adjusting the width of the cut on pe^+e^- missing mass distribution as a function of the proton momentum, in order to optimize the signal-to-background ratio because the resolution on mass depends strongly on the proton momentum [Morinière, 2008]. However, due to the worse than expected resolution, and more precisely to the tails of the non-Gaussian distribution of the momentum

resolution, this method has not been used.

As a consequence, the Δ Dalitz decay signal is extracted from the (e^+, e^-) invariant mass above 0.14 GeV/c where the π^0 Dalitz decay does not contribute.

In the following, we will summarize the results of the exclusive $pp \to ppe^+e^-$ analysis using pe^+e^- events, currently performed by Witold Przygoda. The data are compared to a Pluto simulation including π^0 and Δ Dalitz decays.

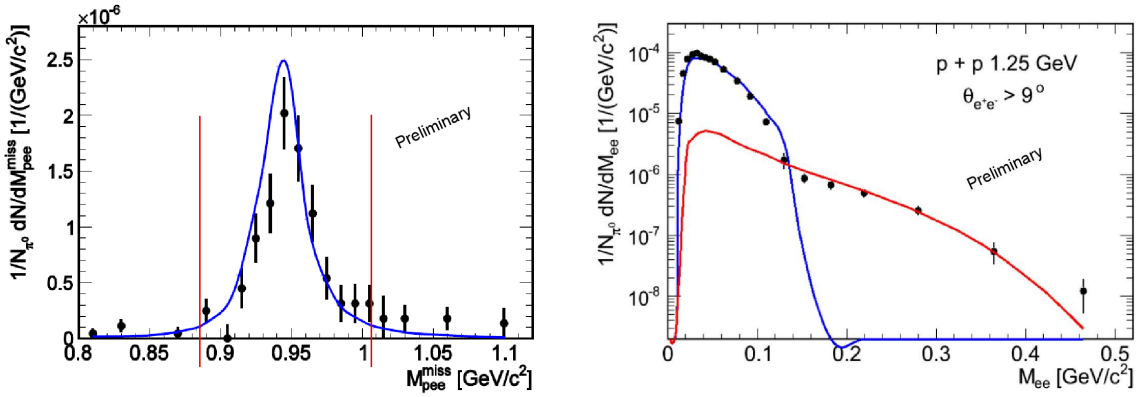

FIG. 6.2 – **Left :** pe^+e^- missing mass distribution in the region of $M_{\text{inv}}(e^+, e^-) > 0.14$ GeV/c^2. The data are drawn in black dots and the Pluto simulation is drawn in blue solid curve. **Right :** (e^+, e^-) invariant mass distribution with a 3σ cut around the proton mass (red bars) imposed on pe^+e^- missing mass. The Pluto simulation for the Δ Dalitz decay channel and for the π^0 Dalitz decay channel are drawn respectively in red and in blue. Both spectra are measured in the $pp \to pe^+e^-X$ reaction at 1.25 GeV in HADES acceptance.

The pe^+e^- missing mass distribution is obtained in the left panel of fig. 6.2. It peaks at the proton mass as expected, showing that the $pp \to ppe^+e^-$ reaction has been measured. The position and width of the proton peak is well reproduced by the simulation which confirms the efficiency of the background subtraction strategy and the good description of the resolution in the simulation. The contribution at missing masses higher than 1.08 GeV/c^2 which would correspond to the production of an additional pion is small. As a last step, a 3σ cut is imposed on the pe^+e^- missing mass to remove the bad resolution events. Totally, about 200 counts are selected corresponding to the $pp \to ppe^+e^-$ reaction.

In the right panel of fig. 6.2, the exclusive (e^+, e^-) invariant mass distribution is shown for all pe^+e^- events inside the 3σ cut on pe^+e^- missing mass. Unlike the other distributions, this spectrum is obtained without $M_{\text{inv}}(e^+, e^-) > 0.14$ GeV/c^2 cut in order to have a global view in both π^0 and Δ Dalitz decay regions. Within error bars, the measured di-electron yield is satisfactorily reproduced by the simple simulation. As mentioned before, the sensitivity to the $N-\Delta$ transition form factor is expected in the higher e^+e^- invariant mass region above 0.3 GeV/c^2. However, due to the lower statistic, the sensitivity in the exclusive measurement is smaller than in the inclusive one (left panel of fig. 1.11).

In order to further prove the measurement of Δ Dalitz decays, the Δ mass distribution and its center-of-mass angular distribution are checked by comparison with Pluto simulation. Here, the "standard" Pluto simulation is used. The Δ is reconstructed from the pe^+e^- triplets

considering at the same time the detected proton and the reconstructed missing proton. The measured invariant mass of pe^+e^- is well reproduced by simulation, whereas only a small shift of 20 MeV/c^2 to the higher mass can be seen (left panel of fig. 6.3). The acceptance corrected Δ center-of-mass angular distribution is also nicely described by the simulation (right panel of fig. 6.3). This confirms that the Δ Dalitz decay is the dominant process and that pp bremsstrahlung is negligible.

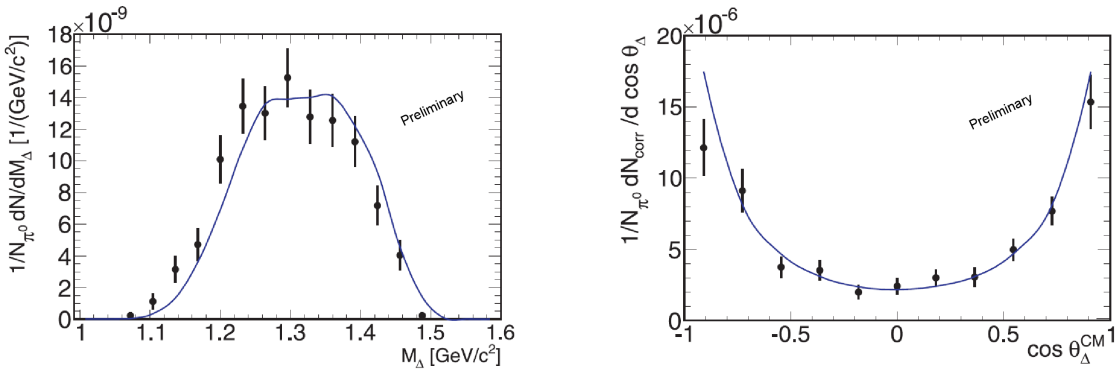

FIG. 6.3 – **Left :** pe^+e^- invariant mass (or called reconstructed "Δ" mass) distribution and **Right :** acceptance and efficiency corrected pe^+e^- angular distribution in the center-of-mass system , compared to a Pluto simulation for the Δ Dalitz decay process (blue lines).

The mass and angular distributions obtained here for $pp \to p\Delta^+$ process can be compared to the ones measured with the hadronic channels $pp \to n\Delta^{++}$ (see section 5.2 and 5.6).

In the case of the pe^+e^- analysis, the cut of $M_{\text{inv}}e^+e^- > 0.14$ GeV/c^2 favors higher Δ masses, which explains why the M_Δ distribution is shifted to higher values with respect to the $M_{\text{inv}}(p,\pi^0)$ distribution measured from $pp \to pp\pi^0$ events (see fig. 5.25). We would like also to note that the observation of the simulations are shifted towards high masses with respect to the data, as seen in both the $M_{\text{inv}}(pe^+e^-)$ distribution (left panel of fig. 6.3) and the $M_{\text{inv}}(p,\pi^+)$ distribution (fig. 5.25).

For the $\cos\theta_\Delta$ distribution, a connection can be made with the neutron center-of-mass distribution in the $pp \to np\pi^+$ reaction which reflects the Δ^{++} production angular distribution (see section 5.6). The $\cos\theta_\Delta$ is in good agreement with the simulation within error bars in the case of the pe^+e^- channel and no clear evidence can be seen here for a flatter angular distribution as was observed in the $np\pi^+$ channel and was simulated using a larger cut-off parameter $\Lambda_\pi = 0.75$ GeV in the OPEM.

In addition, the measured yields are in good agreement with the cross section adopted from the resonance model for the Δ production $\sigma_{pp\to p\Delta^+} = 4.0$ mb. Considering the statistical and systematical errors on the measured yield, which are 9% and less than 20%, respectively, and neglecting the pp bremsstrahlung, the branching ratio is in agreement with the value $4.2 \cdot 10^{-5}$ as predicted by QED calculations.

6.3 Helicity distributions

6.3.1 Motivation

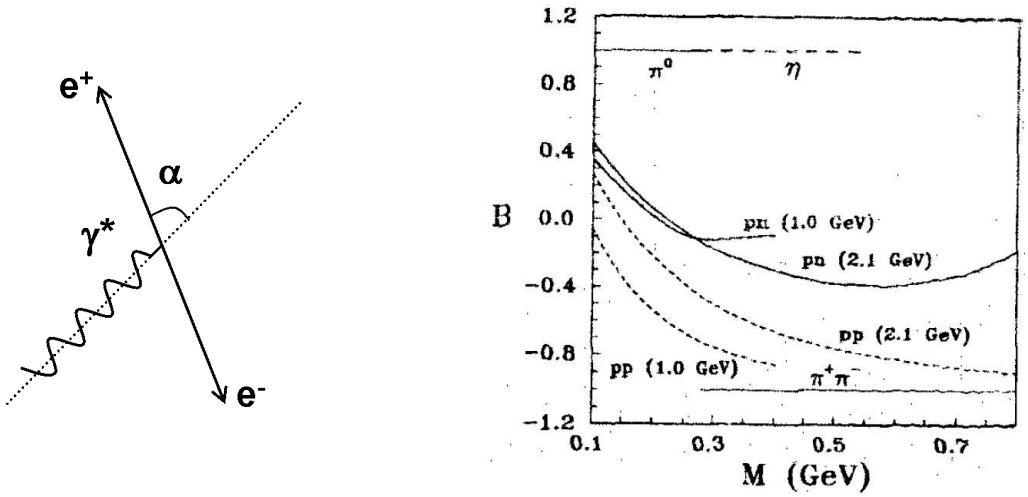

FIG. 6.4 – **Left :** Sketch of the helicity angle α in the Δ Dalitz decay process. **Right :** Anisotropy coefficient (B) for different elementary di-electron sources as a function of di-electrion mass (M) [Bratkovskaya et al., 1995].

In the exclusive analysis of pe^+e^- events, the helicity distribution has been carefully studied as another useful quantity to characterize the Δ Dalitz decay process.

The helicity h is defined as the projection of the spin $\vec{S}$ onto the direction of momentum $\hat{p}$: $h = \vec{S} \cdot \hat{p}$. h can take values ± 1 or 0 for a virtual photon due to its spin 1. The shape of the distribution of the e^+/e^- angle (α in fig. 6.4 (left panel)) in the γ^* frame in the decay process $\gamma^* \rightarrow e^+e^-$ depends on the population of the different helicities of the γ^* ($h = \pm 1,\ 0$). Starting from the reference frame of the decaying particle (the Δ), the helicity angle is defined as the e^+/e^- angle in the γ^* rest frame with respect to the direction of γ^* momentum.

In the case of the π^0 Dalitz decay, or η Dalitz decay, the helicity distribution is well known and should be in the form of $1 + \cos^2 \alpha_e$ due to the fact that these mesons have spin 0. In fact this has been confirmed by HADES in the exclusive analysis ($pp \rightarrow ppe^+e^-\gamma$) of $p+p$ reactions at 2.2 GeV [Wiśniowski, 2009]. In the vector meson decays, this distribution is expected to be isotropic. In the NN bremsstrahlung process, the anisotropy of this distribution is close to 0 or even negative [Bratkovskaya et al., 1995] (right panel of fig. 6.4).

From the QED calculation of the $N - \Delta$ electromagnetic transition, using a purely magnetic transition [Martemyanov, 2009, Bratkovskaya et al., 1995, Van de Wiele and Ramstein, 2009], the q^2 and α_e dependent differential decay width can be calculated. It factorizes as :

$$\frac{d^2\Gamma}{dq^2\ d\cos\alpha_e} = \frac{d\Gamma}{dq^2}(1 + \cos^2\alpha_e) \tag{6.1}$$

where Γ is the Dalitz decay width of the Δ mass and q is the four-momentum transfer. This result can be explained as follows : for magnetic or electric transitions, transverse photons (with helicities ± 1) are selected [Martemyanov, 2009]. In addition, due to the small mass of e^+/e^-,

they are produced with opposite helicities. The distribution given by equation 6.1 is used in the Pluto generator for the Δ Dalitz decay description.

The strategy related to the helicity distribution is to reconstruct experimentally the α_e distribution with pe^+e^- events. If the Δ Dalitz decay is the dominant process, a $1+\cos^2\alpha_e$ helicity angle distribution is expected.

6.3.2 Definitions of helicity

HADES helicity definition

In the HADES data analysis, technically, the helicity angle for the $\Delta \to p\gamma^* \to pe^+e^-$ decay is calculated from the four-momentum in the laboratory system with following steps :

- Take (p, e^+, e^-) four-momenta in laboratory system
- Boost (p, e^+, e^-) four-momenta to Δ^+ rest frame
- Boost e^+, e^- to γ^* rest frame
- Calculate the angle between e^+/e^- and γ^*

The one-boost / two-boost problem

The procedure described above implies two boosts for the leptons, i.e. the first boost from lab frame to the Δ^+ rest frame and the second boost from the Δ^+ rest frame to the γ^* rest frame. This is important and needs to be specified in the definition of the helicity angle. We will make this point more explicit since it was at the origin of some confusion in the analysis discussions.

Taking the definition of helicity angle mentioned above, and starting from four-momenta in lab, we could think of boosting directly e^+/e^- from lab to the γ^* frame. In this case, a flatter distribution is however obtained. This is in fact due to a relativistic effect. The sequence of two boosts is indeed not equivalent to the direct boost from the first reference frame to the final one, it produces an additional rotation. If one wants to recover the direct boost, the inverse rotation which can be calculated from the two individual boost vectors has to be applied. These effects are known under Thomas precession and Wigner rotations [Van de Wiele, 2002]. They appear only for very fast moving reference frames. In our case, due to the high velocity of the γ^*, the effect is sizable.

So, with the HADES helicity definition, it is needed to have the e^+/e^- and γ^* firstly in the Δ^+ reference frame before boosting e^+/e^- to the γ^* reference frame. This can be understood since the $1+\cos^2\alpha$ distribution is obtained for a QED calculation in the Δ^+ reference frame.

BABAR helicity definition

We found in the litterature other ways to define this quantity. For example, in the analysis tools of the BABAR collaboration [BABAR Collaboration, 2007], the helicity angle is calculated as follows :

- Take (p, e^+, e^-) four-momenta in the laboratory system
- Boost Δ^+ and e^+/e^- four-momenta to the γ^* rest frame
- Calculate the angle between e^+/e^- and Δ^+

Equivalence of "BABAR helicity" to "HADES helicity"

Is the "BABAR helicity" definition equivalent to the 'HADES helicity" definition ? They differ apparently by the fact that in HADES case, the angle of e^+/e^- in the γ^* rest frame is measured with respect to the γ^* momentum in the Δ^+ rest frame ; while in the BABAR case, the reference axis is the direction of Δ^+ momentum in γ^* rest frame. However, both directions are opposite since the (Δ^+ momentum in γ^* rest frame) is obtained by boosting the null vector along the direction of (γ^* momentum in Δ^+ rest frame). So the two definitions are in fact equal modulus π. In the BABAR definition, the vectors are both in the same reference frame, the γ^* rest frame. So the effects of rotations cancel and this definition is therefore independent of possible intermediate boosts. This means that the first step described above : "Take all four-momenta in lab" is not necessary and that one can start from any reference frame.

A third alternative is to take an expression which is Lorentz-invariant [BABAR Collaboration, 2007], where no boost at all is needed and which is also equivalent to the other mentioned above. All these definitions are equivalent, the HADES one which is also found in the transport model calculations, requires however to boost the four-momenta first to the Δ^+ reference frame.

In the Pluto event generator, the helicity distribution is implemented as $1+cos^2\alpha$ according to the QED calculation (see fig.6.5).

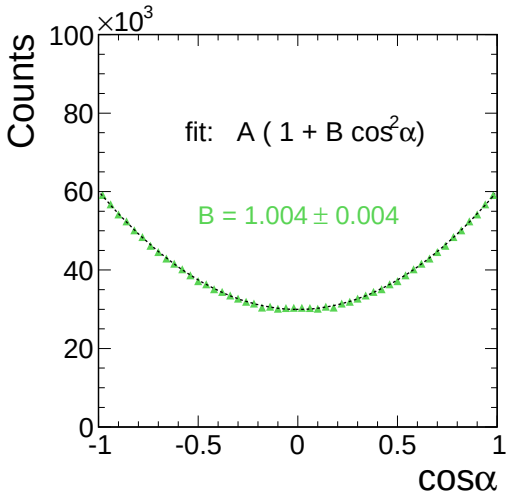

FIG. 6.5 – Helicity angle distribution (green triangles) in 4π fitted with $A(1+B\cos^2\alpha)$ (black dashed line) in our Pluto simulation.

6.3.3 HADES helicity distribution

In the exclusive pe^+e^- data analysis, the helicity angle is calculated following the "HADES helicity" definition. The Δ^+ is reconstructed taking both detected and reconstructed protons into account as mentioned in section 6.2. Then the distribution is corrected for detector efficiency and acceptance and is extrapolated to the whole invariant mass range using the simulation. The preliminary result (fig.6.6) is found to be in good agreement with the $1+cos^2\alpha$ expected from QED.

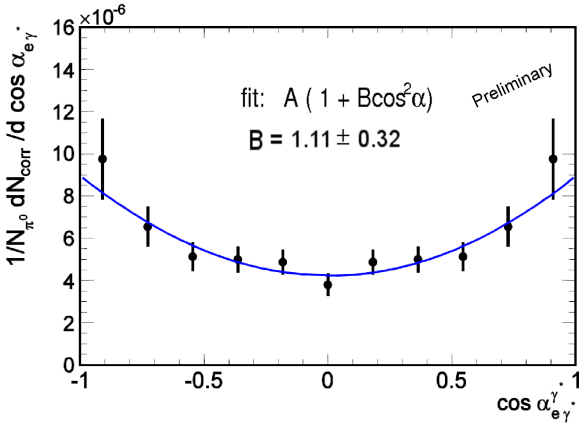

FIG. 6.6 – Helicity angle distribution measured by HADES after acceptance and efficiency correction. Data are shown as black dots and fitted by a function of type $A(1 + B\cos^2\alpha)$ with $B = 1.11 \pm 0.32$.

For now, only statistic errors are presented in this distribution (fig 6.6). However, the distribution shown above is obtained after a whole analysis chain. The systematic errors related to the correction procedure should be considered.

Fig 6.7 shows the correction factors for each cut as a function of $\cos\alpha$ in the left column, together with the helicity angle distribution after corresponding cuts on the right side. The idea is to illustrate the effect of each cut, and the corresponding influence to the correction. Note that in the simulation, the helicity distribution is implemented following $1 + \cos^2\alpha$.

In the first row, we show the effects of the (e^+, e^-) opening angle cut and the (e^+, e^-) invariant mass cut. In fact, the former cut is included in the latter one, because most of the events corresponding to a (e^+, e^-) opening angle smaller than 9^o are found in the π^0 region ($M_{\text{inv}}e^+e^- < 0.14$ GeV/c^2). These two cuts remove in total 92.5% of the events and result in a globally down scaled distribution. But its shape is not yet very much distorted. After filtering through the detector efficiency and acceptance matrices (second row), 96% of the residual events are cut. The forward and backward angles are strongly cut so that the shape of the distribution is now completely changed.

The $M_{\text{inv}}(e^+e^-)$ distribution is quite precisely known and the related variation of the correction factor is quite smooth. We can conclude that the uncertainties from the opening angle cut and invariant mass cut are very small and can be ignored. The main source of systematic error is no doubt from the detector acceptance and efficiency correction, because the correction factor varies rapidly with $\cos\alpha$ and it deforms strongly the distribution. From the left-bottom panel of fig. 6.7, we can see that the correction factor for small angles is huge and vary steeply. So for these bins, the careful treatment of corrections and good evaluation of errors are extremely important. The systematic error should be estimated and included in the helicity angle distribution for the further anisotropy parameter fitting.

Influence from the scattered proton

The helicity angle distribution obtained by HADES results in $1 + cos^2\alpha$ (see fig.6.6), which fulfills the QED prediction. This effect is interpreted as an additional proof of the dominance of the Δ Dalitz decay process. However, different effects might distort the initial $1 + cos^2\alpha$ angular

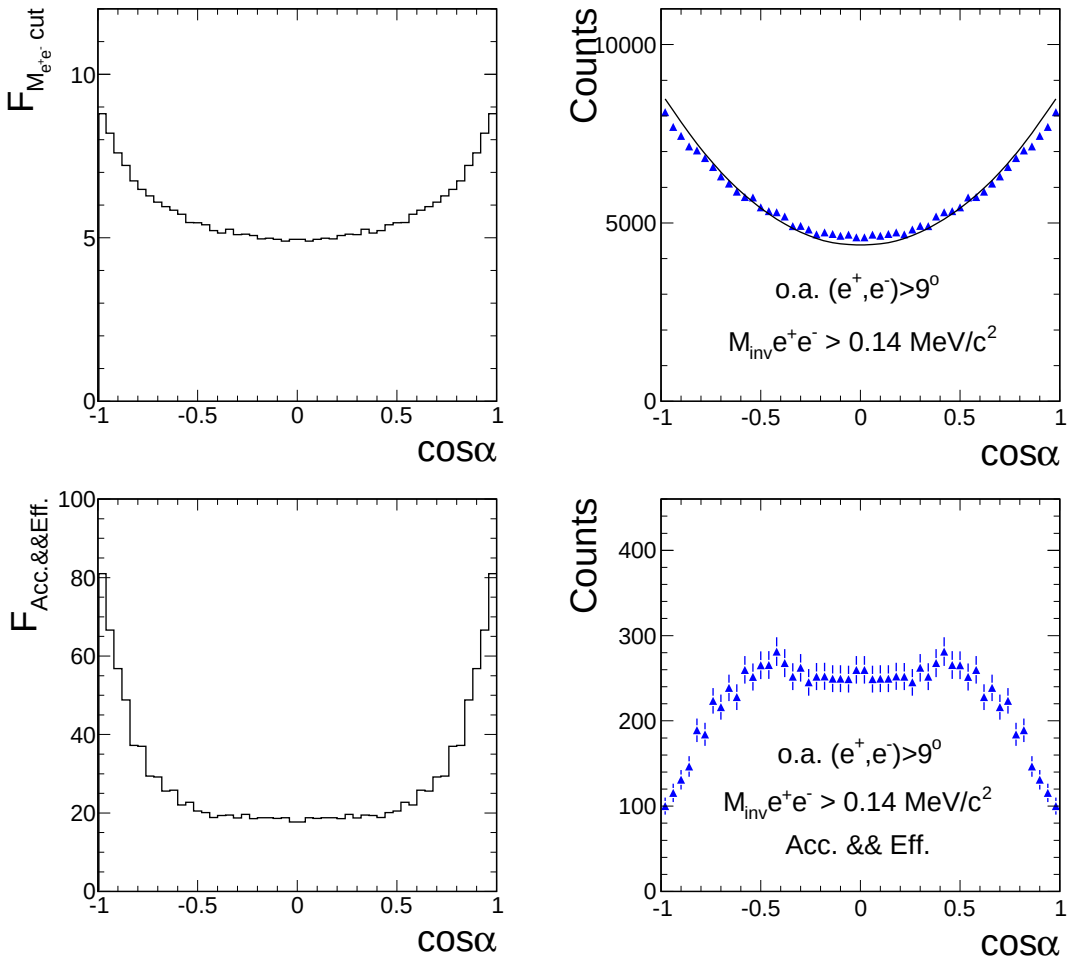

FIG. 6.7 – **Left :** Distribution of correction factors of different imposed cuts and conditions. **Right :** Helicity angle distributions ("true Δ" + "fake Δ") with corresponding conditions. The simulated spectrum (triangles) is compared with the $1 + \cos^2\theta$ function after normalization to the same total yield.

distribution. Investigations related to this question have been performed and will be shown in the following.

As the Δ^+ resonance can not be unambiguously reconstructed, one can naturally expect a different distribution for the Δ^+ reconstructed with the scattered proton (so called "fake" Δ) (see fig. 6.1).

This effect has been studied using our simulation where the two protons can of course be identified. However, taking into account both protons, the helicity distribution is only slightly distorted as shown in fig 6.8. For the "fake" Δ, the anisotropy parameter is 0.94 instead of 1 (see fig. 6.8). This distortion becomes larger when we compare these distributions as a function of (e^+, e^-) invariant mass, as in fig. 6.9. The "true" Δ (reconstructed with proton from Δ^+ Dalitz decay) contributions keeps the anisotropy parameter ($B = 1$) while the "fake" Δ contribution gives anisotropy parameters B which are smaller than 1 and decrease with increasing e^+e^- invariant mass.

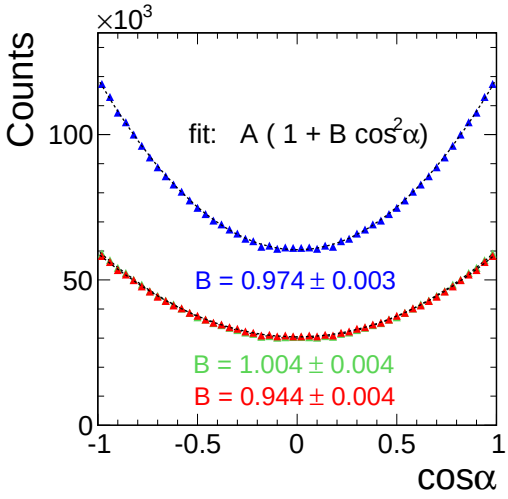

FIG. 6.8 – Simulated helicity angle distribution (blue triangles) in 4π fitted with $A(1+B\cos^2\alpha)$ (dashed line). The "true Δ" contribution is shown in green and the "fake" Δ contribution is shown in red.

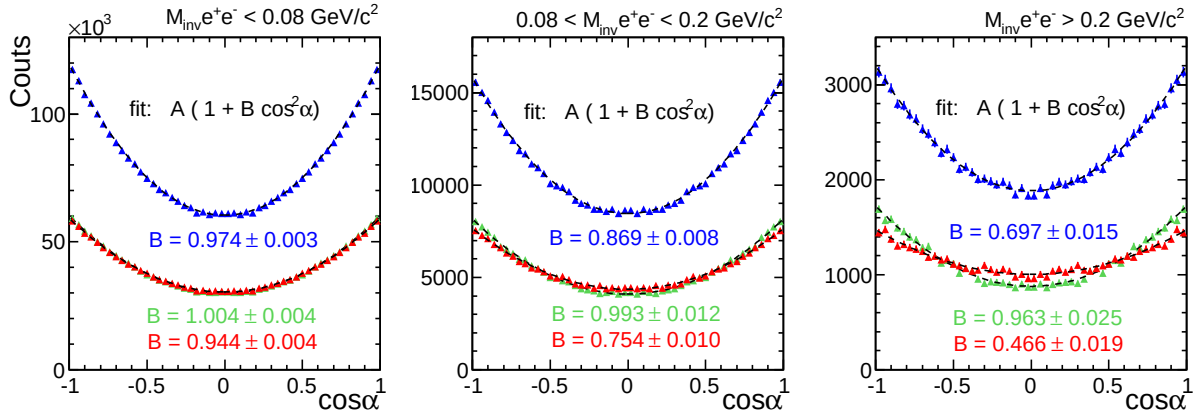

FIG. 6.9 – Simulated helicity angle distribution (blue triangles) in 4π fitted with $A(1+B\cos^2\alpha)$ (dashed line) in different mass slices. The "true Δ" contribution is shown in green and the "fake" Δ contribution is shown in red.

As explained in section 6.2, the analysis of the Δ Dalitz decay is performed for $M_{\text{inv}}(e^+,e^-) > 0.14$ GeV/c^2. In this condition, the anisotropy parameter is expected to be $B = 0.77$ (see fig. 6.10) and not 1.

As a conclusion, due to the ambiguity in the Δ reconstruction, the helicity distribution is distorted, mainly in the high e^+e^- mass region and the anisotropy parameter for helicity distribution averaged over the γ^* mass distribution is expected to be only slightly smaller than 1.

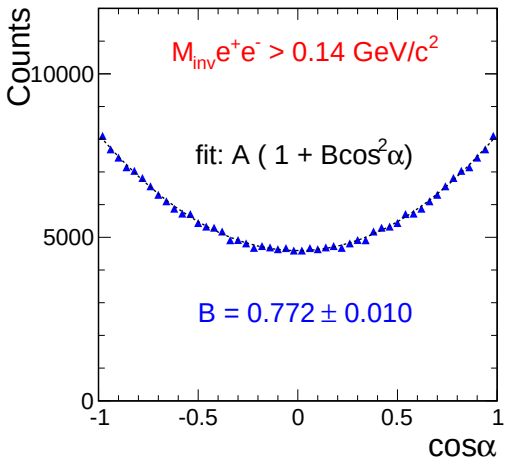

FIG. 6.10 – Simulated helicity angle distribution (blue triangles) in 4π fitted with $A(1+Bcos^2\alpha)$ (black dashed line) for e^+e^- invariant mass greater than 0.14 GeV/c^2.

6.3.4 Pseudo-helicity distributions

The helicity distribution has been investigated also in our inclusive e^+e^- analysis, especially in the case of heavy-ion reactions for which exclusive measurements cannot be performed. In this context, the helicity as defined in 6.3.2 (called "true helicity" in this section) cannot be reconstructed.

Definition of pseudo-helicity distributions

But a pseudo-helicity angle can be calculated, in two different ways as explained in Annex B. The difference with respect to the "true helicity" angle comes from the reference frame for the γ^* direction which is taken in the laboratory system (lab. pseudo-helicity) or center-of-mass (CM pseudo-helicity) frame instead of the reconstructed Δ reference frame.

Results from the $Ar + KCl$ reactions

The CM pseudo-helicity angle distribution has been used in the $Ar + KCl$ analysis and the preliminary result is shown in fig. 6.11. The black points present in fact the ratio

$$\frac{N^{\text{exp}}}{N^{\text{sim}}}, \tag{6.2}$$

where the N^{exp} is the measured counts in a CM pseudo-helicity bin; N^{sim} is the simulated Pluto cocktail in which an isotropic helicity angle distribution is assumed, and is filtered through acceptance/efficiency matrices and smeared for momentum resolution. The pink curves show the results from a fit of this ratio according to the function

$$A(1 + B\cos^2\theta) \tag{6.3}$$

where A is the normalization factor and B is the anisotropy coefficient which we are interested in.

In the region of $0.13 < M_{\text{inv}}e^+e^- < 0.5$ MeV/c^2, the N^{exp} in each bin is obtained by subtracting the known η contribution using the simulation (blue curve). The idea is to look whether the helicity distribution helps to identify the source of di-electrons which are in excess with respect to the already well known η.

The CM pseudo-helicity has been studied as a function of e^+e^- invariant mass. The anisotropy is clearly non-zero for the first invariant mass slices and it is compatible with 0 in the last slice. The latter result is consistent with the di-electron decay of vector mesons where an isotropic angular distribution is expected, but statistics is very low. While in the low mass region, a clear anisotropy is observed. When $M_{\text{inv}}(e^+e^-) < 0.14$ GeV/c^2, the anisotropy is expected because the π^0 Dalitz decay dominates. At larger invariant masses, after η substraction, it could be the hint of the Δ Dalitz decay process.

It is however important to study how the original distributions, which are $1 + \cos^2\theta$ in the case of π^0 and Δ Dalitz decay, are distorted when the γ^* momentum is taken in the center-of-mass. We will also consider the expected results for the lab. pseudo-helicity.

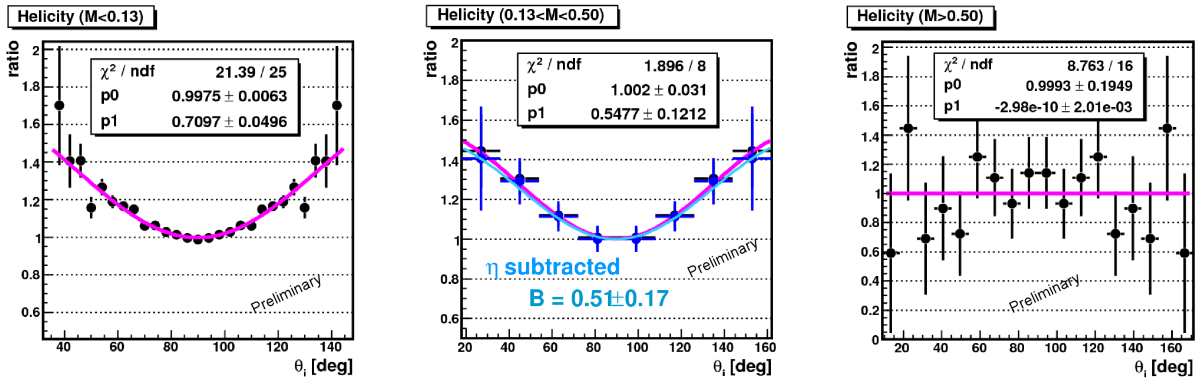

FIG. 6.11 – Ratio of CM pseudo-helicity angular distribution measured in $Ar + KCl$ at 1.76 A GeV and the simulated Pluto cocktail in which isotropic helicity angle distribution is assumed, in different e^+e^- invariant mass ranges. Data are presented by black dots and are fitted with $A(1 + B\cos^2\theta)$.

Simulation study with $p + p$ reactions

In the context of the discussions related to the preliminary analysis of the $Ar + KCl$ data mentioned above, a simulation study was therefore performed for the $p+p$ reaction at 1.25 GeV, assuming the Δ Dalitz decay process. The aim was to check the behavior of the pseudo-helicity for the Δ Dalitz decay and provide a reference for the heavy-ion results. The input to this simulation were the same as described in section 6.1.

Firstly, we compare all the helicity angle distributions using the three definitions and taking into account only the true Δ. The anisotropy coefficients of the pseudo-helicity distributions are slightly smaller than 1, but still very close to 1 (see fig. 6.12).

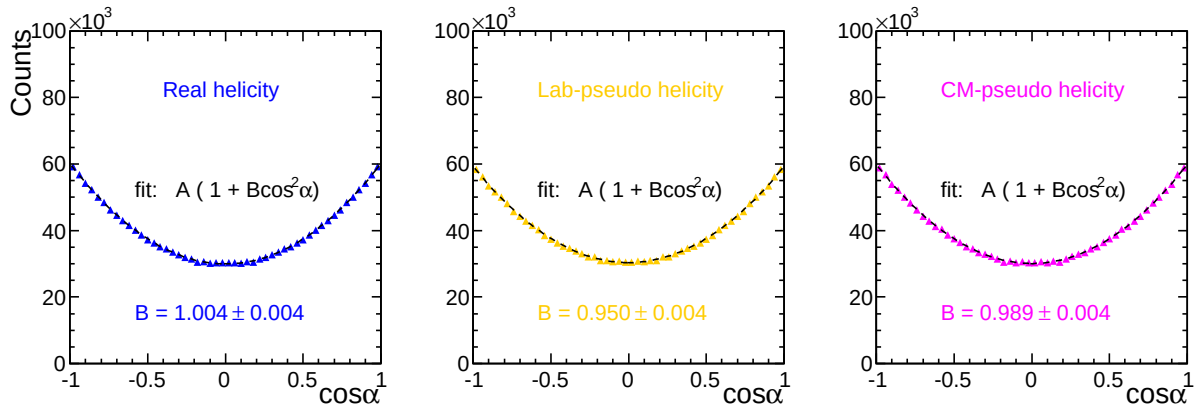

FIG. 6.12 – Helicity angle distributions (only "true Δ") in 4π fitted with $A(1 + B\cos^2\alpha)$. Blue : true helicity, orange : lab. pseudo-helicity and pink : CM pseudo-helicity.

Secondly, we compare them in slices of e^+e^- invariant mass and taking into account the "fake Δ" as well. The latter condition will not affect pseudo helicities because the protons are not involved in the definition. From fig.6.13, we see that the pseudo-helicities follow the trend to be more isotropic for higher e^+e^- invariant mass than the real ones. The lab. pseudo-helicity distribution shows the strongest dependence on mass. The CM pseudo-helicity distribution keeps

always very close to the real one.

Thus the CM pseudo-helicity is recommended for inclusive analysis since the distribution is less sensitive to e^+e^- invariant mass.

Despite the distortion at large invariant masses, the anisotropy is still significant. It can therefore allow to identify the Δ Dalitz decay contribution more easily from other isotropically distributed sources than lab. pseudo one. This justifies a posteriori the fact that the analysis of heavy-ion data was based on the CM pseudo-helicity. It confirms that the CM pseudo-helicity is a useful quantity to investigate the di-electron sources which produces an excess with respect to the η contribution.

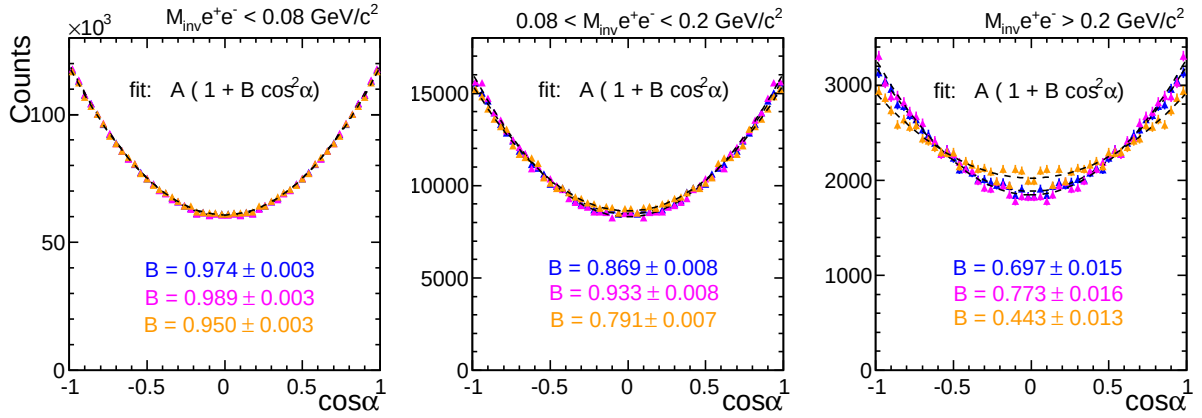

FIG. 6.13 – Helicity angle distributions ("true Δ" + "fake Δ") in 4π fitted with $A(1+B\cos^2\alpha)$ in different e^+e^- invariant mass regions. Blue : true helicity, orange : lab. pseudo-helicity and pink : CM pseudo-helicity.

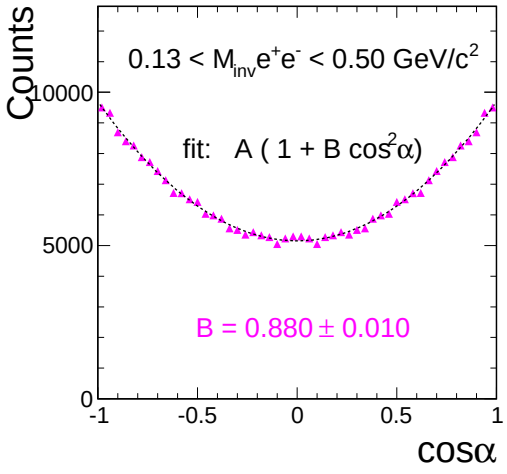

FIG. 6.14 – CM pseudo-helicity angle distributions ("true Δ" + "fake Δ") in 4π fitted with $A(1+B\cos^2\alpha)$ for $0.13 < M_{\rm inv}e^+e^- < 0.5$ MeV/c^2.

The original distribution of helicity angles in the Δ Dalitz decay, which is expected to be $1+\cos^2\theta$, is smeared by the use of the CM-pseudo helicity. It results in a distribution $1+B\cos^2\theta$, with B decreasing as a function of e^+e^- invariant mass. The coefficient $B = 0.51$ found in the

analysis of helicities for heavy-ion has to be compared to the coefficient $B = 0.88 \pm 0.01$ (instead of 1) found in the simulations of the $p + p$ reaction under the same analysis conditions (see fig. 6.14), i.e. in the e^+e^- invariant mass range $0.13 < M_{\text{inv}}e^+e^- < 0.5$ MeV/c^2.

Further smearing due to the Fermi momentum or to the multi-step collisions are likely to distort the distribution, a more realistic study could be done using e.g. transport models or thermal sources.

Chapitre 7

Conclusion and outlook

Exclusive measurements in proton-proton reactions at a kinetic energy of 1.25 GeV were presented in this thesis. This work is realized in the framework of the HADES experiment. The main goal was to investigate the di-electron production related to the Δ (1232) Dalitz decay. The analysis of these data requires a control of the cross sections and mechanisms of the Δ resonance production.

This was the motivation for the full analysis of the $pp \rightarrow np\pi^+$ reaction at 1.25 GeV and the comparison to other one-pion production channels measured at 1.25 and 2.2 GeV, which is the main contribution of this PhD work.

One of the difficulties of the $pp \rightarrow np\pi^+$ analysis comes from the unexpected inefficiency problem as a function of the π^+ angle and a not fully suited trigger. In order to minimize the related effects and take properly the possible uncertainties into account, a specific analysis strategy including trigger correction and accurate error estimation and propagation were developed.

The results obtained for the $pp \rightarrow np\pi^+$ channel show an overall good agreement between the HADES data and the standard Pluto simulation, where the resonance model with Δ excitation in the one-π exchange assumption is implemented.

- The dominance of one-pion production via Δ resonance at 1.25 GeV has been clearly seen. Other contributions, such as $N^*(1440)$ and non-resonant pion production can also play a role, but the sensitivity of the HADES data to these contributions is small due to the strong dominance of the Δ.
- The neutron-proton final state interaction has been observed and has been satisfactorily reproduced by implementing the Jost function.
- The $N\pi$ invariant masses and neutron angular distributions show a fairly good agreement with the one-pion exchange model of Dmitriev *et al.* [Dmitriev and Sushkov, 1986]. However, a less forward/backward peaked Δ production angular distribution has been observed. By increasing the value of the cut-off parameter Λ_π=0.75 GeV, the measured data got nicely reproduced.
- Consistently with previous data, the HADES data favor a anisotropic Δ resonance decay. This has been concluded by considering of the measured yields and by studying the π^+ angular distribution in the (p, π^+) reference frame.

From the observations listed above, modifications of the Pluto simulation are proposed to better describe the data. The latter can be useful to have a precise estimation of the systematic errors for the $pp \rightarrow pp e^+ e^-$ channel. We would however like to mention that these changes should be validated simultaneously by the $pp \rightarrow pp\pi^0$ channel.

With the large statistics achieved, the mass and neutron angular distributions were extrapolated to full phase space using a 2-dimensional acceptance correction with a minimized model dependence. From the acceptance corrected spectra, a rather precise total cross section for the $pp \rightarrow np\pi^+$ channel has been extracted $\sigma = 18.17 \pm 1.85$ mb. This value has been compared to the available data and is found to be in full agreement.

The π angular distribution in the center-of-mass system has been studied as well. This study was triggered by the HADES results obtained with the $C+C$ experiments, and by the interpretation that the charged π angular distribution in the center-of-mass could reflect the thermalization of the system. Due to the π-angle dependent inefficiency observed in the $pp \rightarrow np\pi^+$ channel, a study of the center-of-mass π angular distribution would have needed a thorough investigation of systematic errors which was unfortunately not possible within the present time limit. However, these distributions were investigated in the $pp \rightarrow np\pi^+$ simulation. The results from this simulation show the same tends as observed in $C + C$ data, which leads to the conclusion that the smaller anisotropies observed at low $p_{\pi^+}^{CM}$ in the case of heavy-ion collisions can not be taken as a proof of the thermalization of the system.

The analysis work presented in this PhD was performed in the framework of a very simple resonance model, i.e. the Teis model [Teis et al., 1997], which is similar to the ones used in transport models. These exclusive data should be compared in the future to more sophisticated models, including all resonant and non-resonant graphs in a coherent way. Such a comparison should be made, for example, with the full OBE calculation [Shyam and Mosel, 2009], which were already used for the inclusive di-electron production. This would be an important consistency check of these models.

Another contribution that I also presented in this PhD is a simulation work on helicity angle distributions, which was proposed as a support to the data analysis of the Δ Dalitz decay exclusive measurements using pe^+e^- events. A distortion of the helicity angle distribution has been observed due to the ambiguously reconstructed Δ resonance, especially for the high di-electron masses. But it confirms that an anisotropy of the angular distribution close to 1 is expected in the case of exclusive Δ Dalitz decay analysis. This distribution can therefore be used as an additional proof of the dominance of the Δ Dalitz decay process. So, the conclusion that the Δ Dalitz decay was measured for the first time with a branching ratio in agreement with the QED calculation $(4.2 \cdot 10^{-5})$ seems to be confirmed. However, calculations of the distributions of pe^+e^- events and especially of the helicity distribution in pp bremsstrahlung process would be highly needed.

On the other hand, a dedicated simulation work has been done to give a reference to the preliminary results of helicity angle distribution carried out with inclusive e^+e^- event from the $ArKCl$ experiments. It confirms that the CM pseudo-helicity is a useful quantity to investigate the di-electron sources and distinguish sources in $1 + \cos^2\theta$, like Dalitz decay of Δ resonances from other sources, like pn bremsstrahlung, which are supposed to have lower or even negative anisotropies [Bratkovskaya et al., 1995].

During 2009-2010, HADES suspended the data production and has performed an upgrade of the detector. The new RPC detector was installed in the place of TOFINO detector since the former one provides a larger granularity. Also a new trigger and readout board (TRB) system has been implemented and tested. With this new system, it is possible to connect all types of detector readout boards and improves the overall data taking efficiency. In addition, the option that the current HADES PreShower detector could be replaced by an electromag-

netic calorimeter used in the former OPAL[1] experiment at LEP[2] is currently under investigation.

Taking benefit of the recent detector upgrade, HADES will now continue its program towards heavier systems. The $Ag + Ag$ run at 1.65 A GeV and $Au + Au$ run at 1.25 A GeV are scheduled in 2011, aiming at investigating the medium effect with the highest beam energies and largest system sizes. In the meantime, the πA experiments are also foreseen in 2013, to study the ρ and ω mesons spectral functions.

The work presented in this PhD demonstrated that the exclusive measurements performed with the elementary reactions are a powerful tool to constrain the models used to describe the elementary processes, as the ones used in transport models for heavy-ion studies. This is and will be in the future taken as one of the important goals of the HADES experiment. With the elementary reactions induced by pion beams, exclusive measurements will provide even more strict checks of the models and will bring information on di-electron production by baryonic resonances beyond the Δ.

[1] Omni-Purpose Apparatus at LEP
[2] Large ElectronPositron Collider

Annexe A

The isospin coefficients

$pp \to \Delta^+ p$	$pp \to \Delta^{++} n$
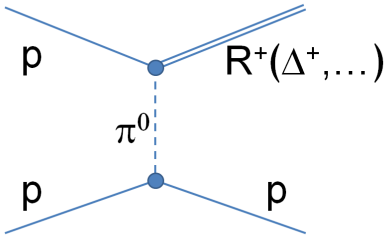	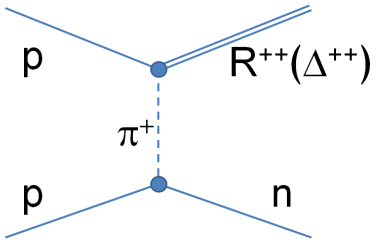
$p\pi^0\Delta^+ : \ \lvert C_{iso}\rvert \ = \ \sqrt{\frac{2}{3}}$ $p\pi^0 p : \ \lvert C_{iso}\rvert \ = \ 1$	$p\pi^+\Delta^{++} : \ \lvert C_{iso}\rvert \ = \ 1$ $p\pi^+ n : \ \lvert C_{iso}\rvert \ = \ \sqrt{2}$

TAB. A.1 – Isospin coefficients $|C_{iso}|$ in the $pp \to N\Delta$ process. $|C_{iso}|$ is given for each vertex.

$\Delta^+ \to p\pi^0$	$\Delta^+ \to n\pi^+$	$\Delta^{++} \to p\pi^+$
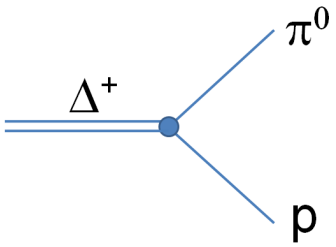	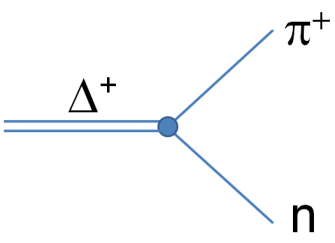	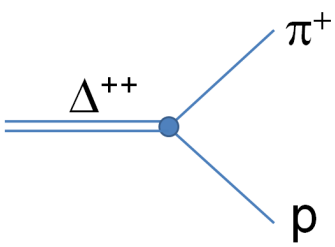
$p\pi^0\Delta^+ : \ \lvert C_{iso}\rvert \ = \ \sqrt{\frac{2}{3}}$	$n\pi^+\Delta^+ : \ \lvert C_{iso}\rvert \ = \ \sqrt{\frac{1}{3}}$	$p\pi^+\Delta^{++} : \ \lvert C_{iso}\rvert \ = \ 1$

TAB. A.2 – Isospin coefficients $|C_{iso}|$ for the Δ pionic decay vertex.

Annexe B

Helicity distribution definitions

The definition of the real helicity and pseudo helicity are described as following :
(1) "True" helicity : HADES helicity definition
- Proton, e^+ and e^- detected in lab frame, reconstruct γ^* in lab = $e^+ + e^-$ and Δ^+ in lab = proton + $e^+ + e^-$
- γ^* boosted to Δ^+ rest frame
- e^+/e^- boosted to the Δ^+ rest frame first, then to the γ^* (in Δ^+ rest frame) rest frame.
- Calculate $\cos\alpha$, where α is the helicity angle between e and γ^* as defined above

(2) Lab-pseudo helicity : Pseudo helicity with γ^* in lab, e^+/e^- in γ^* rest frame :
- e^+ and e^- detected in lab frame, reconstruct γ^* in lab = $e^+ + e^-$.
- e^+/e^- boosted to the γ^* rest frame.
- Calculate $\cos\alpha$, where α is the helicity angle between e and γ^* as defined above

(3) Pseudo helicity with γ^* in total center of mass frame (proton-proton CM), e^+/e^- in γ^* rest frame :
- e^+ and e^- detected in lab frame, reconstruct γ^* in lab = $e^+ + e^-$.
- γ^* boosted to the pp CM rest frame.
- e^+/e^- boosted to pp CM, then to the γ^* (in CM frame) rest frame.
- Calculate $\cos\alpha$, where α is the helicity angle between e and γ^* as defined above

Liste des tableaux

Table des figures

Bibliographie

S. Abd El-Samad et al. "Single-pion production in *pp* collisions at 0.95 GeV/c (II)". *Eur. Phys. J.*, A39 :281–289, 2009.

S. Abd El-Samad et al. "Single-pion production in *pp* collisions at 0.95 GeV/c (I)". *Eur. Phys. J.*, A30 :443–453, 2006.

G. Agakichiev et al. (HADES collaboration) "Dielectron production in $^{12}C +^{12} C$ collisions at 2 A GeV with HADES". *Phys. Rev. Lett.*, 98 :052302, 2007.

G. Agakichiev et al. (HADES collaboration) "Study of dielectron production in $^{12}C +^{12} C$ collisions at 1 A GeV". *Phys. Lett.*, B663 :43–48, 2008.

G. Agakichiev et al. (HADES collaboration) "Deep sub-threshold Xi-production in $Ar + KCl$ reactions at 1.76 A GeV". *Phys. Rev. Lett.*, 103 :132301, 2009a.

G. Agakichiev et al. (HADES collaboration) "Measurement of charged pions in $^{12}C +^{12} C$ collisions at 1 A GeV and 2 A GeV with HADES". *Eur. Phys. J.*, A40 :45–59, 2009b.

G. Agakichiev et al. (HADES collaboration) "The High-Acceptance Dielectron Spectrometer HADES". *Eur. Phys. J.*, A41 :243–277, 2009c.

G. Agakichiev et al. (HADES collaboration) "Origin of the low-mass electron pair excess in light nucleus-nucleus collisions.". *Phys. Lett.*, B690 :118–122, 2010.

D. Albers et al. "A precision measurement of pp elastic scattering cross sections at intermediate energies". *Eur. Phys. J.*, A22 :125–148, 2004.

BABAR Collaboration. "EvtGen A Monte Carlo Generator for B-Physics". Technical report, 2007.

T.C. Bacon, F. M. Bomse, T. B. Cochran, W. J. Fickinger, E. R. Goza, H. W. K. Hopkins, and E. O. Salant. "Comparison of isobar production in *pp* anf $\bar{p}n$ interactions at 2.8 GeV/c". *Phys. Rev.*, 162(9) :1320–1322, May 1967.

A. Baldini et al. *"Total cross sections for reactions of high energy particles (including elastic, topological, inclusive and exclusive reactions)"*. Springer, Berlin, 1988.

E. L. Bratkovskaya and W. Cassing. "Dilepton production and off-shell transport dynamics at

SIS energies". *Nucl. Phys.*, A807 :214, 2008.

E. L. Bratkovskaya, O. V. Teryaev, and V. D. Toneev. "Anisotropy of dilepton emission from nuclear collisions". *Phys. Lett.*, B348 :283–289, 1995.

E. L. Bratkovskaya, W. Cassing, R. Rapp, and J. Wambach. "Dilepton production and m(T)-scaling at BEVALAC/SIS energies". *Nucl. Phys.*, A634 :168–189, 1998.

T. Bretz. *"Magnetfeldeigenschaften des Spektrometers HADES"*. PhD thesis, Technische Universität München, 1999.

G. E. Brown and Mannque Rho. "Scaling effective Lagrangians in a dense medium". *Phys. Rev. Lett.*, 66 :2720–2723, 1991. doi : 10.1103/PhysRevLett.66.2720.

R. Brun and F. Rademakers. "ROOT, an object-orientied data analysis framework". *Nucl. Instr. Meth.*, A389 :81, 1997.

D. V. Bugg et al. "Proton-proton scattering at 970 MeV". *Phys. Rev.*, 133 :B1017–B1031, 1964.

H. Clement et al. "Evidence for a 'narrow' Roper resonance - the breathing mode of the nucleon". *arXiv :nucl-ex/0612015v1*, 2006.

M. D. Cozma, C. Fuchs, E. Santini, and A. Faessler. "Dilepton production at HADES : theoretical predictions". *Phys. Lett.*, B640 :170–175, 2006.

R. Dahl. "Angular correlations in Δ decay". Master's thesis, 1995.

V. Dmitriev and O. Sushkov. "Δ-formation in the ${}^1H({}^3He,{}^3H)\Delta^{++}$ reaction at intermediate energies". *Nuclear Physics A*, 459 :503–524, 1986.

A. M. Eisner, E. L. Hart, R. I. Louttit, and T. W. Morris. "Proton-proton scattering at 1.48 BeV". *Phys. Rev.*, 138(3B) :B670–B677, May 1965.

C. Ernst, S. A. Bass, M. Belkacem, H. Stoecker, and W. Greiner. "Intermediate mass excess of dilepton production in heavy ion collisions at BEVALAC energies". *Phys. Rev.*, C58 :447–456, 1998.

E. Ferrari and F. Selleri. "Pionic Form Factor Effects in Peripheral Nucleon-Nucleon Collisions". *Phys. Rev. Lett.*, 7 :387–390, 1961.

W. J. Fickinger, E. Pickup, D. K. Robinson, and E. O. Salant. "p-p Interactions at 2 Bev. I. Single-Pion Production". *Phys. Rev.*, 125 :2082–2090, 1962.

I. Froehlich et al. "A versatile method for simulating $pp \rightarrow ppe^+e^-$and $dp \rightarrow pne^+e^-p_{spec}$ reactions". arXiv :0909.5373[nucl-ex].

I. Froehlich et al. "Pluto : A Monte Carlo Simulation Tool for Hadronic Physics". *PoS*,

ACAT2007 :076, 2007.

I. Froehlich et al. "Design of the Pluto Event Generator". *J. Phys. Conf. Ser.*, 219 :032039, 2010.

T. Galatyuk. *"Di-electron spectroscopy in HADES and CBM : from $p+p$ and $n+p$ collisions at GSI to $Au+Au$ collisions at FAIR"*. PhD thesis, Johann Wolfgang Goethe-Universität Frankfurt am Main, 2009.

C. Gale and J. Kapusta. "Dilepton radiation from high temperature nuclear matter". *Phys. Rev.*, C35 :2107, 1987.

K. Gottfried and John David Jackson. "On the connection between production mechanism and decay of resonances at high-energies". *Nuovo Cim.*, 33 :309–330, 1964.

T. Hatsuda and S. H. Lee. "QCD sum rules for vector mesons in nuclear medium". *Phys. Rev.*, C46 :34–38, 1992. doi : 10.1103/PhysRevC.46.34.

S. Huber and J. Aichelin. "Production of Delta and N^* resonances in the one boson exchange model". *Nucl. Phys.*, A573 :587–625, 1994.

J. Hudomalj-Gabitzsch et al. "Production of the Δ^{++} in the reaction $pp \to p\pi^+ n$ at 800 MeV". *Phys. Rev.*, C18 :2666, 1978.

Hughes et al. *Phys. Mag.*, 2 :344, 1957.

L. P. Kaptari and B. Kämpfer. "Di-electron bremsstrahlung in intermediate-energy pn and dp collisions". *Nucl. Phys.*, A764 :338–370, 2006.

L. P. Kaptari and B. Kämpfer. "Di-Electrons from resonances in nucleon-nucleon collisions". *Phys. Rev.*, c80 :064003, 2009.

A. König and P. Kroll. "A study of single pion production in nucleon-nucleon collisons". *Nucl. Phys.*, A356 :345–364, 1981.

M. I. Krivoruchenko and A. Faessler. "Comment on Delta radiative and Dalitz decays". *Phys. Rev.*, D65 :017502, 2002.

M. I. Krivoruchenko, B. V. Martemyanov, A. Faessler, and C. Fuchs. "Electromagnetic transition form factors and dilepton decay rates of nucleon resonances". *Annals Phys.*, 296 :299–346, 2002.

K. Lapidus. *"Analysis of di-electron production in dp interactions at 1.25 GeV/u" with HADES" (in preparation).* PhD thesis, Institut of Nuclear Research, Russian Academy of Science, Moskow, Russia.

S. Leupold, V. Metag, and U. Mosel. "Hadrons in strongly interacting matter". *Int. J. Mod.*

Phys., E19 :147–224, 2010.

T. Liu et al. (HADES collaboration) "Hadronic channels measured with HADES in the p+p reaction at 1.25 GeV ". Bormio conference proceedings vol. 99, SIF, Bologna, 2010a. XLVII International winter meeting on nuclear physics, Bormio (Italy), Jan. 26-30, 2009.

T. Liu et al. (HADES collaboration) "Study of the $pp \to np\pi^+$ reaction at 1.25 GeV with HADES". arXiv :0909 :3399, 2010b. 12th International conference on nuclear reaction mechanisms, Varenna, Villa Monastero, Italy, 15-19 Jun 2009.

J. Markert. *"Untersuchung zum Ansprechverhalten der Vieldraht-Driftkammern niedriger Massenbelegung des HADES-Experiments"*. PhD thesis, 2005.

B. Martemyanov. private communication, 2009.

V. Metag. "Medium modifications of vector mesons in elementary reactions and heavy-ion collisions". *J. Phys.*, G34 :S397–S404, 2007.

E. J. Moniz and A. Sevgen. "Pauli blocking in the nuclear medium πN transition matrix". *Phys. Rev.*, C24 :224–230, 1981.

E. Morinière. *"Contribution à l'analyse de réactions de productions de dileptons en collision proton-proton avec HADES"*. PhD thesis, Université Paris XI, 2008.

K. Nakamura et al. (Particle Data Group). *J. Phys.*, G37 :075021, 2010.

R. J. Porter et al. "Dielectron cross section measurements in nucleus nucleus reactions at 1.0 A GeV". *Phys. Rev. Lett.*, 79 :1229–1232, 1997.

D. L. Prout et al. "Spin decomposition of the Δ resonance cross section using the $^{12}C(p(\text{polarized}), n(\text{polarized}))$ reaction at $E_p = 795$ MeV". *Phys. Rev. Lett.*, 76 :4488–4491, 1996.

W. Przygoda. (HADES collaboration) "Exclusive $\text{pp}e^+e^-$ channel from $p + p$ reaction at 1.25 GeV". *GSI scientific report*, 2009.

B. Ramstein et al. (HADES collaboration) "Study of elementary reactions with the HADES dielectron spectrometer ". Acta Phys. Polon. B41 :365-378, 2010. Mazurian Lakes Conference on Physics, Piaski, Poland, August 30 - September 6, 2009.

R. Rapp and J. Wambach. "Low mass dileptons at the CERN-SPS : Evidence for chiral restoration ?". *Eur. Phys. J.*, A6 :415–420, 1999.

R. Rapp, J. Wambach, and H. van Hees. "The chiral restoration transition of QCD and low mass dileptons". 2009.

J. J. Sakurai. "Vector-meson dominance and high-energy electron-proton inelastic scattering".

Phys. Rev. Lett., 22(18) :981–984, May 1969.

V. V. Sarantsev et al. "The study of the neutral pion production in proton proton collisions at beam momenta 1581-MeV/c and 1683-MeV/c". *Eur. Phys. J.*, A21 :303–312, 2004.

K. Schmidt et al. "Production and evolution path of dileptons at energies accessible to the HADES detector". *Phys. Rev.*, C79 :064908, 2009.

F. Shimizu et al. "Study of *pp* interactions in the momentum range 0.9 GeV/c to 2.0 GeV/c". *Nucl. Phys.*, A389 :445, 1982.

R. Shyam and U. Mosel. "Dilepton production in proton-proton and quasi-free proton-neutron reactions at 1.25 GeV". *arXiv :1006.3873*, 2010.

R. Shyam and U. Mosel. "Role of baryonic resonances in the dilepton emission in nucleon nucleon collisions". *Phys. Rev.*, C67 :065202, 2003.

R. Shyam and U. Mosel. "Dilepton production in nucleon-nucleon collisions revisited". *Phys. Rev.*, C79 :035203, 2009.

T. Skorodko. *"Production of $\pi^0\pi^0$ and $\pi^+\pi^+$ pairs in proton-proton collisions"*. PhD thesis, University of Santiago de Compostela, 2009.

S. Teis et al. "Pion-production in heavy-ion collisions at SIS energies". *Z. Phys.*, A356 :421–435, 1997.

M. Thomère, C. Hartnack, G. Wolf, and J. Aichelin. "Analysis of dilepton invariant mass spectrum in $C + C$ at 2 and 1 A GeV". *Phys. Rev.*, C75 :064902, 2007.

L. Tiator et al. "Electromagnetic form factor of the $\Delta(1232)$ excitation". *Eur. Phys. J.*, A17 : 357–363, 2003.

A. I. Titov, B. Kämpfer, and B. L. Reznik. "Production of ϕ mesons in near-threshold πN and NN reactions". *Eur. Phys. J.*, A7 :543–557, 2000.

J. Van de Wiele. *"Rotations et moments angulaires en mécanique quantique"*. EDP Sciences S.A., 2002.

J. Van de Wiele and B. Ramstein. private communication, 2009.

Q. Wan and F. Iachello. "A unified description of baryon electromagnetic form factors". *Int. J. Mod. Phys.*, A20 :1846–1849, 2005.

A. B. Wicklund et al. "Study of the reaction p(polarized)$p \to p\pi^+ n$ with polarized beam from 3 to 12 GeV/c". *Phys. Rev.*, D34 :19, 1986.

A. B. Wicklund et al. "Study of the reaction p(polarized)$p \to p\pi^+ n$ with polarized beam from

1.18 GeV/c to 1.98 GeV/c". *Phys. Rev.*, D35 :2670, 1987.

W. Wilson. "Inclusive dielectron cross sections in $p+p$ and $p+d$ interactions at beam energies from 1.04 to 4.88 GeV". *Phys. Rev.*, C57 :1865, 1998.

M. Wiśniowski. *"Pomiar produkcji mezonów π^0/η w realcji $p+p$ przy energii 2.2 GeV za pomo ca spektrometru HADES"*. PhD thesis, Jagiellonian university of Cracow, Poland, 2009.

O. Zhen et al. "Role of the $N^*(1440)$ resonance in the $pp \to np\pi^+$ reaction". *Nucl. Phys.*, A821 : 220–234, 2009.

Résumé

L'étude précise de la décroissance pionique et la première mesure de décroissance Dalitz de la résonance $\Delta(1232)$ sont obtenues par la collaboration HADES (High Acceptance Di-Electron Spectrometer) à GSI, Darmstadt. HADES a développé dans les dernières années un programme de réactions élémentaires visant à fournir une information sélective sur les différentes sources d'émission d'électrons en complément des expériences en ions lourds. Les mesures discutées dans cette thèse se réfèrent à l'étude des collisions proton-proton à une énergie de faisceau de 1.25 GeV. Cette énergie, juste en dessous du seuil de production du η, est adaptée à l'étude de la décroissance Dalitz du Δ, qui est l'une des sources importantes d'émission d'électrons dans la région de masse intermédiaire ($0.15\ \mathrm{GeV}/c^2 < M_{e^+e^-} < 0.5\ \mathrm{GeV}/c^2$). Pour valider les sections efficaces et les mécanismes de la production de Δ utilisées dans l'étude de la décroissance Dalitz du Δ, l'analyse complète de la $pp \to np\pi^+$ réaction à 1.25 GeV a été réalisée, ce qui constitue la contribution principale de cette thèse. Les résultats, e.g. la distribution en masse, en angle après correction d'acceptance de la production $pp \to N\Delta$ et les distributions angulaires de la décroissance $\Delta \to N\pi$ sont montrées et les comparaisons aux modèles sont discutées. Une autre contribution de cette thèse est une étude de simulation des distributions d'angle d'hélicité, qui a été proposée d'une part comme un support à l'analyse exclusive de la décroissance Dalitz du Δ et d'autre part comme une référence à des résultats préliminaires de distribution d'angle d'hélicité obtenus dans les mesures inclusives de di-électrons dans les collisions $Ar + KCl$.

Abstract

The detailed study of the pionic decay and the first measurement of Dalitz decay of $\Delta(1232)$ resonance have been carried out with the High Acceptance Di-Electron Spectrometer (HADES) at GSI, Darmstadt. HADES developed in the last years an elementary reaction program aimed at providing selective information on different sources of di-electron emission as a complement to the heavy-ion experiments. The measurements discussed in this thesis refer to one experiment in this program, the study of proton-proton collisions at a kinetic beam energy of 1.25 GeV. This energy is chosen just below the η production threshold and devoted to study the Δ Dalitz decay, which is one of the main sources of di-electron emission at intermediate e^+e^- invariant masses (0.15 GeV/$c2 < M_{e^+e^-} < 0.5$ GeV/$c2$). To provide a control of the cross sections and on the Δ resonance production mechanisms required by the study of the Δ Dalitz decay process, the full analysis of the $pp \rightarrow np\pi^+$ at 1.25 GeV has been performed, which is the main contribution of this PhD work. The results, such as the acceptance corrected mass and angular distributions of the $pp \rightarrow N\Delta$ process and the $\Delta \rightarrow N\pi$ decay angular distribution are shown and the comparisons to models are discussed. Another contribution of this PhD is a simulation study on helicity angle distributions, which was proposed on the one hand as a support to the data analysis of the Δ Dalitz decay exclusive measurements and on the other hand as a reference to the preliminary results of helicity angle distribution obtained with inclusive e^+e^- in $Ar + KCl$ collisions.